Higher-order accurate and locking-free explicit dynamics in isogeometric structural analysis

A THESIS
SUBMITTED TO DEPARTMENT OF CIVIL AND ENVIRONMENTAL ENGINEERING
OF THE TECHNICAL UNIVERSITY OF DARMSTADT
BY

Thi-Hoa Nguyen

IN FULFILLMENT OF THE REQUIREMENTS
FOR THE DEGREE OF
DOKTOR-INGENIEUR (DR.-ING.)

First referee: Prof. Dr.-Ing. Dominik Schillinger

Second referee: Prof. Dr.-Ing. Josef Kiendl

TECHNISCHE
UNIVERSITÄT
DARMSTADT

Darmstadt, 2023

Thi-Hoa Nguyen
Higher-order accurate and locking-free explicit dynamics in isogeometric structural analysis

Darmstadt, Technical University of Darmstadt
Published year on TUprints: 2023
Date of thesis defense: November 29, 2023

`URN`: urn:nbn:de:tuda-tuprints-264017
`URI`: https://tuprints.ulb.tu-darmstadt.de/id/eprint/26401

Higher-order accurate and locking-free explicit dynamics in isogeometric structural analysis

Submitted doctoral thesis by Thi-Hoa Nguyen from Hanoi, Vietnam

In fulfillment of the requirements for the degree of Doktor-Ingenieur (Dr.-Ing.)

Date of submission: September 28, 2023

Date of thesis defense: November 29, 2023

Primary advisor: Prof. Dr.-Ing. Dominik Schillinger

Committee members:

Prof. Dr.-Ing. Dominik Schillinger	Technical University of Darmstadt
Prof. Dr.-Ing. Josef Kiendl	University of the Bundeswehr Munich
Prof. Dr.-Ing. Ralf Müller	Technical University of Darmstadt
Prof. Dr.-Ing. Friedrich Gruttmann	Technical University of Darmstadt
Prof. Eva Kaßens-Noor	Technical University of Darmstadt

Acknowledgements

This thesis has been carried out during my occupation at the Institut für Baumechanik und Numerische Mechanik, Leibniz Universität Hannover, and the Institut für Mechanik, Technische Universität Darmstadt. I would like to express my deepest gratitude to the exceptional individuals who supported and guided me throughout this transformative journey.

First and foremost, I would like to thank my supervisor and mentor, Prof. Dr.-Ing. **Dominik Schillinger**, for his unwavering support, patience, and valuable advice. Thank you very much for guiding me through the entire journey and for the opportunity to follow this work. Your guidance and advice have kept me on an academic track, provided me with plenty of encouragement, and greatly contributed to my development.

Second, I would like to thank my co-mentor and colleague, **René Hiemstra**, for his guidance and support. I highly appreciate our discussions and ideas, which essentially helped to develop this work. Your broad knowledge gave me a lot of material to think about.

In addition, I also want to thank **Stein Stoter, Sascha Eigenträger, Bruno Roccia, and Cristian Gebhardt** for their collaboration on several parts of this work. Cristian and Bruno, thank you for arranging and hosting my visit to your research group at Bergen Offshore Wind Centre, University of Bergen. I am deeply grateful for the knowledge and friendships during that time, which have been and will remain one of the most enjoyable experiences during my journey.

Furthermore, I would like to thank my colleagues in Hannover and Darmstadt for making this journey a pleasant time. **Marco, Tarun, Adnan, Etienne, Mika, Vahid**, and others, thank you for our tea/coffee breaks, nice dinners, activities, and trips. Thank you for your valuable advice and interesting discussions.

Lastly, I wish to express my thanks to **my family and friends** for their unconditional and most appreciated support throughout the years, particularly for their encouragement and affection, without which this work could not have been completed.

Thi-Hoa Nguyen
Darmstadt, September, 2023

Abstract

Explicit structural dynamics codes simulating, for example, crash-tests and metal forming processes rely on the spectral properties of the chosen finite elements combined with locking-preventing mechanisms, such as reduced quadrature, to achieve higher-order spatial accuracy. To achieve highly efficient computations, these codes rely on three key ingredients: (1) low memory requirements; (2) an efficient solver; and (3) relatively large critical time step values. These three ingredients are present in contemporary linear finite element codes based on mass lumping, which, however, generally limits the spatial accuracy to second order. Overcoming this limitation to obtain a higher-order accurate and locking-free explicit scheme is the main objective of this work. We focus on isogeometric discretizations which are particularly attractive for higher-order accuracy due to their well-behaved spectral properties.

To this end, this thesis accomplishes the following tasks: (i) We propose to "measure" locking by assessing the spectral accuracy of different finite element discretizations. (ii) We introduce a variational approach based on perturbed eigenvalue analysis for improving spectral properties of isogeometric multipatch discretizations. (iii) We develop an isogeometric Petrov-Galerkin formulation that enables higher-order spatial accuracy in explicit dynamics when the mass matrix is lumped, and (iv) we extend this approach to a Hellinger-Reissner mixed formulation, attempting to eliminate membrane locking for Kirchhoff-Love shells.

In the first task, we use eigenvalue and mode errors to assess five finite element formulations in terms of their locking-related efficiency: the displacement-based formulation with full and reduced integration, the B-bar, discrete strain gap, and Hellinger-Reissner methods. In the second task, we demonstrate that our approach allows for a much larger critical time step size in explicit dynamics calculations, which does not depend on the polynomial degree of spline basis functions. In the third task, we discretize the test functions using the so-called "approximate" dual functions that are smooth, have local support, and satisfy approximate bi-orthogonality with respect to a trial space of B-splines. This enables higher-order accurate mass lumping using the standard row-sum technique. In the last task, to increase efficiency, we integrate a boundary treatment with built-in Dirichlet boundary constraints, a strong outlier removal approach to increase the critical time step size, and a reduced quadrature rule with a minimal number of quadrature points. We numerically demonstrate, via spectral analysis and convergence studies of beam, plate, and shell models, that our Petrov-Galerkin approach leads to higher-order accurate and locking-free computations in explicit dynamics. In addition, we extend the horizon of this work by exploring the application of isogeometric analysis, together with the outlier removal approach, to nonlinear dynamics of shear- and torsion-free rods, combining with a robust implicit time integration scheme.

Zusammenfassung

Explizite Simulationsprogramme zur Strukturdynamik, die beispielsweise bei Crashtests oder Metallumformprozessen zum Einsatz kommen, basieren auf den spektralen Eigenschaften der ausgewählten finiten Elemente in Kombination mit Methoden zur Vermeidung von Locking-Phänomenen, um eine räumliche Genauigkeit höherer Ordnung zu erreichen. Eine der am meisten verwendeten Methoden ist die reduzierte Quadratur. Zur Erreichung hocheffizienter Berechnungen verfolgen explizite Simulationsprogramme drei Hauptstrategien: (1) geringer Speicherbedarf; (2) ein effizienter Löser; und (3) relativ große kritische Zeitschrittwerte. Diese drei Bestandteile sind in modernen linearen Finite-Elemente-Programmen vorhanden, die auf Massenmatrizen mit Massenkonzentration basieren, was jedoch im Allgemeinen die räumliche Genauigkeit auf zweite Ordnung beschränkt. Das Hauptziel dieser Arbeit besteht darin, diese Einschränkung zu überwinden, um ein präzises und lockingfreies explizites Schema höherer Ordnung zu erhalten. Der Schwerpunkt liegt auf isogeometrischen Diskretisierungen, die aufgrund ihrer guten spektralen Eigenschaften besonders attraktiv für die Genauigkeit höherer Ordnung sind.

Daher wird sich in dieser Arbeit auf die folgenden Aufgaben fokussiert: (i) Wir schlagen vor, die Locking-Effekte zu „messen“, indem wir die spektrale Genauigkeit verschiedener Diskretisierungen bewerten. (ii) Wir führen einen auf der gestörten Eigenwertanalyse basierenden Variationsansatz ein, um die spektralen Eigenschaften isogeometrischer Multipatch-Diskretisierungen zu verbessern. (iii) Wir entwickeln eine isogeometrische Petrov-Galerkin-Formulierung, die eine räumliche Genauigkeit höherer Ordnung bei der Verwendung konzentrierter Massen in der expliziten Dynamik ermöglicht, und (iv) wir erweitern diese Formulierung auf eine gemischte Hellinger-Reissner Mehrfeldformulierung, um das Membran-Locking-Phänomen für die Kirchhoff-Love-Schalenelemente zu eliminieren.

Im ersten Teil der Arbeit verwenden wir die Genauigkeit der Eigenwerte und Eigenmoden zur Bewertung von fünf Formulierungen hinsichtlich ihrer lockingbezogenen Effizienz: die verschiebungsbasierte Formulierung mit vollständiger und reduzierter Integration, die B-Bar-Methode, die Discrete-Strain-Gap-Methode und die Hellinger-Reissner-Methode. Im zweiten Teil der Arbeit zeigen wir, dass unser Variationsansatz viel größere kritische Zeitschritte in expliziten Dynamikberechnungen ermöglicht, wobei die kritische Größe der Zeitschritte nicht vom Polynomgrad der Spline-Ansatzfunktionen abhängt. Im dritten Teil der Arbeit diskretisieren wir die Testfunktionen mithilfe der sogenannten „approximate dual Spline“-Funktionen, die glatt sind, lokalen Träger haben und eine ungefähre Bi-Orthogonalität in Bezug auf die zugeordneten B-Splines erfüllen. Dies ermöglicht eine genaue Konzentration der Massenmatrix höherer Ordnung unter Verwendung der standardmäßigen Zeilensummen-Methode. Im letzten Teil der Arbeit kombinieren wir zur Steigerung der Effizienz die gemischte Mehrfeldformulierung mit einer Behandlung von Dirichlet-Randbedingungen, einem starken Outlier-Entfernungsansatz zur Erhöhung der kritischen Zeitschritte und einer reduzierten Quadratur mit einer minimalen Anzahl von Integrationspunkten. Mithilfe von Spektralanalysen und Konvergenzstudien von Balken-, Platten- und Schalenmodellen zeigen wir numerisch, dass unser Ansatz zu präzisen und lockingfreien Berechnungen höherer Ordnung in der expliziten Dynamik führt. Darüber hinaus erweitern wir den Horizont dieser Arbeit, indem wir die Anwendung der isogeometrischen Analyse im Zusammenhang mit dem Outlier-Entfernungsansatz in der nichtlinearen Dynamik von scher- und torsionsfreien Stäben untersuchen und mit einem robusten impliziten Zeitintegrationsschema kombinieren.

Contents

1 A short introduction to isogeometric analysis

Before presenting the main research themes and objectives of this thesis in the next chapter, we briefly introduce the fundamental concept of isogeometric analysis (IGA) and its terminology, which are required throughout this work. We begin, in Section 1.1, with a brief review of the spline basis functions and their properties that are important in design and analysis. In Section 1.2, we then briefly review the basis in geometry representation that goes hand in hand with IGA. Lastly, in Section 1.3, we recall the most important concepts in analysis using isogeometric finite elements.

1.1 Spline basis functions

Spline basis functions provide the basis for geometric modeling and isogeometric analysis. We now briefly review their formulation and their most important properties in this context.

1.1.1 B-splines

A B-spline, or basis spline, is a piecewise polynomial function that is characterized by the polynomial degree, its smoothness, and its domain partition [1], [2]. Let $\Xi = [\xi_0, \ldots, \xi_m]$ denote a non-decreasing sequence of real numbers in an interval $I = [a, b] \subset \mathbb{R}$, that is:

$$a = \xi_0 \leq \ldots \leq \xi_{j-1} \leq \xi_j \leq \ldots \leq \xi_m = b\,. \tag{1.1}$$

ξ_j is called the j^{th}–*knot* and Ξ is the *knot vector*. The interval $[\xi_0,\, \xi_m]$ is called a *patch*. The i^{th}–B-spline basis function of degree p, denoted $N_{i,p}(\xi)$, $i = 1, \ldots, M$, is recursively defined using the Cox-de Boor formula as follows:

$$p = 0: \quad N_{i,p=0}(\xi) = \begin{cases} 1, & \xi_i \leq \xi < \xi_{i+1}\,, \\ 0, & \text{otherwise,} \end{cases} \tag{1.2a}$$

$$p \geq 1: \quad N_{i,p}(\xi) = \frac{\xi - \xi_i}{\xi_{i+p} - \xi_i}\, N_{i,p-1}(\xi) + \frac{\xi_{i+p+1} - \xi}{\xi_{i+p+1} - \xi_{i+1}}\, N_{i+1,p-1}(\xi)\,. \tag{1.2b}$$

Figure 1.1 illustrates an example of cubic B-spline basis functions defined on a knot vector of $\Xi = [0.0, 0.0, 0.0, 0.0, 0.25, 0.50, 0.75, 1.0, 1.0, 1.0, 1.0]$. Such knot vectors with uniformly spaced knots are called *uniform* knot vectors. Otherwise, they are called *non-uniform.* The knot vector of this example has the first and last knots repeated $p + 1$

times, while the interior knots are non-repeated. This kind of knot vector is called an *open* knot vector. Basis functions defined on open knot vectors are interpolatory at the left and right ends, but generally are not interpolatory at the interior knots, as shown in Figure 1.1. If a knot has a multiplicity of k, $k \geq 1$, the basis function is C^{p-k}–continuous at that position. Hence, the maximal regularity of B-spline basis functions of degree p is C^{p-1}.

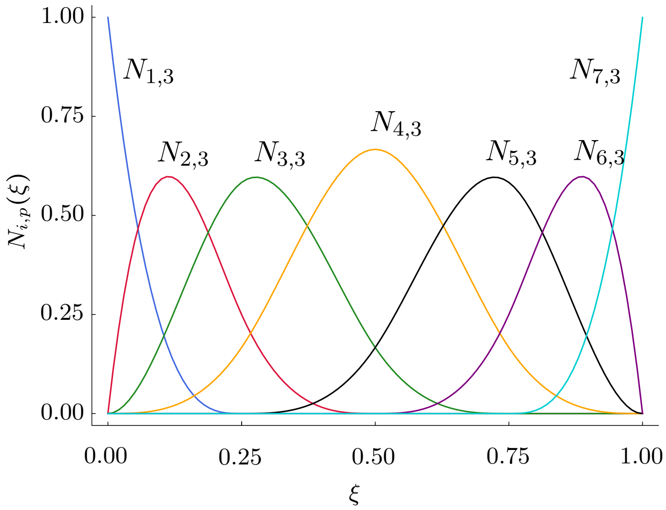

Figure 1.1: A basis of cubic C^2 B-splines defined on an open, uniform knot vector of $\Xi = [0.0, 0.0, 0.0, 0.0, 0.25, 0.50, 0.75, 1.0, 1.0, 1.0, 1.0]$.

Other important properties of B-splines, which are useful in design and analysis, are:

- Partition of unity, i.e. $\sum_{i=1}^{M} N_i(\xi) = 1, \ \forall \, \xi$.
- Local support, i.e. $N_i(\xi) \neq 0 \ \forall \, \xi \in [\xi_i, \xi_{i+p+1}]$ and $N_i(\xi) = 0 \ \forall \, \xi \notin [\xi_i, \xi_{i+p+1}]$.
- Non-negativity, i.e. $N_i(\xi) \geq 0, \ \forall \, \xi$.

1.1.2 Non-uniform rational B-spline basis functions

The non-uniform rational B-spline (NURBS) basis functions of degree p, denoted as $R_{i,p}$, $i = 1, \ldots, M$, are defined as follows [1], [2]:

$$R_{i,p}(\xi) = \frac{N_{i,p}(\xi) \, w_i}{\sum_{i=1}^{M} N_{i,p}(\xi) \, w_i} \, , \tag{1.3}$$

where $N_{i,p}$ is the corresponding B-spline basis function, defined in (1.2), and w_i is its weight. While the term non-uniform refers to the knot vector, rational B-spline indicates that NURBS consists of piecewise rational polynomials. When all weights are equal, NURBS basis functions become B-spline basis functions. Hence, B-splines can be considered a special case of NURBS. If the weights are non-negative, which is typically

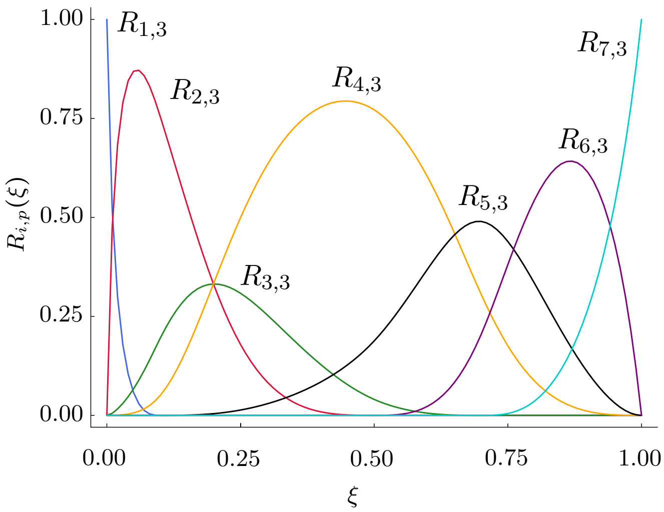

Figure 1.2: A basis of cubic C^2 NURBS defined on an open, non-uniform knot vector of $\Xi = [0.0, 0.0, 0.0, 0.0, 0.1, 0.5, 0.7, 1.0, 1.0, 1.0, 1.0]$ with the weights w_i, $i = 1, \dots, 7$, $[0.4, 1.0, 0.5, 1.5, 0.75, 1.25, 1.0]$.

the case, they inherit properties such as continuity and local supports from each other. Figure 1.2 illustrates an example of cubic NURBS basis functions defined on an open, non-uniform knot vector with positive weights. We observe that these functions inherit the C^2-continuity and local support property of the corresponding cubic B-splines. NURBS basis functions that are defined on an open knot vector, also constitute a partition of unity. NURBS are able to represent free-form shapes, sharp edges, and kinks, as well as spheres, cylinders, etc. [1], [2] Thus, they are established in standard CAD models and are the broadest technology employed in CAD programs.

1.2 Geometry representation

The most common geometry description in computer-aided design (CAD) is the boundary representation (B-rep), where the object is presented by its bounding surfaces rather than by volume elements [3]. The construction of these surfaces is typically independent of each other and involves trimming that “cut away” the superfluous areas, i.e. regions that are not parts of the actual object. We start with a brief recap of the construction of fundamental objects such as curves and surfaces, before discussing the main aspects and challenges regarding trimmed geometries.

1.2.1 Curves and surfaces

Consider a set of n points $\mathbf{P}_1, \dots, \mathbf{P}_n$. An arbitrary curve can be represented as a parametric curve that is a linear combination of basis functions of polynomial degree p,

$B_{i,p}(\xi)$, $i = 1, \ldots, n$, and these points $\mathbf{P}_i$:

$$\mathbf{C}(\xi) = \sum_{i=1}^{n} B_{i,p}(\xi)\, \mathbf{P}_i\,. \tag{1.4}$$

The points $\mathbf{P}_i$ are called *control points* and can be considered as the geometric coefficients of the curve. The curve $\mathbf{C}(\xi)$ is a vector-valued function of the parameter ξ, that maps a straight line segment in the parametric domain into the Euclidean two-dimensional space.

One possible choice of the basis functions $B_{i,p}(\xi)$ in (1.4) is the Bernstein polynomials [4], [5], which results in the so-called Bézier curve [1], [2], [6]. The definition of these polynomials requires that $\xi \in [0,1]$, and their polynomial degree p depends linearly on the number of control points: $p = n-1$. Hence, a direct consequence is that increasing the number of control points requires a higher polynomial degree. Furthermore, since the polynomial spans over the complete domain $[0,1]$, modifying one control point affects the whole curve, i.e. no local changes are possible. Instead of the Bernstein polynomials, one can employ B-spline or NURBS, reviewed in the previous section, as basis functions to represent the curve (1.4) [1], [2]. Since these spline basis functions are defined piecewise on an arbitrary number of intervals, the polynomial degree and the number of control points can be chosen independently, and local changes are possible. Furthermore, since the smoothness of the resulting spline curve is defined by that of the basis functions and their continuity between intervals, modifying the control points does not alter the curve continuity. In Figure 1.3, we illustrate an example of a B-spline curve, expressed by (1.4), that is defined by basis functions in Figure 1.1. We observe in Figure 1.3b that modifying the last control point solely affects the last segment of the curve while other segments remain unchanged.

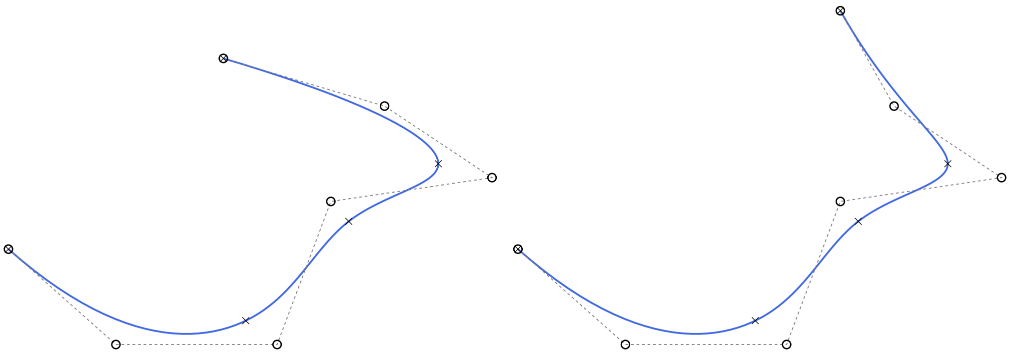
(a) Initial curve

(b) Modification of the last control point

Figure 1.3: A B-spline curve defined with cubic C^2 B-splines in Figure 1.1 and its control net (dotted). Local change is possible for spline curves (b).

To construct surfaces, the most common and widely applied method in geometric modeling applications is the tensor product method. Consider a net of $n \times m$ control points $\mathbf{P}_{11}, \ldots, \mathbf{P}_{nm}$, a tensor-product surface can be expressed as [1], [2]:

$$\mathbf{S}(\xi_1, \xi_2) = \sum_{i=1}^{n} \sum_{j=1}^{m} B_{1,i}(\xi_1)\, B_{2,j}(\xi_2)\, \mathbf{P}_{ij}\,, \tag{1.5}$$

where $B_{1,i}(\xi_1)$ and $B_{2,j}(\xi_2)$ are the univariate basis functions in the first and second parametric direction, ξ_1 and ξ_2, respectively. $\mathbf{S}(\xi_1, \xi_2)$ is a vector-valued function of (ξ_1, ξ_2), that maps a rectangle plane in the parametric domain into the Euclidean three-dimensional space. Analogous to representing a curve, the univariate basis functions can be chosen as Bernstein polynomials, B-splines, or NURBS. In Figure 1.4, we plot an example of a circular NURBS curve (a) and spherical surface (b). The curve is defined by quadratic C^1 NURBS with control points given in Figure 1.4a, where four control points on the curve have a weight of $w = 1.0$ and the other four a weight of $w = 1/\sqrt{2}$. The spherical surface, in the form of (1.5), is constructed using the tensor product of two circles 1.4a.

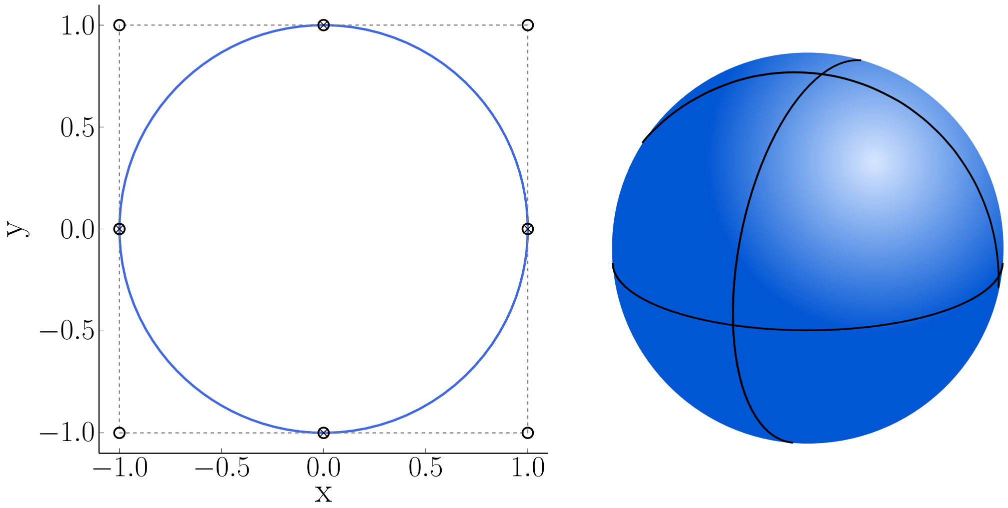

(a) Circle

(b) Sphere

Figure 1.4: A circular NURBS curve (a) and spherical NURBS surface (b).

1.2.2 Trimmed geometry

In CAD, the boundary representation (B-rep) commonly involves trimming to divide the surfaces into relevant and superfluous areas. To this end, trimming curves that are representations of intersection curves between two surfaces need to be computed. Figure 1.5 illustrates an example of a simple CAD solid model [7], which is represented by its bounding surfaces. We observe that even a simple model such as this one includes several trimmed surfaces and trimming curves (dashed lines).

In general, one can divide the trimming procedure into two main steps: the first step is to solve the surface intersection problem, and the second step is to represent its

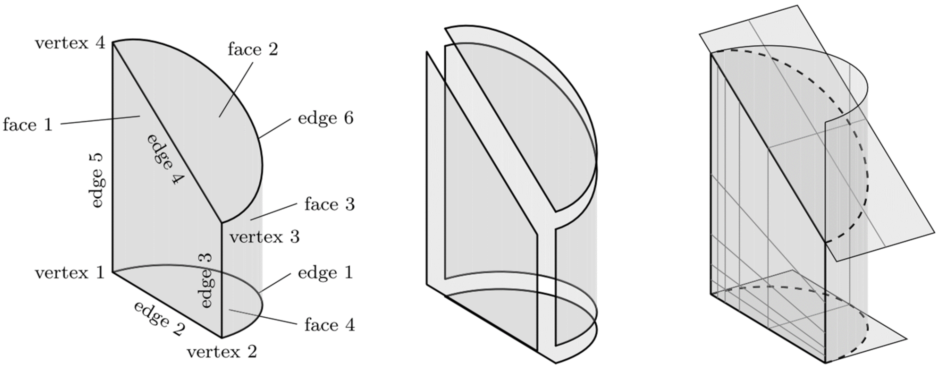

(a) Solid model (b) Bounding surfaces (c) Parameterization with trimming curves (dashed)

Figure 1.5: Boundary representation (B-rep) of a CAD solid model [7].

result. There exist several techniques and approaches for the first step, for example, analytical methods [8], [9], lattice evaluation [10], [11], subdivision methods [12], [13], and marching (or tracing) methods [14]–[16]. For an overview and summary of these methods, we refer to [7]. These intersection algorithms lead to an approximate solution including sampling points of the intersection. Based on these sampling points, one can represent the intersection curve in the model space, using for instance B-splines and either interpolation schemes or curve-fitting techniques [17]. Since the resulting approximate curve does not lie on any of the trimmed surfaces, it needs to be represented in each parameter space of these surfaces, based on the sampling points given there [18]. The resulting curves are referred to as trimming curves. One can then compute the corresponding curves in the model space by evaluating the surface equation along its trimming curve. For more detailed discussions on the representation of intersection curves, we refer to [7], [18] and references therein.

We note that the trimming curves do not coincide with the intersection curve in the model space, and also not with each other, since the representation procedure is performed separately for each trimmed surface. Hence, gaps and overlaps between these surfaces may occur. This inaccuracy could lead to inconsistent geometries and other robustness issues [7]. In addition, different kernels of different CAD applications define and represent trimming curves differently [19], [20]. This could lead to accuracy loss or undesirable artifacts such as gaps or overlaps during data exchange. Instead of trimmed objects, there exist several approaches to remodel or replace them, such as using a set of regular patches [21]–[23], subdivision surfaces [24]–[27], or T-splines [28], [29]. These techniques are promising, however, only suitable for certain surface types, as reviewed and summarized in [7].

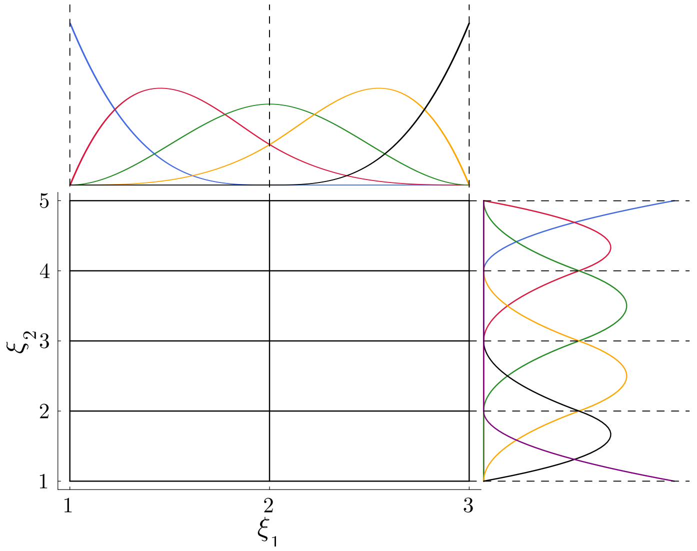

Figure 1.6: A mesh of **2** × **4** element in the parametric domain with **cubic** C^2 **and quadratic** C^1 B-splines in ξ_1- and ξ_2-directions, respectively

1.3 Isogeometric discretizations

Isogeometric analysis is based on the isoparametric concept [30]. The unknown variables, such as displacements, velocity, temperature, etc., are represented in terms of basis functions which represent the geometry, i.e. spline basis functions such as B-splines or NURBS. The coefficients of these basis functions are then the degrees-of-freedom, or *control variables*, i.e. the unknown variables of the control points. Hence, control points in the context of IGA are equivalent to nodes of classical finite elements. Univariate spline basis functions are defined on a patch, as discussed in Section 1.1. In general, the parametric domain can consist of more than one patch, i.e. multipatches. Each patch is divided in intervals by the knot vector. These intervals are defined as elements (see also Figure 1.6). We note that, different from basis functions in classical finite elements, the spline basis function spans over several elements, up to $p + 1$ elements, where p is the polynomial degree of the basis function. This allows higher-order continuity over element boundaries, which is an important property in analysis. Elements in the context of IGA can be treated in the same way as classical finite elements, i.e. the same assembly routine on element level in finite element codes.

A mesh for a patch is defined by the product of knot vectors [30], as illustrated in Figure 1.6. One can refine the mesh with h-refinement or p-refinement in the same way as with classical finite elements. In the context of IGA, a third strategy, the so-called k-refinement [30], is possible, which is a combination of p- and h-refinement with p-refinement performed before h-refinement.

We note that in cases involving trimmed geometries, the analysis poses additional challenges, such as identifying the trimmed elements, integration in these elements and possibly along the trimming curve, and stabilization of the trimmed basis. In the context of IGA, one of the most well-established approaches to tackle these issues is the finite cell methods [31]–[33], where the parameter space of the trimmed patch is employed as a background discretization while the trimming curve defines the boundary of the domain of interest. A second class of methods is to employ the remodeling of the trimmed surfaces, for instance using subdivision surfaces [34]–[36] or T-splines [37]–[39], discussed in the previous section. In addition, an analysis of trimmed geometries also involves coupling of multiple patches [40]–[42], which could require a treatment of non-matching parameterizations, possible gaps, and overlaps between different patches and trimming curves.

2 Main research themes and objectives

In structural dynamics, particularly in impact, crash-test, and metal forming simulations, explicit methods have a wide range of applications. To achieve higher-order accuracy, commercial codes of these kinds of simulations rely on the spectral properties of the chosen finite elements combined with locking-preventing mechanisms such as reduced quadrature. To achieve highly efficient computations, these codes rely on three ingredients: (1) low memory requirements; (2) an efficient solver; and (3) relatively large critical time step values. Contemporary linear finite element codes achieve these three ingredients based on diagonalizing the mass matrix using lumping techniques. Mass lumping, however, generally achieves only second-order accuracy even with higher-order basis functions [43], [44]. This prevents explicit dynamics calculations from exploiting the higher-order accuracy of the corresponding finite elements, especially isogeometric discretizations, which are particularly attractive due to their well-behaved spectral properties. In this work, our main objective is to overcome this issue, attempting to develop a higher-order accurate explicit scheme with mass lumping in isogeometric structural analysis. To this end, we discuss in Section 2.1 the key components affecting the spatial accuracy and efficiency of an explicit scheme, before introducing the main contributions of this work in Section 2.2. We then close this chapter with the outline of this thesis in Section 2.3.

2.1 Spatial accuracy and efficiency in isogeometric explicit dynamics

In this section, we discuss the key components that affect the spatial accuracy of explicit dynamics computations, such as the spectral accuracy of the finite discretizations, locking phenomena, and locking-preventing technology. We also discuss the diagonal mass matrix that has a crucial impact on both the accuracy and the efficiency, as well as the critical time step size that plays an essential role regarding the latter.

2.1.1 Spectral accuracy of isogeometric discretizations

Isogeometric analysis (IGA) was first introduced in 2005 as a computational framework to improve the integration of computer-aided design (CAD) and finite element analysis (FEA) [30]. The main idea is to employ the higher-order smooth splines, such as standard uniform B-splines and non-uniform rational B-Splines (NURBS), to describe the geometry of the CAD models and to approximate the solution fields in FEA at the same time, i.e. an isoparametric concept. Since 2005, several approaches in the context of

IGA are developed for various research fields such as structural shell analysis [45]–[49], solid mechanics [50], [51], fluid mechanics [52], [53], fracture mechanics [54], [55], and optimization [56]–[58]. IGA is particularly attractive for higher-order accurate structural dynamics. A key property of higher-order IGA, already discussed in one of the first articles [43], is its well-behaved discrete spectrum of eigenfrequencies and eigenmodes. Compared with classical C^0 FEA, isogeometric discretizations exhibit better spectral properties [59]–[62]. Figure 2.1 illustrates an example obtained from the generalized eigenvalue problem of a bar, discretized with cubic Lagrange polynomials (FEA) and cubic smooth splines (IGA) [43], [51]. We plot the discrete frequencies, ω_n^h, normalized with respect to the exact solution, ω_n, versus the mode number, n, normalized by the total number of degrees of freedom, N. We observe that for FEA, the spectrum (red curve) contains the so-called "optical" branches, separated by distinct jumps, which compromise the accuracy of the high frequency range. For IGA (blue curve), however, the accurate "acoustic" branch of the spectrum covers almost the entire frequency range. Good spectral accuracy is an essential factor guaranteeing the higher-order spatial accuracy of the numerical solution and its optimal convergence behavior.

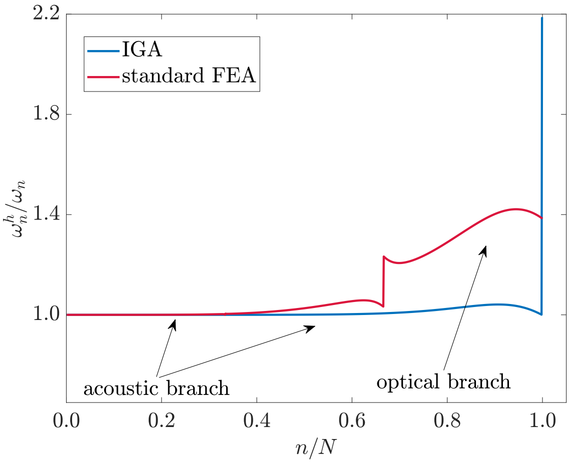

Figure 2.1: Normalized discrete spectrum of eigenfrequencies obtained from a generalized eigenvalue problem for a bar, computed with FEA and IGA, both with 1,000 cubic basis functions.

2.1.2 Locking phenomena in finite element formulations

Locking, that is a phenomenon where artificial numerical stiffness occurs, leads to a parameter-dependent reduced convergence rate in the pre-asymptotic range [63]. It negatively affects the accuracy and convergence. The most well-known locking phenomena are membrane locking [64], [65], transverse shear locking in beam, plate, and shell elements [64], and volumetric locking due to incompressibility in solid elements [66]. The development of locking-preventing technology has a history of more than 40 years, first within classical finite elements (C^0 FEA) and then in IGA. Well-established methods in IGA are, for example, field consistent approach [67]–[69], approaches using higher-order basis [46], [70], using selective reduced integration [71]–[73], using reduced integration with hourglass mode control [68], [74], B-bar method [70], [75], [76], assumed natural strain [75], [77], [78], enhanced assumed strain [79], discrete shear/strain gap [47], [80], and methods using variational principles such as Hu-Washizu [47], [81] or Hellinger-Reissner principle [67], [81], [82]. For explicit dynamics calculations in the context of IGA, the most common approach to alleviate locking is (selective) reduced quadrature rule, possibly combined with hourglass control, [83], [84], which is also the standard approach in commercial codes such as LS-Dyna [85]. Another approach is the isogeometric collocation method [86]–[88], which is applied to explicit dynamics and shown to alleviate locking phenomena based on its one-point quadrature rule [88]. In this work, we focus on using spectral analysis to elucidate the impact of locking phenomena and these different locking-preventing techniques, which also illustrates the intimate relation between locking and spectral accuracy of finite discretizations. We also apply this to assess the unlocking of our isogeometric mixed formulation based on the Hellinger-Reissner principle, which we develop in this work with an attempt to eliminate membrane locking for explicit dynamics of Kirchhoff-Love shells.

2.1.3 Diagonal mass matrix

A key component to achieve highly efficient explicit dynamics calculations is the diagonal mass matrix since it requires only low memory usage and a simple vector-vector multiplication at each time integration step to solve the system of equations. The most common and well-established technique to diagonalize the mass matrix in this context is mass lumping [66]. Various lumping techniques exist, such as row-summing [44], [66], diagonal scaling [89], manifold-based methods [90], and lumping by nodal quadrature [91]–[93]. While row-summing is very easy to implement, it suffers from the fact that the lumped mass matrix is not necessarily positive-definite as negative or zero diagonal values are possible. In contrast, diagonal scaling and the manifold-based scheme guarantee the positive definiteness of the lumped mass matrix, however, suffer from suboptimal convergence rates [94], [95]. For the approach of lumping by nodal quadrature, the choice of basis functions and nodal distributions plays an essential role, particularly in guaranteeing optimal convergence as well as a positive-definite lumped mass matrix [95]. Employing the Lagrangian basis functions with Gauss-Lobatto-Legendre quadrature points as interpolation nodes and integrating using the Gauss-Lobatto-Legendre quadrature rule results in a diagonal matrix. This is also known as the spectral element method [92], [96], [97]. The *hp*-collocation method [93], which employs the Gauss-Lobatto Lagrange test functions and Gauss-Lobatto points as collocation points, can also be categorized in this lumping technique.

In terms of accuracy, lumping schemes generally achieve second-order accuracy irrespective of the polynomial degree of the basis functions [43], [44], i.e. for lower-order elements the optimal accuracy is preserved. For higher-order elements, the optimal accuracy and convergence behavior can be achieved, given that additional accuracy conditions of the quadrature rule are satisfied [91], or employing either the spectral element method based on Gauss-Lobatto-Legendre quadrature points (i.e. lumping using nodal quadrature) or combining lumping techniques with the spectral element method based on Gauss-Lobatto-Chebyshev quadrature points [95]. The spectral element method is the only technique established so far in classical FEA that obtains higher-order spatial accuracy in explicit dynamics with a diagonal mass matrix [94]–[96]. There are various attempts of improving the accuracy of the lumped mass such as the explicit predictor multicorrector of [66], [86], [87], which, nevertheless, results in a mass matrix that is no longer diagonal but has a band structure. For IGA, one recent work on improving the accuracy of a lumped mass matrix is [98], where the authors construct a set of transformed spline basis functions that are interpolatory at the Greville points and lumped the resulting Galerkin consistent mass matrix using the row-sum lumping technique. It is shown, that the spectral accuracy and convergence obtained with these transformed basis functions are improved, however, not yet optimal. Recently, also to improve the spectral accuracy of row-sum lumped mass matrix, [99] develops preconditioners for this type of mass lumping scheme. The improved mass matrix potentially achieves better accuracy in explicit dynamics, however, is no longer diagonal, but has a band structure.

Another idea to diagonalize the mass matrix instead of lumping schemes is to exploit the bi-orthogonality of a dual basis. One of the first attempts to employ this idea for IGA in explicit dynamics is [100], where the authors utilize the dual space to discretize the test functions, which corresponds to the spline space discretizing the trial functions. The key property of these spaces is that they satisfy the bi-orthogonality constraint in the physical domain. [100] constructs such dual spaces for Non-uniform rational B-splines (NURBS), based on their Bernstein-Bézier representation, with dual functions that have the same supports as the primal one, nevertheless, are C^{-1}-continuous. Furthermore, this approach requires the inverse of the geometrical mapping, which is not trivial for curved multidimensional geometries, and does not preserve the tensor-product structure in such cases. We note that this way of construction is not the most common choice. Standard approaches are developed in the parametric domain [101]–[107], which are employed for patch coupling in the context of dual mortar methods [105], [107]–[110] and, recently, for preventing locking phenomena for Reissner-Mindlin shell elements [82]. The resulting dual basis functions, however, generally do not lead to a diagonal mass matrix when it is mapped to the physical domain. Using the dual basis functions of [100] as test functions leads to an isogeometric Petrov-Galerkin formulation, which is shown, via numerical results of quadratic and cubic basis functions, to result in good spectral properties and the same optimal convergence behavior as using standard Galerkin consistent mass matrix. In this work, we will focus on a new Petrov-Galerkin method that enables a higher-order accurate mass lumping, whose application is straightforward for arbitrary geometrical mapping.

2.1.4 Critical time step size

In explicit time integration schemes, the critical time step size, Δt_{crit}, plays a crucial role, since it is the upper bound of their time step size [111]. Δt_{crit} is inversely proportional to the maximum eigenfrequency, $\omega_{\max}$, of the discretization. Hence, controlling the highest frequency is requisite for guaranteeing efficient explicit dynamics calculations. One of the

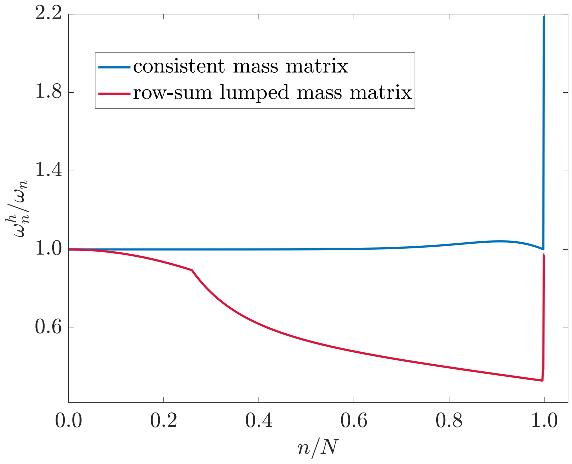

Figure 2.2: Normalized discrete spectrum of the exemplary bar in Figure 2.1, computed with IGA using consistent and row-sum lumped mass matrix.

most common approaches to alleviate the impact of $\omega_{\max}$ is mass scaling, where artificial terms are added to the mass matrix [112]–[115]. One of the most extended variants of this approach is to scale the density in combination with a mass lumping approach [116]. Another mass scaling approach is to add a weighting of some form of stiffness matrix as a mass scaling [117]–[120]. This type of approach is also called *selective mass scaling* when it targets specific frequencies and modes [120]. We note that, albeit mass lumping techniques are not developed to reduce $\omega_{\max}$, it results in a smaller value of $\omega_{\max}$, and thus can be also applied to control $\omega_{\max}$. Figure 2.2 demonstrates this effect of the standard row-sum lumping technique for the exemplary bar in Figure 2.1, computed with IGA. We observe that row-summing the consistent mass matrix, whose spectrum is plotted in blue, reduces not only $\omega_{\max}$, but also most of the spectrum (red curve), and leads to a significant decrease in spectral accuracy. This indicates the negative impact of mass lumping on spatial accuracy in explicit dynamics calculations, discussed in the previous subsection. Mass scaling and lumping techniques can be combined. However, since the added artificial mass terms generally correspond to a non-diagonal matrix, when applying mass scaling approaches to a lumped mass matrix, they break its diagonal structure. A solution could be applying these approaches before lumping the mass matrix or employing the mass scaling variant of [116].

Alternative approaches for controlling $\omega_{\max}$ are outlier removal approaches, which aim at removing spurious "outliers" modes that usually associate with the highest frequencies of isogeometric discretizations [43], [51]. An example is illustrated in Figure 2.1, where we observe a small number of modes that form the optical branch at the end of the blue spectrum (IGA) and are significantly overestimated. One of the first attempts to remove these outliers is introduced in [51], which is based on the nonlinear parameterization of the domain via a uniform distribution of the control points. More recent approaches for single-patch discretizations [121]–[123] enforce additional boundary constraints arising from higher-order eigenvalue problems, either by building these into the basis [122], [123] or via penalization [121]. While the latter only reduces the outlier frequencies, the former removes the corresponding spurious outlier modes entirely, for arbitrary degree p in one- and multidimensional settings. For multipatch discretizations, where additional outliers occur due to reduced continuity at patch interfaces, [124] also imposes additional higher-order continuity constraints at these interfaces using a penalty approach. By using large values penalty parameters, this approach indicates the outlier frequencies which are then removed using a cut-off normalized frequency. In the framework of mortar methods, similar penalty approaches are developed to suppress the outlier frequencies [125], [126], or by applying the *optimally-blended* quadratures [127] in [62], [128]–[130]. In such penalty approaches, the penalty parameters are usually chosen based on empirical results and may depend on the geometry, material, and discretization parameters. In this work, we will focus on an approach to estimate optimal scaling parameters in the framework of a variational approach based on perturbed eigenvalue analysis, that could help solve this issue.

2.2 Contributions of this work in the context of isogeometric analysis

The first contribution of this work is to extend spectral analysis as a tool for identifying locking behavior and assessing the effectiveness of locking-free formulations. One motivation is that the discrete spectrum contains all aspects of the employed locking-preventing formulations since the discrete solution of the eigenvalue problem depends on the variational formulation, its evaluation, and the solution space spanned by the basis functions of the discretization. Compared to the standard convergence study based on error norms, which is the standard way to elucidate locking-prone and locking-free formulations, spectral analysis includes information that this way of using error norms cannot obtain. We propose to compare the spectrum computed on coarse and "overkill" meshes to "measure" locking or unlocking. The method is locking-free if the corresponding spectrum converges on coarse meshes, that is does not differ from that on "overkill" meshes. Consequently, the method is locking if the spectra obtained on coarse and "overkill" meshes differ significantly. We demonstrate this via the example of a circular ring discretized with isogeometric curved Euler-Bernoulli beam elements, that is subjected to membrane locking. We show that the transverse-displacement-dominating modes are locking-prone, while the circumferential-displacement-dominating modes are naturally locking-free. We then employ our approach to compare and assess three representative locking-free formulations in terms of their locking-related efficiency: the B-bar, discrete strain gap, and Hellinger-Reissner methods.

The second contribution is a novel variational approach based on perturbed eigenvalue analysis for improving spectral properties of isogeometric multipatch discretizations. The main idea is to penalize both the stiffness and the mass matrix [121] and to add higher-order continuity constraints at patch interfaces [124], such that the suppression of the outlier frequencies caused by reduced continuity at these interfaces is improved. In particular, we add scaled perturbation terms that weakly enforce these continuity constraints to both matrices. This necessarily means that both the left- and right-hand sides of the standard explicit dynamics formulation are modified. Our approach distinguishes from a mass scaling approach that modifies only the mass matrix. Furthermore, to remove the outliers caused by reduced continuity at the boundaries, we combine the proposed approach with the method introduced in [122]. We then propose an iterative scheme to estimate optimal scaling parameters of the perturbation term, such that the outlier frequencies are effectively reduced without affecting the accuracy of the remainder of the spectrum. We demonstrate this achievement via numerical examples of bars, beams, membranes, and plates. We also illustrate that our approach allows for a much larger critical time step size in explicit dynamics calculations, which does not depend on the polynomial degree of spline basis functions.

The third contribution of this work is an isogeometric Petrov-Galerkin method that combines the dual basis concept and standard row-sum lumping and achieves higher-order accuracy in explicit dynamics irrespective of the polynomial degree of the spline approximation. In particular, we employ a class of "approximate" dual spline functions introduced in [131], which only approximately satisfy the discrete bi-orthogonality property, but preserves all other properties of the original B-spline basis, such as C^{p-1} smoothness, polynomial reproduction, and local support. To preserve the approximate bi-orthogonality in the mapped domain, we divide these dual functions by the Jacobian determinant. We employ this modified approximate dual basis to discretize the test functions while discretizing the trial functions with the corresponding B-splines. This leads to a semidiscrete Petrov–Galerkin formulation, whose consistent mass matrix is not diagonal but is, in some sense, "close" to the identity matrix. Applying the row-sum technique to this mass matrix yields then the identity matrix, eliminating the need for matrix inversion, which preserves all polynomials up to the same degree as the employed spline basis functions. Accordingly, employing this lumped mass matrix in explicit dynamics does not compromise the higher-order spatial accuracy. We numerically confirm this via spectral analysis and convergence study of beam and plate models.

The fourth contribution is an isogeometric Petrov-Galerkin mixed formulation based on the Hellinger-Reissner principle that enables higher-order spatial accuracy in explicit dynamics. It is an extension of our Petrov-Galerkin approach above with an attempt to eliminate locking phenomena in explicit calculations. It considers the displacement and strain fields as two independent variable fields. To eliminate, for instance, the effect of membrane locking for Kirchhoff-Love shell formulation, we discretize the latter with a basis of one degree lower than the former. We adopt the higher-order mass lumping scheme of our first Petrov-Galerkin approach and employ smooth B-splines to discretize the solution fields and the corresponding approximate dual functions to discretize the test functions. We apply the boundary treatment that is recently developed in [132] to be able to row-sum lump the entire mass matrix without compromising higher-order accuracy. To increase the efficiency of our approach, we combine the strong approach of outlier removal to increase the critical time step size [122] and apply the reduced quadrature rule [133] that leads to a minimal number of quadrature points without compromising accuracy. We demonstrate the favorable numerical behavior of the introduced Petrov–Galerkin scheme via spectral analysis and convergence studies for curved beam and shell models.

In addition, we extend the horizon of this work by exploring the application of isogeometric analysis, combined with the strong outlier removal approach [122], to nonlinear dynamics of shear- and torsion-free rods [134]. Using isogeometric discretizations enables the omission of the director as an independent variable field, and thus a reduction of the number of degrees of freedom. They lead to discrete solution in the Euclidean space $\mathbb{R}^3$ that is larger than the one when using the standard nodal finite elements based on cubic Hermit functions. Moreover, we apply the strong approach of outlier removal [122] to reduce the high-frequency content in the response without affecting the accuracy, ensuring robustness of our nonlinear discrete formulation. For robust time integration, we choose an implicit scheme that is a hybrid form of the mid-point rule and the trapezoidal rule that preserves the linear angular momentum exactly and approximates the energy accurately. We illustrate the efficiency of our nonlinear discrete formulation for static and transient rods under different loading conditions, demonstrating good accuracy in space, time and the frequency domain. Our numerical example coincides with a relevant application case, the simulation of mooring lines.

2.3 Outline

This thesis is a cumulative work and composed of five publications, each presenting one of its contributions. The first three publications have been accepted and published in the peer-reviewed journal *Computer Methods in Applied Mechanics and Engineering* (CMAME), while the fourth one has been submitted to *International Journal for Numerical Methods in Engineering*, and the fifth publication to *Computational Mechanics*. For the sake of uniformity, we number the sections, equations, figures, tables, and references, consecutively.

The structure of this thesis is as follows: In Chapter 3, we present the first publication extending spectral analysis as a tool for "measuring" locking in finite element formulations. Chapter 4 consists of our work in the second publication introducing a variational approach based on perturbed eigenvalue analysis, together with a scheme for estimating optimal scaling parameters, for improving spectral properties of isogeometric multipatch discretizations. In Chapter 5, we introduce our third publication presenting an isogeometric Petrov-Galerkin method that enables higher-order accurate mass lumping in explicit dynamics. In Chapter 6, we present the fourth publication on the Petrov-Galerkin mixed formulation to achieve locking-free discretizations and a higher-order accurate explicit scheme based on a row-sum lumped mass matrix. In Chapter 7, we explore the performance of IGA, combined with a strong outlier removal approach, in terms of its accuracy and robustness in nonlinear dynamics of shear- and torsion-free rods. The structure of each publication in Chapters 3 to 7 is maintained within each chapter. We close this thesis with Chapter 8 which summarizes the presented results, draws conclusions, and outlines future research directions.

3 Leveraging spectral analysis to elucidate membrane locking and unlocking in isogeometric finite element formulations of the curved Euler-Bernoulli beam

This chapter is reproduced from [135]:

T.-H. Nguyen, R. R. Hiemstra, and D. Schillinger. *Leveraging spectral analysis to elucidate membrane locking and unlocking in isogeometric finite element formulations of the curved Euler-Bernoulli beam*, Comput. Meth. Appl. Mech. and Engrg. 388 (2022) 114240. DOI: `10.1016/j.cma.2021.114240`. URL: `https://linkinghub.elsevier.com/retrieve/pii/S0045782521005636`.

Abstract

In this paper, we take a fresh look at using spectral analysis for assessing locking phenomena in finite element formulations. We propose to "measure" locking by comparing the difference between eigenvalue and mode error curves computed on coarse meshes with "asymptotic" error curves computed on "overkill" meshes, both plotted with respect to the normalized mode number. To demonstrate the intimate relation between membrane locking and spectral accuracy, we focus on the example of a circular ring discretized with isogeometric curved Euler-Bernoulli beam elements. We show that the transverse-displacement-dominating modes are locking-prone, while the circumferential-displacement-dominating modes are naturally locking-free. We use eigenvalue and mode errors to assess five isogeometric finite element formulations in terms of their locking-related efficiency: the displacement-based formulation with full and reduced integration and three locking-free formulations based on the B-bar, discrete strain gap and Hellinger-Reissner methods. Our study shows that spectral analysis uncovers locking-related effects across the spectrum of eigenvalues and eigenmodes, rigorously characterizing membrane locking in the displacement-based formulation and unlocking in the locking-free formulations.

3.1 Introduction

In finite element discretizations of curved beam and shell models, membrane locking refers to the phenomenon of artificial bending stiffness due to the coupling of the bending response and membrane response caused by the local curvature [64], [65]. Membrane locking negatively affects accuracy and convergence, illustrated in Fig. 3.1 for an isogeometric finite element discretization of a curved Euler-Bernoulli cantilever [136]. We observe that for practically relevant coarse meshes, the accuracy of the displacement solution measured via the relative error in the L^2 norm does not improve when the mesh is refined. The size of the resulting plateau in the convergence curve indicates the severity of membrane locking. We can also see that locking becomes more severe with increasing slenderness of the beam, and seems to reduce with increasing polynomial degree of the basis functions. We note that purely displacement-based finite element formulations of the Euler-Bernoulli beam model require basis functions in the Sobolev space H^3 to achieve optimal convergence rates $\mathcal{O}(p+1)$ in the L^2 norm [137], [138]. In Fig. 3.1a, we therefore observe convergence order two for quadratic B-splines that are only in H^2.

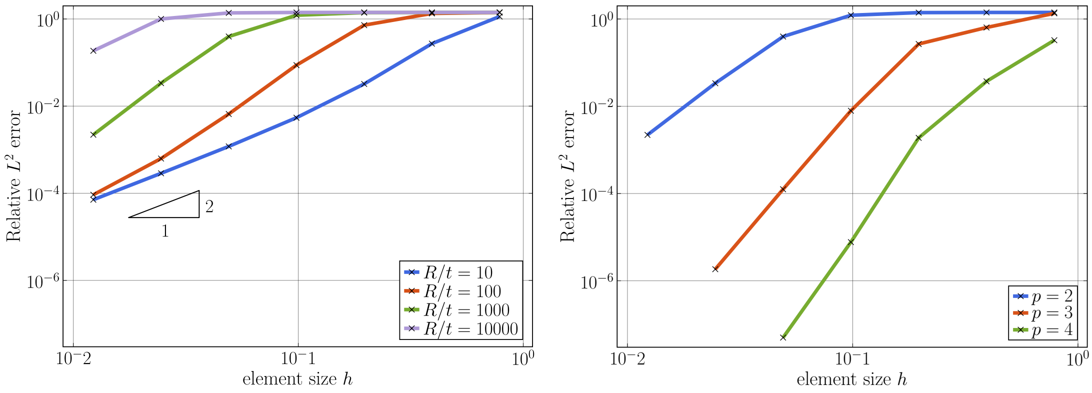

(a) Increasing slenderness R/t, $p = 2$

(b) Increasing p, $R/t = 1 \cdot 10^3$

Figure 3.1: Convergence of the relative L^2-norm errors of the displacements field of a curved Euler-Bernoulli beam (quarter circle cantilever, unit shear force at the free end, radius R, thickness t), discretized with B-splines of degree p and uniform h-refinement.

Locking-free finite element discretizations do not show any pre-asymptotic plateau, but converge right away with the optimal rate on coarse meshes. For completeness, we note that membrane locking is only one of several sources of locking, the most well-known being transverse shear locking in beam, plate and shell elements [64] and volumetric locking due to incompressibility in solid elements [66]. The development of locking-preventing discretization technology has a history of more than 40 years, first within classical finite elements and then in isogeometric analysis. Without any claim to completeness, Table 3.1 summarizes the most important locking-preventing formulations that can be applied against membrane locking, using the standard classifications into higher-order methods, the field-consistent approach, reduced integration, strain modification, and variational principles. For details on the underlying ideas and derivations,

Approach, concept derivation via principle of virtual work $(\star)$ or as a mixed method $(\diamond)$		**Application in**	
		nodal finite elements	isogeometric analysis
Higher-order basis $(\star)$		[139], [140]	[46], [70]
Field consistent approach $(\star)$		[141]–[143]	[67]–[69]
Reduced integration	Selective reduced integration $(\star)$	[144]–[148]	[68], [70]–[73]
	Hourglass mode control $(\star)$	[149]–[152]	[68], [74]
Strain modification	B-bar method $(\star)$	[144], [153], [154]	[68], [70], [75], [76]
	Assumed natural strain (ANS) $(\star)$	[155]–[157]	[75], [77], [78], [158]
	Enhanced assumed strain (EAS) $(\diamond)$	[159]–[162]	[79]
	Discrete shear/strain gap (DSG) $(\star)$	[163]–[165]	[47], [68], [80]
Variational principles	Hu-Washizu $(\diamond)$	[145], [146], [166], [167]	[47], [81]
	Hellinger-Reissner $(\diamond)$	[161], [168], [169]	[47], [67], [81], [82]

Table 3.1: Overview of locking-preventing finite element technology, developed in the context of standard finite element and isogeometric analysis, and associated literature (without claim to completeness).

we refer the interested reader to the pertinent literature, also given in Table 3.1 for nodal finite elements and isogeometric analysis.

To illustrate the effect of locking-free formulations, we compare the results obtained with the standard finite element formulation, using full and reduced integration, to the results obtained with three representative variants, namely B-bar strain projection, the discrete strain gap (DSG) method and a Hellinger-Reissner approach. For the curved cantilever problem described above, Figure 3.2 plots the resulting convergence curves in terms of the L^2-norm errors of the displacements for quadratic, cubic, quartic and quintic B-spline basis functions. We observe that all three locking-free formulations mitigate the effect of membrane locking with respect to the standard finite element formulation that is affected significantly by membrane locking. For quadratic basis functions on finer meshes, reduced integration mitigates the effect of membrane locking, but does not have any effect for $p \geq 3$. We also see that the DSG method does not consistently perform well for all polynomial degrees. This example illustrates that convergence studies of simple benchmark problems do not constitute a satisfactory way of assessing discretization methods in terms of their locking-related robustness and accuracy. Given the multitude of formulations addressing membrane locking, the question arises how to best compare and assess their accuracy and effectivity.

The analysis of the discrete spectrum of eigenvalues and eigenmodes constitutes an alternative way of assessing the accuracy of a discretization scheme. Eigenvalues and eigenmodes are computed from a discrete generalized eigenvalue problem that for models in structural mechanics corresponds to the discretized variational formulation of the associated free vibration problem without damping. Spectral accuracy directly relates to

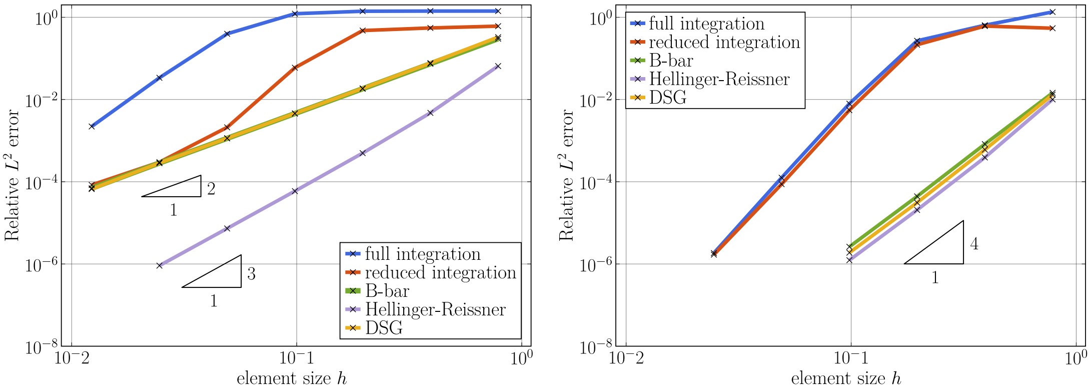

(a) Quadratic B-splines ($p = 2$) (b) Cubic B-splines ($p = 3$)

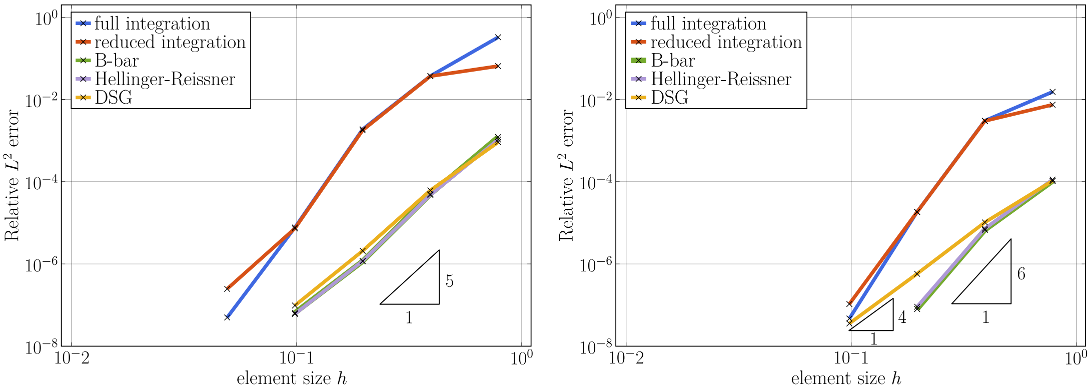

(c) Quartic B-splines ($p = 4$) (d) Quintic B-splines ($p = 5$)

Figure 3.2: Relative L^2-norm errors of the displacements field of a curved Euler-Bernoulli beam (quarter circle cantilever, unit shear force at the free end, radius R, thickness t, slenderness $R/t = 1 \cdot 10^3$), obtained with different locking-free formulations via uniform h-refinement of quadratic, cubic, quartic and quintic B-spline basis functions.

the accuracy of a discretized boundary value problem, as the solution of the latter can be represented in terms of eigenvalues and eigenmodes. For instance, spectral analysis has been recently used to explain the superior per-degree-of-freedom accuracy and robustness that is achieved by isogeometric analysis with smooth spline functions [61].

In this paper, we take first steps towards establishing spectral analysis as a tool for identifying locking behavior and assessing the effectiveness of locking-free formulations. Our approach is global, that is, we look at the complete spectrum and modal behavior, and it thus goes far beyond existing work [73], [170]. On the one hand, the solution to the discrete eigenvalue problem depends on the terms that appear in the variational formulation, their evaluation, and the solution space spanned by the basis functions of the finite element discretization. Therefore, all aspects of the various locking-preventing formulations given in Table 3.1 are reflected in the discrete spectrum. On the other hand, spectral analysis provides access to information that cannot be obtained via standard convergence measures based on error norms. Moreover, we propose a practical way of "measuring" locking (or unlocking) in the spectrum by comparing normalized spectra computed on coarse and "overkill" meshes. We define a method as locking-free if the normalized spectra are converged on coarse meshes, that is, the spectra obtained from coarse and "overkill" meshes do not differ. Accordingly, we define a method as locking if the normalized spectra are not converged on coarse meshes, that is, the spectra obtained from coarse and "overkill" meshes differ significantly. We illustrate the validity and significance of spectral analysis in this context via the example of a circular ring discretized with isogeometric curved Euler-Bernoulli beam elements susceptible to membrane locking. We then compare and assess the effectivity of the three representative locking-free formulations selected above in terms of their impact on the accuracy of the eigenvalues and eigenmodes.

The structure of the paper is as follows: in Section 3.2, we briefly review the generalized eigenvalue problem and associated error measures in spectral analysis. In Section 3.3, we introduce the circular ring problem and its discretization via isogeometric Euler-Bernoulli beam elements. In Section 3.4, we review the three representative locking-free formulations. In Section 3.5, we present detailed spectral analysis carried out for isogeometric discretizations of the thin circular ring and various locking and locking-free formulations. In addition, we provide an in-depth discussion of the validity and strengths of spectral analysis to interpret membrane locking in this context. In Section 3.6, we summarize our results and conclusions.

3.2 Generalized eigenvalue problem and error measures in spectral analysis

3.2.1 Generalized eigenvalue problem

We recall the generalized eigenvalue problem that governs free vibrations of an undamped linear structural system in the continuous setting. Each continuous eigenmode $U_n(x)$, with $n \in \mathbb{N}^+$ and defined on a domain Ω, satisfies the eigenvalue problem: find $(U_n, \lambda_n) \in \mathcal{V} \times \mathbb{R}^+$ such that:

$$(\mathcal{K} - \lambda_n \mathcal{M})\, U_n(x) \;=\; 0\,, \quad x \in \Omega\,. \tag{3.1}$$

Here, $\mathcal{M}$ and $\mathcal{K}$ are the mass and stiffness operators, $\lambda_n = \omega_n^2$ is the n^{th} eigenvalue equal to the square of the n^{th} eigenfrequency ω_n, and $\mathcal{V}$ is the space of functions with sufficient regularity that allows the differential operators in $\mathcal{M}$ and $\mathcal{K}$ to be applied.

The strong form of the generalized eigenvalue problem (3.1) can be transferred into a variational form via the standard Galerkin method and subsequently discretized with N finite element basis functions $B_i(x)$. The resulting discrete eigenvalue problem can be expressed via the following matrix equations: find $(U_n^h, \lambda_n^h) \in \mathcal{V}^h \times \mathbb{R}^+$ such that:

$$\left(\mathbf{K} - \lambda_n^h \mathbf{M}\right) \mathbf{U}_n^h \;=\; 0\,, \qquad n = 1, 2, \ldots, N\,, \tag{3.2}$$

where $\mathbf{U}_n^h$ denotes the vector of unknown coefficients, such that the n^{th} discrete eigenmode is:

$$U_n^h(x) = \left[B_1(x) \; \dots \; B_N(x)\right] \mathbf{U}_n^h \,, \qquad U_n^h(x) \in \mathcal{V}^h \subset \mathcal{V} \,.$$

Here, $\mathbf{K}$ and $\mathbf{M}$ denote the stiffness and consistent mass matrix, $\lambda_n^h = (\omega_n^h)^2$ is the n^{th} discrete eigenvalue equal to the square of the n^{th} discrete eigenfrequency ω_n^h, and $\mathcal{V}^h$ is the space of finite element basis functions with sufficient regularity. The discrete eigenmodes U_n^h are orthogonal in the L^2 norm and thus form a basis for the solution of any boundary value problem defined with the same model.

We note that in many applications, the use of a lumped mass matrix instead of the consistent mass matrix is common. Lumping schemes, however, often significantly affect the accuracy of the discrete spectrum, see e.g. [43], and are therefore not considered in this study.

3.2.2 Ordering of eigenvalues, rank sufficiency

We recall the following important properties due to their relevance in the remainder of the paper. The eigenvalues λ_n^h can be sorted in ascending order, where the corresponding eigenmodes can be ordered arbitrarily. Under the condition that (3.2) is derived from a homogeneous Neumann eigenvalue problem, that is, no Dirichlet boundary conditions are specified, the $N \times N$ stiffness matrix is symmetric positive semi-definite and the $N \times N$ consistent mass matrix is symmetric positive definite for linear structural systems. As a consequence, all eigenvalues are nonnegative real numbers ordered as:

$$0 \le \lambda_1^h \le \lambda_2^h \le \dots \le \lambda_n^h \le \dots \le \lambda_N^h \,, \tag{3.3}$$

A stable finite element scheme satisfies the notion of rank sufficiency based on the following three requirements [66], [171]:

1. The number of zero eigenvalues corresponds exactly to the number of rigid body modes, given by the specific structural system under consideration. The proper imposition of Dirichlet boundary conditions removes all rigid body modes and corresponding zero eigenvalues.
2. All eigenvalues are real, and the smallest non-zero eigenvalue converges to a finite value larger than zero. This ensures that no further zero eigenvalues occur, since the set of eigenvalues is bounded from below due to (3.3).
3. The set of eigenvalues is bounded from above, i.e. the largest eigenvalue is finite.

3.2.3 Error measures in spectral analysis

In this paper, we will investigate the error globally across the complete spectrum of eigenvalues and eigenmodes. To this end, we first define the following two error measures:

$$\left| \frac{\lambda_n^h - \lambda_n}{\lambda_n} \right| , \qquad \text{relative eigenvalue error,} \tag{3.4}$$

$$\frac{\|U_n^h - U_n\|}{\|U_n\|}, \qquad \text{relative mode error in the } L^2\text{-norm}, \tag{3.5}$$

which we will use extensively throughout this paper to quantify locking effects. We recall that for every mode n, the relative errors in the corresponding eigenvalue and mode, (3.4) and (3.5), sum to the mode error in the energy norm [172, Section 6.3, p. 233]:

$$\frac{\lambda_n^h - \lambda_n}{\lambda_n} + \frac{\|U_n^h - U_n\|^2}{\|U_n\|^2} = \frac{\|U_n^h - U_n\|_E^2}{\|U_n\|_E^2}, \quad \forall\, n = 1, 2, \dots, N\,, \tag{3.6}$$

provided that $\|U_n^h\|_{L^2} = \|U_n\|_{L^2}$. This relationship, denoted as the *Pythagorean eigenvalue error theorem*, is used extensively in [61] to evaluate both standard finite element and isogeometric approximations of eigenvalue, boundary-value, and initial-value problems. We refer to [61] for an in-depth discussion of error measures used in eigenvalue problems.

3.2.4 The role of the lowest eigenvalues and eigenmodes

It is important to note that for the approximation power of a finite element scheme, the accuracy of the lower part of the discrete spectrum is particularly crucial. To illustrate this key statement, we consider the discrete form $\mathbf{K}\mathbf{x} = \mathbf{f}$ that results from a finite element discretization of an elliptic boundary value problem, where $\mathbf{K}$ and $\mathbf{f}$ denote the stiffness matrix and the force vector, and $\mathbf{x}$ is the vector of unknowns. As the discrete eigenmodes U_n^h form a basis for the solution, we can expand the solution coefficients of the finite element basis in terms of the coefficients of the eigenmodes as:

$$\mathbf{x} = \sum_n \mathbf{U}_n^h\, c_n\,. \tag{3.7}$$

Using basic algebra and the orthogonality properties of the eigenmodes with respect to the stiffness and mass matrices, one can derive a closed-form expression for each unknown c_n of the eigenmode expansion (3.7) that reads:

$$c_n = \frac{1}{\lambda_n^h}\, \frac{(\mathbf{U}_n^h)^T}{(\mathbf{U}_n^h)^T \mathbf{M}\, \mathbf{U}_n^h}\, \mathbf{f}\,. \tag{3.8}$$

For the intermediate steps of this derivation, we refer to [171], [173]. Each coefficient c_n is inversely proportional to the size of the corresponding eigenvalue λ_n^h. Due to the ordering (3.3), the magnitude of the eigenvalues monotonically increases with mode number n. Therefore, for discretized elliptic boundary value problems, the contribution of higher eigenmodes with $n \gg 1$ will typically be significantly smaller than the contribution of the lowest eigenmodes $n = 1, 2, 3, 4, \dots$ For practical meshes with more than a few basis functions, we can even discard the contribution of the high modes completely, as this tendency becomes more pronounced, when the number of degrees of freedom and hence the number of eigenvalues is increased.

3.3 Free vibration of the Euler-Bernoulli circular ring

To illustrate our idea to apply spectral analysis for assessing locking phenomena, we consider the free vibration response of a thin circular ring that we will model as a curved Euler-Bernoulli beam in two dimensions and numerically solve with different finite element formulations, both locking and locking-free. A basic illustration of the Euler-Bernoulli ring, which we assume to be unconstrained and undamped, is given in Fig. 3.3. Focusing our attention on a single benchmark entails the following advantages. On the one hand, the resulting discrete model is a representative example for membrane locking, but not susceptible to any other form of locking. Therefore, we can a priori exclude any interaction of different locking phenomena. In addition, the continuous problem still allows for an analytical solution, so that the error measures (3.4) and (3.5) can be evaluated. On the other hand, beam formulations can be written up in concise format, including their different locking free variants, which facilitates comparison and avoids deviation from our main focus on the assessment of membrane locking through spectral analysis.

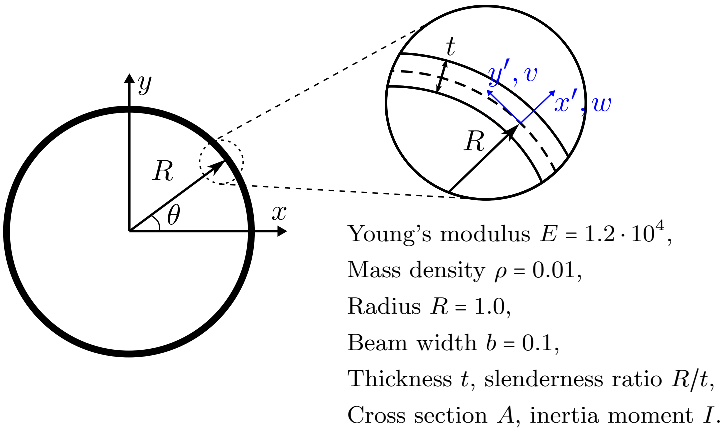

Young's modulus $E = 1.2 \cdot 10^4$,
Mass density $\rho = 0.01$,
Radius $R = 1.0$,
Beam width $b = 0.1$,
Thickness t, slenderness ratio R/t,
Cross section A, inertia moment I.

Figure 3.3: Closed circular ring modeled as a curved Euler-Bernoulli beam.

3.3.1 Strong form of the eigenvalue problem in mixed format

We briefly review the derivation of the generalized eigenvalue problem that governs the free vibration response of the unconstrained Euler-Bernoulli ring from the system of equations of motion. For a circular ring, the radius of curvature R is constant and the arc-length coordinate $s = R\theta$ can be expressed in terms of the angle $\theta \in [0, 2\pi]$ [174]. To facilitate the application to some of the locking-free formulations later on, we state the equations of motion in mixed form, where the kinematic relations are added as individual constraint equations:

$$\frac{EI}{R^2}\kappa_{,\theta} + \frac{EA}{R}\epsilon_{,\theta} = \rho A \ddot{v}\,, \tag{3.9a}$$

$$\frac{EI}{R^2}\kappa_{,\theta\theta} - \frac{EA}{R}\epsilon = \rho A\ddot{w}\,, \tag{3.9b}$$

$$\epsilon = \frac{1}{R}v_{,\theta} + \frac{1}{R}w\,, \tag{3.9c}$$

$$\kappa = \frac{1}{R^2}v_{,\theta} - \frac{1}{R^2}w_{,\theta\theta}\,. \tag{3.9d}$$

The field variables are the circumferential and transverse displacement components v and w, respectively, the membrane strain ϵ, and the change of curvature κ, which, at fixed radius R, are functions of the angle θ and time t. Young's modulus E, cross-section area A, moment of inertia I, and mass density ρ are assumed constant. The double dot operator indicates second derivatives with respect to time t, and $(\cdot)_{,\theta}$ and $(\cdot)_{,\theta\theta}$ indicate first and second derivatives with respect to the angular coordinate θ.

We now assume that the field solutions of the free vibration problem are composed of a set of spatial solutions that depend on θ, multiplied by a modulation T_n that depends on time t:

$$\begin{aligned} v(\theta,t) &= \sum_n \hat{v}_n(\theta)T_n(t), \quad & w(\theta,t) &= \sum_n \hat{w}_n(\theta)T_n(t)\,, \\ \epsilon(\theta,t) &= \sum_n \hat{\epsilon}_n(\theta)T_n(t)\,, \quad & \kappa(\theta,t) &= \sum_n \hat{\kappa}_n(\theta)T_n(t)\,, \end{aligned} \tag{3.10}$$

where $n = 1,2,\ldots,\infty$. We note that the time modulation is of the form $T = \exp(j\,\omega_n t)$, where ω_n is an eigenfrequency of the ring and j is the imaginary unit. When we insert relations (3.10) into the equations of motion (3.9a) and (3.9b), we find for each component n of the solution

$$\left[\frac{EI}{R^2}\hat{\kappa}_{n,\theta} + \frac{EA}{R}\hat{\epsilon}_{n,\theta}\right]T_n - \left[\rho A\hat{v}_n\right]\ddot{T}_n = 0\,, \tag{3.11}$$

$$\left[\frac{EI}{R^2}\hat{\kappa}_{n,\theta\theta} - \frac{EA}{R}\hat{\epsilon}_n\right]T_n - \left[\rho A\hat{w}_n\right]\ddot{T}_n = 0\,. \tag{3.12}$$

For each n, we can now separate the field variables that depend on space and time by dividing (3.11) and (3.12) by $T_n\,(\rho A\hat{v}_n)$ and $T_n\,(\rho A\hat{w}_n)$, respectively. After this operation, the first term in (3.11) and (3.12) only depends on θ and the second term only on t. For the equations of motion (3.11) and (3.12), separation of variables thus allows us to write:

$$\frac{\frac{EI}{R^2}\hat{\kappa}_{n,\theta} + \frac{EA}{R}\hat{\epsilon}_{n,\theta}}{\rho A\hat{v}_n} = \frac{\frac{EI}{R^2}\hat{\kappa}_{n,\theta\theta} - \frac{EA}{R}\hat{\epsilon}_n}{\rho A\hat{w}_n} = \frac{\ddot{T}_n}{T_n} = -\lambda_{in}\,. \tag{3.13}$$

As the angular coordinate θ and the time coordinate t can be varied independently, all terms in (3.13) must remain equal to a constant, denoted here as $-\lambda_{in}$. As a result of the system of two equations of motion, one can show that for each n, two different constants exist [174], which we refer to with the additional index $i = 1,2$.

Combining (3.13) and the kinematic relations (3.9c) and (3.9d) that are obviously true for each n and arbitrary mode coefficients $T_n(t)$ results in the generalized eigenvalue problem for the unconstrained circular Euler-Bernoulli ring: find $(\{\hat{v}_n, \hat{w}_n, \hat{\epsilon}_n, \hat{\kappa}_n\}, \lambda_{in}) \in \mathcal{V} \times \mathbb{R}^+$ such that

$$\frac{EI}{R^2}\hat{\kappa}_{n,\theta} + \frac{EA}{R}\hat{\epsilon}_{n,\theta} + \lambda_{in}\,\rho A \hat{v}_n = 0\,, \tag{3.14a}$$

$$\frac{EI}{R^2}\hat{\kappa}_{n,\theta\theta} - \frac{EA}{R}\hat{\epsilon}_{n} + \lambda_{in}\,\rho A \hat{w}_n = 0\,, \tag{3.14b}$$

$$\hat{\epsilon}_n = \frac{1}{R}\hat{v}_{n,\theta} + \frac{1}{R}\hat{w}_n\,, \tag{3.14c}$$

$$\hat{\kappa}_n = \frac{1}{R^2}\hat{v}_{n,\theta} - \frac{1}{R^2}\hat{w}_{n,\theta\theta}\,. \tag{3.14d}$$

where $n = 1, 2, \ldots, \infty$, $i = 1, 2$, and $\mathcal{V}$ is a set of four spaces of continuous functions with sufficient regularity. Equations (3.14a) and (3.14b) can be identified as a generalized eigenvalue problem of the form (3.1), accompanied by two additional kinematic constraints (3.14c) and (3.14d). The constants λ_{in} form the n^{th} eigenvalue pair, the square of the n^{th} eigenfrequency pair ω_{in} of the ring.

An analytical solution of the eigenvalue problem of the circular Euler-Bernoulli ring is due to Soedel [174], which is summarized in Appendix 3.A for completeness. As a consequence of the eigenvalue pairs, the solution naturally splits into two types of eigenmodes, which can be associated with transverse and circumferential displacement behavior. In this paper, we we refer to the transverse and circumferential deflection dominating modes of [174] as transverse and circumferential modes. Figures 3.4 and 3.5 illustrate the analytical shapes of some of the transverse and circumferential modes, plotted for the geometric and material parameters given in Fig. 3.3, and a slenderness $R/t = 1 \cdot 10^3$, where t is the thickness of the ring.

Remark 3.3.1. *The first two transverse modes in Figure 3.4 denote a rigid body rotation ($n = 0$) and translation in x-direction ($n = 1$), respectively. The remaining rigid body translation in y-direction is part of another solution set,* (3.46) - (3.47)*, with a $\pi/2$ phase-shift, see [174] and Appendix 3.A. The first circumferential mode in Figure 3.5 is called "breathing mode" [174]. For our numerical studies in Section 3.5, we exclude the rigid body modes and the corresponding zero eigenvalues in both the numerical and analytical solutions.*

Remark 3.3.2. *The "kinks" that appear in the circumferential modes shown in Fig. 3.5 do not represent singularities, but are an artifact from plotting the modes for a finite displacement increment.*

3.3.2 Variational formulation

For ease of notation, we omit the hat on all displacement and strain field variables that we introduced in (3.10), with the understanding that from now on all displacement and strain fields will only depend on a spatial variable. We also define the following strain-displacement operators for membrane strain and change of curvature that act on

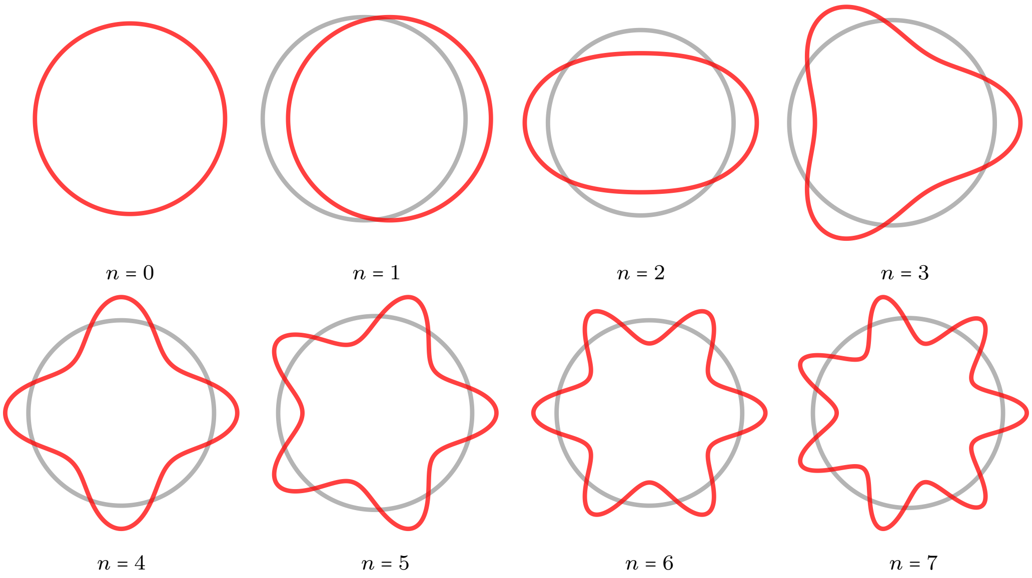

$n = 0$ $n = 1$ $n = 2$ $n = 3$

$n = 4$ $n = 5$ $n = 6$ $n = 7$

Figure 3.4: Analytical transverse eigenmodes (corresponding to λ_{1n}) of the circular ring with a slenderness ratio of $R/t = 1 \cdot 10^3$, where R is the radius and t the thickness of the ring. The plotted modes represent displacements in Cartesian coordinates, (U_x, U_y), obtained via the transformation (3.21).

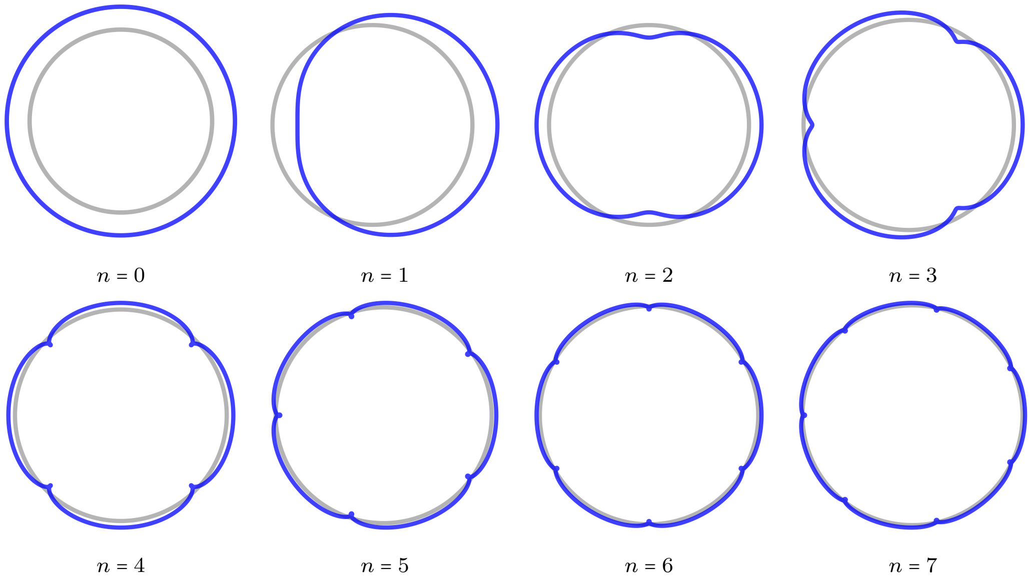

$n = 0$ $n = 1$ $n = 2$ $n = 3$

$n = 4$ $n = 5$ $n = 6$ $n = 7$

Figure 3.5: Analytical circumferential eigenmodes (corresponding to λ_{2n}) of the circular ring with a slenderness ratio of $R/t = 1 \cdot 10^3$, where R is the radius and t the thickness of the ring. The plotted modes represent displacements in Cartesian coordinates, (U_x, U_y), obtained via the transformation (3.21).

circumferential and transverse displacements v and w:

$$L_\epsilon(v,w) = \frac{1}{R} v_{,\theta} + \frac{1}{R} w\,, \tag{3.15a}$$

$$L_\kappa(v,w) = \frac{1}{R^2} v_{,\theta} - \frac{1}{R^2} w_{,\theta\theta}\,, \tag{3.15b}$$

where we assume sufficient regularity, such that all derivatives with respect to θ are well defined.

Curvilinear displacements

To transfer the strong form of the generalized eigenvalue problem (3.14a) and (3.14b) with kinematic constraints (3.14c) and (3.14d) into a variational format, we can apply the weighted residual method [66]. To this end, we bring each equation in residual form, multiply with a suitable test function and integrate over the ring domain:

$$\int_0^{2\pi} \left[\frac{EI}{R^2} \kappa_{n,\theta} + \frac{EA}{R} \epsilon_{n,\theta} + \lambda_{in}\, \rho A\, v_n \right] \delta v\, R\, \mathrm{d}\theta = 0\,, \tag{3.16a}$$

$$\int_0^{2\pi} \left[\frac{EI}{R^2} \kappa_{n,\theta\theta} - \frac{EA}{R} \epsilon_n + \lambda_{in}\, \rho A\, w_n \right] \delta w\, R\, \mathrm{d}\theta = 0\,, \tag{3.16b}$$

$$\int_0^{2\pi} \left[L_\epsilon(v_n, w_n) - \epsilon_n \right] \delta N\; R\, \mathrm{d}\theta = 0\,, \tag{3.16c}$$

$$\int_0^{2\pi} \left[L_\kappa(v_n, w_n) - \kappa_n \right] \delta M\; R\, \mathrm{d}\theta = 0\,. \tag{3.16d}$$

From an energetic consistency viewpoint, we can identify the test functions as the virtual displacements δv and δw in circumferential and transverse direction, and the virtual membrane force and bending moment δN and δM, respectively.

Assuming sufficient regularity, we now integrate (3.16a) and (3.16b) by parts to shift all derivatives from the strain field variables to the virtual displacements:

$$\begin{aligned}
&\int_0^{2\pi} \left[-\frac{EI}{R^2} \kappa_n\, \delta v_{,\theta} - \frac{EA}{R} \epsilon_n\, \delta v_{,\theta} + \lambda_{in}\, \rho A v_n\, \delta v \right] R\, \mathrm{d}\theta = 0\,, \\
&\int_0^{2\pi} \left[\frac{EI}{R^2} \kappa_n\, \delta w_{,\theta\theta} - \frac{EA}{R} \epsilon_n\, \delta w + \lambda_{in}\, \rho A w_n\, \delta w \right] R\, \mathrm{d}\theta = 0\,.
\end{aligned} \tag{3.17}$$

We note that due to the periodic nature of the ring, the integration by parts procedure does not produce any boundary terms.

In (3.16c) and (3.16d), we use the constitutive relations for the membrane force and the bending moment, $\delta N = EA\,\delta\epsilon$ and $\delta M = EI\,\delta\kappa$, to obtain expressions based on corresponding virtual membrane strain and change of curvature functions:

$$\begin{aligned}
&\int_0^{2\pi} \left[EA\; L_\epsilon(v_n, w_n)\, \delta\epsilon - EA\, \epsilon_n\, \delta\epsilon \right] R\, \mathrm{d}\theta = 0\,, \\
&\int_0^{2\pi} \left[EI\, L_\kappa(v_n, w_n)\, \delta\kappa - EI\, \kappa_n\, \delta\kappa \right] R\, \mathrm{d}\theta = 0\,.
\end{aligned} \tag{3.18}$$

Summing up the two equations in (3.17) and the two equations in (3.18), we can write the variational mixed formulation of the circular Euler-Bernoulli ring in curvilinear coordinates in concise format: find $(\{v_n, w_n\}, \{\epsilon_n, \kappa_n\}, \lambda_{in}) \in \mathcal{W} \times \mathcal{S} \times \mathbb{R}^+$ such that

$$\int_0^{2\pi} \left[EA\,\epsilon_n\, L_\epsilon(\delta v, \delta w) + EI \kappa_n\, L_\kappa(\delta u, \delta w)\right] R\,\mathrm{d}\theta \; - \\ \lambda_{in} \int_0^{2\pi} \rho A \left[v_n\, \delta v + w_n\, \delta w\right] R\,\mathrm{d}\theta \; = \; 0 \qquad \forall\ \{\delta v, \delta w\} \in \mathcal{W}\,, \tag{3.19}$$

$$\int_0^{2\pi} \left[EA\, L_\epsilon(v_n, w_n)\, \delta\epsilon + EI\, L_\kappa(v_n, w_n)\, \delta\kappa\right] R\,\mathrm{d}\theta \; - \\ \int_0^{2\pi} \left[EA\,\epsilon_n\, \delta\epsilon + EI\,\kappa_n\, \delta\kappa\right] R\,\mathrm{d}\theta \; = \; 0 \qquad \forall\ \{\delta\epsilon, \delta\kappa\} \in \mathcal{S}\,, \tag{3.20}$$

where $\mathcal{W} = (H^1 \times H^2)$ and $\mathcal{S} = (L^2 \times L^2)$ are the Sobolev spaces of periodic functions, all defined on the ring domain $[0, 2\pi]$.

Cartesian displacements

At each point of the ring parametrized by the angular coordinate θ, we can express circumferential and transverse displacements v and w in terms of Cartesian displacements u_x and u_y that refer to a fixed global coordinate system (see Fig. 3.3). The corresponding transformation rule is:

$$\begin{bmatrix} w \\ v \end{bmatrix} = \begin{bmatrix} \cos(\theta) & \sin(\theta) \\ -\sin(\theta) & \cos(\theta) \end{bmatrix} \begin{bmatrix} u_x \\ u_y \end{bmatrix}. \tag{3.21}$$

Substituting this transformation in (3.15a) and (3.15b), we obtain the corresponding strain-displacement operators:

$$L_\epsilon(u_x, u_y) = \frac{1}{R}\left(-u_{x,\theta} \sin(\theta) + u_{y,\theta} \cos(\theta)\right) \tag{3.22a}$$

$$L_\kappa(u_x, u_y) = \frac{1}{R^2}\left(-u_{x,\theta\theta} \cos(\theta) + u_{x,\theta} \sin(\theta) - u_{y,\theta\theta} \sin(\theta) - u_{y,\theta} \cos(\theta)\right), \tag{3.22b}$$

that act on Cartesian displacements. From (3.19), we can derive the variational formulation of the generalized eigenvalue problem with respect to Cartesian displacements by replacing all circumferential and transverse displacements via (3.21), (3.22a) and (3.22b).

The result is: find $(\{u_{x,n}, u_{y,n}\}, \{\epsilon_n, \kappa_n\}, \lambda_{in}) \in \mathcal{U} \times \mathcal{S} \times \mathbb{R}^+$ such that:

$$\int_0^{2\pi} \left[EA\,\epsilon_n\, L_\epsilon(\delta u_x, \delta u_y) + EI\,\kappa_n\, L_\kappa(\delta u_x, \delta u_y)\right] R\,\mathrm{d}\theta \; - \\ \lambda_{in} \int_0^{2\pi} \rho A \left[u_{x,n}\, \delta u_x + u_{y,n}\, \delta u_y\right] R\,\mathrm{d}\theta \; = \; 0 \qquad \forall\ \{\delta v, \delta w\} \in \mathcal{U}\,, \tag{3.23}$$

$$\int_0^{2\pi} \left[EA\, L_\epsilon(u_{x,n}, u_{y,n})\, \delta\epsilon + EI\, L_\kappa(u_{x,n}, u_{y,n})\, \delta\kappa \right] R\, \mathrm{d}\theta \;\; - \;\; \int_0^{2\pi} \left[EA\, \epsilon_n\, \delta\epsilon + EI\, \kappa_n\, \delta\kappa \right] R\, \mathrm{d}\theta \; = \; 0 \qquad \forall\; \{\delta\epsilon, \delta\kappa\} \in \mathcal{S}\,, \tag{3.24}$$

where $\mathcal{U} = (H^2 \times H^2)$ and $\mathcal{S} = (L^2 \times L^2)$ are the Sobolev spaces of periodic functions, defined on the ring domain $[0, 2\pi]$. In the remainder of this work, we will apply the variational formulation (3.23) and (3.24) as well as the strain-displacement relations (3.22a) and (3.22b) as the basis for understanding different finite element discretization schemes.

3.3.3 Standard isogeometric finite element discretization

In this paper, we employ splines as basis functions, which are widely used today in the context of isogeometric analysis [30], [51]. For further details, we refer to the recent reviews [175]–[177] and the references therein.

Uniform periodic B-splines on a circular ring

A spline is a piecewise polynomial, characterized by the polynomial degree p of its segments and the prescribed smoothness at the segment interfaces. In the following, we employ smooth B-splines with maximum continuity C^{p-1} with $p \geq 2$, defined on a uniform partition of the circle. We construct periodic spline discretizations of dimension $\hat{n}_b$ by taking $\hat{n}_b + p$ sequential B-splines and applying suitable end conditions to the last p B-splines. We denote the resulting discrete space spanned by the $\hat{n}_b$ periodic B-spline basis functions of polynomial degree p with continuity C^{p-1} as $\mathcal{V}^{p,p-1}_{\hat{n}_b}$. For the circular ring, we apply an exact geometric mapping, $\mathbf{F}$, using trigonometric functions:

$$(x, y) = \mathbf{F}(\theta) = (R\cos(\theta), R\sin(\theta)) \tag{3.25}$$

Figure 3.6 shows a graphical illustration. Construction, differentiation and integration of B-splines can be performed using standard spline formulae, see [1], [2].

Remark 3.3.3. *Spline discretization with repeated knots lead to the appearance of outlier eigenvalues and eigenmodes at the end of the spectrum [43], [60], [122]. The use of uniform periodic B-spline discretizations of the circular ring eliminates this issue entirely, highlighting another advantage of our choice of benchmark problem.*

Displacement-based stiffness and mass matrices

Standard displacement-based finite element methods presume that the strain-displacement relations are exactly satisfied by the finite element approximation. On the one hand, the strain field variables can therefore be eliminated from the variational formulation

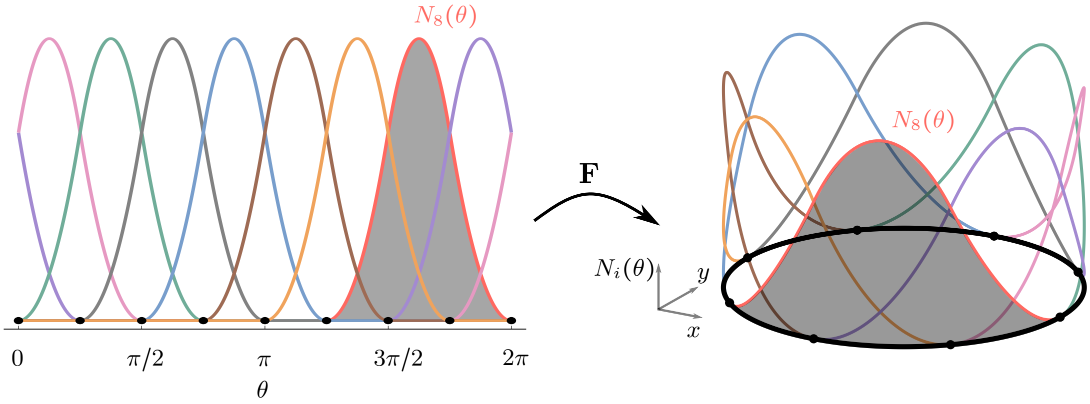

Figure 3.6: The space $\mathcal{V}_8^{2,1}(0,2\pi)$, consisting of $\hat{n}_b = 8$ quadratic periodic B-splines on the circle.

by replacing them by the displacement-based expressions incorporated in the strain-displacement operators (3.22a) and (3.22b). It is thus sufficient to discretize the Cartesian displacements and virtual displacements by a finite sum of $\hat{n}_b$ B-spline basis functions $N_i(\theta)$ multiplied by unknown coefficients:

$$u_x^h(\theta) = \sum_{i=1}^{\hat{n}_b} N_i(\theta)\, U_x^i\,, \qquad u_y^h(\theta) = \sum_{i=1}^{\hat{n}_b} N_i(\theta)\, U_y^i\,, \tag{3.26}$$

$$\delta u_x^h(\theta) = \sum_{i=1}^{\hat{n}_b} N_i(\theta)\, \delta U_x^i\,, \qquad \delta u_y^h(\theta) = \sum_{i=1}^{\hat{n}_b} N_i(\theta)\, \delta U_y^i\,. \tag{3.27}$$

On the other hand, the weak form of the kinematic constraints (3.24) is a priori satisfied strongly, and can thus be removed from the variational formulation.

Inserting (3.26) and (3.27) in the remaining weak form (3.23) yields the standard finite element formulation of the generalized eigenvalue problem: find $(\{u_{x,n}^h, u_{y,n}^h\}, \lambda_{in}^h) \in \mathcal{V} \times \mathbb{R}^+$ such that:

$$\int_0^{2\pi} \left[EA\, L_\epsilon(u_{x,n}^h, u_{y,n}^h)\, L_\epsilon(\delta u_x^h, \delta u_y^h) + EI\, L_\kappa(u_{x,n}^h, u_{y,n}^h)\, L_\kappa(\delta u_x^h, \delta u_y^h) \right] R\, \mathrm{d}\theta \;\; - \\ \lambda_{in}^h \int_0^{2\pi} \rho A \left[u_{x,n}^h\, \delta u_x^h + u_{y,n}^h\, \delta u_y^h \right] R\, \mathrm{d}\theta \;=\; 0 \qquad \forall\ \{\delta v, \delta w\} \in \mathcal{V}_{\hat{n}_b}^{p,p-1}\,, \tag{3.28}$$

with $n = 1, 2, \ldots, \hat{n}_b$ and $i = 1, 2$. The space $\mathcal{V} = (\mathcal{V}_{\hat{n}_b}^{p,p-1} \times \mathcal{V}_{\hat{n}_b}^{p,p-1})$, where $p \geq 2$, consists of $\hat{n}_b$ periodic C^{p-1} B-spline functions of at least quadratic polynomial degree defined on the ring domain $[0, 2\pi]$. It entails displacements and virtual displacements in the sense of the Galerkin method.

From (3.28), it is straightforward to retrieve the standard form of a discrete generalized eigenvalue problem (3.2) [66]. For the circular Euler-Bernoulli ring, the stiffness matrix of the standard displacement-based finite element method is:

$$\mathbf{K} = \underbrace{EA \int_0^{2\pi} \mathbf{B}_m^T \, \mathbf{B}_m \, R \, \mathrm{d}\theta}_{\mathbf{K}_m} + \underbrace{EI \int_0^{2\pi} \mathbf{B}_b^T \, \mathbf{B}_b \, R \, \mathrm{d}\theta}_{\mathbf{K}_b} \,, \tag{3.29}$$

that can be divided into a membrane part, $\mathbf{K}_m$, and a bending part, $\mathbf{K}_b$. The discrete strain-displacement matrices for the membrane strain and the change of curvature, $\mathbf{B}_m$ and $\mathbf{B}_b$, are:

$$\mathbf{B}_m = \frac{1}{R} \left[-N_{1,\theta}(\theta) \sin(\theta) \; \dots \; -N_{\hat{n}_b,\theta}(\theta) \sin(\theta) \;\; N_{1,\theta}(\theta) \cos(\theta) \; \dots \; N_{\hat{n}_b,\theta}(\theta) \cos(\theta) \right] , \tag{3.30}$$

$$\mathbf{B}_b = \frac{1}{R^2} \left[-N_{1,\theta\theta}(\theta) \cos(\theta) + N_{1,\theta}(\theta) \sin(\theta) \; \dots \; -N_{1,\theta\theta}(\theta) \sin(\theta) - N_{1,\theta}(\theta) \cos(\theta) \; \dots \right] . \tag{3.31}$$

The consistent mass matrix is a 2×2 block diagonal matrix of the following form:

$$\mathbf{M} = \begin{bmatrix} \mathsf{M} & \\ & \mathsf{M} \end{bmatrix}, \text{ with } M_{ij} = \rho A \int_0^{2\pi} N_i(\theta) \, N_j(\theta) \, R \, \mathrm{d}\theta \,, \; \{i,j\} = 1, 2, \dots, \hat{n}_b \,. \tag{3.32}$$

Full versus reduced integration

The standard finite element formulation (3.28) of the Euler-Bernoulli circular ring uses Gauss quadrature with $(p+1)$ quadrature points to numerically integrate the entries of the stiffness and mass matrices (3.29) and (3.32), commonly denoted as full integration. It is well-known, however, that the standard formulation with full integration suffers from severe membrane locking.

In the case of the Euler-Bernoulli beam, selective reduced integration performs numerical integration of the membrane part of the stiffness matrix in (3.29) with a quadrature rule that accurately integrates only a subset of all polynomials within an element. On the one hand, reduced selective integration is simple to implement and operates with the same displacement-based standard variational formulation (3.28). On the other hand, reduced integration can imply unstable solution behavior due to the appearance of spurious zero-energy modes [149], [150], [178]. For other reduced quadrature schemes suitable for IGA, we refer the reader to [73], [74], [133] and the references therein. In this study, we will employ a reduced quadrature scheme based on Gaussian quadrature that uses p quadrature points per spline segment for the integration of the membrane stiffness matrix $\mathbf{K}_m$ in (3.29), and $p+1$ quadrature points for the integration of the bending stiffness and mass matrices $\mathbf{K}_b$ in (3.29) and $\mathbf{M}$ in (3.32). One can show that this choice preserves full accuracy and still avoids spurious modes [171].

3.4 Three membrane locking-free finite element formulations

In the following, we briefly review and compare the key concepts of three well-established methods that are widely used to mitigate membrane locking. These are B-bar strain projection, the discrete strain gap method, and a mixed formulation based on the Hellinger-Reissner principle. We note that their use is not limited to membrane locking in the Euler-Bernoulli beam formulation, but all three have been successfully employed for mitigating a variety of locking phenomena in different structure and material models. For the sake of conciseness, we state their formulation directly for the Euler-Bernoulli ring and refer to the literature for a more general presentation.

Remark 3.4.1. *The assumed natural strain (ANS) method is equivalent to the B-bar method, since the spaces of assumed strain fields and projection spaces are equivalent to appropriate projection operators [75]. The ANS method can thus be expected to provide similar results to the B-bar method. The enhanced assumed strain (EAS) method is in some sense equivalent to the Hellinger-Reissner formulation [161], and can thus be expected to provide similar results. We therefore do not include the ANS and EAS methods in the following study.*

3.4.1 B-bar strain projection

The B-bar strain projection method was initially developed to treat volumetric locking [144], [153] and then extended to isogeometric analysis and other types of locking such as transverse shear and membrane locking [70], [75], [76]. The basic idea is to project the strain components associated with locking onto a basis of lower dimension so that the locking effect is alleviated. A common choice for the definition of a projector is the minimization of the L^2 norm. The B-bar strain projection method can be applied for any type of locking phenomenon and with any polynomial basis of arbitrary degree and spatial dimension. The projected strain fields result in a modified strain tensor and modified strain-displacement matrix, $\mathbf{B}$, hence the name. There are no additional point sets to evaluate and no additional stiffness terms or variables are required.

For our study, we adapt the Timoshenko beam formulation presented in [68] to the Euler-Bernoulli case, resulting in a modification of the membrane stiffness matrix $\mathbf{K}_m$ in (3.29). We choose a projection using the L^2 norm for the membrane strain and a basis of degree $p-1$ with continuity C^{p-2} and p with continuity C^{p-1}, where $p \geq 2$, for the projected membrane strain and the displacement field, respectively. The modified membrane stiffness matrix is then:

$$\bar{\mathbf{K}}_m = EA \;\; \bar{\mathbf{B}}_m^T \, \bar{\mathbf{M}}^{-1} \, \bar{\mathbf{B}}_m \, . \tag{3.33}$$

For our example of the circular Euler-Bernoulli ring discretized with a periodic B-spline basis, the matrices resulting from the projection procedure are defined as:

$$\bar{\mathbf{B}}_m = \left[\bar{\mathbf{B}}_1 \, \bar{\mathbf{B}}_2\right], \;\; \text{with} \;\; \bar{B}_{1,ij} = -\int_0^{2\pi} \sin(\theta)\, \bar{N}_i \, N_{j,\theta} \, \mathrm{d}\theta \, , \;\; \bar{B}_{2,ij} = \int_0^{2\pi} \cos(\theta)\, \bar{N}_i \, N_{j,\theta} \, \mathrm{d}\theta,$$

$$\text{and } \bar{M}_{ij} = \int_0^{2\pi} \bar{N}_i\, \bar{N}_j\, R\, \mathrm{d}\theta\,, \quad \text{where } \{i,j\} = 1,2,\ldots,\hat{n}_b\,,\ (N,\bar{N}) \in \mathcal{V}^{p,p-1}_{\hat{n}_b} \times \tilde{\mathcal{V}}^{p-1,p-2}_{\hat{n}_b}\,.$$

The entries in $\bar{\mathbf{B}}$ and $\bar{\mathbf{M}}$, corresponding to the projected strain in a basis of degree $p-1$, are evaluated with p quadrature points in each Bézier element. The bending stiffness matrix, $\mathbf{K}_b$, and the consistent mass matrix, $\mathbf{M}$, remain unaffected by the projection.

3.4.2 Discrete strain gap method

The discrete strain gap (DSG) method was originally developed to alleviate transverse shear locking in plates and shells [163], [164], and then extended to membrane locking [165] and isogeometric analysis [47], [68], [80]. Its main idea is to enable the strain fields associated with locking to represent zero strains by modifying the interpolation of these strain fields. The DSG method can be classified as a B-bar method since it results in a modified strain-displacement matrix. For details on the procedure to modify the strain interpolation and obtain the modified stiffness matrix, we refer to [68], [80]. For our example of the circular Euler-Bernoulli ring, we adapt the procedure described for the Timoshenko curved beam in [68] and obtain the modified strain-displacement matrix, $\bar{\mathbf{B}}_m$, in the following form:

$$\bar{\mathbf{B}}_m = \frac{1}{R}\left[\tilde{N}_{1,\theta}(\theta)\ \tilde{N}_{2,\theta}(\theta)\ \ldots \tilde{N}_{N,\theta}(\theta)\right] \mathbf{A}^{-1}\mathbf{C}\,\mathbf{D}\,. \tag{3.34}$$

The matrices are defined as:

$$A_{ij} = \tilde{N}_j(\theta_i)\,, \quad C_{ij} = -\frac{1}{R}\int_0^{\theta_i} \sin(\theta)\, N_{j,\theta}(\theta)\, R\, \mathrm{d}\theta\,,$$

$$D_{ij} = \frac{1}{R}\int_0^{\theta_i} \cos(\theta)\, N_{j,\theta}(\theta)\, R\, \mathrm{d}\theta,$$

where $N_i(\theta)$ and $\tilde{N}_i(\theta)$ denote the basis functions interpolating the displacement fields and the modified membrane contribution, respectively, and θ_i is the angular coordinate corresponding to the i^{th} collocation point. Substituting the modifed matrix, $\bar{\mathbf{B}}_m$, in (3.29) results in the modifed membrane stiffness matrix, following the DSG method, which is equivalent to what is described in [68, eq. 55]. The evaluation of the matrices, $\mathbf{A}, \mathbf{C}, \mathbf{D}$, depends only on the set of collocation points and does not require any assembly routine. The basis functions $\tilde{N}_{i,\theta}(\theta)$ in the first term of $\bar{\mathbf{B}}_m$ (the first row vector) are evaluated in an assembly routine at quadrature points in each element.

In [68], [80], the authors apply NURBS to describe the geometry and to interpolate all variable fields including the modified strain contribution (i.e. NURBS basis functions as $\tilde{N}_i$). In our computations in section 3.5, we choose a space of uniform B-splines that is of the same degree and defined on the same uniform open knot vector as the space of the uniform periodic C^{p-1} B-splines, $\mathcal{V}^h_p$, to interpolate the modified membrane contribution. Thus:

$$(N,\tilde{N}) \in \mathcal{V}^{p,p-1}_{\hat{n}_b} \times \mathcal{S}^{p,p-1}_{\tilde{n}_b}\,,$$

where $\mathcal{V}_{\hat{n}_b}^{p,p-1}$ denotes the space of uniform periodic B-splines of degree p with continuity C^{p-1}, and $\mathcal{S}_{\hat{n}_b}^{p,p-1}$ denotes the space of uniform B-splines of degree p with continuity C^{p-1}, defined on an open knot vector. Our choice of collocation points is the Greville abscissa corresponding to the uniform B-splines of the modified membrane contribution [68].

3.4.3 Hellinger-Reissner principle

The third locking-free formulation that we consider is the mixed formulation that follows from the Hellinger-Reissner principle [47], [81], [161], [169]. This is a two-field formulation of displacement and either stress or strain fields. When we choose appropriate approximation spaces for these fields, we can eliminate locking. The Hellinger-Reissner mixed formulation can be derived from the general three-field mixed formulation (Hu-Washizu principle) by satisfying the constitutive relation strongly [161].

The mixed variational formulation based on the Hellinger-Reissner principle of the eigenvalue problem for an Euler-Bernoulli circular ring in Cartesian coordinates was derived in section 3.3.2. Discretizing the independent variable fields, $\left(\mathbf{u}^h, \boldsymbol{\epsilon}^h\right) = \left([u_x, u_y]^T, [\epsilon, \kappa]^T\right) \in \mathcal{V}_{\hat{n}_b}^{p,p-1} \times \tilde{\mathcal{V}}_{\hat{n}_b}^{p-1,p-2}$, and inserting those in the variational formulation, (3.23) and (3.24), yields the following matrix equation of the eigenvalue problem based on the Hellinger-Reissner principle for the Euler-Bernoulli circular ring:

$$\begin{bmatrix} \mathbf{K}_{11} & \mathbf{K}_{12} \\ \mathbf{K}_{12}^T & 0 \end{bmatrix} \begin{bmatrix} \boldsymbol{\epsilon} \\ \mathbf{U} \end{bmatrix} = \begin{bmatrix} 0 \\ \boldsymbol{\lambda}\mathbf{M}\mathbf{U} \end{bmatrix}, \quad \text{with} \quad \mathbf{K}_{11} = \begin{bmatrix} \mathbf{k}_{11} & 0 \\ 0 & \mathbf{k}_{22} \end{bmatrix}, \quad \mathbf{K}_{12} = \begin{bmatrix} \mathbf{k}_{13} & \mathbf{k}_{14} \\ \mathbf{k}_{23} & \mathbf{k}_{24} \end{bmatrix},$$

where the entries of the different blocks of the stiffness matrix are defined as:

$$k_{11,ij} = -EA \int_0^{2\pi} \bar{N}_i \bar{N}_j \, R \, \mathrm{d}\theta, \quad k_{22,ij} = -EI \int_0^{2\pi} \bar{N}_i \bar{N}_j \, R \, \mathrm{d}\theta, \tag{3.35}$$

$$k_{13,ij} = EA \int_0^{2\pi} \bar{N}_i \left(-\frac{1}{R} \sin(\theta) N_{j,\theta} \right) R \, \mathrm{d}\theta \tag{3.36}$$

$$k_{14,ij} = EA \int_0^{2\pi} \bar{N}_i \left(\frac{1}{R} \cos(\theta) N_{j,\theta} \right) R \, \mathrm{d}\theta \tag{3.37}$$

$$k_{23,ij} = EI \int_0^{2\pi} \bar{N}_i \left(-\frac{1}{R^2} \cos(\theta) N_{j,\theta\theta} + \frac{1}{R^2} \sin(\theta) N_{j,\theta} \right) R \, \mathrm{d}\theta \tag{3.38}$$

$$k_{24,ij} = EI \int_0^{2\pi} \bar{N}_i \left(-\frac{1}{R^2} \sin(\theta) N_{j,\theta\theta} - \frac{1}{R^2} \cos(\theta) N_{j,\theta} \right) R \, \mathrm{d}\theta \,, \tag{3.39}$$

$$\text{where } \{i,j\} = 1, 2, \ldots, \hat{n}_b \,, \quad (N, \bar{N}) \in \mathcal{V}_{\hat{n}_b}^{p,p-1} \times \tilde{\mathcal{V}}_{\hat{n}_b}^{p-1,p-2} \,.$$

To eliminate the secondary field, we can apply static condensation which leads to the final stiffness matrix of the eigenvalue problem based on the Hellinger-Reissner mixed formulation:

$$\mathbf{K} = -\mathbf{K}_{12}^T \mathbf{K}_{11}^{-1} \mathbf{K}_{12} \,. \tag{3.40}$$

We note that the mass matrix $\mathbf{M}$ remains unchanged to what is defined in (3.32).

3.5 Assessing membrane locking and unlocking via spectral analysis

In this section, we demonstrate for a slender Euler-Bernoulli circular ring that spectral analysis can be an effective tool to assess locking and unlocking in finite element formulations. To this end, we compare the errors of the eigenvalues and eigenmodes across the spectrum for the standard finite element formulations with full and reduced integration as well as the three locking-free formulations that we reviewed above. In particular, we use spectral analysis to assess their sensitivity to locking on a coarse mesh, under mesh refinement, and for p-refinement (i.e. increasing polynomial degree as well as smoothness). We show that the spectral approximation properties of each formulation can be directly related to its locking deficiency or unlocking capability.

3.5.1 Locking indicator based on spectral analysis

In the following, we measure locking and unlocking from a spectral analysis viewpoint based on the following criterion:

Locking indicator: A method is locking-free if the normalized spectra obtained on coarse meshes are "close" to asymptotic refinement curves obtained from "overkill" discretizations, that is, the normalized spectra do not significantly change with mesh refinement. Accordingly, a method is locking-prone if its normalized spectra differ significantly from on asymptotic refinement curves obtained from "overkill" discretizations, that is, the normalized spectra significantly change with mesh refinement.

The above statement is best described by means of an illustration. Fig 3.7 depicts the normalized error in the eigenvalues λ_1^h computed with quadratic B-splines ($p = 2$) on a mesh of 64 elements ($N = 32$), for "large" slenderness ratio $R/t = 2000/3$. We observe from the plot that the spectra obtained with full integration and reduced integration differ significantly from the asymptotic refinement curves, and hence the corresponding formulations severely lock over the entire range of the spectrum. In contrast, the discrete spectra of the B-bar, Hellinger-Reissner and DSG methods are close their asymptotic refinement curves, and are thus locking-free.

From a practical standpoint, we can now proceed as follows. For the finite element formulation in question, eigenvalue and mode errors are computed on a coarse discretization and corresponding asymptotic eigenvalue and mode errors are computed with an "overkill" discretization. The eigenvalue and mode errors from the coarse mesh are related to the corresponding asymptotic eigenvalue and mode errors by plotting both sets with respect to the normalized mode number n/N, where N denotes the total number of modes in each discretization. This relation is based on the notion that - given the underlying solution behavior is sufficiently resolved - all spectral error curves plotted over their normalized mode numbers must be identical, irrespective of the mesh size

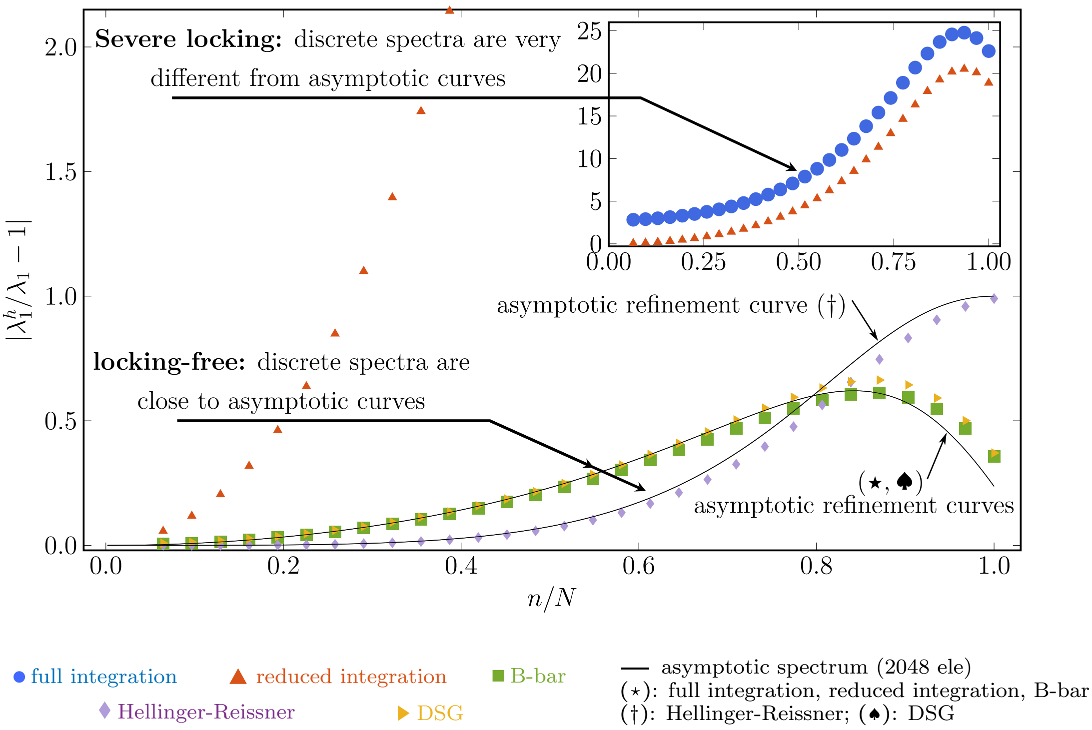

Figure 3.7: Our locking indicator provides a visual tool to understand locking and unlocking in discrete spectra.

and the associated number of degrees of freedom. As a consequence, the finite element formulation is locking-free, if the corresponding spectral error curves are matching up irrespective of the mesh size, and the finite element formulation is locking-prone, if the corresponding spectral error curves are different, implying that the spectral error curve changes with mesh refinement.

3.5.2 In-depth comparison for quadratic splines

In the first step, we study the effect of membrane locking on the spectral approximation properties for "large" ring slenderness $R/t = 2000/3$. For this case, we can expect severe membrane locking to occur, as demonstrated in our initial cantilever example in the introduction (see Fig. 3.1). For each finite element formulation, we compute the discrete eigenvalues and modes using periodic uniform B-splines of polynomial degree two, defined on 64 Bézier elements. Figs. 3.8 and 3.9 plot the relative eigenvalue errors (3.4) and the relative L^2-norm mode errors (3.5) across the normalized spectrum for the transverse eigenmodes U_1^h and the associated eigenvalues λ_1^h and the circumferential eigenmodes U_2^h and the associated eigenvalues λ_2^h, respectively. The eigenvalue and mode errors are obtained with respect to the analytical solutions given in Appendix 3.A. Furthermore, we compute asymptotic spectral error curves numerically for each finite element formulation with an "overkill" discretization of 2048 elements.

Remark 3.5.1. *Readers interested in the technical details for identifying transverse and circumferential modes and ordering them correctly to comply with the analytical ordering are referred to Appendix 3.B.*

Standard formulation with full and reduced integration

We start by considering the spectral analysis results obtained with the standard formulation with full integration, plotted in Figs. 3.8 and 3.9 with blue circles. We would like to identify the impact of membrane locking on the accuracy of the spectrum. Firstly, we focus on the eigenvalue error corresponding to the transverse modes, plotted in Fig. 3.8a. We observe that the transverse eigenvalues obtained with the standard finite element formulation show significant error levels, with the error curves being far away from the asymptotic reference curve plotted in black. We attribute this increase in error level to the effect of membrane locking, which is further supported by a look at the locking-free formulations that do not show a similar increase, producing transverse eigenvalue errors that match the asymptotic reference curve. As the accuracy of the transverse eigenvalues is heavily affected over the complete spectrum, we conclude that beam computations with the standard formulation at this mesh size will yield completely inaccurate results. This is confirmed by the convergence plots in Fig. 3.2a computed for our initial cantilever example, where the standard formulation does not converge for practical mesh sizes.

Secondly, we focus on the remaining spectral error quantities, that is, the mode errors for the transverse and circumferential mode shapes and the eigenvalue error corresponding to the circumferential modes, plotted in Fig. 3.8b, Fig. 3.9a and Fig. 3.9b. We observe that they show exactly the same error as the locking-free formulations, with the error curves being practically identical to the asymptotic reference curves. We conclude that for the case of the Euler-Bernoulli ring, membrane locking only influences the accuracy of the eigenvalues of the transverse modes, while the transverse mode shapes and both the eigenvalues and mode shapes of the circumferential modes do not lock.

Thirdly, we consider the spectral analysis results obtained with the standard formulation with selective reduced integration, which in Figs. 3.8 and 3.9 are plotted with red triangles. On the one hand, we observe in Fig. 3.8a that compared to full integration, selective reduced integration is able to improve the spectral accuracy of the lowest eigenvalues of the transverse modes. On the other hand, the spectral accuracy degenerates very quickly with increasing mode number. As a consequence, accurate finite element approximations of beam solutions on coarse meshes, where most of the spectrum is required to actively contribute, are not possible. Our conclusion is supported by Fig. 3.2a for the cantilever example, where convergence at the best possible accuracy level can only be achieved for finer mesh sizes.

B-bar method

We then move forward to the locking-free formulations. We first consider the results obtained with the B-bar formulation, which in Figs. 3.8 and 3.9 are plotted with green squares. We observe that the B-bar method eliminates the effect of membrane locking

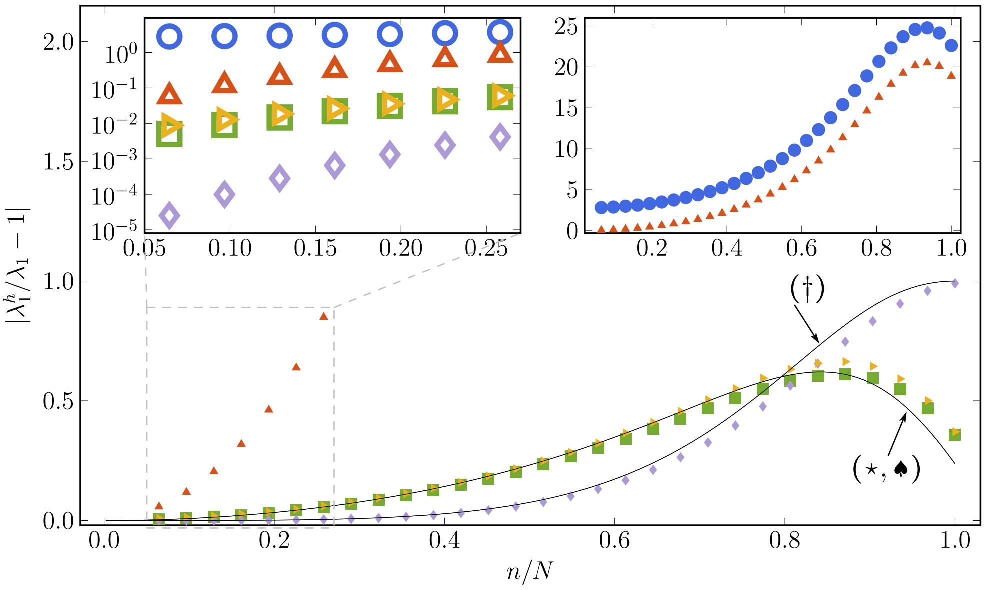

(a) Normalized error in eigenvalues λ_1^h (associated with transverse modes U_1^h)

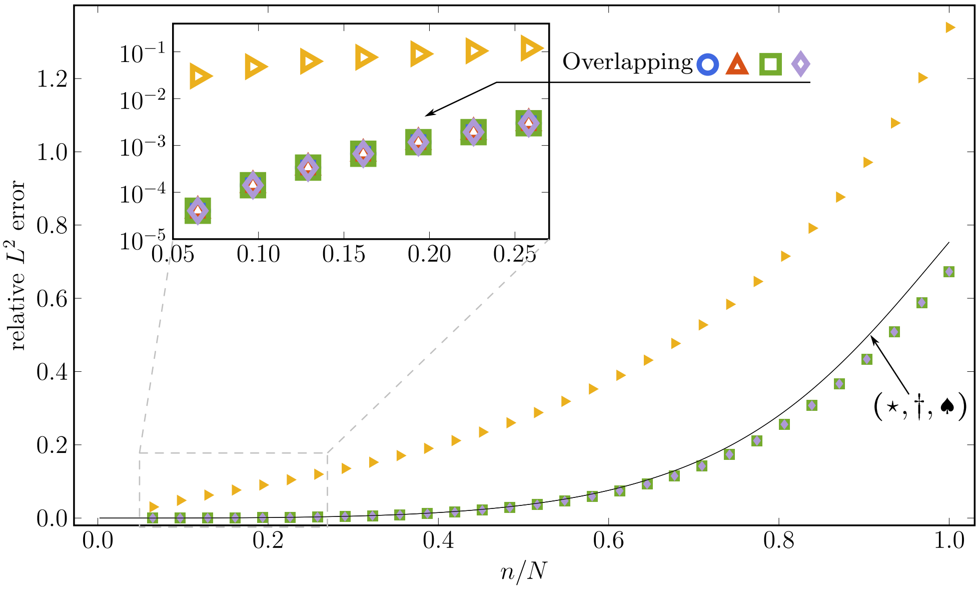

(b) Normalized L^2-norm error in transverse mode shapes U_1^h

● full integration ▲ reduced integration ■ B-bar
◆ Hellinger-Reissner ▶ DSG

— asymptotic spectrum (2048 ele)
(⋆): full integration, reduced integration, B-bar
(†): Hellinger-Reissner; (♠): DSG

Figure 3.8: Normalized errors in eigenvalues λ_1^h and **transverse** mode shapes U_1^h computed with **quadratic B-splines** ($p = 2$) on a mesh of **64 elements** ($N = 32$), for "large" slenderness ratio $R/t = 2000/3$.

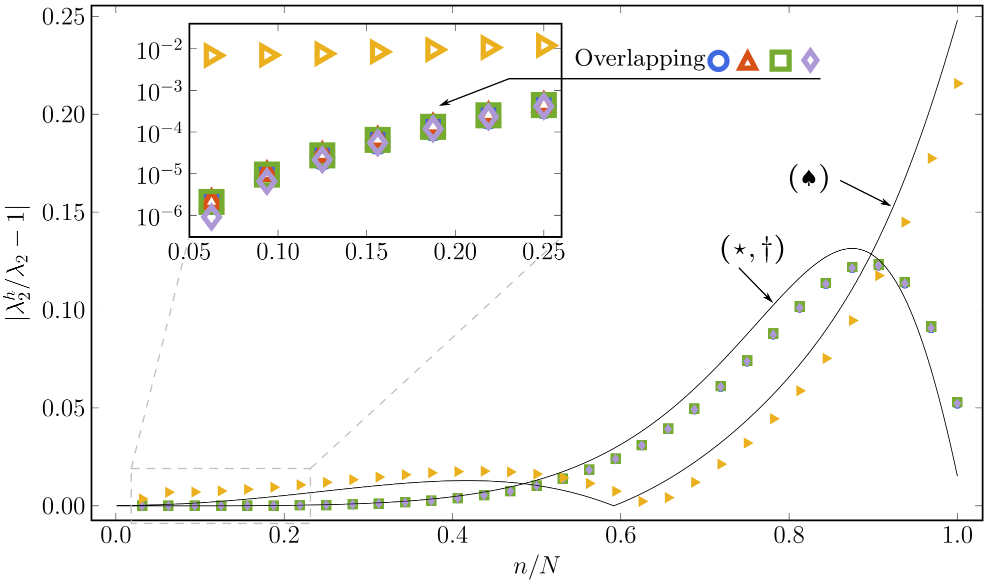

(a) Normalized error in eigenvalues λ_2^h (associated with circumferential modes U_2^h)

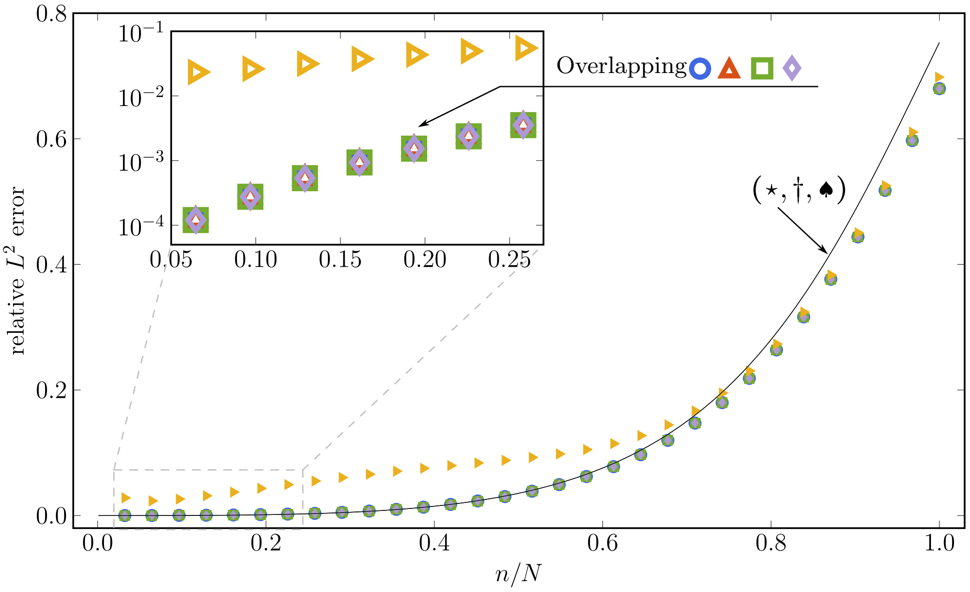

(b) Normalized L^2-norm error in circumferential mode shapes U_2^h

● full integration ▲ reduced integration ■ B-bar
◆ Hellinger-Reissner ▶ DSG

— asymptotic spectrum (2048 ele)
(⋆): full integration, reduced integration, B-bar
(†): Hellinger-Reissner; (♠): DSG

Figure 3.9: Normalized errors in eigenvalues λ_2^h and **circumferential** mode shapes U_2^h computed with **quadratic B-splines** ($p = 2$) on a mesh of **64 elements** ($N = 32$), for “large” slenderness ratio $R/t = 2000/3$.

in the entire spectrum of the eigenvalues corresponding to the transverse modes plotted in Fig. 3.8a. In addition, all error curves, both for the transverse and circumferential mode shapes and associated eigenvalues, correspond well to the asymptotic error curves, irrespective of the mesh size. This indicates that the finite element formulation with the B-bar method already achieves full spectral accuracy on the current coarser mesh. On the one hand, we conclude that the B-bar formulation successfully mitigates membrane locking. On the other hand, we can preclude any negative effect from the B-bar method on the convergence properties of the finite element formulation. Our conclusions therefore confirm that the B-bar method is an effective locking-free finite element formulation for the Euler-Bernoulli beam. They are supported by our initial cantilever example whose convergence results in Fig. 3.2a show the best possible accuracy on coarse and fine meshes that can be achieved for $p = 2$ in a purely displacement based formulation.

DSG method

We then consider the results obtained with the DSG formulation, which in Figs. 3.8 and 3.9 are plotted with yellow triangles. On the one hand, Fig. 3.8a shows that the DSG method completely eliminates the effect of locking on the locking-prone eigenvalues of the transverse modes, with the error curve closely matching the asymptotic error curve. On the other hand, the DSG method exhibits an increased level of error across large parts of the spectrum for the transverse mode shapes, the circumferential mode shapes and the eigenvalue error of the circumferential modes, which can be observed in Fig. 3.8b, Figs. 3.9a and 3.9b. These observations are remarkable as we concluded in the discussion above that these three quantities are not affected by membrane locking for the current Euler-Bernoulli ring problem. In particular, we can see in the inset plots that the low modes that are important for the approximation power of the basis (see Section 3.2.4) are significantly less accurate compared to the other formulations. We therefore conclude that the DSG formulations itself is responsible for the increase in error levels, and thus deteriorates the accuracy of the original standard finite element formulation with respect to part of the spectrum. We note that in Fig. 3.2a, the DSG method still achieves the best possible accuracy on coarse and fine meshes, as in our cantilever example, the transverse mode behavior dominates the overall accuracy of the analysis.

Remark 3.5.2. *The kink in the circumferential eigenvalue spectrum obtained with the DSG method is due to the fact that the ratio* λ_2^h/λ_2 *changes from positive to negative at that location.*

Hellinger-Reissner formulation

We finally consider the results obtained with the Hellinger-Reissner formulation, which in Figs. 3.8 and 3.9 are plotted with purple diamonds. We observe that the effect of membrane locking is eliminated in the entire spectrum of the eigenvalues of the transverse modes. The corresponding error curve closely matches the asymptotic error curve, irrespective of the mesh size. We note that the Hellinger-Reissner formulation has a different

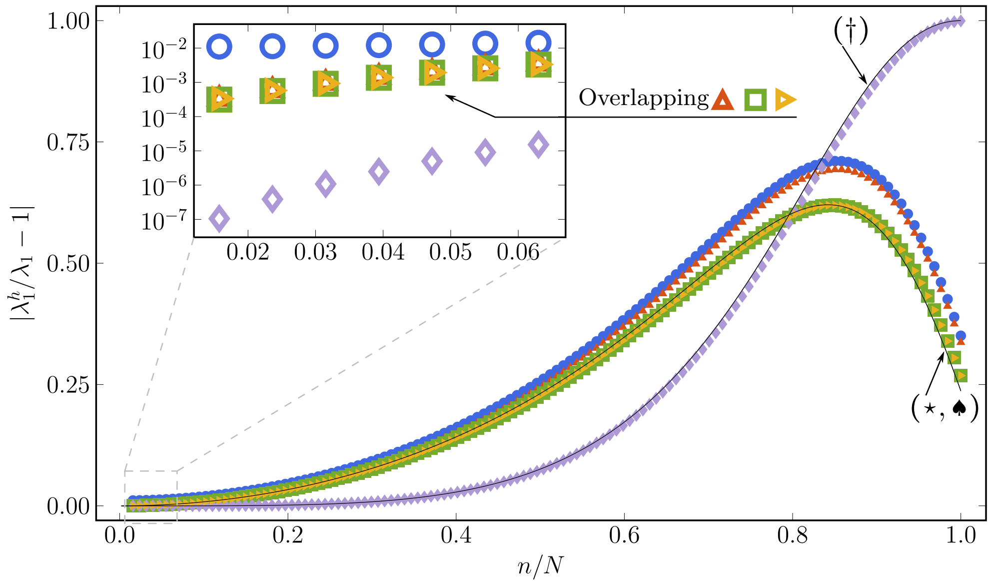

(a) Normalized error in eigenvalues λ_1^h (associated with transverse modes U_1^h)

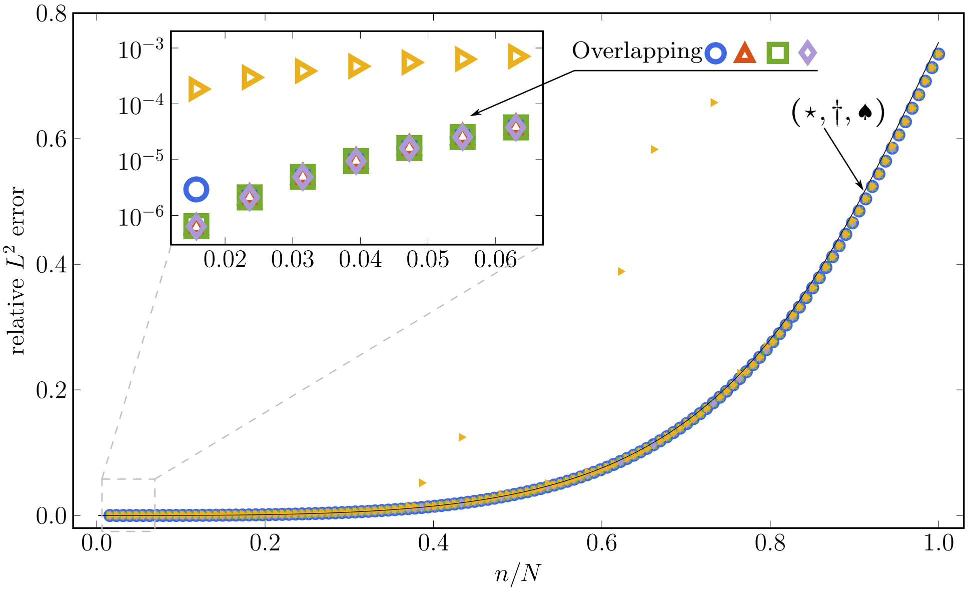

(b) Normalized L^2-norm error in transverse mode shapes U_1^h

Figure 3.10: Normalized errors in eigenvalues λ_1^h and **transverse** mode shapes U_1^h computed with **quadratic B-splines** ($p = 2$) on a mesh of **256 elements** ($N = 128$), for "large" slenderness ratio $R/t = 2000/3$.

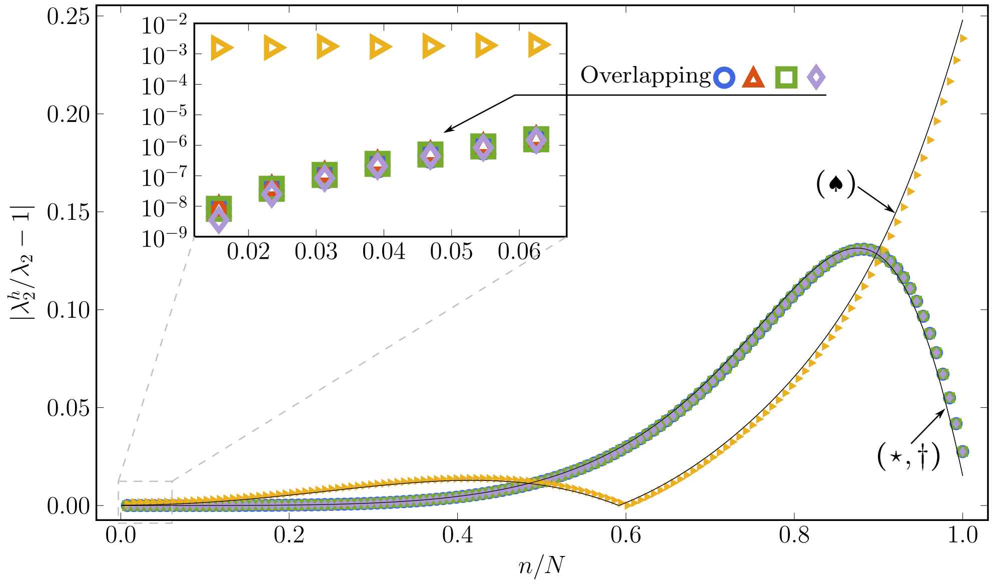

(a) Normalized error in eigenvalues λ_2^h (associated with circumferential modes U_2^h)

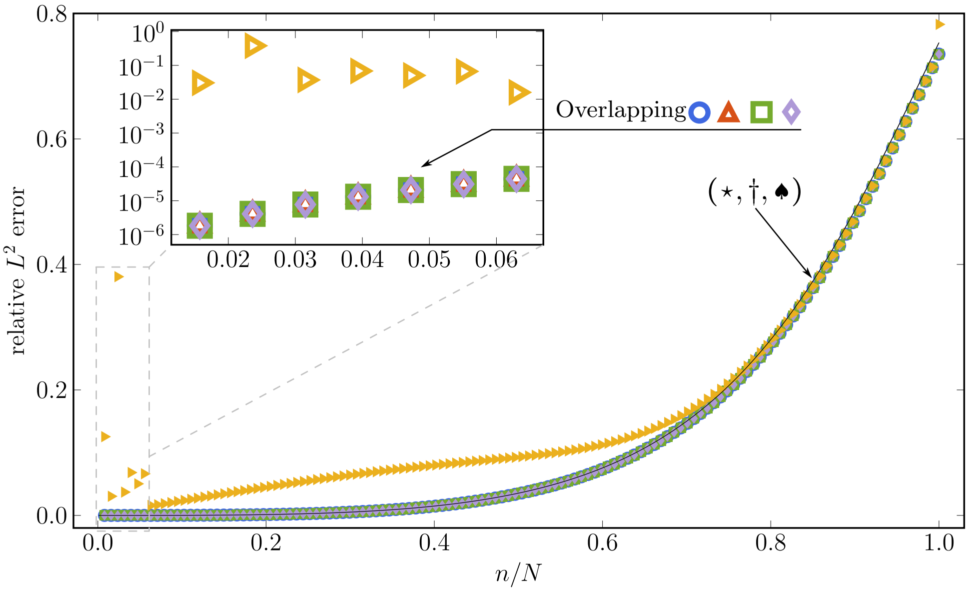

(b) Normalized L^2-norm error in circumferential mode shapes U_2^h

● full integration ▲ reduced integration ■ B-bar
◆ Hellinger-Reissner ▶ DSG

— asymptotic spectrum (2048 ele)
(⋆): full integration, reduced integration, B-bar
(†): Hellinger-Reissner; (♠): DSG

Figure 3.11: Normalized errors in eigenvalues λ_2^h and **circumferential** mode shapes U_2^h computed with **quadratic B-splines** ($p = 2$) on a mesh of **256 elements** ($N = 128$), for "large" slenderness ratio $R/t = 2000/3$.

asymptotic error curve, which is different from all other formulations considered here. We observe in the inset plot of Fig. 3.8a that the Hellinger-Reissner formulation achieves the best accuracy of the lowest eigenvalues of the locking-prone transverse modes, which are of particular importance for the approximation power of the basis, see Section 3.2.4. This accuracy advantage is maintained over 80% of the normalized spectrum.

The Hellinger-Reissner formulation is a mixed method, which requires the discretization of both displacement and strain fields. To render it comparable to the other methods that rely only on displacement variables, the Hellinger-Reissner formulation requires additional computational effort for the static condensation of the strain variables. In addition, for the Euler-Bernoulli beam model, a mixed formulation does not require basis functions that are in the space H^3 to achieve optimal rates of convergence [137], [138]. As a consequence, for quadratic basis functions that are only in H^2, the displacements converge with $\mathcal{O}(3)$ in the L^2 norm in the Hellinger-Reissner formulation, while displacement-based formulations achieve only $\mathcal{O}(2)$. This advantage of the Hellinger-Reissner formulation, however, is expected to disappear, when we consider basis functions of polynomial degree $p \geq 3$ that are in H^3, for which all methods achieve the same optimal rates $\mathcal{O}(p+1)$.

We therefore conclude that in terms of the effective prevention of membrane locking, the Hellinger-Reissner formulation hits a sweet spot for $p = 2$ and therefore seems to be the most effective choice for quadratic spline discretizations. This conclusion is confirmed by our initial cantilever example, where the accuracy gap between the Hellinger-Reissner formulation on the one hand and the B-bar and DSG methods on the other hand is clearly demonstrated by Fig. 3.2a.

3.5.3 Sensitivity with respect to mesh refinement

Mesh refinement will eventually remove most locking phenomena. This comes, however, at the price of a significantly increased computational cost that is always uneconomical and often prohibitive with respect to the available computing resources. Therefore, from a practical viewpoint, mesh refinement is not a viable option to mitigate locking. We use spectral analysis to illustrate the lacking efficiency of mesh refinement. To this end, we compute the discrete eigenvalues and modes for each finite element formulation at hand, using quadratic B-splines defined on 256 Bézier elements. Figs. 3.10 and 3.11 plot the relative eigenvalue errors (3.4) and the relative L^2-norm mode errors (3.5) across the normalized spectrum for the transverse and circumferential modes, respectively.

Inefficiency of the standard formulation

We first focus on the spectrum of eigenvalues λ_1^h associated with the transverse modes plotted in Fig. 3.10a, which is the quantity affected by membrane locking. We observe that the results obtained with the standard finite element formulation with full and reduced integration both improve significantly, with their spectral error now being in range of the error of the locking-free asymptotic solution. For selective reduced integration, we achieve the same accuracy in the lowest modes as for the locking-free B-bar and DSG methods. For full integration, however, the error of the lowest modes is still two orders of magnitude larger than the error level of the locking-free formulations, and therefore still prevents a high-fidelity solution despite the prohibitively fine mesh size. The effect on the accuracy in analysis that corresponds to these observations is illustrated in Fig. 3.2a for our initial cantilever example. While the convergence curve obtained with selective reduced integration catches up with the locking-free solutions for finer mesh sizes, the curve obtained with full integration still lags significantly behind.

DSG method and the circumferential modes

Looking at the complete set of spectral plots, we observe that the issues we detected for the DSG method on a mesh with 64 elements do not vanish under mesh refinement. In Fig. 3.10b, we can see that the lowest transverse mode shapes are approximated at an accuracy level that is two orders of magnitude below the locking-free standard solution. In addition, several modes in the center of the spectrum seem completely inaccurate. Figs. 3.11a and 3.11b that illustrate the spectral behavior of the circumferential modes show that the error of the lowest eigenvalues and mode shapes are both four to five orders of magnitude larger than the error of the locking-free solution. These results support our notion that the DSG formulation itself is responsible for the increase in spectral error levels, and thus deteriorates the accuracy of the standard finite element formulation in part of the spectrum. As membrane unlocking is associated primarily with the proper behavior in the transverse eigenvalues, this shortcoming of the DSG method seems not to affect its analysis capabilities in this particular case, as demonstrated for our initial cantilever example in Fig. 3.2a.

3.5.4 Sensitivity with respect to p-refinement

It has been often maintained that p-refinement constitutes an effective way to counteract locking phenomena, for instance in the context of the p-version of the finite element method [179]–[181]. A presumed key argument in support of p-refinement is that it mitigates locking when applied within a standard displacement-based formulation and thus bypasses the derivation and implementation of special locking-free formulations. In the following, we will use spectral analysis to shed light on the efficiency of p-refinement with respect to mitigating membrane locking in the Euler-Bernoulli ring example.

Classical p-refinement: standard formulation

We first move to cubic B-splines defined on 64 Bézier elements, re-computing the discrete eigenvalues and eigenmodes for each finite element formulation at hand. We note that due to periodicity, the cubic discretization of the circular ring exhibits the same number of spline basis functions and hence the same number of degrees of freedom as the quadratic discretization. For polynomial degree $p = 3$, Figs. 3.12 and 3.13 plot the relative eigenvalue errors (3.4) and the relative L^2-norm mode errors (3.5) across the normalized spectrum for the transverse and circumferential modes, respectively. They can

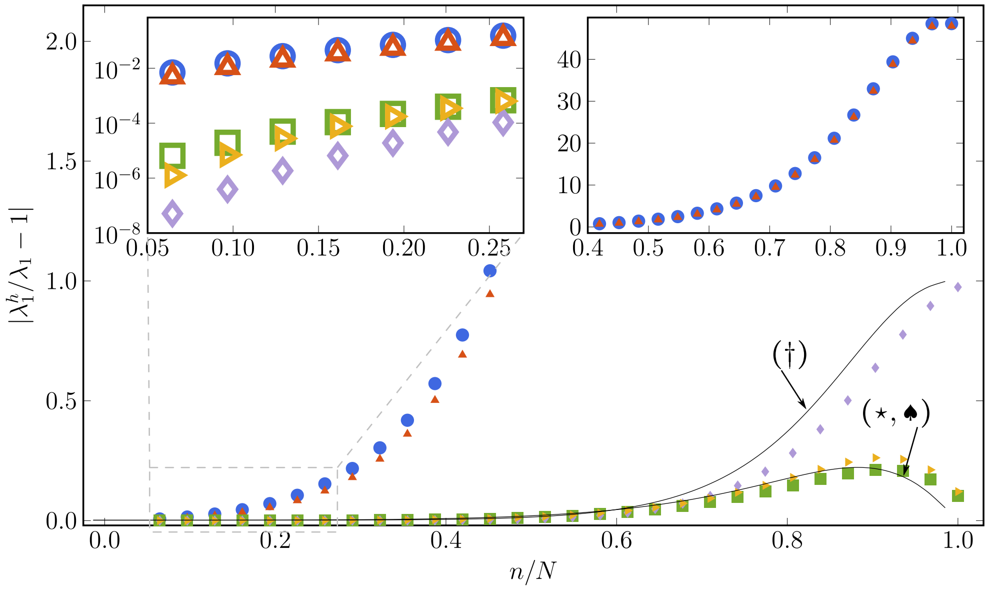

(a) Normalized error in eigenvalues λ_1^h (associated with transverse modes U_1^h)

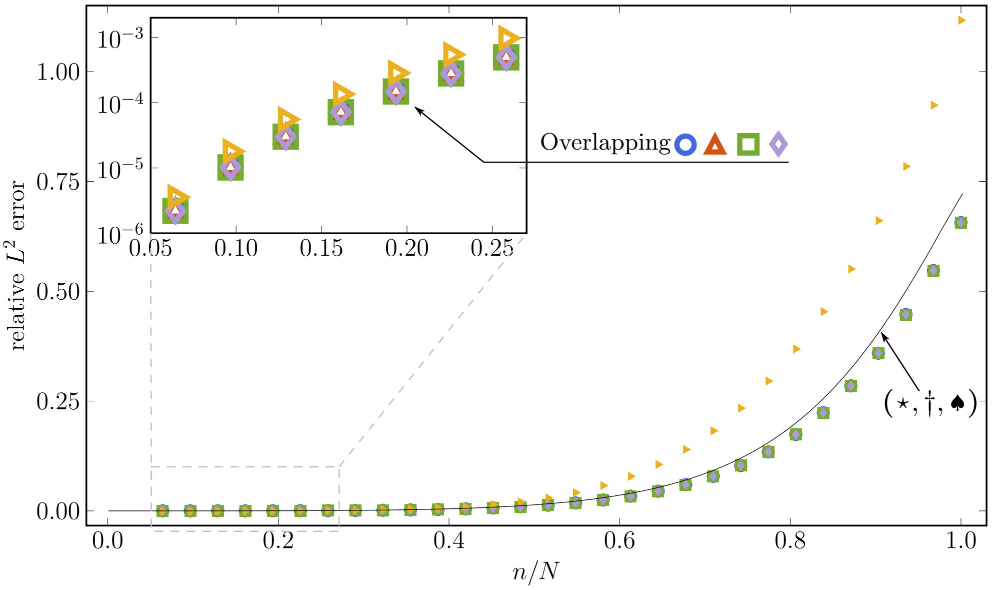

(b) Normalized L^2-norm error in transverse mode shapes U_1^h

● full integration ▲ reduced integration ■ B-bar
♦ Hellinger-Reissner ▶ DSG

— asymptotic spectrum (2048 ele)
(⋆): full integration, reduced integration, B-bar
(†): Hellinger-Reissner; (♠): DSG

Figure 3.12: Normalized errors in eigenvalues λ_1^h and **transverse** mode shapes U_1^h computed with **cubic B-splines** (p = 3) on a mesh of **64 elements** (N = 32), for “large” slenderness ratio R/t = 2000/3.

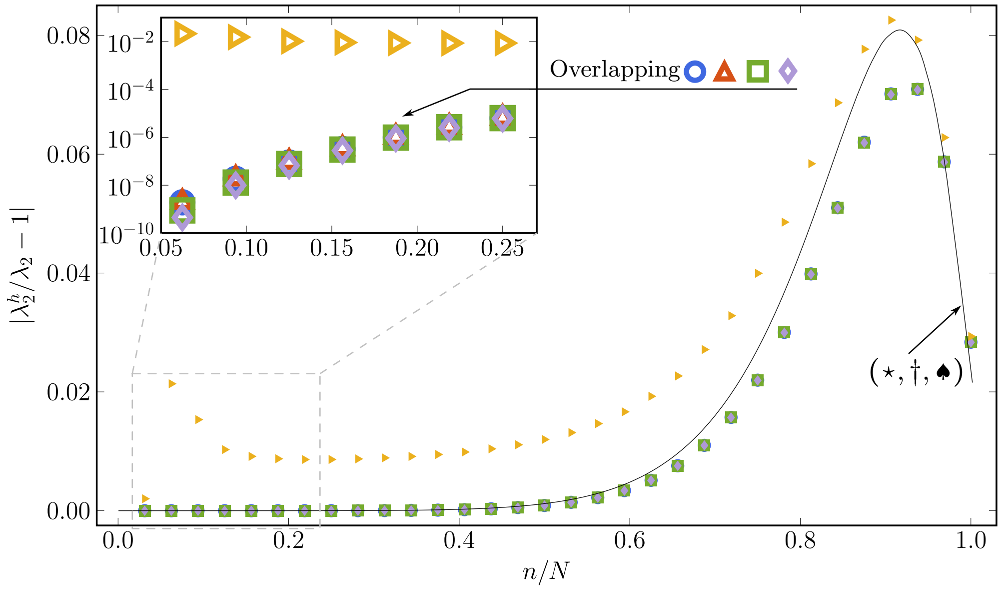

(a) Normalized error in eigenvalues λ_2^h (associated with circumferential modes U_2^h)

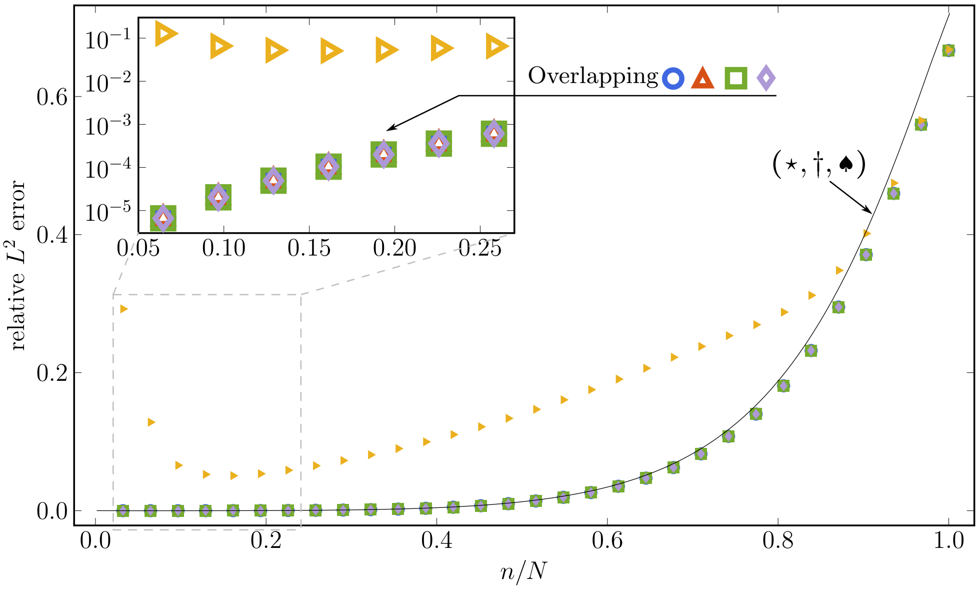

(b) Normalized L^2-norm error in circumferential mode shapes U_2^h

● full integration ▲ reduced integration ■ B-bar
◆ Hellinger-Reissner ▶ DSG

— asymptotic spectrum (2048 ele)
$(\star)$: full integration, reduced integration, B-bar
$(\dagger)$: Hellinger-Reissner; $(\spadesuit)$: DSG

Figure 3.13: Normalized errors in eigenvalues λ_2^h and **circumferential** mode shapes U_2^h computed with **cubic B-splines** ($p = 3$) on a mesh of **64 elements** ($N = 32$), for "large" slenderness ratio $R/t = 2000/3$.

be directly compared to Figs. 3.8 and 3.9 that plot the equivalent results for quadratic B-splines.

We first consider the spectrum of eigenvalues λ_1^h associated with the transverse modes, which is the relevant spectral quantity for membrane locking. Focusing on the lowest eigenvalues, we compare the corresponding error levels shown in the inset figures of Fig. 3.8a for quadratics and Fig. 3.12a for cubics. We observe that the error level of the standard formulation improves by two orders of magnitude as a result of moving from quadratics to cubics. At the same time, however, we also see that the error levels of all locking-free formulations discretized with the same cubic B-splines improve by three to four orders of magnitude. The standard formulation thus lags far behind its true higher-order approximation power as a result of locking. Therefore, the reduction of locking with $p = 3$ seems to be merely due to the increase of the approximation order, as also exemplified by higher convergence rates, but not to the mitigation of the locking phenomenon itself. We conclude that the standard formulation when discretized with cubic B-splines suffers from the effect of locking to (at least) the same extent as when it is discretized with quadratic B-splines. In addition, we observe that the standard formulation with selective reduced integration that employs p quadrature points per Bézier element produces practically the same locking-prone results as the standard formulation with full integration. This observation indicates that reduced quadrature loses its locking-reducing effect when the polynomial degree is increased.

Increasing p in locking-free formulations

Comparing Fig. 3.8b and Fig. 3.12b, we see that for the DSG method, the mode error in the transverse mode shapes significantly improves when we move from $p = 2$ to $p = 3$, and is now in the same range as the mode error of all other formulations. Figs. 3.13a and 3.13b show, however, that for the eigenvalues and mode shapes of the circumferential modes, the accuracy issues shown by the DSG methods remain and seem not to improve under p-refinement.

As discussed above, the accuracy advantage of the Hellinger-Reissner formulation as a mixed method over purely displacement based formulations based on the B-bar and DSG methods reduces. We observe in Fig. 3.12a that all locking-free formulations achieve very good accuracy, with advantages of the Hellinger-Reissner formulation in the lowest modes and advantages of the B-bar and DSG methods in the high modes. The effect of this observation is illustrated in Figs. 3.2b and 3.2c for our initial cantilever example, where for cubic and quartic spline discretizations, all locking-free methods exhibit optimal convergence rates at practically the same accuracy level on both coarse and fine meshes.

Classical versus locking-free p-refinement

To corroborate our observations, we carry out a p-refinement study (i.e. increasing polynomial degree and smoothness) that drives the polynomial degree beyond cubics on a fixed mesh of 64 Bézier elements. We compare the spectrum of eigenvalues λ_1^h associated with the transverse modes, computed via the standard formulation ("classi-

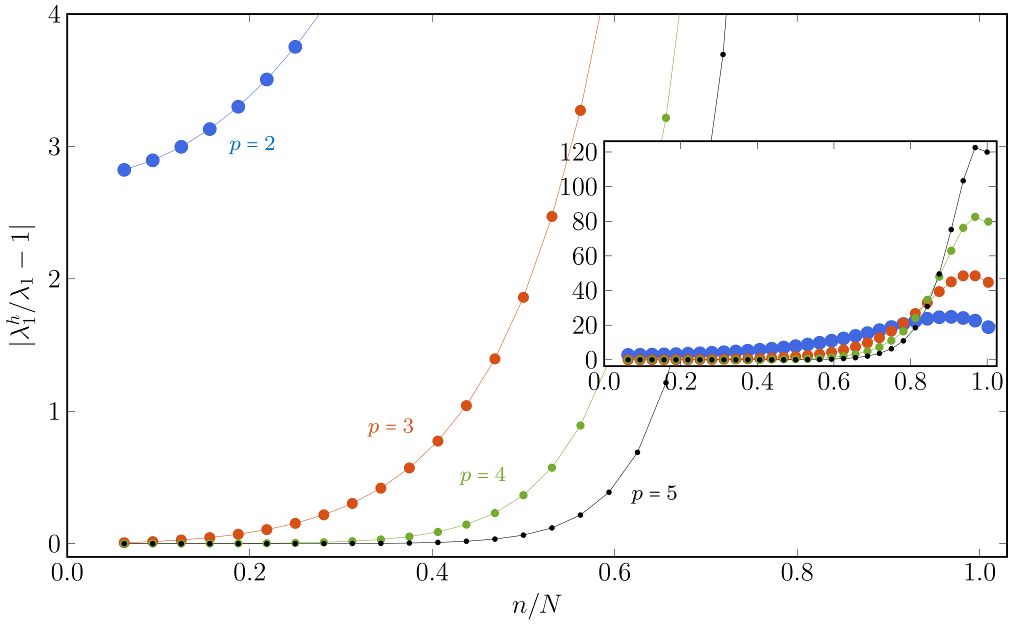

(a) Overall behavior of the transverse eigenvalue error

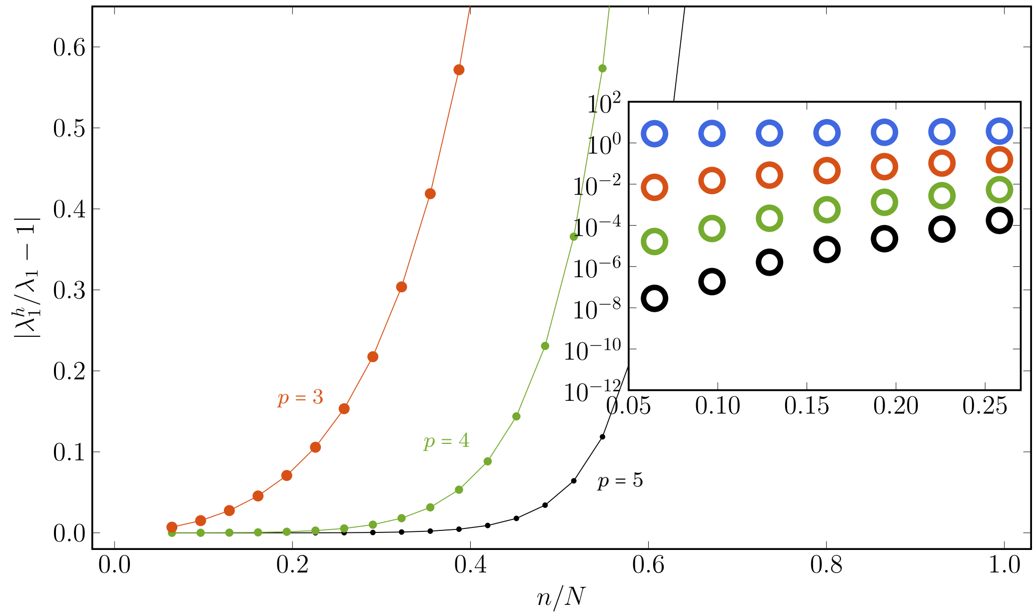

(b) Behavior of the transverse eigenvalue error in the lower spectrum part

Figure 3.14: **Standard formulation, p-refinement:** normalized errors in the transverse eigenvalues λ_1^h, computed on a fixed mesh of **64 elements** ($N = 32$), for "large" slenderness ratio $R/t = 2000/3$.

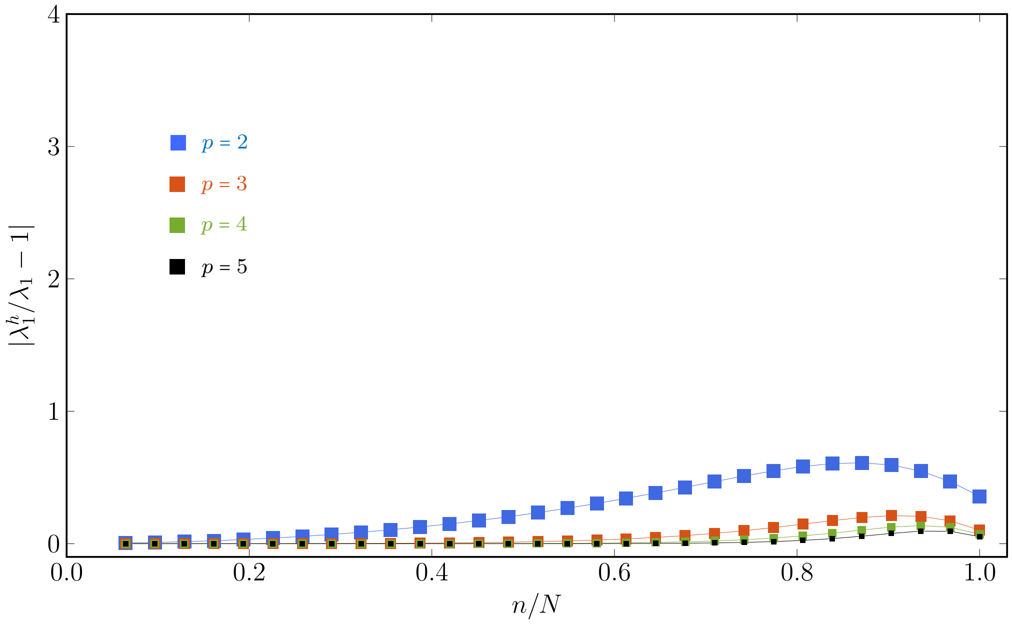

(a) Overall behavior of the transverse eigenvalue error

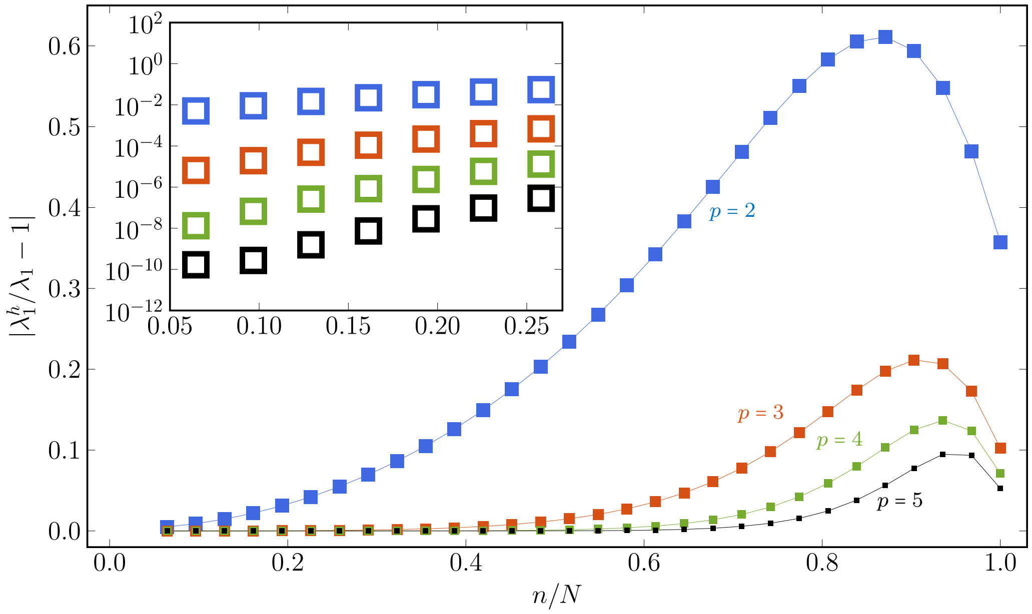

(b) Behavior of the transverse eigenvalue error in the lower spectrum part

Figure 3.15: **B-bar formulation, p-refinement:** normalized errors in the transverse eigenvalues λ_1^h, computed on a fixed mesh of **64 elements** ($N = 32$), for "large" slenderness ratio $R/t = 2000/3$.

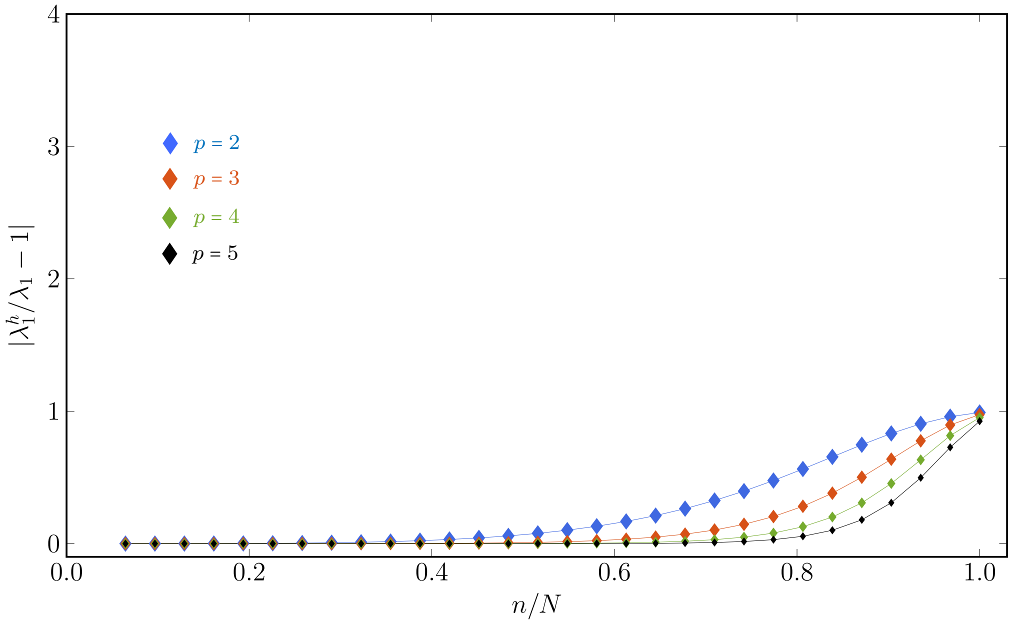

(a) Overall behavior of the transverse eigenvalue error

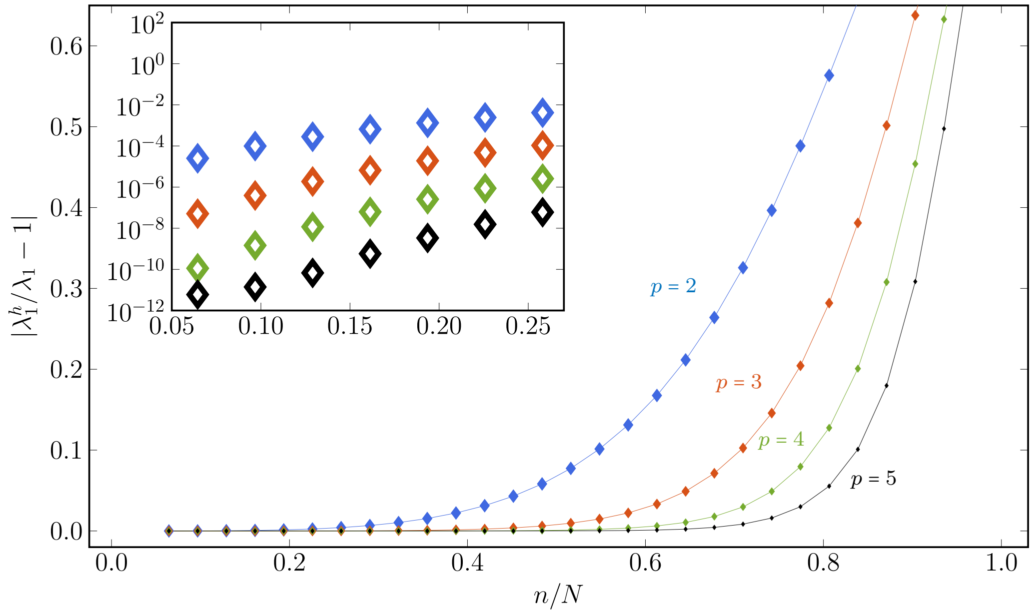

(b) Behavior of the transverse eigenvalue error in the lower spectrum part

Figure 3.16: **Hellinger-Reissner formulation, *p*-refinement:** normalized errors in the transverse eigenvalues λ_1^h, computed on a fixed mesh of **64 elements** ($N = 32$), for “large” slenderness ratio $R/t = 2000/3$.

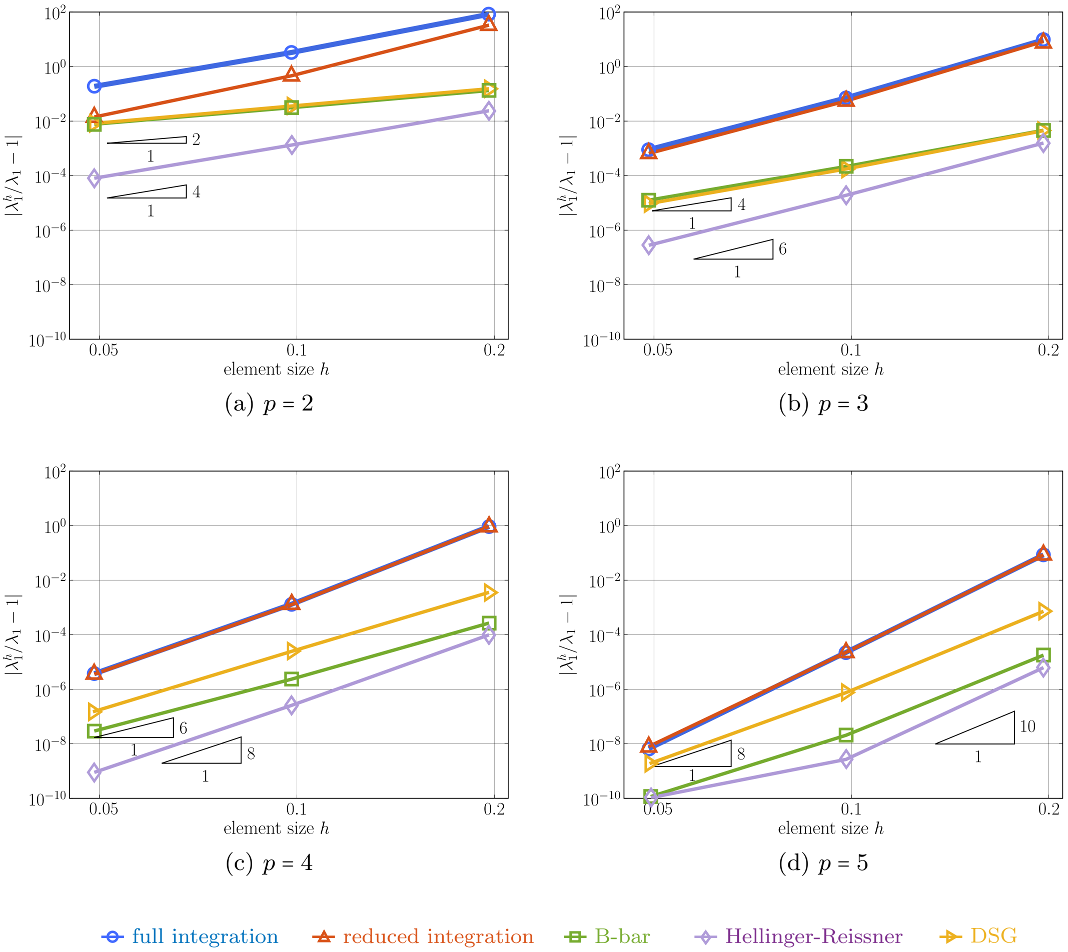
(a) $p = 2$ (b) $p = 3$ (c) $p = 4$ (d) $p = 5$

Figure 3.17: Convergence of the relative error in the fifth transverse eigenvalue, obtained with different formulations and quadratic, cubic, quartic and quintic B-spline basis functions, for “large” slenderness ratio $R/t = 2000/3$.

cal” p-refinement) and via a-priori locking-free p-refinement based on the B-bar and the Hellinger-Reissner formulations.

In Figs. 3.14, 3.15, and 3.16, we plot the transverse eigenvalue errors for each formulation at two different scales. We first focus on the overall behavior of the eigenvalue error across the complete spectrum. We observe in Fig. 3.14a that the spectral accuracy of the standard formulation significantly improves with p-refinement in the lower part of the spectrum. At the same time, however, the high modes seem to diverge with increasing polynomial degree p of the basis functions. Fig. 3.15a plots the corresponding eigenvalue error obtained with the B-bar formulation. We observe that the overall error levels are significantly smaller across the complete spectrum, and in particular for the high modes. We conclude that in contrast to the standard formulation, the B-bar method converges with increasing p in the high modes. Fig. 3.16a plots the corresponding eigenvalue error

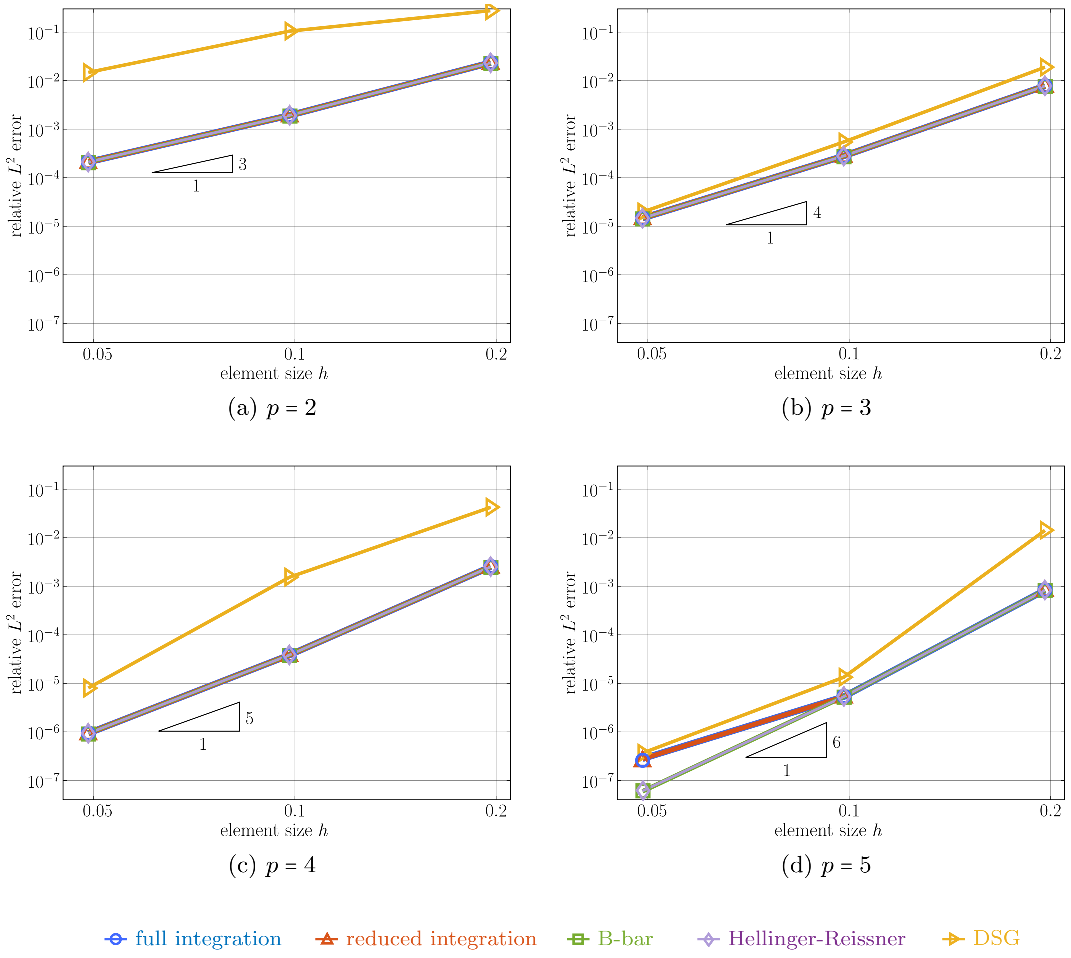

(a) $p = 2$ (b) $p = 3$ (c) $p = 4$ (d) $p = 5$

Figure 3.18: Convergence of the relative error in the fifth transverse eigenmode, obtained with different formulations and quadratic, cubic, quartic and quintic B-spline basis functions, for "large" slenderness ratio $R/t = 2000/3$.

obtained with the Hellinger-Reissner formulation. The overall error levels are significantly smaller as well. The highest modes, however, seem not to converge, but remain at the same error level.

Due to its importance for the approximation power of the basis (see Section 3.2.4), we then focus on the accuracy of the lower part of the spectrum. We observe in Fig. 3.14b that p-refinement in the standard formulation continuously improves the accuracy of the lowest modes. A comparison with the results of the locking-free B-bar and Hellinger-Reissner formulations plotted in Figs. 3.15b and 3.16b, however, clearly demonstrates that the negative impact of membrane locking persists with increasing p in the standard formulation. For instance, for $p = 3$, the eigenvalue error level of the lowest modes obtained with the B-bar method is three orders of magnitude smaller, and for the Hellinger-Reissner method even five orders of magnitude smaller, than the one obtained with the standard formulation. We note that for the B-bar and Hellinger-Reissner methods at $p = 5$, the eigenvalue solver hits the level of machine accuracy, preventing the further decrease of the eigenvalue error of the lowest mode.

Our observations confirm that p-refinement in a standard displacement-based finite element formulation reduces the effect of membrane locking with respect to a low-order locking-prone discretization. A comparison with the true approximation power of the higher-order basis obtained in a locking-free formulation, however, clearly shows that membrane locking continues to heavily affect the accuracy of the standard formulation at high polynomial degrees. Therefore, we conclude that p-refinement is not an effective way to mitigate the effect of locking, at least not for the curved Euler-Bernoulli beam model. In addition, our results indicate that the divergence of the higher transverse modes with increasing p is another negative effect of membrane locking that, to our knowledge, has not been reported before. We note that inaccurate and divergent high modes can have significant negative effects in explicit dynamics and nonlinear analysis.

3.5.5 Convergence of the lowest eigenvalues and mode shapes

As outlined in Section 3.2.4, the accuracy of the lowest eigenvalues and mode shapes directly relate to the accuracy of the approximation that can be achieved with a specific finite element discretization. It is therefore worthwhile to take a closer look at the accuracy and rate of convergence of the lower eigenvalues and mode shapes that are obtained with the different formulations. Figs. 3.17 and 3.18 plot the convergence of the relative error of the fifth transverse eigenvalue and the convergence of the relative L^2-norm error of the fifth transverse eigenmode obtained with 32, 64 and 128 Bézier elements and polynomial degrees $p = 2$ through 5.

For the eigenvalue error, an eigenvalue problem with fourth-order differential operators achieves optimal rates of convergence of $\mathcal{O}(2(p-1))$, while an eigenvalue problem with second-order differential operators achieves optimal rates of $\mathcal{O}(2p)$ [43], [182]. We observe in Fig. 3.17 that the standard formulation with full and reduced integration exhibits a significantly increased level of eigenvalue error. In particular, we can see that the error gap to the locking-free B-bar formulation decreases with each mesh refinement step, but does not decrease when the polynomial degree is increased on a fixed mesh. The locking-free B-bar and DSG methods based on a displacement-based formulation achieve optimal rates of convergence for all polynomial degrees. We observe that the eigenvalue error of the DSG method for $p = 4$ and $p = 5$ is slightly larger than the one for the B-bar method. The Hellinger-Reissner formulation also achieves optimal rates, which are consistently higher than the ones for the B-bar and DSG methods due to its mixed-method formulation. This confirms the increased accuracy of the eigenvalues obtained with the Hellinger-Reissner formulation that we observed in many of the inset figures of the previous plots.

For the L^2-norm mode error, the optimal convergence is always $\mathcal{O}(p+1)$. We observe in Fig. 3.18 that all methods with the exception of the DSG method achieves practically the accuracy in the mode shapes, indicated by indistinguishable mode errors that converge optimally. The mode error of the DSG method, however, is significantly larger.

3.6 Summary and conclusions

In this paper, we have taken first steps towards establishing spectral analysis as a tool for understanding and assessing locking phenomena in finite element formulations and comparing their effectivity with respect to unlocking. We proposed to "measure" locking (or unlocking) from a spectral analysis viewpoint as follows. For the finite element formulation in question, eigenvalue and mode errors are computed on a coarse discretization and corresponding asymptotic eigenvalue and mode errors are computed with an "overkill" discretization. The eigenvalue and mode errors from the coarse mesh are related to the corresponding asymptotic eigenvalue and mode errors by plotting both sets with respect to the normalized mode number n/N, where N denotes the total number of modes in each discretization. The finite element formulation is locking-free, if the corresponding spectral error curves are matching up irrespective of the mesh size, and the finite element formulation is locking-prone, if the corresponding spectral error curves are different, implying that the spectral error curve changes with mesh refinement.

To illustrate the validity and significance of spectral analysis in the context of assessing locking, we employed the example of a circular ring discretized with curved Euler-Bernoulli beam elements, which are susceptible to membrane locking. We showed that for the Euler-Bernoulli circular ring, membrane locking heavily affects the accuracy of the eigenvalues of the transverse modes, while the transverse mode shapes and both the eigenvalues and mode shapes of the circumferential modes do not lock. We assessed and compared the effectivity of the standard displacement-based formulation with full and selective reduced integration as well as three representative locking-free formulations (B-bar method, DSG method, Hellinger-Reissner formulation) in terms of their accuracy in the eigenvalues and eigenmodes. Our study showed that spectral analysis can rigorously characterize membrane locking. With respect to mitigating membrane locking in curved Euler-Bernoulli beams, we summarize the essential results of our study in Table 3.2.

Our spectral analysis results illustrate that the standard formulation with full integration is severely affected by membrane locking and does not enable efficient and accurate finite element solutions, even when the mesh is heavily refined. The standard formulation with selective reduced integration removes membrane locking for finer meshes for quadratic discretizations, but do not remove membrane locking on coarse meshes and for polynomial degrees larger than quadratics.

The B-bar, DSG and Hellinger-Reissner methods all enable effective locking-free finite element formulations for curved Euler-Bernoulli beams, leading to accurate results on coarse meshes. Due to its mixed-method character, the Hellinger-Reissner formulation hits a sweet spot for quadratic basis functions, since it converges with $\mathcal{O}(3)$ in the L^2 displacement norm unlike the purely displacement-based B-bar and DSG formulations that achieve only $\mathcal{O}(2)$ for quadratic basis functions. For polynomial degrees larger than two, all methods achieve the same optimal convergence rates, so that practically, all locking-free formulations achieve the same accuracy.

For the DSG method, we observed an increased level of error across large spectrum parts for the transverse mode shapes, the circumferential mode shapes and the eigen-

	Standard formulation		**Locking-free formulation**		
	Full integration	Reduced integration	B-bar	DSG	Hellinger-Reissner
Locking-free on coarse meshes (accuracy low transverse modes)	✗	✗	✓	✓	✓
Locking-free with increasing p (accuracy low transverse modes)	✗	✗	✓	✓	✓
Upper transverse modes converge with increasing p	✗	✗	✓	✓	✗
No negative effect on accuracy of circumferential modes	✓	✓	✓	✗	✓
Convergence rate $\mathcal{O}(p+1)$ for quadratic FE approximations	✗	✗	✗	✗	✓
No additional cost, e.g., due to static condensation or projection	✓	✓	✗	✗	✗

Table 3.2: Summary of the comparative spectral analysis study for the Euler-Bernoulli circular ring problem.

value error of the circumferential modes. When we refined the mesh or increased the polynomial degree p, this issue only improved for the transverse mode error, but persisted for the circumferential eigenvalue and mode errors. We hypothesize that the DSG formulation itself is responsible for this issue, since the accuracy with respect to the standard formulation decreases in parts of the spectrum. As membrane unlocking is associated primarily with the proper behavior in the eigenvalues of the transverse modes, this issue seems not to affect the unlocking capability of the DSG approach.

Classical p-refinement in our study we use splines of maximum smoothness, where the polynomial degree is driven beyond cubics on a fixed coarse mesh, reduces the effect of membrane locking with respect to a low-order locking-prone discretization. Membrane locking, however, continues to heavily affect the accuracy of the standard formulation with respect to a locking-free formulation at high polynomial degrees. Therefore, p-refinement by itself is not an effective way to mitigate the effect of locking. In addition, we observed that the higher transverse modes diverge with increasing p as a result of membrane locking. Divergent high modes deteriorate the conditioning of the system matrix, and can seriously affect the approximation accuracy and robustness in structural dynamics [66]. In contrast, we showed that locking-free formulations unlock the full potential of higher-order accurate discretizations. We observed that the low modes obtained with the locking-free formulations consistently were several orders of magnitude more accurate than the ones obtained with standard formulations, also at high polynomial degrees beyond cubics, and the high modes converged for the B-bar formulation and did not diverge for the Hellinger-Reissner formulation.

In summary, the results presented in this paper demonstrate the potential of spectral analysis as a tool to help assess locking phenomena in finite element formulations. In the future, we plan to extend the approach and corroborate its potential for finite element formulations of more complex structural models, in particular Kirchhoff-Love and Reissner-Mindlin shells.

Appendix 3.A

Analytical solution of the freely vibrating circular ring

Soedel solved the eigenvalue problem of a circular Euler-Bernoulli ring analytically [174, p.82-85] using the equations of motion in curvilinear coordinates. He assumed the mode shapes of a free floating closed ring, that are:

$$v_n(\theta) = A_{1n}\sin(n\theta), \tag{3.41}$$

$$w_n(\theta) = A_{2n}\cos(n\theta), \tag{3.42}$$

where $n \in \mathbb{N}$ and θ are the mode number and the angular coordinate, respectively. The n^{th} pair of the analytical eigenvalues are then:

$$\lambda_{1n} = \omega_{1n}^2 = \frac{k_{1n}}{\rho A}, \quad \lambda_{2n} = \omega_{2n}^2 = \frac{k_{2n}}{\rho A} \tag{3.43}$$

where ρ and A are the density and the cross section area of the ring, and the parameters k_{in} are defined as:

$$\begin{aligned} & k_{1n} = \frac{C-B}{2R^4}, \quad k_{2n} = \frac{C+B}{2R^4}, \quad \text{with} \\ & C = (\mathrm{EA}\,R^2 + \mathrm{EI}\,n^2)(n^2+1), \\ & B = \sqrt{(\mathrm{EA}^2\,R^4 + \mathrm{EI}^2\,n^4)(n^2+1)^2 + 2\,\mathrm{EA}\,R^2\,\mathrm{EI}\,n^2(6n^2-n^4-1)}\,. \end{aligned} \tag{3.44}$$

EA and EI denote the membrane and bending stiffness, and R the radius of the ring. The two eigenvalues λ_{1n} and λ_{2n} corresponds to different values of the relative amplitude between the corresponding circumferential and radial modes

$$r_{in} = \frac{A_{1n}}{A_{2n}} = \frac{\frac{\mathrm{EA}}{R^2}n + \frac{\mathrm{EI}}{R^4}n^3}{\rho A\omega_{in}^2 - \frac{\mathrm{EA}}{R^2}n^2 - \frac{\mathrm{EI}}{R^4}n^2}, \quad i = 1, 2. \tag{3.45}$$

The analytical eigenvalues and relative amplitudes of the first twenty modes of the Euler-Bernoulli circular ring used in this study are listed in Table 3.3. For each mode number n, one eigenvalue corresponds to the transverse-deflection-dominating modes, i.e. $A_{1n} \leq A_{2n}$ ($|r_{in}| \leq 1.0$), and one corresponds to the circumferential-deflection-dominating modes ($|r_{in}| \geq 1.0$) (see Table 3.3 and also [174, p.82-85]).

n	eigenvalue pair		amplitude ratio	
	λ_{1n}	λ_{2n}	r_{1n}	r_{2n}
0	0	$1.200000000000000 \cdot 10^{6}$	0	0
1	0	$2.400000450000000 \cdot 10^{6}$	-1	1
2	$1.619999222176224 \cdot 10^{0}$	$6.000002880000779 \cdot 10^{6}$	$-5.000004499999865 \cdot 10^{-1}$	$1.999998200001673 \cdot 10^{0}$
3	$1.295999212658217 \cdot 10^{1}$	$1.200000729000787 \cdot 10^{7}$	$-3.333342333340016 \cdot 10^{-1}$	$2.999991900015852 \cdot 10^{0}$
4	$4.764702716878825 \cdot 10^{1}$	$2.040001355297283 \cdot 10^{7}$	$-2.500013235320360 \cdot 10^{-1}$	$3.999978823599535 \cdot 10^{0}$
5	$1.246152982048443 \cdot 10^{2}$	$3.120002163470180 \cdot 10^{7}$	$-2.000017307755196 \cdot 10^{-1}$	$4.999956730986444 \cdot 10^{0}$
6	$2.681754852697320 \cdot 10^{2}$	$4.440003152451474 \cdot 10^{7}$	$-1.666687950571240 \cdot 10^{-1}$	$5.999923378921967 \cdot 10^{0}$
7	$5.080316340600650 \cdot 10^{2}$	$6.000004321836594 \cdot 10^{7}$	$-1.428596628775543 \cdot 10^{-1}$	$6.999876521178022 \cdot 10^{0}$
8	$8.792855145050755 \cdot 10^{2}$	$7.800005671448547 \cdot 10^{7}$	$-1.250029077240125 \cdot 10^{-1}$	$7.999813909991993 \cdot 10^{0}$
9	$1.422437983402840 \cdot 10^{3}$	$9.840007201201658 \cdot 10^{7}$	$-1.111144038404168 \cdot 10^{-1}$	$8.999733296829945 \cdot 10^{0}$
10	$2.183389483803921 \cdot 10^{3}$	$1.212000891105162 \cdot 10^{8}$	$-1.000036758074283 \cdot 10^{-1}$	$9.999632432768221 \cdot 10^{0}$
11	$3.213440252163006 \cdot 10^{3}$	$1.464001080097479 \cdot 10^{8}$	$-9.091314837369126 \cdot 10^{-2}$	$1.099950906869468 \cdot 10^{1}$
12	$4.569290413144246 \cdot 10^{3}$	$1.740001287095869 \cdot 10^{8}$	$-8.333777137925940 \cdot 10^{-2}$	$1.199936095541999 \cdot 10^{1}$
13	$6.313040026479182 \cdot 10^{3}$	$2.040001512099735 \cdot 10^{8}$	$-7.692789471743249 \cdot 10^{-2}$	$1.299918584374570 \cdot 10^{1}$
14	$8.512189111741010 \cdot 10^{3}$	$2.364001755108883 \cdot 10^{8}$	$-7.143376831426732 \cdot 10^{-2}$	$1.399898148450718 \cdot 10^{1}$
15	$1.123963766205331 \cdot 10^{4}$	$2.712002016123379 \cdot 10^{8}$	$-6.667224211689353 \cdot 10^{-2}$	$1.499874562860407 \cdot 10^{1}$
16	$1.457368565216181 \cdot 10^{4}$	$3.084002295143479 \cdot 10^{8}$	$-6.250595358651052 \cdot 10^{-2}$	$1.599847602702302 \cdot 10^{1}$
17	$1.859803304334188 \cdot 10^{4}$	$3.480002592169566 \cdot 10^{8}$	$-5.882986078224645 \cdot 10^{-2}$	$1.699817043085363 \cdot 10^{1}$
18	$2.340177978620280 \cdot 10^{4}$	$3.900002907202137 \cdot 10^{8}$	$-5.556226441714824 \cdot 10^{-2}$	$1.799782659130378 \cdot 10^{1}$
19	$2.907942582313202 \cdot 10^{4}$	$4.344003240241770 \cdot 10^{8}$	$-5.263866505443284 \cdot 10^{-2}$	$1.899744225971415 \cdot 10^{1}$
20	$3.573087108895835 \cdot 10^{4}$	$4.812003591289111 \cdot 10^{8}$	$-5.000746314489048 \cdot 10^{-2}$	$1.999701518756431 \cdot 10^{1}$

Table 3.3: The first twenty exact eigenvalue pairs of the Euler-Bernoulli circular free floating ring with a slenderness ratio $R/t = 2000/3$

Another set of mode shapes exists:

$$v_n(\theta) = A_{3n}\cos(n\theta), \tag{3.46}$$

$$w_n(\theta) = A_{4n}\sin(n\theta)\,, \tag{3.47}$$

which results in exactly the same analytical eigenvalues. This explains repeated eigenvalues in numerical computations. In our study, we only considered the free-floating modes in (3.41), which satisfy:

$$v_n(\theta = 0) = 0, \quad w_{n,\theta}(\theta = 0) = 0. \tag{3.48}$$

These constraints are also built into the spline trialspaces in order to remove the arbitrary phase shift in the numerical mode shapes; allowing direct comparisons to be made between the discrete and analytical eigenmodes. Because the trialspaces are defined in the Cartesian frame a rotation is necessary, see 3.3.2. The free-floating modes and their constraints in Cartesian coordinates are:

$$U_x(\theta) = A_{2n}\cos(n\theta)\,\cos(\theta) - A_{1n}\sin(n\theta)\,\sin(\theta)\,, \tag{3.49}$$

$$U_y(\theta) = A_{2n}\cos(n\theta)\,\sin(\theta) + A_{1n}\sin(n\theta)\,\cos(\theta)\,, \tag{3.50}$$

and:

$$U_{x,\theta}(\theta = 0) = 0, \quad U_y(\theta = 0) = 0. \tag{3.51}$$

Algorithm 1 Identify mode type corresponding to λ_1 and λ_2

Input: r_{in} ($i = 1, 2$, $n = 1, 2, \ldots, N$) (see equation (3.45))

Output: transverse_mode_numbers_lambda1, circumferential_mode_numbers_lambda1, transverse_mode_numbers_lambda2, circumferential_mode_numbers_lambda2

```
transverse_mode_numbers_lambda1 = findall($|r_{1n}| \leq 1$)
circumferential_mode_numbers_lambda1 = findall($|r_{1n}| > 1$)

transverse_mode_numbers_lambda2 = findall($|r_{2n}| < 1$)
circumferential_mode_numbers_lambda2 = findall($|r_{2n}| \geq 1$)
```

Algorithm 2 Sort discrete transverse and circumferential modes

Input: λ_i^h, $\mathbf{U}_i^h$ ($i = 1, 2, \ldots, 2N$)

Output: transverse_mode_numbers, circumferential_mode_numbers

```
for $i$ in $1 : 2N$ do
    $v_i^h, w_i^h$ = rotate_axes($\mathbf{U}_i^h$)
    $|r_i^h| = \sqrt{\left(\int_0^{2\pi} (v_i^h)^2 \, R \, \mathrm{d}\theta\right) / \left(\int_0^{2\pi} (w_i^h)^2 \, R \, \mathrm{d}\theta\right)}$
    if $|r_i^h| = 1$ & $\lambda_i^h = 0$ then
        transverse_mode_numbers[1] = $i$
    else if $|r_i^h| = 1$ & $\lambda_i^h \neq 0$ then
        circumferential_mode_numbers[1] = $i$
    else if $|r_i^h| < 1$ then
        append(transverse_mode_numbers, $i$)
    else if $|r_i^h| > 1$ then
        append(circumferential_mode_numbers, $i$)
    end if
end for
```

Appendix 3.B

Postprocessing of numerical eigenvalues and modes

The numerical eigenvalues and modes obtained from a finite element discretization are not automatically ordered in the same way as the analytical solution. To correctly identify and assign the numerical solutions to the analytical reference, we compute the L^2-norm error in the mode shape of each discrete mode with respect to all analytical

Algorithm 3 Verify free-floating constraints

```
Input: $\mathbf{U_i^h}$ $(i = 1, 2, \ldots, 2N)$, transverse_mode_numbers, circumferential_mode_numbers
Output: transverse_mode_numbers, circumferential_mode_numbers
for n in (transverse_mode_numbers, circumferential_mode_numbers) do
    for $i$ in n do
        $v^h_{i,0}, w^h_{i,0}$ = rotate_axes($\mathbf{U}^h_i(\theta = 0)$)
        if $v^h_{i,0} \neq 1 \,||\, w^h_{i,0} \approx 0$ then
            $\mathbf{n} \setminus \{i\}$        ▷ Remove index $i$ from current vector of mode numbers
        end if
    end for
end for
```

Algorithm 4 Assign discrete to the correct analytical modes

```
Input: $\mathbf{U}^h_i$, $\mathbf{U}_i$ $(i = 1, 2, \ldots, 2N)$, transverse_mode_numbers,
circumferential_mode_numbers,
transverse_mode_numbers_lambda1, circumferential_mode_numbers_lambda1,
transverse_mode_numbers_lambda2, circumferential_mode_numbers_lambda2
Output: $\lambda_1$_mode_numbers, $\lambda_2$_mode_numbers
for $i$ in transverse_mode_numbers do
    for $n$ in transverse_mode_numbers_lambda1 do
        $e_1[n]$ = compute_$L2$_error($\mathbf{U}^h_i, \mathbf{U}_n$)
    end for
    for $n$ in transverse_mode_numbers_lambda2 do
        $e_2[n]$ = compute_$L2$_error($\mathbf{U}^h_i, \mathbf{U}_n$)
    end for
    if minimal($e_1$) < minimal($e_2$) then
        append($\lambda_1$_mode_numbers, $i \Rightarrow$ argmin($e_1$))
    else
        append($\lambda_2$_mode_numbers, $i \Rightarrow$ argmin($e_2$))
    end if
end for
repeate with circumferential_mode_numbers
```

modes and assign pairs based on the smallest error. We first identify the transverse and circumferential modes, using the criterion of the relative amplitude [174, p. 82-85]. We describe the identification scheme in Algorithms 1 and 2. Since we only consider free-floating modes in this paper, we verify whether each numerical mode satisfies (3.51), see Algorithm 3. We then assign each numerical transverse and circumferential mode to the correct analytical counterpart, see Algorithm 4. The last step is to arrange the numerical eigenvalues and modes in ascending order. Except for the mixed formulation, this ordering scheme results in ascending discrete eigenvalues.

4 A variational approach based on perturbed eigenvalue analysis for improving spectral properties of isogeometric multipatch discretizations

This chapter is reproduced from [183]:

T.-H. Nguyen, R. R. Hiemstra, S.K.F. Stoter, and D. Schillinger. *A variational approach based on perturbed eigenvalue analysis for improving spectral properties of isogeometric multipatch discretizations*, Comput. Meth. Appl. Mech. and Engrg. 392 (2022) 114671. DOI: `10.1016/j.cma.2022.114671`. URL: `https://linkinghub.elsevier.com/retrieve/pii/S0045782522000615`.

Abstract

A key advantage of isogeometric discretizations is their accurate and well-behaved eigenfrequencies and eigenmodes. For degree two and higher, however, optical branches of spurious outlier frequencies and modes may appear due to boundaries or reduced continuity at patch interfaces. In this paper, we introduce a variational approach based on perturbed eigenvalue analysis that eliminates outlier frequencies without negatively affecting the accuracy in the remainder of the spectrum and modes. We then propose a pragmatic iterative procedure that estimates the perturbation parameters in such a way that the outlier frequencies are effectively reduced. We demonstrate that our approach allows for a much larger critical time-step size in explicit dynamics calculations. In addition, we show that the critical time-step size obtained with the proposed approach does not depend on the polynomial degree of spline basis functions.

4.1 Introduction

Isogeometric analysis (IGA) was first introduced in 2005 as a computational framework to improve the integration of computer-aided design (CAD) and finite element analysis (FEA) [30]. Compared with classical C^0 FEA, isogeometric discretizations exhibit better spectral properties [59]–[62]. While the upper part of the spectrum in classical FEA is inaccurate [66], [172] and the errors diverge with increasing interpolation degree p, almost the entire spectrum converges with increasing p in the case of smooth isogeometric discretizations [59]–[62]. A small number of modes, however, form the so-called *optical branch* at the end of the spectra and are denoted as “outliers” [43], [51]. Isogeometric discretizations using multiple patches with lower smoothness at patch interfaces increase the number of spurious outlier frequencies [62], as illustrated in Figure 4.1. In the case where the number of patches equals the number of elements (dark red curves), the outliers form the well-known three branches of cubic C^0 finite elements in classical FEA, see e.g. [61]. We can also see that the highest frequencies are significantly overestimated, which may negatively affect the stable critical time-step size in explicit dynamics calculations. The outlier modes, illustrated in Figure 4.2 for a single-patch discretization and Figure 4.3 for a two-patch discretization, behave in a spurious manner and may negatively affect the solution accuracy and robustness, particularly in hyperbolic problems [61]. We observe two types of outliers: one with all strain energy located near the boundaries (Figures 4.2, 4.3c) and one near the patch interface (Figure 4.3a), to which we refer as boundary and interior outliers, respectively. For an in-depth discussion of these outlier types, we refer to [62] (interior outliers) and [43], [122] (boundary outliers). Some of the outlier modes result from the combination of boundary and interior outliers, as illustrated in Figures 4.3b and d. We list the number of interior outliers in Tables 4.1 and 4.2 for univariate multipatch discretizations of second-order and fourth-order problems, respectively, after removing the boundary outliers using the reduced spline basis introduced in [122]. We count the number of interior outliers as a function of the degree p and the number of patches n_{pa}. We also note that the total number of outliers is obtained by adding the number of interior outliers when the boundary ones are removed, and the number of boundary outliers when the interior outliers are not present. For counting boundary outliers dependent on the boundary types and the degree p, we refer to [122]. For multivariate tensor-product discretizations, the authors of [122] also provide formulas for the number of boundary outliers for multivariate tensor-product discretizations, which can be straightforwardly extended to discretizations with interior outliers.

The first idea on how to remove boundary outliers in an IGA context was based on the nonlinear parameterization of the domain via a uniform distribution of the control points [51]. On the one hand, this approach removes the outliers for arbitrary degree p. On the other hand, a nonlinear parameterization changes the original geometry representation from CAD, which contradicts the isogeometric paradigm of using the same geometry in design and analysis. Furthermore, in [122], the authors verified that this approach leads to a loss of spatial accuracy of the low modes and frequencies. In more recent contributions [121]–[123], the authors imposed additional boundary constraints arising

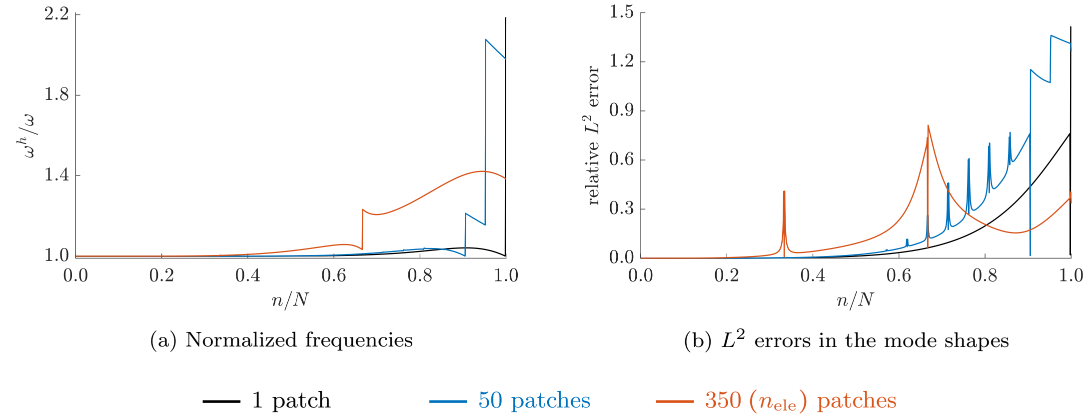

(a) Normalized frequencies

(b) L^2 errors in the mode shapes

Figure 4.1: Normalized frequencies and L^2 errors in the mode shapes of a free vibrating **bar with free boundary conditions**, unit length and unit material parameters, computed with **cubic** C^2 **B-splines** ($p = 3$), $N = 1050$ **modes** and **increasing number of patches with** C^0 **continuity at patch interfaces**. The rigid body mode is excluded.

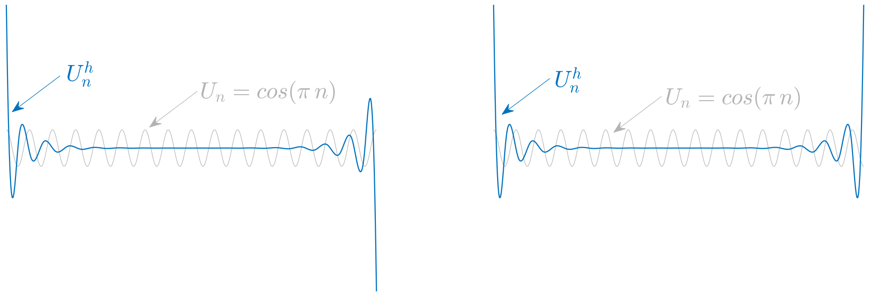

(a) mode $N - 1$

(b) mode N

Figure 4.2: Discrete outlier modes U_n^h (**blue**) corresponding to the example of **the free bar studied in Figure 4.1**, computed with **one patch of cubic** C^2 **B-splines** ($p = 3$) and discretized with 30 elements. These modes behave significantly differently compared to the exact modes (**gray**) $U_n = \cos(\pi\, n), n = 1, \ldots, N$, where $N = 33$ is the number of modes.

Number of patches	Polynomial degree				
	2	3	4	5	p
2	1	2	3	4	$p - 1$
3	2	4	6	8	$2(p - 1)$
n_{pa}	$n_{\text{pa}} - 1$	$2(n_{\text{pa}} - 1)$	$3(n_{\text{pa}} - 1)$	$4(n_{\text{pa}} - 1)$	$(n_{\text{pa}} - 1)(p - 1)$

Table 4.1: Number of interior outlier modes in one-dimensional **multipatch discretizations with** C^0 **patch continuity** applied to a second-order problem, e.g. the axial vibration of **a bar**.

from higher-order eigenvalue problems, either by building constraints into the basis [122], [123] or via penalization [121], to improve the spectral properties of isogeometric dis-

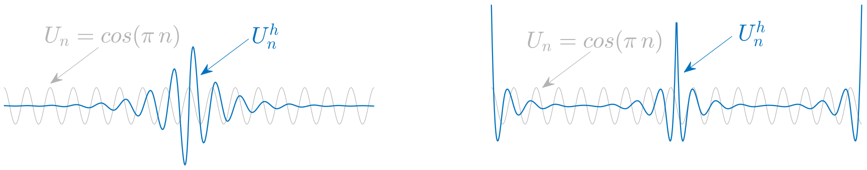

(a) mode $N-3$ (b) mode $N-2$

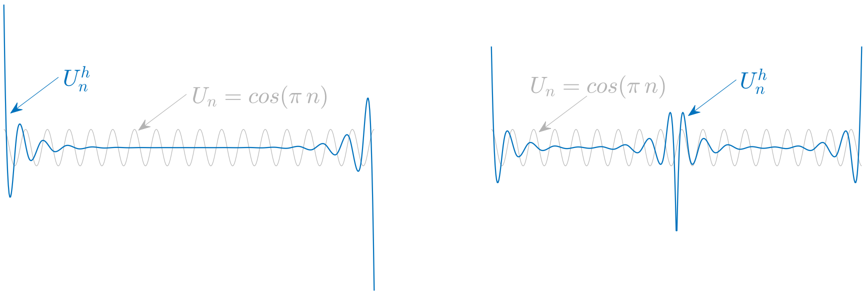

(c) mode $N-1$ (d) mode N

Figure 4.3: Discrete outlier modes U_n^h (**blue**) corresponding to the example of **the free bar studied in Figure 4.1**, computed with **two patches of cubic C^2 B-splines ($p=3$), and C^0 patch continuity**. Each patch is discretized with 15 elements. These modes behave significantly different compared to the exact modes (**gray**) $U_n = \cos(\pi n), n = 1, \dots, N$, where $N = 35$ is the number of modes.

Number of patches	Polynomial degree				
	3	4	5	6	p
2	1	2	3	4	$p-2$
3	2	4	6	8	$2(p-2)$
n_{pa}	$n_{\text{pa}}-1$	$2(n_{\text{pa}}-1)$	$3(n_{\text{pa}}-1)$	$4(n_{\text{pa}}-1)$	$(n_{\text{pa}}-1)(p-2)$

Table 4.2: Number of interior outlier modes in one-dimensional **multipatch discretizations with C^1 patch continuity** applied to a fourth-order problem, e.g. the transverse vibration of **a beam**.

cretizations. The strong approach entirely removes the outlier frequencies and modes for arbitrary degree p in one- and multidimensional settings. The penalty approach reduces the outlier frequencies, but does not remove the corresponding spurious outlier modes. An alternative treatment is the penalty approach introduced in [124] that imposes additional higher-order continuity constraints at interfaces of multipatch discretizations, as well as the first-order derivative at the Neumann boundary, i.e. a penalty treatment of both boundary and interior outliers. The authors reported an improvement of the eigenvalue spectra after removing "unphysical" modes using a cut-off normalized eigenvalue. The penalty approach of [124], using large values of penalty parameters, serves purely as an indicator for the outlier eigenvalues / frequencies such that these are identified easily, as verified in subsequent sections in this paper. Another approach is to weakly enforce the continuity constraints at patch interfaces in the framework of mortar methods [125], [126], or to apply the *optimally-blended* quadratures [127] that can suppress the boundary outlier [128]–[130] as well as the interior outlier frequencies [62].

Alternatively, the highest frequencies may be reduced via mass scaling. Its idea is to add artificial terms to the mass matrix in such a way that high frequencies are affected and any negative impact on the lower frequencies and modes is kept at a minimum. A widely used variant scales the density in combination with mass lumping, see e.g. [116]. One existing mass-scaling technique is to add a weighting of some form of stiffness matrix as a mass scaling [117]–[120]. The approach is then called *selective mass scaling* when it targets specific frequencies and modes [120]. In another technique, the added mass follows from a penalized Hamilton's principle [114], [115], which is a variationally consistent approach. Further artificial mass terms are also developed to optimize accuracy and efficiency in e.g. [112], [113].

In this paper, we introduce a novel variational approach based on perturbed eigenvalue analysis that improves the spectral properties of isogeometric multipatch discretizations. We combine the ideas of penalizing both the stiffness and the mass matrix [121] and of adding higher-order continuity constraints at patch interfaces [124] to arrive at an improved suppression of the interior outlier frequencies. In particular, we add scaled perturbation terms that weakly enforce the patch continuity constraints of [124] to both the stiffness and the mass matrix. We note that this approach results in modified left- and right-hand sides of the standard formulation in explicit dynamics, where the term involving the stiffness matrix affects the right-hand side residual. This differs from a mass scaling approach which modifies only the mass matrix. To remove boundary outliers, we combine the proposed variational approach with the methodology introduced in [122]. The proposed approach is consistent given that the analytical solution satisfies the patch continuity constraints of [124], i.e. the solution is sufficiently smooth, as well as the additional boundary constraints of [122]. Moreover, we introduce an approach for estimating optimal scaling parameters of the perturbation term, in the sense that the outlier frequencies are effectively reduced and the accuracy in the remainder of the spectrum and modes is not negatively affected. We also show how this approach can be cast into a pragmatic iterative procedure that can be readily implemented in any IGA framework.

We discuss different perturbation variants, such as perturbation of the stiffness matrix only (equivalent with the approach of [124]), perturbation of the mass matrix only (equivalent with a selective mass scaling approach), and perturbation of both stiffness and mass matrices. The proposed iterative procedure can also be applied to approximate the optimal scaling parameters for the approach of [121] such that the boundary outliers are optimally suppressed. We verify numerically via spectral analysis of second- and fourth-order problems that the proposed approach improves spectral properties of isogeometric multipatch discretizations in one- and multidimensional settings. For the examples of membrane and plate structures in an explicit dynamics setting, we confirm that our approach maintains spatial accuracy and enables a larger critical time-step size. We also demonstrate that it is effective irrespective of the polynomial order p.

The structure of the paper is as follows: In Section 4.2, we derive the variational formulation based on perturbed eigenvalue analysis. In Section 4.3, we motivate the iterative scheme for parameter estimation, focusing on a one-dimensional problem. In Section 4.4, we generalize our approach to multidimensional discretizations, including its practical implementation, and demonstrate its effectiveness for discretizations of second- and fourth-order problems. In Section 4.5, we discuss its advantages in explicit dynamics. In Section 4.6, we summarize our results and draw conclusions.

4.2 Variational formulation

We start this section with a brief review of the equations of motion that govern free vibrations of an undamped linear structural system, and derive the corresponding generalized eigenvalue problem in the continuous and discrete settings. We then introduce a variational formulation based on a perturbed eigenvalue problem that weakly enforces additional continuity constraints at patch interfaces. These additional constraints suppress only the interior outliers and do not negatively affect the important low frequency part.

4.2.1 Natural frequencies and modes

The equation of motion that governs the free vibration of an undamped linear structural system is:

$$\mathcal{K}\, u(\boldsymbol{x},t) + \mathcal{M}\, \frac{d^2}{d\,t^2}\, u(\boldsymbol{x},t) \;=\; 0\,, \quad \boldsymbol{x} \in \Omega\,, \quad t > 0\,. \tag{4.1}$$

Here, $\mathcal{M}$ and $\mathcal{K}$ are the mass and stiffness operators, respectively, and $u(\boldsymbol{x},t)$ is the displacement of a point $\boldsymbol{x}$ in the domain Ω. Using separation of variables, the displacement can be expanded in terms of the eigenmodes $U_n(\boldsymbol{x})$ and the time-dependent coefficients $T_n(t)$, that is $u(\boldsymbol{x},t) = \sum_n U_n(\boldsymbol{x})\; T_n(t)$. Substitution in (4.1) leads to two results. Firstly, $T_n(t) = C_+\, e^{i\,\omega_n\,t} + C_-\, e^{-i\,\omega_n\,t}$, which satisfies the equation:

$$\frac{d^2}{d\,t^2} T_n(t) + \omega_n^2\, T_n(t) \;=\; 0\,, \tag{4.2}$$

and describes an oscillation at a frequency ω_n. Here, C_+ and C_- are constants determined from initial conditions. Secondly, it results in the strong form of the generalized eigenvalue problem in the continuous setting, that is: find eigenmodes $U_n(\boldsymbol{x})$ and eigenfrequencies ω_n, $(U_n, \omega_n) \in \mathcal{V} \times \mathbb{R}^+$ such that:

$$\left(\mathcal{K} - \omega_n^2 \mathcal{M}\right) U_n(\boldsymbol{x}) \;=\; 0\,. \tag{4.3}$$

Here, $\mathcal{V}$ is the space of functions with sufficient regularity that allows the differential operators in $\mathcal{M}$ and $\mathcal{K}$ to be applied.

Applying the standard Galerkin method and subsequently discretizing with N finite element basis functions $B_i(\boldsymbol{x})$ results in the following semi-discrete system of equations:

$$\mathbf{K}\,\mathbf{u}^h(t) + \mathbf{M}\,\frac{d^2}{dt^2}\,\mathbf{u}^h(t) \;=\; 0\,, \tag{4.4}$$

where $\mathbf{K}$ and $\mathbf{M}$ denote the stiffness and consistent mass matrix, respectively, and $\mathbf{u}^h(t)$ is the unknown time-dependent displacement vector, such that:

$$u^h(\boldsymbol{x},t) = \left[B_1(\boldsymbol{x}) \;\ldots\; B_N(\boldsymbol{x})\right]\,\mathbf{u}^h(t)\,, \qquad u^h(\boldsymbol{x},t) \in \mathcal{V}^h \subset \mathcal{V}\,.$$

Here, $u^h(\boldsymbol{x},t)$ is the discrete displacement and $\mathcal{V}^h$ is a discrete space spanned by sufficiently smooth basis functions $B_i(\boldsymbol{x})$, $i = 1,\ldots,N$. The corresponding discrete eigenvalue problem can be expressed in the following matrix equation:

$$\mathbf{K}\,\mathbf{U}_n^h \;=\; \left(\omega_n^h\right)^2\,\mathbf{M}\,\mathbf{U}_n^h\,, \tag{4.5}$$

where $\mathbf{U}_n^h$ denotes the vector of unknown coefficients corresponding to the n^{th} discrete eigenmode U_n^h, and ω_n^h is the n^{th} discrete eigenfrequency.

4.2.2 Perturbed second- and fourth-order eigenvalue problems

In this paper, we focus on second-order eigenvalue problems involving rods and membranes, and fourth-order problems involving square plate structures. These are of unit size and unit material parameters and include either homogeneous Dirichlet or homogeneous Neumann boundary conditions. Since we consider spaces with sufficient regularity, as discussed in the previous subsection, the minimum patch continuity of multipatch discretizations is C^0 and C^1 for second- and fourth-order problems, respectively. We employ spaces of C^{p-1} B-splines of degree p that are free of boundary outliers, i.e. spaces with outlier removal constraints that are strongly enforced at the boundary [122].

Remark 4.2.1. *The choice of unit material parameters, i.e. unit mass and stiffness, is not a realistic scenario and does not represent the true conditioning of the problem. In this paper, however, this choice is trivial since we mostly look at the normalized eigenfrequency. We plan to further study realistic scenarios and the problem conditioning in future research.*

The discrete eigenvalue problem (4.5) can be expressed in the following variational form: find $(U_n^h, \omega_n^h) \in \mathcal{V}^h \times \mathbb{R}^+$, for $n = 1, 2, \ldots, N$, such that:

$$a(U_n^h, v^h) = \left(\omega_n^h\right)^2\, b(U_n^h, v^h) \qquad \forall\, v^h \in \mathcal{V}^h \subset \mathcal{V}\,. \tag{4.6}$$

Here, the bilinear form $b(\cdot,\cdot)$ is:

$$b(u^h, w^h) = \int_\Omega u^h \, w^h \, \mathrm{d}x \, . \tag{4.7}$$

The bilinear form $a(\cdot,\cdot)$ of a discrete second-order eigenvalue problem is:

$$a(u^h, w^h) = \int_\Omega \nabla u^h \cdot \nabla w^h \, \mathrm{d}x \, , \tag{4.8}$$

which corresponds to the second-order stiffness operator of the strong form (4.3):

$$\mathcal{K} := -\Delta = -\sum_{k=1}^{d} \frac{\partial^2}{\partial x_k^2} \qquad d = 1, 2, 3 \, , \tag{4.9}$$

where d is the dimension of the problem.

For fourth-order problems, the bilinear form $a(\cdot,\cdot)$ is:

$$a(u^h, w^h) = \int_\Omega \Delta u^h \, \Delta w^h \, \mathrm{d}x \, , \tag{4.10}$$

which corresponds to the bi-harmonic operator:

$$\mathcal{K} = \Delta^2 = \Delta \, \Delta \, . \tag{4.11}$$

In two-dimensional settings, i.e. the case of a vibrating plate, we consider the simply supported boundary conditions in this paper, since only the analytical solution of this case is known [184].

For improving the spectral properties of isogeometric multipatch discretizations, focussing on the interior outliers, we weakly enforce the following C^{p-1} continuity constraints at patch interfaces:

$$\left[\!\left[\partial_{\boldsymbol{\nu}}^l U_n(\boldsymbol{x}) \right]\!\right] = 0 \qquad \text{on } \Gamma^e \, , \; l = 1, \ldots p-1 \; , \tag{4.12}$$

where Γ^e denotes the e^{th} patch interface, $e = 1, \ldots, \mathcal{E}$ and $\mathcal{E}$ is the number of patch interfaces. $\boldsymbol{\nu}$ denotes the outward unit normal to the patch interface, and $[\![\cdot]\!]$ denotes the jump across the interface, $[\![w]\!] = w_+ - w_-$. The l^{th} constraint of (4.12), i.e. the C^l continuity constraint, at the e^{th} patch interface corresponds to the bilinear form:

$$c_e^l(u^h, w^h) = \int_{\Gamma^e} \left[\!\left[\partial_{\boldsymbol{\nu}}^l u^h \right]\!\right] \left[\!\left[\partial_{\boldsymbol{\nu}}^l w^h \right]\!\right] \mathrm{d}x \, . \tag{4.13}$$

We propose the following variational formulation for perturbing the eigenvalue problem (4.6) that weakly enforces (4.12): find $(\tilde{U}_n^h, \tilde{\omega}_n^h) \in \mathcal{V}^h \times \mathbb{R}^+$, for $n = 1, 2, \ldots, N$, such that

$\forall\, v^h \in \mathcal{V}^h \subset \mathcal{V}$:

$$a(\tilde{U}_n^h, v^h) + \sum_{l=1}^{p-1} \sum_{e=1}^{\mathcal{E}} \alpha_e^l\, c_e^l(\tilde{U}_n^h, v^h) = \left(\tilde{\omega}_n^h\right)^2 \left[b(\tilde{U}_n^h, v^h) + \sum_{l=1}^{p-1} \sum_{e=1}^{\mathcal{E}} \beta_e^l\, c_e^l(\tilde{U}_n^h, v^h) \right], \tag{4.14}$$

where α_e^l and β_e^l are scaling factors of the perturbation $c_e^l(\cdot,\cdot)$. The tilde in the superscript of $\tilde{U}_n^h$ and $\tilde{\omega}_n^h$ distinguishes the eigenmode and frequency corresponding to the perturbed eigenvalue problem (4.15) from those corresponding to the standard non-perturbed problem (4.6).

Based on empirical observation, we find that, for uniform discretizations, $\alpha_1^l = \ldots = \alpha_{\mathcal{E}}^l = \alpha^l$ and $\beta_1^l = \ldots = \beta_{\mathcal{E}}^l = \beta^l$. The variational formulation (4.14) then becomes: find $(\tilde{U}_n^h, \tilde{\omega}_n^h) \in \mathcal{V}^h \times \mathbb{R}^+$, for $n = 1, 2, \ldots, N$, such that $\forall\, v^h \in \mathcal{V}^h \subset \mathcal{V}$:

$$a(\tilde{U}_n^h, v^h) + \sum_{l=1}^{p-1} \alpha^l\, c^l(\tilde{U}_n^h, v^h) = \left(\tilde{\omega}_n^h\right)^2 \left[b(\tilde{U}_n^h, v^h) + \sum_{l=1}^{p-1} \beta^l\, c^l(\tilde{U}_n^h, v^h) \right], \tag{4.15}$$

where

$$c^l(u^h, w^h) = \sum_{e=1}^{\mathcal{E}} c_e^l(u^h, w^h)\,. \tag{4.16}$$

The matrix equation of the perturbed eigenvalue problem (4.15) is:

$$\left(\mathbf{K} + \sum_{l=1}^{p-1} \alpha^l\, \mathbf{K}_\Gamma^l \right) \tilde{\mathbf{U}}_n^h \; = \; \left(\tilde{\omega}_n^h\right)^2 \left(\mathbf{M} + \sum_{l=1}^{p-1} \beta^l\, \mathbf{K}_\Gamma^l \right) \tilde{\mathbf{U}}_n^h, \tag{4.17}$$

where the stiffness matrix $\mathbf{K}$ and the consistent mass matrix $\mathbf{M}$ correspond to the bilinear forms $a(\cdot,\cdot)$ from (4.8) or (4.10) and $b(\cdot,\cdot)$ from (4.7), respectively, which are symmetric positive definite matrices; and the perturbation matrix $\mathbf{K}_\Gamma^l$ corresponds to the bilinear form $c^l(\cdot,\cdot)$ from (4.16), which is a symmetric positive semi-definite matrix.

We note that the proposed approach (4.14) is applicable to non-uniform discretizations while the approach (4.15) is developed for uniform mesh discretizations. In this paper, we focus on uniform discretizations.

4.2.3 A note on consistency vs. variational consistency

Consistency and variational consistency are important properties of a finite element formulation. They play key roles in error analysis and are necessary for ensuring optimal orders of convergence of the method [66], [172], [185]. Additionally, they guarantee that the method yields the true solution if that solution lies in the trial function space. The variational approach proposed in the previous subsection is consistent when the true solution is sufficiently smooth, but it is not variationally consistent.

Variational consistency relates to the equivalence of the strong and weak forms in the limit $h \to 0$, with h being the characteristic mesh size. If the formulation is also stable, and when the data (body force and boundary conditions) are sufficiently regular, then variational consistency ensures that the finite element approximation converges to the strong solution with mesh refinement [66], [172], [185]. The variational formulation (4.14) is not equivalent to the strong formulation of the eigenvalue problem (4.3) as $h \to 0$. Instead, we obtain the following alternative strong formulation after performing integration by parts on a patch level:

$$\begin{aligned} \left(\mathcal{K} - \left(\omega_n^h\right)^2 \mathcal{M}\right) U_n(\boldsymbol{x}) &= 0 && \text{in } \Omega\,, && (4.18a)\\ \left[\!\left[\partial_{\boldsymbol{\nu}}^l U_n(\boldsymbol{x})\right]\!\right] &= 0 && \text{on } \Gamma\,,\ l = 1, \dots p-1\,, && (4.18b) \end{aligned}$$

where Γ is a collection of all patch interfaces. This corresponds to the following strong form of the governing equation of free vibrations:

$$\begin{aligned} \mathcal{K}\, u(\boldsymbol{x},t) + \mathcal{M}\, \frac{d^2}{dt^2} u(\boldsymbol{x},t) &= 0 && \text{in } \Omega\,, && (4.19a)\\ \left[\!\left[\partial_{\boldsymbol{\nu}}^l u(\boldsymbol{x},t)\right]\!\right] &= 0 && \text{on } \Gamma\,,\ l = 1, \dots p-1\,, && (4.19b) \end{aligned}$$

which thus involves more constraints on jumps of higher order derivatives across the patch interface compared to the strong form (4.1).

In a broader sense, *consistency* refers to some specific solution. A formulation is consistent with respect to the solution u_{true} if the variational statement is satisfied when u_{true} is substituted in the trial function slot. This property immediately implies a form of Galerkin orthogonality with respect to u_{true}, i.e.:

$$a(u_{true} - u^h, v^h) = 0 \quad \forall\, v^h \in \mathcal{V}^h \subset \mathcal{V} \tag{4.20}$$

Céa's lemma then only requires that the formulation satisfies a stability criterion (i.e., coercivity) to yield the optimal order of convergence to the solution u_{true} in the natural norm [172], [185]:

$$||u_{true} - u^h||_{H^1} \leq \frac{C_b}{C_c} \min_{v^h \in \mathcal{V}^h} ||u_{true} - v^h||_{H^1} \tag{4.21}$$

where C_b is the boundedness coefficient and C_c is the coercivity coefficient.

Our formulation (4.14) is consistent with respect to solutions that satisfy the conditions of (4.19). This means that we can expect to converge optimally to solutions that satisfy these conditions. Put simply, we can expect to converge optimally for solutions in $H^p(\Omega)$. Such solutions often correspond to system response governed by free vibrations. For an isogeometric discretization, these are generally the solutions we focus on, since the optimal order of convergence to a function in $H^m(\Omega)$ in the $H^q(\Omega)$ norm is $\min(p+1, m) - q$, with $0 \leq q = \min(p+1, m, s)$, where p is the polynomial degree of the B-spline basis function, m is the order of smoothness of the solution, and s is the minimum global regularity of the basis functions [138], [186]. We thus see that our formulation is consistent with respect to solutions for which the B-spline discretization yields optimal convergence and not for those solutions for which the B-spline discretization convergences suboptimally anyway.

4.3 Parameter estimation for a one-dimensional case study

In the next step, we will address the systematic choice of the open parameters α and β in (4.17). To approach this aspect, we consider the perturbed eigenvalue problem (4.17) of a fixed bar (unit length, unit axial stiffness, unit mass), discretized by a univariate multipatch discretization with quadratic C^1 B-splines ($p = 2$) and sufficient regularity, i.e. C^0 patch continuity. The perturbed eigenvalue problem (4.17) then simplifies to:

$$[\mathbf{K} + \alpha \mathbf{K}_\Gamma]\,\tilde{\mathbf{U}}_n^h = \left(\tilde{\omega}_n^h\right)^2 [\mathbf{M} + \beta \mathbf{K}_\Gamma]\,\tilde{\mathbf{U}}_n^h\,, \qquad n = 1, \ldots, N\,. \tag{4.22}$$

We consider a discretization of two patches ($n_{\text{pa}} = 2$). The resulting spectrum consists of one interior outlier frequency (see Table 4.1) which is the maximum frequency.

4.3.1 First-order approximation of the perturbation

The objective of the perturbation is to ensure that $\tilde{\omega}_n^h$ is a good approximation to the true eigenfrequency over the complete spectrum. Specifically, the parameters α and β need to be chosen to reduce the severely over-estimated maximum ω_n^h without compromising the accuracy of the lower ω_n^h's. Focusing on the highest frequency mode, relation (4.22) becomes:

$$\mathbf{K}\tilde{\mathbf{U}}_{max}^h + (\alpha - \beta\left(\tilde{\omega}_{max}^h\right)^2)\mathbf{K}_\Gamma \tilde{\mathbf{U}}_{max}^h = \left(\tilde{\omega}_{max}^h\right)^2 \mathbf{M}\tilde{\mathbf{U}}_{max}^h\,, \tag{4.23}$$

and after premultiplying by $\tilde{\mathbf{U}}_{max}^{h\,T}$:

$$\tilde{\mathbf{U}}_{max}^{h\,T}\mathbf{K}\tilde{\mathbf{U}}_{max}^h + (\alpha - \beta\left(\tilde{\omega}_{max}^h\right)^2)\tilde{\mathbf{U}}_{max}^{h\,T}\mathbf{K}_\Gamma\,\tilde{\mathbf{U}}_{max}^h = \left(\tilde{\omega}_{max}^h\right)^2\,, \tag{4.24}$$

where we assume that the eigenmodes are normalized with respect to the unperturbed mass matrix (i.e., $\tilde{\mathbf{U}}_n^{h\,T}\mathbf{M}\tilde{\mathbf{U}}_m^h = \delta_{nm}$).

A first order approximation of a perturbed eigenvalue problem reveals that $\left(\omega_n^h\right)^2$ changes with order $\mathcal{O}(\|U_n^h\|^2)$ and eigenmode U_n^h changes with order $\mathcal{O}(\|U_n^h\|^2/\left(\omega_{max}^h\right)^2)$ [187, Section 15.4]. Since ω_{max}^h is large, the relative change in eigenmodes can be expected to be much smaller than the relative change in frequencies. This implies that, for small α and β, we may approximate $\tilde{\mathbf{U}}_{max}^h \approx \mathbf{U}_{max}^h$ and thus also:

$$\tilde{\mathbf{U}}_{max}^{h\,T}\mathbf{K}\tilde{\mathbf{U}}_{max}^h \approx \mathbf{U}_{max}^{h\,T}\mathbf{K}\mathbf{U}_{max}^h = \left(\omega_{max}^h\right)^2 \mathbf{U}_{max}^{h\,T}\mathbf{M}\mathbf{U}_{max}^h = \left(\omega_{max}^h\right)^2\,. \tag{4.25}$$

4.3.2 Identifying (un)suitable parameter windows

To help identify suitable ranges of parameter values, we choose to write β in terms of α and a scaling factor f as:

$$\beta = f \, \frac{1}{\left(\tilde{\omega}^h_{max}\right)^2} \, \alpha \, . \tag{4.26}$$

Substitution of (4.25) and (4.26) into (4.24) gives:

$$\alpha \, (1 - f) \approx \frac{\left(\tilde{\omega}^h_{max}\right)^2 - \left(\omega^h_{max}\right)^2}{\mathbf{U}^{h\,T}_{max} \mathbf{K}_\Gamma \mathbf{U}^h_{max}} \, . \tag{4.27}$$

Depending on our choice of the scaling factor f, we can identify different parameter windows that we will briefly discuss in the following.

Case $\boldsymbol{f} = \mathbf{0}$ (no perturbation of the mass matrix): The left-hand side is positive for positive choice of α. This necessarily means that $\tilde{\omega}^h_{max} > \omega^h_{max}$, which is precisely not our goal: the frequency ω^h_{max} needs to be reduced. Adding perturbations only to the stiffness matrix is thus unsuitable for improving the spectrum.

We note that this case is equivalent to the formulation introduced in [124], excluding the penalty terms on the Neumann boundary and at cross-points. In Figure 4.4, we illustrate the discrete frequencies of a fixed bar with values for α that are scaled with $1/h$ based on [124], without removing any outlier frequency. We note that α scaled with $1/h$ is not a consistent scaling factor of the matrices $\mathbf{K}$ and $\mathbf{K}_\Gamma$ (to the contrary, a consistent scaling factor would be $\alpha = h$). As expected, we observe in Figure 4.4 that the outlier frequency $\tilde{\omega}^h_N$ increases with increasing α.

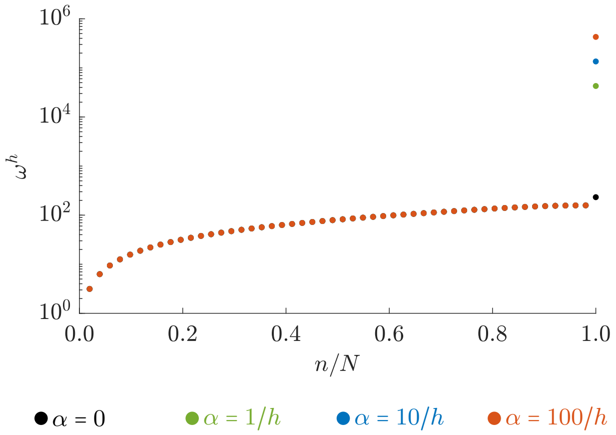

Figure 4.4: Discrete frequencies of a freely vibrating fixed bar, computed with $\boldsymbol{f} = \mathbf{0}$ and different values of α chosen according to [124]. We apply two patches of quadratic C^1 B-splines and discretize each patch with 25 elements ($h = 0.01$).

Remark 4.3.1. *Instead of ordering the discrete frequencies in ascending order, as is typically done, the frequencies in Figures 4.4 to 4.7 are ordered in such a way that the corresponding analytical frequencies are ascending. The corresponding pairs of discrete and analytical frequencies are identified by inspecting the corresponding mode shapes. In particular, we find the discrete mode that best fits, in the* L^2 *sense, a certain analytical mode.*

Case $0 < f < 1$: The left-hand side of (4.27) is also positive when α is chosen larger than zero, i.e. $\tilde{\omega}^h_{max} > \omega^h_{max}$. Thus, a choice of f in $(0, 1)$ does not improve the spectrum. In Figure 4.5, we illustrate the discrete frequencies of a fixed bar using $f = 0.5$. We choose $\alpha = h$ and $\beta = \alpha\, f/(\omega^h_N)^2$, where ω^h_N is the N^{th} frequency of the non-perturbed eigenvalue problem, i.e. the maximum outlier frequency. As expected, $\tilde{\omega}^h_N$ increases.

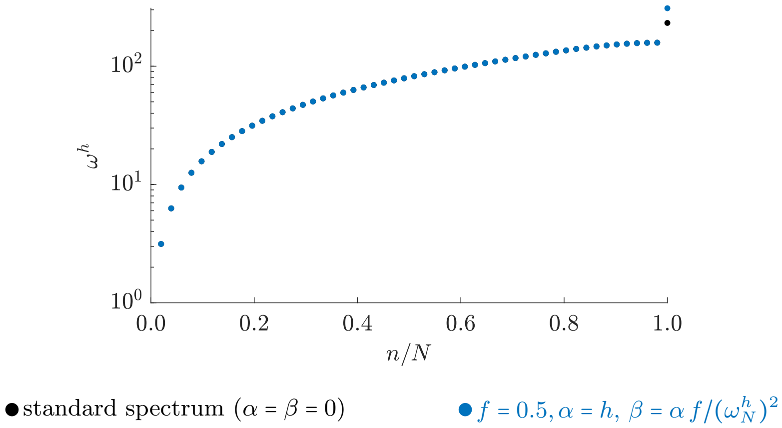

Figure 4.5: Discrete frequencies of a freely vibrating fixed bar, computed with $\boldsymbol{f = 0.5}$. We apply two patches of quadratic C^1 B-splines and discretize each patch with 25 elements.

Case $f > 1$: For a choice of α larger than zero, the left-hand side of (4.27) is negative, such that $\tilde{\omega}^h_{max} < \omega^h_{max}$. We thus observe that it is the mass matrix to which we should add the perturbation to improve the spectrum. In Figure 4.6, we illustrate the discrete frequencies of a fixed bar computed with a value $f = 2$. We compute α and β using (4.26)-(4.27). As expected, the resulting frequency $\tilde{\omega}^h_N$ is reduced.

Case $\alpha = 0$ and $\beta > 0$: Based on the previous observation, we may consider only adding the perturbation to the mass matrix, which can be interpreted as an approach of selective mass scaling [115], [120]. In this case, values of β that are scaled with h^3 are consistent scaling factors of the matrices $\mathbf{M}$ and $\mathbf{K}_\Gamma$. In Figure 4.7, we illustrate the discrete frequencies of a fixed bar using a factor $\beta = h^3$. We observe that the outlier frequency is also effectively reduced.

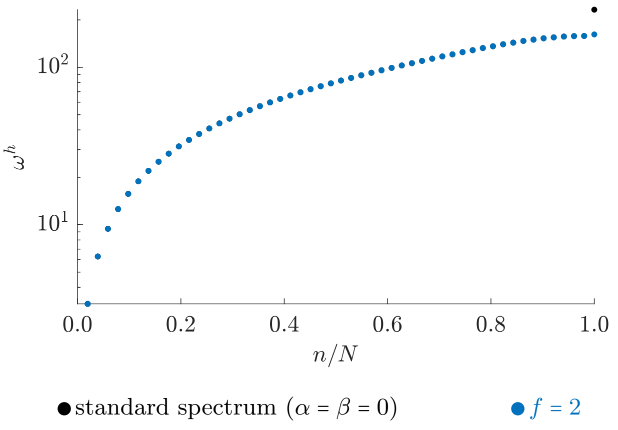

Figure 4.6: Discrete frequencies of a freely vibrating fixed bar, computed with $\boldsymbol{f} = \mathbf{2}$. We apply two patches of quadratic C^1 B-splines and discretize each patch with 25 elements.

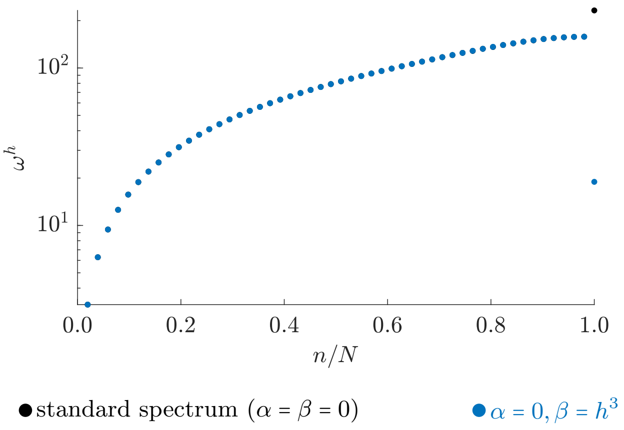

Figure 4.7: Normalized frequencies of a freely vibrating fixed bar, computed with $\boldsymbol{\alpha} = \mathbf{0}, \boldsymbol{\beta} = h^3$. We apply two patches of quadratic C^1 B-splines and discretize each patch with 25 elements.

4.3.3 An iterative scheme based on first-order perturbed eigenvalue analysis

In this work, we focus on the parameter estimation in the case of perturbing both the stiffness and mass matrix that reduces the outlier frequency, i.e. the case of $\boldsymbol{f} > \mathbf{1}$.

Suppressing a single outlier frequency

Based on the first-order perturbation discussed above, we propose to use the following iterative procedure for approximating α and β in the case $\boldsymbol{f} > \mathbf{1}$:

$$\alpha^{(i)} = \frac{\left(\omega^{h\,*}_{max}\right)^2 - \tilde{\mathbf{U}}^{h\,(i-1)\,T}_{max}\mathbf{K}\tilde{\mathbf{U}}^{h\,(i-1)}_{max}}{\tilde{\mathbf{U}}^{h\,(i-1)\,T}_{max}\,\mathbf{K}_\Gamma\,\tilde{\mathbf{U}}^{h\,(i-1)}_{max}}\,\frac{1}{1-f}\,, \tag{4.28}$$

$$\beta^{(i)} = f \, \frac{1}{\left(\omega_{max}^{h\,*}\right)^2} \alpha^{(i)} \,, \tag{4.29}$$

where $\tilde{\mathbf{U}}_{max}^{h\,(i-1)}$ correspond to the eigenvalue problem (4.22) that is:

$$\left(\mathbf{K} + \alpha^{(i-1)} \, \mathbf{K}_\Gamma\right) \tilde{\mathbf{U}}_n^{h\,(i-1)} = \left(\tilde{\omega}_n^{h\,(i-1)}\right)^2 \left(\mathbf{M} + \beta^{(i-1)} \, \mathbf{K}_\Gamma\right) \tilde{\mathbf{U}}_n^{h\,(i-1)} \,, \tag{4.30}$$

and $\omega_{max}^{h\,*}$ is the target maximum frequency. A practical choice of the target maximum frequency is a fraction of the unperturbed outlier frequency ω_{max}^{h}. In this section, to illustrate the effectiveness of the proposed iterative scheme, we choose as target value $\omega_{max}^{h\,*}$ the maximum analytical frequency. For the studied benchmarks of bars and beams, the analytical solution is well-known. We find that only three or four iterations are required to obtain sufficiently converged values for α and β, i.e. these parameters converge within a small number of iterations. In Section 4.4, we propose an alternate strategy that avoids the need for a known analytical solution.

Suppressing multiple outlier frequencies

We now discuss the parameter estimation of an example using cubic C^2 B-splines ($p = 3$) with C^0 patch continuity. The resulting spectrum of a two-patches-discretization ($n_{\text{pa}} = 2$) consists of two interior outliers (see Table 4.1). The perturbed eigenvalue problem (4.17) then simplifies to:

$$\left[\mathbf{K} + \alpha^1 \mathbf{K}_\Gamma^1 + \alpha^2 \mathbf{K}_\Gamma^2\right] \tilde{\mathbf{U}}_n^h = \left(\tilde{\omega}_n^h\right)^2 \left[\mathbf{M} + \beta^1 \mathbf{K}_\Gamma^1 + \beta^2 \mathbf{K}_\Gamma^2\right] \tilde{\mathbf{U}}_n^h \,. \tag{4.31}$$

To iteratively estimate the parameters α^l and β^l, $l = 1, 2$, in each iteration, we first identify the two outlier modes corresponding to each continuity constraint of (4.12) as follows:

$$n^l = \underset{N^l}{\arg\max} \left(\tilde{\mathbf{U}}_n^{h\,T} \, \mathbf{K}_\Gamma^l \, \tilde{\mathbf{U}}_n^h\right) \,, \quad N^l = \{1, \ldots, N\} \setminus \left\{n^1, \ldots, n^{l-1}\right\} \,. \tag{4.32}$$

Inserting these outlier modes in (4.31), aiming at the corresponding target frequencies, and performing the steps (4.23)-(4.24), as well as expressing β^l in terms of α^l and the target frequencies, we obtain the following system of equations:

$$\alpha^1 \left(1 - f^1\right) \tilde{\mathbf{U}}_{n^1}^{h\,T} \, \mathbf{K}_\Gamma^1 \, \tilde{\mathbf{U}}_{n^1}^h + \alpha^2 \left(1 - f^2 \frac{\omega_{n^1}^{h\,*}}{\omega_{n^2}^{h\,*}}\right) \tilde{\mathbf{U}}_{n^1}^{h\,T} \, \mathbf{K}_\Gamma^2 \, \tilde{\mathbf{U}}_{n^1}^h = \left(\tilde{\omega}_{n^1}^{h\,*}\right)^2 - \tilde{\mathbf{U}}_{n^1}^{h\,T} \, \mathbf{K} \, \tilde{\mathbf{U}}_{n^1}^h \,, \tag{4.33a}$$

$$\alpha^1 \left(1 - f^1 \frac{\omega_{n^2}^{h\,*}}{\omega_{n^1}^{h\,*}}\right) \tilde{\mathbf{U}}_{n^2}^{h\,T} \, \mathbf{K}_\Gamma^1 \, \tilde{\mathbf{U}}_{n^2}^h + \alpha^2 \left(1 - f^2\right) \tilde{\mathbf{U}}_{n^2}^{h\,T} \, \mathbf{K}_\Gamma^2 \, \tilde{\mathbf{U}}_{n^2}^h = \left(\tilde{\omega}_{n^2}^{h\,*}\right)^2 - \tilde{\mathbf{U}}_{n^2}^{h\,T} \, \mathbf{K} \, \tilde{\mathbf{U}}_{n^2}^h \,, \tag{4.33b}$$

where

$$\beta^1 = f^1 \frac{1}{\left(\omega_{n^1}^{h\,*}\right)^2} \alpha^1 \,, \qquad \beta^2 = f^2 \frac{1}{\left(\omega_{n^2}^{h\,*}\right)^2} \alpha^2 \,. \tag{4.34}$$

Solving this system of equations, we obtain α^l and β^l at each iteration. We find that only four or five iterations are required to obtain sufficiently converged values for α^l, $l = 1, 2$.

In general, the resulting system of equations consists of $(p-1)$ equations and $(p-1)$ unknown parameters α^l. Given a choice of $(p-1)$ factors f^l, we obtain β^l in terms of f^l, α^l, and the target maximum frequency, see (4.29). We note that the proposed iterative scheme requires $(p-1)$ target maximum frequencies and an identification of $(p-1)$ outlier modes corresponding to the continuity constraint (4.12) at each iteration.

4.3.4 Spectral analysis of a second-order problem

The proposed iterative parameter estimation still requires a choice of the scaling factor $f > 1$ between α and β. Figure 4.8 illustrates the relative error in the frequency, $|\omega_n^h/\omega_n - 1|$, and the relative L^2 error in the mode, $\|U_n^h - U_n\|_{L^2} \,/\, \|U_n\|_{L^2}$, of a fixed bar discretized with two patches of quadratic C^1 B-splines. We order these results in the same way as described in Remark 4.3.1. We observe that optimal accuracy is preserved in the remainder of the spectrum and modes for all values $f > 1$. In all numerical studies that follow we choose a factor $f = 2$.

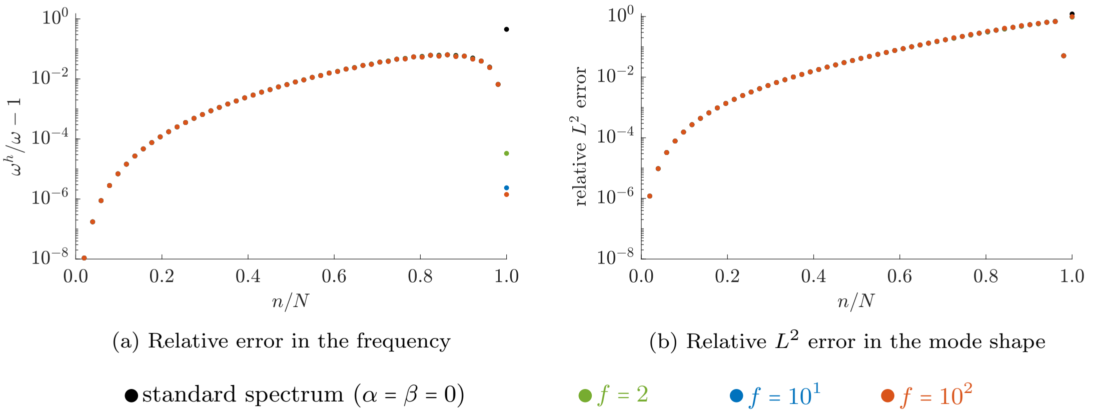

(a) Relative error in the frequency

(b) Relative L^2 error in the mode shape

Figure 4.8: Relative error in frequencies and L^2 error in the mode shapes of a freely vibrating fixed bar, computed with different values $\boldsymbol{f > 1}$. We apply two patches of quadratic C^1 B-splines and discretize each patch with 25 elements.

The corresponding outlier mode, as expected, remains spurious as illustrated in Figure 4.9, since the addition of perturbations improves the eigenvalue spectrum, but does not remove spurious outlier modes. Nevertheless, the introduced perturbation reduces the error in the outlier mode, as demonstrated in Figure 4.8b, since the perturbed outlier mode approximates the analytical solution better than the unperturbed mode, as shown in Figure 4.9.

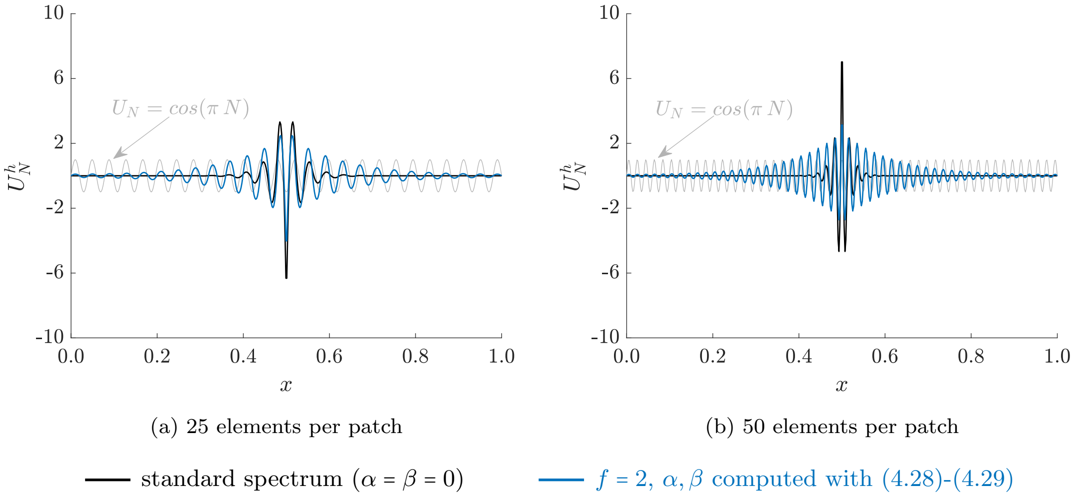

(a) 25 elements per patch

(b) 50 elements per patch

Figure 4.9: Outlier mode of a freely vibrating fixed bar, computed with 2 patches of quadratic C^1 B-splines and normalized such that $\left\|U_n^h\right\|_{L^2} = \|U_n\|_{L^2}$.

We now consider the free axial vibration of a fixed bar with unit length, unit axial stiffness and unit mass. We employ a multipatch discretization with two patches ($n_{\text{pa}} = 2$) of C^{p-1} B-splines of different polynomial degrees $p = 2$ through 5 where interior outliers exist (see Table 4.1), and C^0 patch continuity. Figures 4.10 and 4.11 illustrate the normalized frequency and the relative L^2 error in the mode shapes of the studied bar, respectively. We compare results obtained with multipatch discretizations based on non-perturbed and perturbed eigenvalue problems (plotted in black and blue, respectively). We include results of the single-patch discretization in Figures 4.10 and 4.11 in gray as the reference solution, and keep the same number of degrees of freedom N for the single- and multipatch discretizations. The discrete frequencies are ordered as described in Remark 4.3.1.

We first focus on the normalized frequencies plotted in Figure 4.10. The inset figures of Figure 4.10 focus on the last four frequencies including the outlier frequencies that are present in the upper part of the spectra. It can be observed that the entire spectrum obtained with multipatch discretizations without perturbations (in black) is accurate except for the $(p-1)$ interior outlier frequencies at the end of the spectrum (see also Table 4.1). These outliers are significantly reduced by our approach (in blue), while the remaining frequencies are not negatively affected. We observe that the reduction factor increases with increasing p since the outlier frequencies increase. We note that the reduced normalized outlier frequencies are not at the same level for all cases, as illustrated via small jumps at the end of the blue spectra for $p = 4$ and 5 in Figures 4.10c and d. The mode errors are plotted in Figure 4.11. We observe that our approach results in smaller errors in the outlier modes (in blue), as discussed in the previous subsection, without

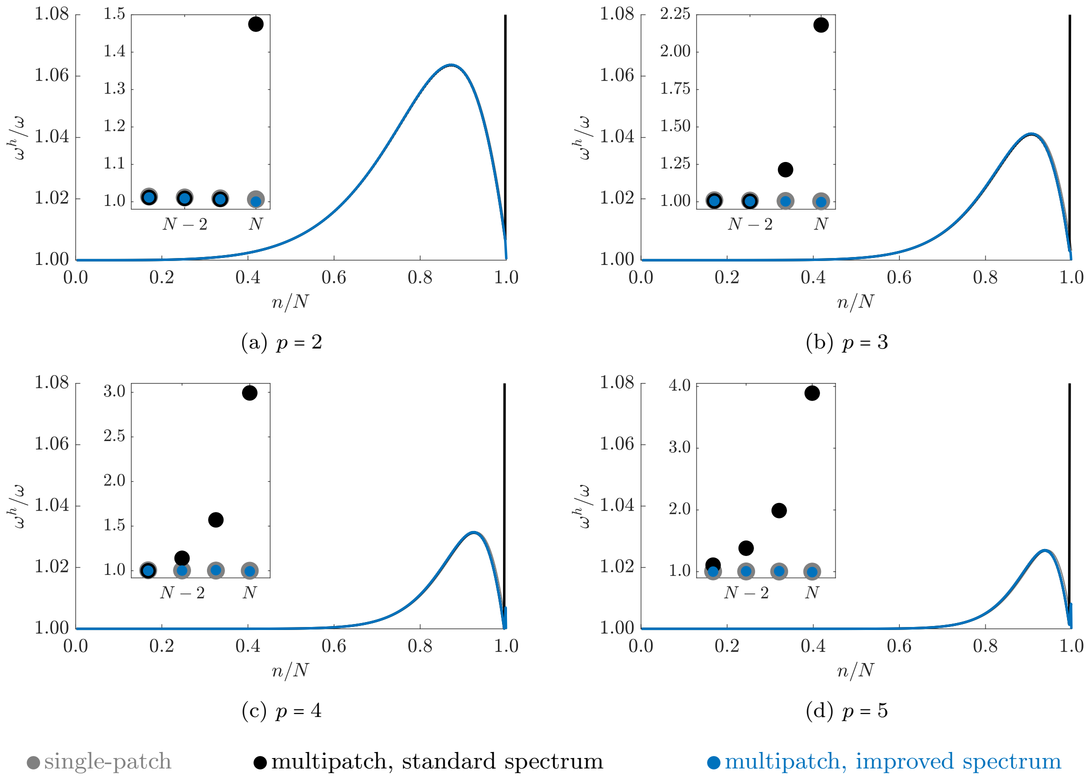

(a) $p = 2$

(b) $p = 3$

(c) $p = 4$

(d) $p = 5$

Figure 4.10: Normalized frequencies of a freely vibrating **fixed bar**, computed with **two patches** of C^{p-1} B-splines and discretized with 500 **elements**.

affecting the remaining modes. We conclude that our approach improves the spectral properties of univariate multipatch discretizations without affecting the accuracy of the remaining frequencies and modes.

We then verify that the proposed approach does not negatively affect the accuracy nor the optimal convergence behavior of the lower frequencies and modes. For second-order problems, the optimal convergence rate of the frequency error and the L^2 error in the mode is $\mathcal{O}(2p)$ and $\mathcal{O}(p+1)$, respectively [43], [66]. Figure 4.12 illustrates the convergence of the relative error in the 18th frequency (left) and the L^2 errors in the corresponding mode (right) of the bar. We plot these errors vs. the mode number N for degrees $p = 2$ through 5. We observe that our approach preserves the optimal accuracy of the frequency and mode. We can also see in Figure 4.12 that the error converges optimally in all cases.

4.3.5 Spectral analysis of a fourth-order problem

We then consider the free transverse vibration of a fixed beam with unit length, unit bending stiffness and unit mass. We employ a multipatch discretization with two patches ($n_{\text{pa}} = 2$) of C^{p-1} B-splines of different polynomial degrees $p = 3$ through 6 where interior

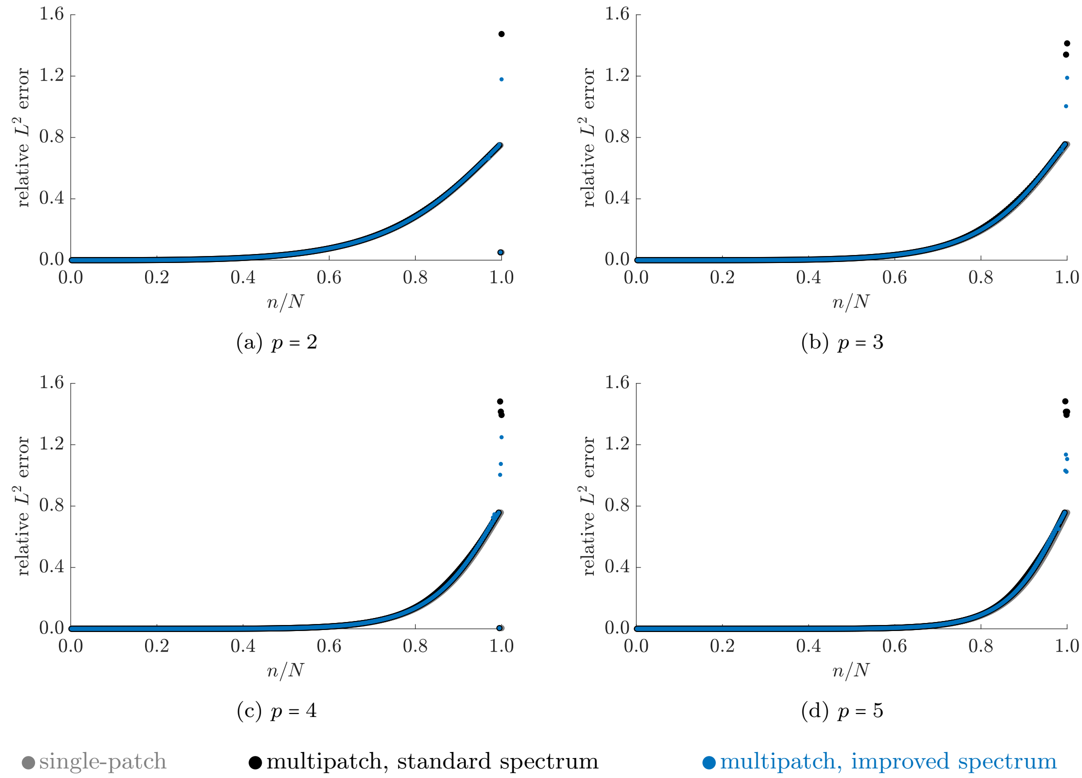

(a) $p = 2$ (b) $p = 3$

(c) $p = 4$ (d) $p = 5$

Figure 4.11: L^2 errors in the mode shapes of a freely vibrating **fixed bar**, computed with **two patches** of C^{p-1} B-splines and discretized **with** 500 **elements**.

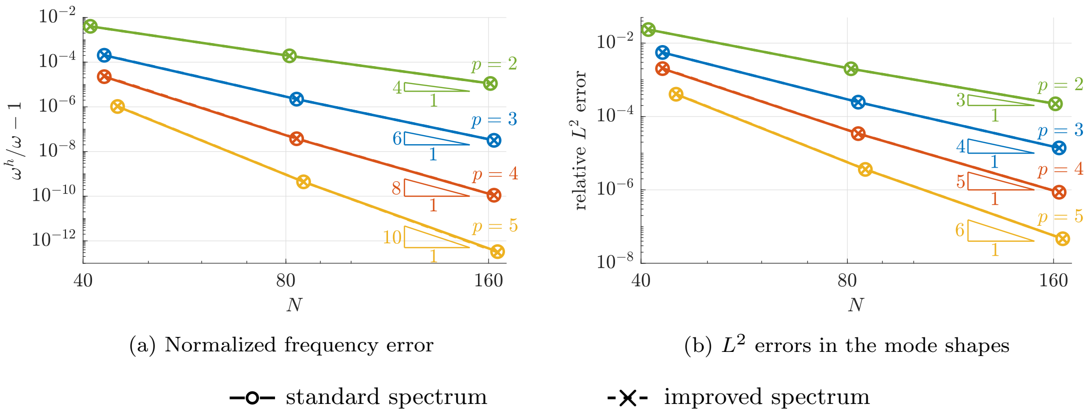

(a) Normalized frequency error (b) L^2 errors in the mode shapes

Figure 4.12: Convergence of the relative error in the **18th** eigenfrequency and mode of **a fixed bar**, obtained with 2 **patches** of quadratic, cubic, quartic and quintic C^{p-1} B-spline basis functions.

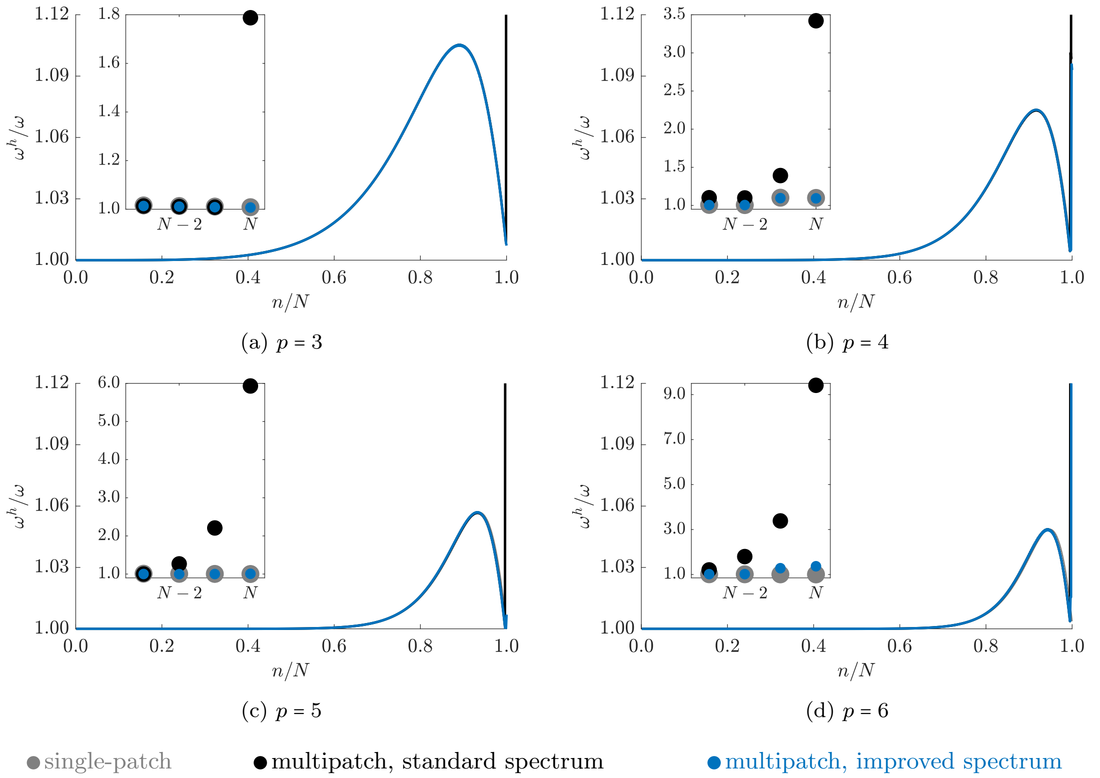

(a) $p = 3$

(b) $p = 4$

(c) $p = 5$

(d) $p = 6$

Figure 4.13: Normalized frequencies of a freely vibrating **fixed beam**, computed with **two patches** of C^{p-1} B-splines and discretized **with** 500 **elements**.

outliers exist (see Table 4.2), and with sufficient regularity, i.e. C^1 patch continuity. Figures 4.13 and 4.14 illustrate the normalized frequency and the L^2 error in the mode shapes corresponding to the studied beam, respectively. We order and present the results in the same way as those of the fixed bar in the previous subsection. We observe a similar effect of the proposed approach on the frequencies and modes as in the case of the fixed bar. Thus, we conclude that the proposed approach improves the spectral properties of univariate multipatch discretizations for both second- and fourth-order problems.

We also verify that the proposed approach preserves the optimal accuracy and optimal convergence behavior of the lower frequencies and modes. For fourth-order problems, the optimal convergence rate of the frequency error and the L^2 error in the mode is $\mathcal{O}(2(p-1))$ and $\mathcal{O}(p+1)$, respectively [43], [66]. Figure 4.15 demonstrates the convergence of the relative error in the 18th frequency (left) and the L^2 errors in the corresponding mode (right) of the beam, as functions of the mode number N with polynomial degrees $p = 3$ through 6. We observe that our approach preserves the optimal accuracy and convergence behavior in all cases.

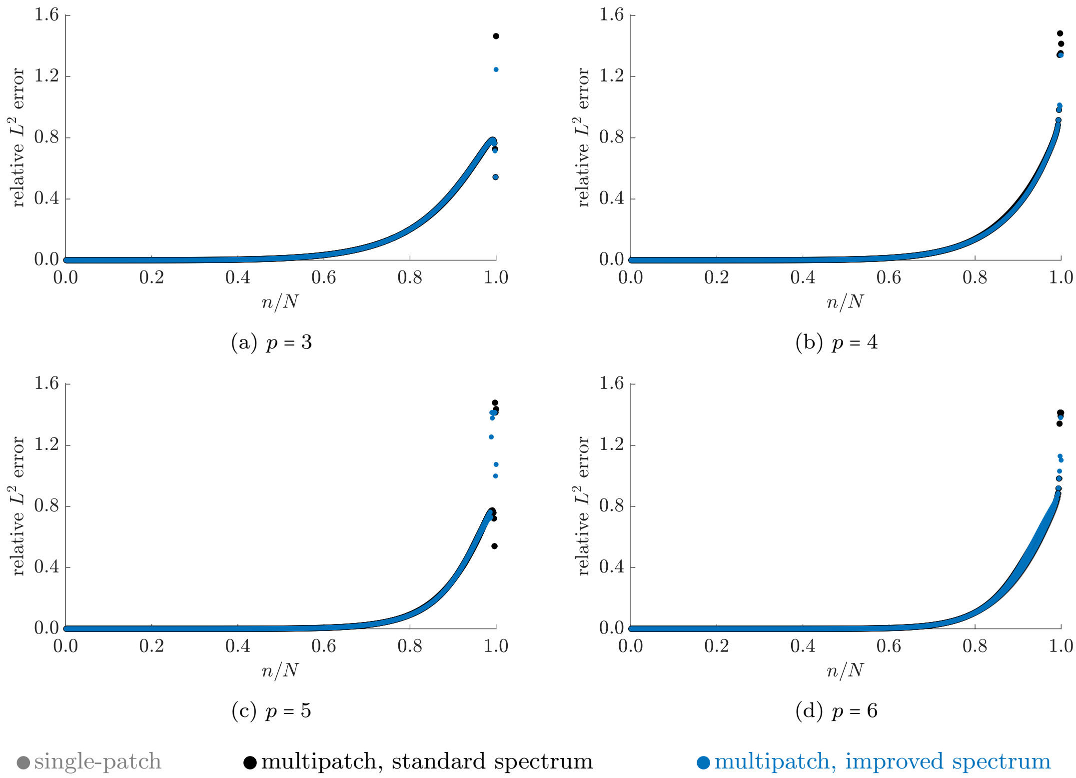

(a) $p = 3$

(b) $p = 4$

(c) $p = 5$

(d) $p = 6$

Figure 4.14: L^2 errors in the mode shapes of a freely vibrating **fixed beam**, computed with **two patches** of C^{p-1} B-splines and discretized **with** 500 **elements**.

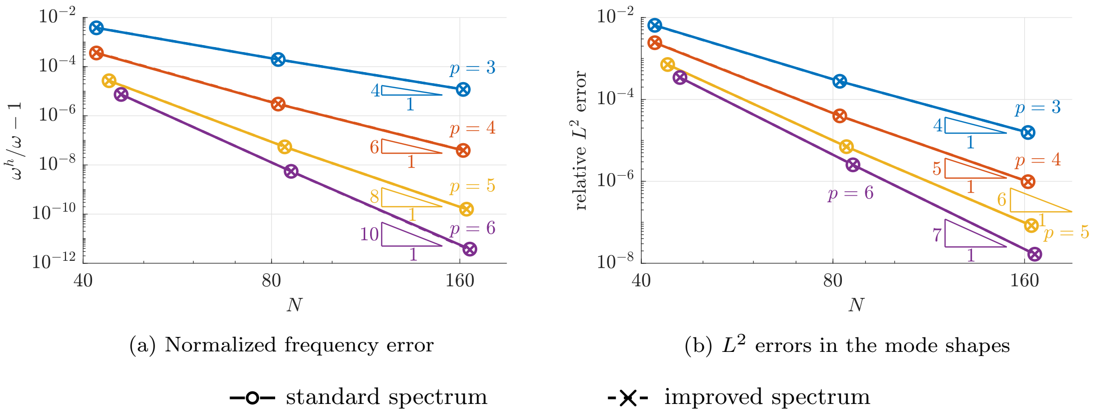

(a) Normalized frequency error

(b) L^2 errors in the mode shapes

Figure 4.15: Convergence of the relative error in the **18th** eigenfrequency and mode of **a fixed beam**, obtained with 2 **patches** of cubic, quartic, quintic and sextic C^{p-1} B-spline basis functions.

4.4 Generalization to multidimensional discretizations

The iterative scheme proposed in the previous section is shown to work effectively for univariate multipatch discretizations. There are two major issues that need to be addressed in order to generalize this scheme to multidimensional discretizations. First, the scheme requires $(p-1)$ target maximum frequencies, which are typically unknown in practical applications. Second, for each continuity constraint (4.12) a corresponding outlier mode needs to be identified that maximizes (4.32). This would necessarily imply that all modes need to be precomputed. In this section, we tackle both these problems by further simplifying the current approach (4.15), giving rise to a new iterative scheme for estimating the scaling parameters of the perturbation terms. We then demonstrate via spectral analysis of two-dimensional second- and fourth-order problems that the simplified approach is able to effectively improve the spectra of multipatch discretizations.

4.4.1 A pragmatic approach to parameter estimation

We assume a uniform mesh with mesh size h. The variational formulation (4.15) can then be simplified by choosing the l^{th} parameter as: $\alpha^l = \alpha\, h^{2l-2}$ and $\beta^l = \beta\, h^{2l-2}$. The scaling factor h^{2l-2} is based on the dimensional consistency of the inner-products of the l^{th} derivatives in the perturbation (4.13). The proposed variational formulation of the perturbed eigenvalue problem (4.15) becomes: find $(\tilde{U}_n^h, \tilde{\omega}_n^h) \in \mathcal{V}^h \times \mathbb{R}^+$, for $n = 1, 2, \ldots, N$, such that $\forall\, v^h \in \mathcal{V}^h \subset \mathcal{V}$:

$$a(\tilde{U}_n^h, v^h) + \alpha \sum_{l=1}^{p-1} h^{2l-2}\, c^l(\tilde{U}_n^h, v^h) = \left(\tilde{\omega}_n^h\right)^2 \left[b(\tilde{U}_n^h, v^h) + \beta \sum_{l=1}^{p-1} h^{2l-2}\, c^l(\tilde{U}_n^h, v^h) \right]. \tag{4.35}$$

The corresponding matrix equation (4.17) is then simplified to:

$$\left(\mathbf{K} + \alpha \underbrace{\sum_{l=1}^{p-1} h^{2l-2}\, \mathbf{K}_\Gamma^l}_{\mathbf{K}_\Gamma} \right) \tilde{\mathbf{U}}_n^h \;=\; \left(\tilde{\omega}_n^h\right)^2 \left(\mathbf{M} + \beta \underbrace{\sum_{l=1}^{p-1} h^{2l-2}\, \mathbf{K}_\Gamma^l}_{\mathbf{K}_\Gamma} \right) \tilde{\mathbf{U}}_n^h\,, \tag{4.36}$$

On this basis, we design Algorithm 5 for estimating the parameters α and β in (4.35) (or (4.36)). Here, we iteratively estimate α and β such that the maximum frequency is reduced by a target factor $c \in (0,1)$ in each iteration, and thus do not require a choice of the target maximum frequency or any analytical value. In Algorithm 5, the target maximum frequency in each iteration, $\hat{\omega}_{max}^h$, is a fraction of the maximum frequency obtained from the previous iteration. To obtain α and β in each iteration, instead of the outlier, we focus on the maximum frequency and corresponding mode, such that no identification of outlier modes is required. The equation for estimating these parameters in Algorithm 5 is based on the iterative scheme (4.28)-(4.29) described in the previous section. We note that to ensure stability, we employ the unperturbed outlier mode U_{max}^h

Algorithm 5: Iterative estimation of the parameters involved in (4.35). The algorithm terminates when the maximum frequency does not correspond to an outlier anymore (see Remark 4.4.1).

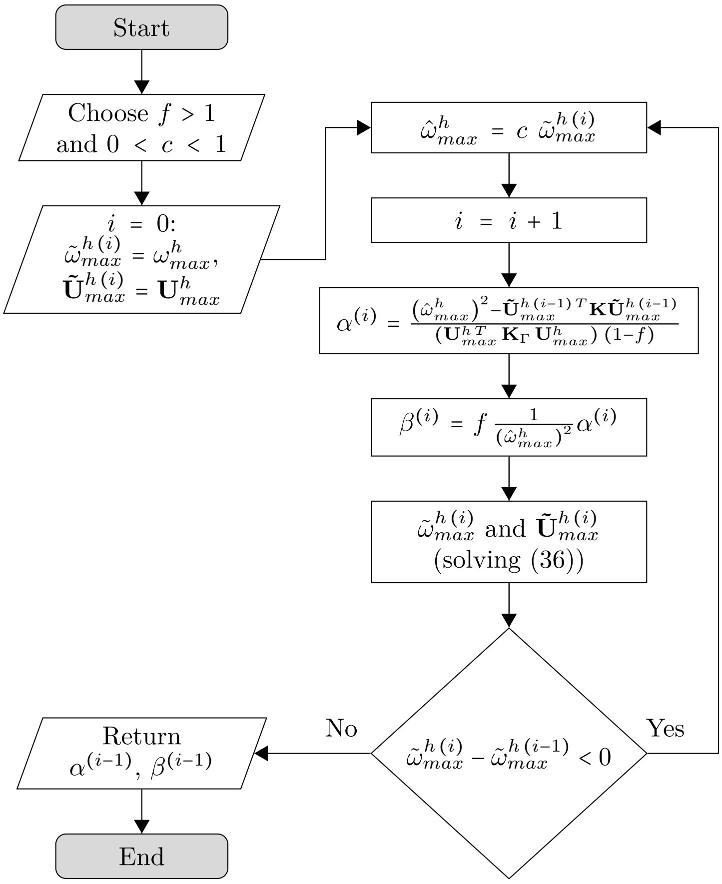

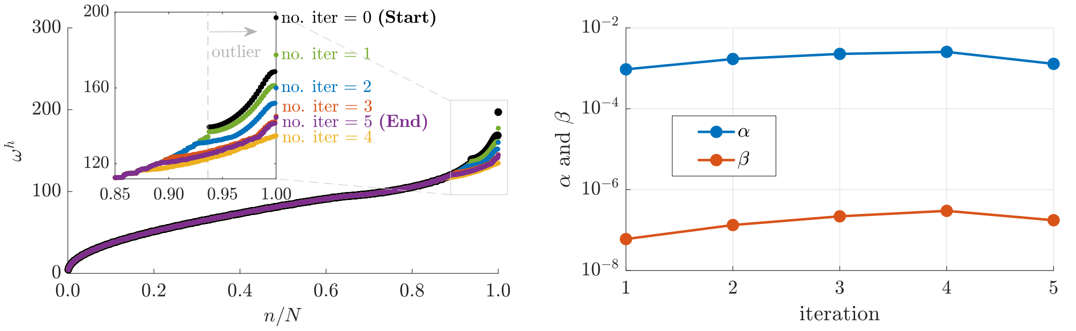

(a) Discrete frequency spectrum

(b) Evolution of α and β

Figure 4.16: Discrete frequencies and parameters, α, β in each iteration, corresponding to a freely vibrating **square membrane with fixed boundary conditions**, computed with 2×2 patches and 15×15 elements of **quadratic B-splines** ($p = 2$) via Algorithm 5 with $\boldsymbol{f = 2, c = 0.9}$.

instead of the perturbed one $\tilde{U}^h_{max}$ in the denominator for computing α, since $\tilde{U}^h_{max}$ is not necessarily an outlier mode in all iterations and thus could result in infinitesimal values in the denominator.

Figure 4.16 illustrates how the Algorithm 5 affects the discrete frequency (left) and changes the parameters α and β (right) in each iteration for a fixed square membrane (see next subsection for details of the example). We observe that the maximum outlier frequency is reduced in each iteration, from the first through the fourth iteration (see Figure 4.16a), and the parameters α and β increase in the same iteration (see Figure 4.16b). We can also see in the inset figure of Figure 4.16a that our approach reduces not only the outlier frequencies (data points on the right of the dashed gray line) but also the non-outlier ones (data points on the left of the dashed gray line). In the last (fifth) iteration, the maximum frequency increases (purple curve in Figure 4.16a), which then meets the stopping criterion defined in Algorithm 5. This increase in the maximum frequency corresponds to decreasing parameters α and β (see Figure 4.16b). Then, the output of Algorithm 5 are the parameters α and β of the previous (fourth) iteration.

Remark 4.4.1. *Algorithm 5 stops when the perturbation reduces the outlier frequencies by such a factor that they become smaller than the highest non-outlier frequency, see Figure 4.16a.*

Remark 4.4.2. *The factor* $c \in (0,1)$ *determines the reduction in each iteration of Algorithm 5. Due to the chosen stopping criterion (Remark 4.4.1), the resulting maximum frequency lies within a range of* $100\cdot(1-c)\%$ *of the minimum value that can be achieved. For example, a choice of* $c = 0.9$ *results in a reduced maximum frequency within* 10% *of the minimum value.*

Algorithm 5 updates only the maximum frequency and the corresponding mode in each iteration. It requires two input parameters: a scaling factor $f > 1$ between α and β, which can be chosen as discussed in the previous section, and a target reduction factor $c \in (0,1)$ in each iteration. A choice of a small c results in a large reduction step of the maximum frequency and a small number of iterations. The reduced maximum frequency, however, could be far away from the minimum value that can be achieved (see Remark 4.4.2), i.e. the maximum frequency is reduced ineffectively. Moreover, a very small c leads to a very small value in the denominator of the equation for β (see Algorithm 5), negatively affecting the convergence of β. Large values of c avoid this issue, but require more iterations. For our numerical studies in the remainder of this paper, we choose $f = 2$ and $c = 0.9$ for all cases. We find that this choice of factor c typically requires only up to five iterations to sufficiently reduce the maximum frequency, i.e. the maximum frequency is significantly reduced within 10% of the lowest possible value (see also 4.4.2) with a small number of iterations.

4.4.2 Spectral analysis of 2D second- and fourth-order model problems

We consider the free transverse vibration of a square membrane, of unit edge size with fixed boundary conditions, unit membrane stiffness and unit mass. We study C^{p-1} B-splines of polynomial degrees $p = 2$ through 5 and C^0 patch continuity. We employ

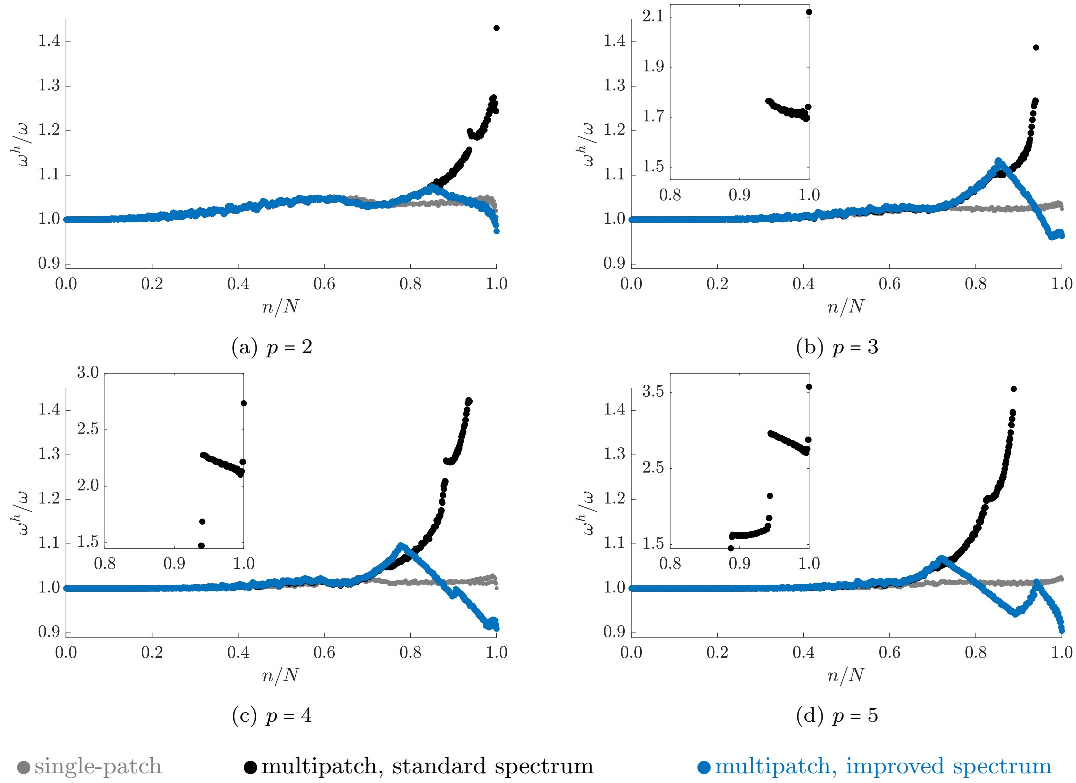

(a) $p = 2$ (b) $p = 3$ (c) $p = 4$ (d) $p = 5$

Figure 4.17: Normalized frequencies of a freely vibrating **square membrane with fixed boundary conditions**, computed with 2×2 **patches of C^{p-1} B-splines**. Each patch is **discretized with 15×15 elements**.

multipatch discretizations of 2×2, 5×5 patches, and the limit case of C^0 Bézier elements (one element per patch, $n_{\text{pa}} = n_{\text{ele}} = 15 \times 15$). Figures 4.17, 4.18, and 4.19 present the normalized frequencies ω_n^h/ω_n corresponding to the square membrane discretized with 2×2, 5×5, and 15×15 patches, respectively. The inset figures of 4.17 focus on the upper last twenty percent of the spectra. Due to their tensor-product structure, the spectra of multivariate discretizations exhibit a higher number of outliers than univariate discretizations.

We then consider the free vibration of a square plate structure of unit edge size with simply supported boundary conditions, unit bending stiffness and unit mass. We use C^{p-1} B-splines of polynomial degrees $p = 3$ through 6 and C^1 patch continuity. We employ multipatch discretizations of 2×2 and the limit case of C^1 Bézier elements (same number of patches and elements, $n_{\text{pa}} = n_{\text{ele}} = 15 \times 15$). Figures 4.20 and 4.21 illustrate the normalized frequencies, ω_n^h/ω_n, corresponding to the square plate discretized with 2×2 and 15×15 patches, respectively. These results confirm that our approach (4.35) in combination with Algorithm 5 reduces the outlier frequencies of multipatch discretizations effectively for both second- and fourth-order problems, without negatively affecting lower frequencies, and works well for different polynomial degrees and patch configurations.

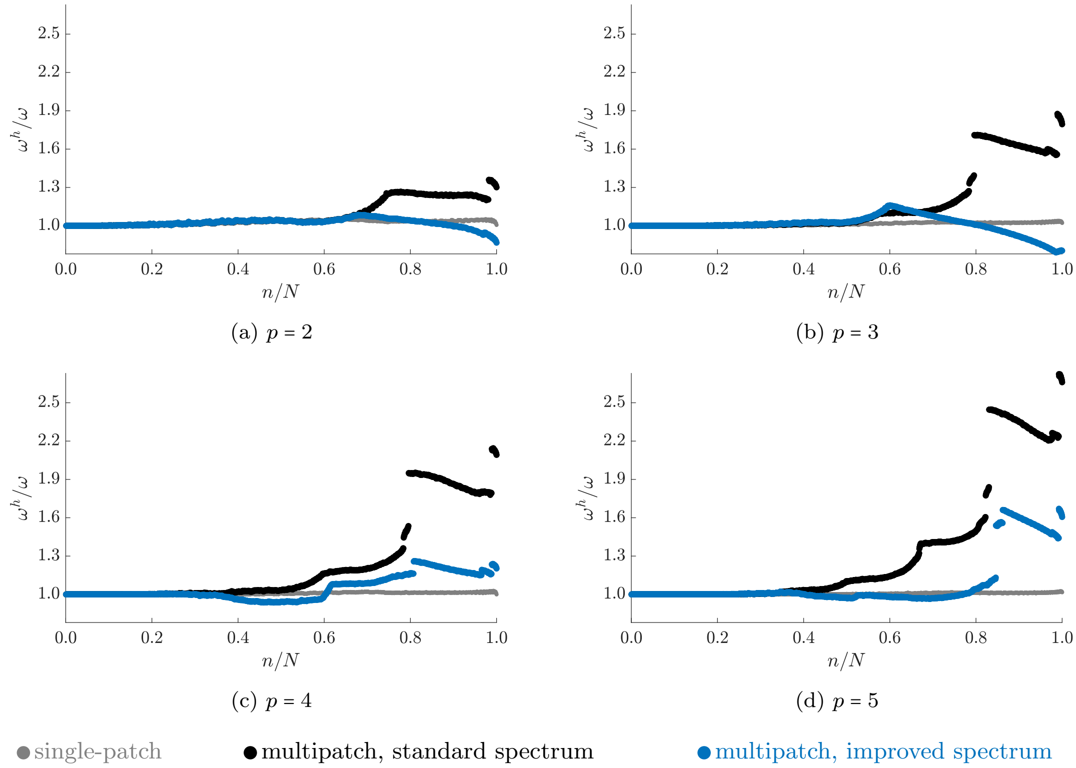

(a) $p = 2$

(b) $p = 3$

(c) $p = 4$

(d) $p = 5$

Figure 4.18: Normalized frequencies of a freely vibrating **square membrane with fixed boundary conditions**, computed with 5×5 **patches of** C^{p-1} **B-splines**. Each patch is **discretized with** 5×5 **elements**.

4.5 Application in explicit dynamics

The critical time-step size in explicit dynamics calculations is inversely proportional to the maximum discrete eigenfrequency [66]. Significantly overestimated outlier frequencies therefore negatively affect the critical time-step size, and hence the computational cost of explicit dynamics calculations. It can be thus expected that the approaches presented in this work are able to effectively improve this issue for multipatch isogeometric discretizations, which we will illustrate in the following.

4.5.1 Semidiscrete formulation

In this section, we consider the semi-discrete form (4.4) of an free-vibrating, undamped linear structural system, which can be expressed as follows:

$$\mathbf{M}\,\frac{d^2}{d\,t^2}\,\mathbf{u}^h(t) \;=\; \underbrace{-\,\mathbf{K}\,\mathbf{u}^h(t)}_{\mathbf{F}_{\text{int}}}, \tag{4.37}$$

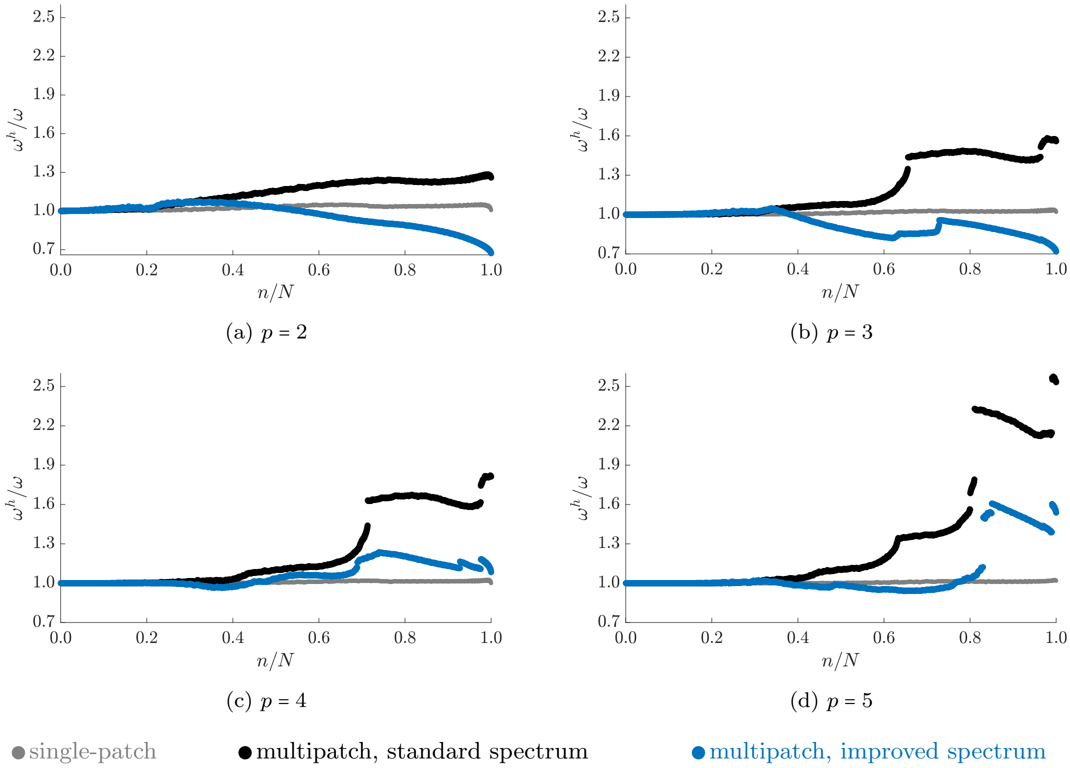

(a) $p = 2$

(b) $p = 3$

(c) $p = 4$

(d) $p = 5$

Figure 4.19: Normalized frequencies of a freely vibrating **square membrane with fixed boundary conditions**, computed for the limit case of C^0 **Bézier elements** ($n_{\text{pa}} = n_{\text{ele}} = 15 \times 15$).

where $\mathbf{F}_{\text{int}}$ is the vector of internal forces. Using the proposed approach in Section 4.4.1 leads to the following semi-discrete form:

$$(\mathbf{M} + \alpha \mathbf{K}_\Gamma) \frac{d^2}{dt^2} \mathbf{u}^h(t) = \underbrace{-(\mathbf{K} + \beta \mathbf{K}_\Gamma) \mathbf{u}^h(t)}_{\tilde{\mathbf{F}}_{\text{int}}}, \tag{4.38}$$

where $\tilde{\mathbf{F}}_{\text{int}}$ is the perturbed vector of internal forces. Both the left- and right-hand sides of the standard formulation (4.37) are modified using our approach. This is not the case when using the mass scaling approach where only the mass matrix on the left-hand side is modified by adding artificial mass terms [113]–[115], [120]. The perturbation matrix $\mathbf{K}_\Gamma$ is computed once and hence no reassembly of the mass matrix is needed, so that this does not increase the computational cost of explicit dynamics calculations.

Remark 4.5.1. *Explicit dynamics applications typically involve the use of a lumped mass matrix in combination with an explicit time integration scheme. There are currently no widely accepted mass lumping techniques that maintain higher-order spatial accuracy. To demonstrate that our methodology maintains higher-order spatial accuracy, we employ the consistent mass matrix in all subsequent computations.*

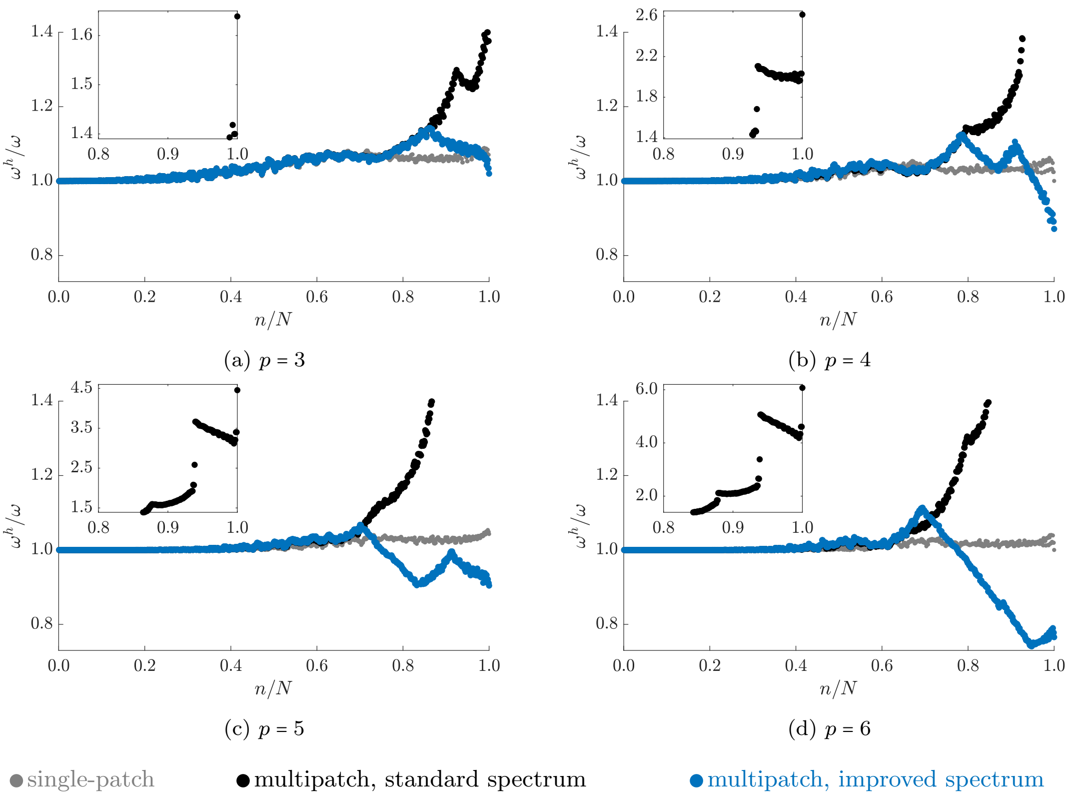

(a) $p = 3$ (b) $p = 4$

(c) $p = 5$ (d) $p = 6$

Figure 4.20: Normalized frequencies of a freely vibrating **square plate with simply supported boundary conditions**, computed with 2×2 **patches of** C^{p-1} **B-splines**. Each patch is **discretized with** 15×15 **elements**.

4.5.2 Optimum spatial accuracy

We consider the free vibration of the annular membrane problem illustrated in Figure 4.22a, see also [122], where boundary conditions are fixed along the inner radius a and outer radius b. We choose the following displacement solution u that satisfies the differential equation (4.1):

$$u(r,\theta,t) = J_4(r)\ \cos(\lambda_2\, t)\ \cos(4\,\theta)\,, \tag{4.39}$$

with radial coordinate r, angular coordinate θ and time t. Here, $J_4(r)$ denotes the 4^{th} Bessel function of the first kind and λ_k, $k = 1, 2, \ldots$ denote its positive zeros. We choose the second and fourth zeros as the inner and outer radii of the annulus, respectively, i.e. $a = \lambda_2 \approx 11.065$ and $b = \lambda_4 \approx 17.616$. The analytical solution (4.39) at time $t = 0$ plotted in Figure 4.22b defines the initial displacement field $u(r,\theta,0)$.

We study the semi-discrete form (4.38) of the annular membrane in explicit dynamics. We employ a multivariate spline space that is an extension of the univariate spaces of the angular coordinate ($\theta \in [0, 2\pi]$) and radial coordinate ($r \in [a,b]$). The univariate spline spaces are free of boundary outliers due to outlier removal boundary constraints

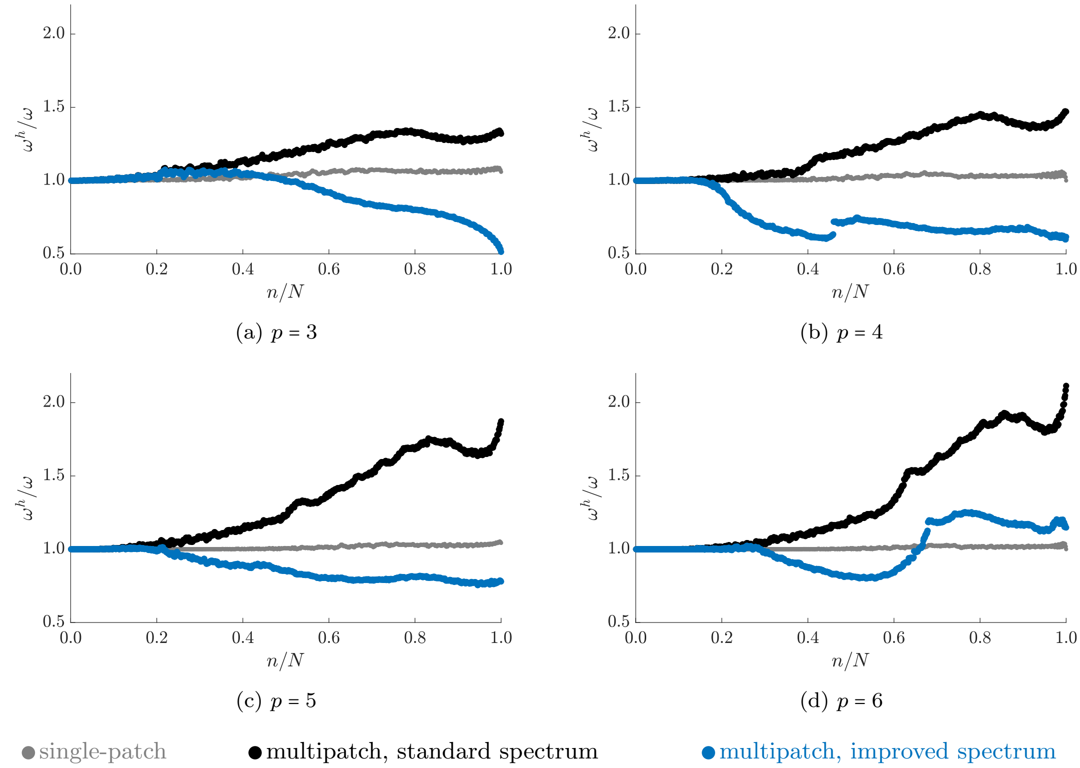

(a) $p = 3$ (b) $p = 4$

(c) $p = 5$ (d) $p = 6$

Figure 4.21: Normalized frequencies of a freely vibrating **square plate with simply supported boundary conditions**, computed for the limit case of C^1 **Bézier elements** ($n_{\text{pa}} = n_{\text{ele}} = 15 \times 15$).

[122]. In the spline space of the angular coordinate, we also build in the periodic end-conditions. We consider C^{p-1} B-splines of different polynomial degrees $p = 2$ through 5 for multipatch discretizations with 2 patches in the radial direction, and 4 patches in the angular direction, and C^0 patch continuity (see Figure 4.22a). We apply the proposed approach to enforce the C^{p-1} continuity constraints (4.12) at patch interfaces (see Figure 4.22a). We perform uniform mesh refinement of each patch with $4, 8, 16$ elements, i.e. $n_{\text{ele}} = 8, 16, 32$ elements in the radial coordinate, and $16, 32, 64$ elements in the angular coordinate. We simulate up to a final time of $T = 2\pi/\lambda_2$ which is one full period of the periodic function $u(r, \theta, t)$ (4.39). For time integration, we apply the central difference method [66]. To verify that spatial accuracy is maintained, we choose a small, order-dependent time step of $\Delta t = (p/(2n_{\text{ele}}))^p$.

Figure 4.23 compares the convergence behavior of the L^2 error in the discrete displacement field $u^h(r, \theta, t)$, when we do standard analysis (circle) and when we do analysis with the proposed approach based on perturbed eigenvalue problems (cross). We observe that the analysis with our perturbation approach maintains optimum spatial accuracy.

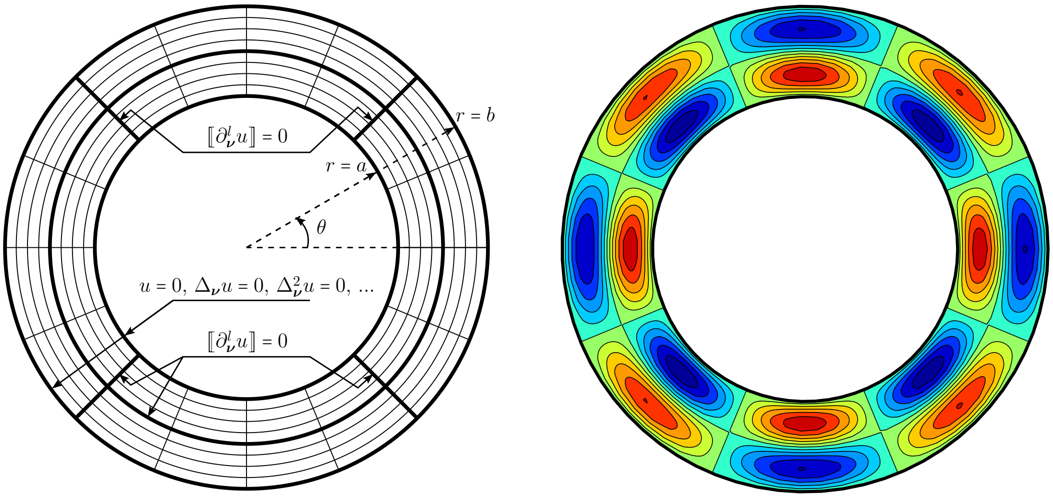

(a) Coarsest Bézier mesh with boundary and interface constraints

(b) Initial displacement field $u(r, \theta, 0)$

Figure 4.22: Transient model problem on an annulus.

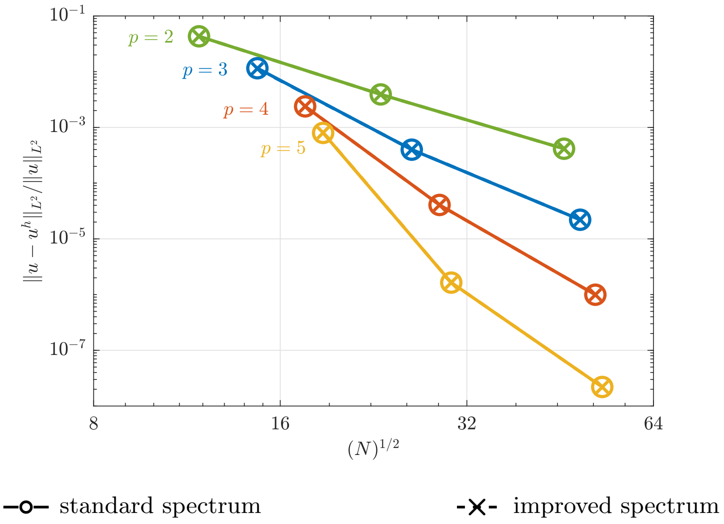

Figure 4.23: Convergence of the relative L^2 error in the vertical displacement field u of **the annular membrane in Figure 4.22**, computed with a small, order-dependent time step of $\Delta t = (p/(2n_{\text{ele}}))^p$.

4.5.3 Critical time-step size

For an undamped problem, the time step Δt in the central difference method is bounded from above by the critical time step Δt_{crit} [66, Chapter 9, p. 492]:

$$\Delta t \leq \Delta t_{crit} = 2/\omega_{\max}^h \,. \tag{4.40}$$

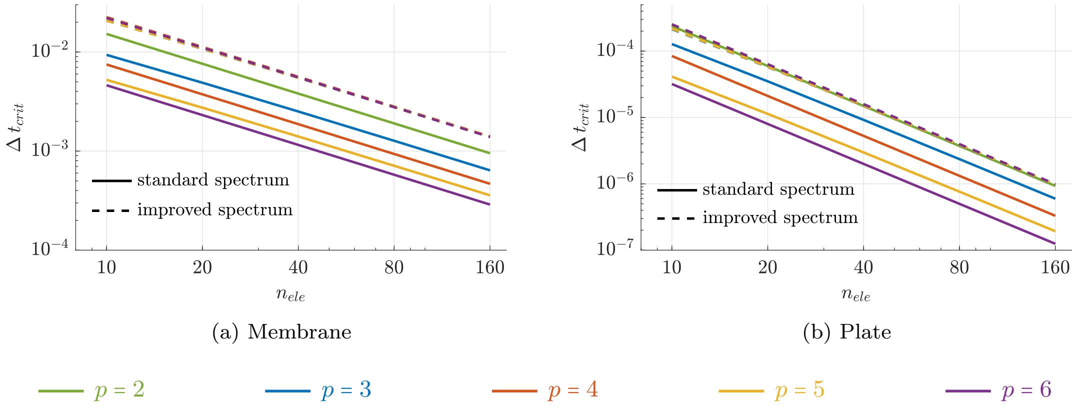

(a) Membrane (b) Plate

Figure 4.24: Critical time step size in explicit dynamics of a **square membrane and plate** with **fixed and simply supported boundary conditions**, respectively, as a function of the mesh $N = 2n_{\text{ele}} \times 2n_{\text{ele}}$ using 2×2 patches, resulting from standard and improved spectrum.

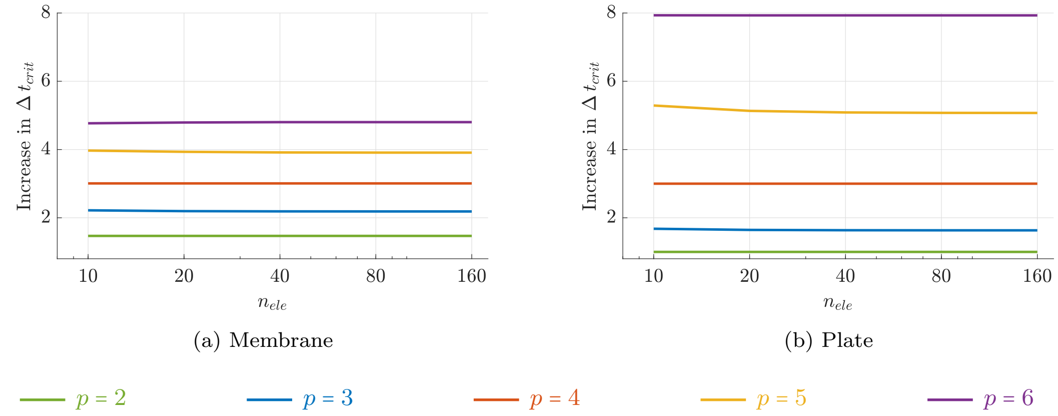

(a) Membrane (b) Plate

Figure 4.25: Increase in critical time step size due to improved spectrum in explicit dynamics of a **square membrane and plate** with **fixed and simply supported boundary conditions**, respectively, as a function of the mesh $N = 2n_{\text{ele}} \times 2n_{\text{ele}}$ using 2×2 patches.

Remark 4.5.2. *The maximum eigenfrequency is obtained as part of Algorithm 5. Hence, in our approach, we directly compute the critical time step size which is inversely proportional to the maximal frequency.*

Figure 4.24 plots the critical time-step size with respect to the number of elements per patch n_{ele}, obtained with our perturbation approach (dashed curves) and with standard analysis (solid curves), for the examples of a square membrane and plate with fixed and simply supported boundary conditions, respectively, as defined in the sections above. We consider C^{p-1} B-splines of polynomial degrees $p = 2$ through 6 and multipatch discretizations of $2{\times}2$ patches with C^0 and C^1 patch continuity for the membrane and plate, respectively. We observe that using our perturbation approach allows for a significantly larger critical time step, and thus effectively reduces the associated computational cost of explicit dynamics calculations. We can also see that the our approach removes the dependency of the critical time-step size on the polynomial degree p, which exists for the standard analysis. Figure 4.25 shows the relative increase in the critical time-step size.

4.6 Summary and conclusions

In this paper, we presented a variational approach based on perturbed eigenvalue analysis that reduces overestimated outlier frequencies due to reduced continuity at patch interfaces in isogeometric multipatch discretizations. It relies on the addition of scaled perturbation terms that weakly enforce C^{p-1} continuity at patch interfaces. We also presented an iterative procedure to estimate effective scaling parameters for the perturbation term. It requires two input parameters (scaling factor $f > 1$ and reduction factor $c \in (0, 1)$) and computation of the maximum eigenfrequency and corresponding mode, which can be efficiently computed via power iteration. We demonstrated that our approach is robust with respect to the scaling factor $f > 1$, i.e. it reduces the outlier frequencies to approximately the same values for all $f > 1$. Furthermore, a reduction factor $c = 0.9$ showed good results in all test cases.

We demonstrated numerically that the proposed approach improves spectral properties of multipatch discretizations for a variety bar, beam, membrane and plate. We showed that the approach effectively addresses the outlier frequencies, while maintaining accuracy in the remainder of the spectrum and modes. We confirmed that spatial accuracy of the response was maintained in an explicit dynamics setting and showed that our approach allows for a much larger time-step size. In particular, we observed that the proposed approach removes the negative dependency of the critical time-step size on the polynomial degree p.

We note that our approach may be combined with the approach of [121] to reduce outlier frequencies due to patch interfaces and boundaries. There are a number of avenues for future work. One aspect is the extension of our approach to non-uniform spline discretizations, trimmed and unfitted spline discretizations, and problems with non-smooth solution fields, where continuity constraints at patch interfaces cannot be consistently formulated. A second aspect is the further exploration of the case when $\alpha = 0$ and $\beta < 1$, which reduces the perturbation approach to the mass matrix, and to further study the resulting perturbation schemes in the context of mass lumping. One could investigate operator splitting techniques to move the added mass matrix to the right-hand side, which enables e.g. row-sum lumping of the unperturbed mass matrix. Another aspect is to study the performance of the proposed approach and the resulting problem conditioning in realistic scenarios with different material parameters.

5 Towards higher-order accurate mass lumping in explicit isogeometric analysis for structural dynamics

This chapter is reproduced from [188]:

T.-H. Nguyen, R. R. Hiemstra, S. Eisenträger, and D. Schillinger. *Towards higher-order accurate mass lumping in explicit isogeometric analysis for structural dynamics*, Comput. Meth. Appl. Mech. and Engrg. (2023) 116233. DOI: `10.1016/j.cma.2023.116233`. URL: `https://linkinghub.elsevier.com/retrieve/pii/S0045782523003572`.

Abstract

We present a mass lumping approach based on an isogeometric Petrov-Galerkin method that preserves higher-order spatial accuracy in explicit dynamics calculations irrespective of the polynomial degree of the spline approximation. To discretize the test function space, our method uses an approximate dual basis, whose functions are smooth, have local support and satisfy approximate bi-orthogonality with respect to a trial space of B-splines. The resulting mass matrix is "close" to the identity matrix. Specifically, a lumped version of this mass matrix preserves all relevant polynomials when utilized in a Galerkin projection. Consequently, the mass matrix can be lumped (via row-sum lumping) without compromising spatial accuracy in explicit dynamics calculations. We also address the imposition of Dirichlet boundary conditions and the preservation of approximate bi-orthogonality under geometric mappings. In addition, we establish a link between the exact dual and approximate dual basis functions via an iterative algorithm that improves the approximate dual basis towards exact bi-orthogonality. We demonstrate the performance of our higher-order accurate mass lumping approach via convergence studies and spectral analyses of discretized beam, plate and shell models.

5.1 Introduction

Isogeometric analysis (IGA) was initiated in 2005 by Tom Hughes and his students [30], [51] with the goal of bridging the gap between computer aided geometric design (CAD) and finite element analysis (FEA). The core idea of IGA is to use the same *smooth* and *higher-order* spline basis functions for the representation of both geometry in CAD and the approximation of physics-based field solutions in FEA [175]. IGA enables finite element approximations that are higher-order smooth, a feature that cannot be achieved in FEA based on nodal basis functions [176]. A key property of higher-order IGA, already discussed in one of the first articles [43], is its well-behaved discrete spectrum of eigenfrequencies and eigenmodes. The associated potential of IGA for higher-order accurate explicit dynamics calculations, however, lies largely idle to this day. One reason is that no practical methodology exists yet that reconciles higher-order accuracy and mass lumping. In this paper, we will focus on a new Petrov-Galerkin method that enables a higher-order accurate mass lumping that could help close this gap.

5.1.1 Explicit dynamics and mass lumping in FEA

Finite element discretizations of transient problems in structural mechanics generate semidiscrete systems of coupled second-order ordinary differential equations of the following type [116]:

$$\mathbf{M}\,\ddot{\boldsymbol{u}}^n = \mathbf{F}^n_{\text{ext}} - \int_\Omega \boldsymbol{B}(\boldsymbol{x}^n)^T\,\boldsymbol{\sigma}^n\,\mathrm{d}\Omega\,, \tag{5.1}$$

where $\mathbf{M}$ is the mass matrix, $\boldsymbol{u}$ the displacement vector, $\mathbf{F}_{\text{ext}}$ the vector of external forces, $\boldsymbol{B}$ the discrete gradient operator, $\boldsymbol{\sigma}$ the Cauchy stress, and Ω the problem domain. The superscript n is the time index that indicates that a variable is evaluated at time instant t^n.

In many applications such as virtual testing of vehicle crashworthiness or the simulation-based design of metal forming processes, the internal force vector of the discrete system (5.1) involves shell elements, nonlinear material models, and contact with friction. For shell problems, most established finite element formulations are based on shear-deformable Reissner-Mindlin-type models [64], which allow the consistent evaluation of the integral in (5.1) with standard nodal basis functions. Due to their cost effectiveness and robustness against locking, state-of-the-art commercial software packages such as LS-Dyna or Pam-Crash mostly rely on lowest-order linear basis functions with reduced quadrature and hourglass control, which require very fine meshes to achieve accurate solutions on complex geometries.

For the resulting large and ill-conditioned systems, however, iterative equation solvers required by implicit methods do not converge well and are thus prohibitively expensive [116].

As a result, explicit dynamics based on explicit second-order accurate time integration methods such as the central difference method or variations thereof [66], has established itself as the key technology for efficiently solving (5.1) [189], [190]. Given a lumping scheme to diagonalize the mass matrix, its inversion in (5.1) becomes trivial and the dominating cost of the explicit multistep procedure shifts entirely to the evaluation of the internal force vector. In addition, a diagonal mass matrix significantly reduces memory and facilitates parallel computing, as global system matrices and the associate assembly or inversion procedures do never explicitly occur. An alternative pathway to explicit dynamics with diagonal mass matrices in FEA is the use of so-called Gauss-Lobatto Lagrange basis functions with nodes at the Gauss-Lobatto points in conjunction with Gauss-Lobatto quadrature [93], [96], [191], [192]. This is the only technique established so far that obtains higher-order spatial accuracy in explicit dynamics with a diagonal mass matrix [94], [95]. We note that within the last decade, there has been a new increase in research and development in higher-order explicit structural analysis with C^0-continuous finite elements, both in academia, see e.g. [95], [193]–[197] and in industry, see e.g. the commercial codes IMPETUS [198] and LS-Dyna [199], which in addition to standard linear elements also promote second- and third-order elements.

Explicit schemes, however, are only conditionally stable. Therefore, the step size, with which they march forward in time, cannot exceed a maximum critical time step size [111], which is inversely proportional to the maximum eigenfrequency $\omega_{\max}$ of the discretization: $\Delta t^n_{\text{crit}} \sim 1/\omega^n_{\max}$. Due to this dependence, control of the highest frequencies in the spectrum is indispensable for guaranteeing acceptable time step sizes and hence efficient explicit dynamics calculations. In FEA, the impact of $\omega_{\max}$ can be alleviated, e.g., via selective mass scaling [115] or time step subcycling [200].

5.1.2 Explicit dynamics and mass lumping in IGA

IGA is particularly attractive for higher-order accurate structural analysis. In addition to mesh refinement, spline functions naturally enable the increase of the polynomial degree (p-refinement), or both at the same time (k-refinement). For elastostatic-type problems, it has been consistently shown across the pertinent literature that higher-order IGA is superior to FEA based on nodal basis functions in terms of per-degree-of-freedom accuracy [201]. A variety of advanced formulations for isogeometric structural analysis have been developed over the past decade, in particular for shells based on Kirchhoff-Love [48], [80], Reissner-Mindlin [46], [202]–[204], and solid-type models [205], [206], and hierarchic combinations thereof [45], [47]. Isogeometric shell formulations have been applied for explicit dynamics calculations, based on the adoption of standard row-sum lumping to diagonalize the mass matrix [207], [208]. In addition, selective mass scaling [116] and different methods to obtain time step estimates [116], [209] known from FEA based on nodal basis functions have been applied in an IGA context. But studies on explicit dynamics with shell IGA and standard mass lumping have reported sub-optimal results. For example, Hartmann and Benson report in [116] that “increasing the degree on a fixed mesh size increases the cost without a commensurate increase in accuracy”, which they call a “disappointing result.”

To put this statement in perspective and illustrate the negative impact of mass lumping on a higher-order Galerkin method, we consider the classical result obtained from the generalized eigenvalue problem of a bar, discretized with cubic Lagrange polynomials

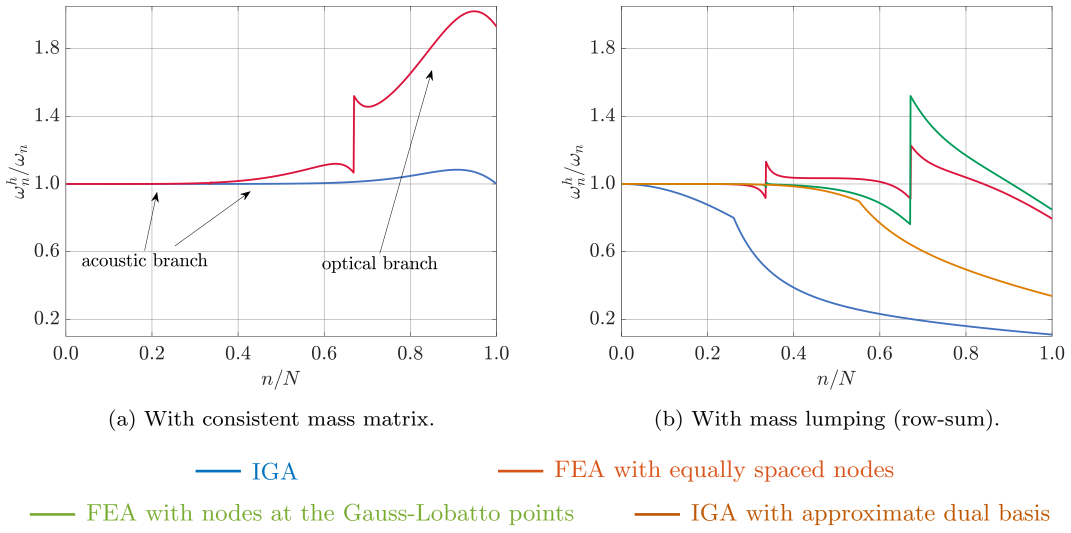

(a) With consistent mass matrix.

(b) With mass lumping (row-sum).

Figure 5.1: Normalized discrete spectrum of eigenfrequencies obtained from a generalized eigenvalue problem for a bar, computed with FEA and IGA, both with 1,000 cubic basis functions. We note that in (a), the orange line and the green line overlap with the blue line and the red line, respectively.

(FEA) and cubic smooth splines (IGA) [43], [51]. The numerically obtained frequencies, ω_n^h, are normalized with respect to the exact solution, ω, and plotted versus the mode number, n, normalized by the total number of degrees of freedom, N. Figure 5.1a shows that for FEA, the spectrum (curve plotted in red) with consistent mass matrix contains so-called “optical” branches, separated by distinct jumps, which compromise the accuracy of the high frequency range. In contrast, we observe that for IGA (curve plotted in blue) with consistent mass matrix, the accurate “acoustic branch” of the spectrum covers the entire frequency range. We note that we removed the outliers at the end of the spectrum [122]. We now apply standard row-sum lumping to the mass matrix in both schemes. Figure 5.1b shows that for FEA with equally spaced nodes, the spectrum exhibits a loss of accuracy in the first optical branch. When we apply FEA with nodes at the Gauss-Lobatto points and Gauss-Lobatto quadrature [96], we naturally arrive at a lumped mass matrix, whose spectrum is more accurate in the medium frequency range. With standard row-sum lumping of the mass matrix, the results for IGA exhibit a significant decrease in spectral accuracy across the entire frequency range. The results shown in Fig. 5.1b thus indicate that one reason for the decrease in accuracy lies in the detrimental impact of row-sum lumping when employed in a standard IGA context, outlined already in the first contribution on IGA for structural dynamics [43].

5.1.3 Mass lumping based on approximate dual spline functions

The removal of this gap requires the development of novel spline-centered technology that leverages the additional opportunities provided by this class of basis functions. A first attempt was presented in [100], based on the idea of using dual spline functions. This set of spline functions is defined "dual" to a set of standard B-splines, such that the inner product of the two integrated over a domain yields a diagonal matrix (bi-orthogonality). Hence, if a dual basis is used as the test space in a finite element formulation, we naturally end up with a consistent diagonal mass matrix [100]. In CAD research, the bi-orthogonality property has been well known for decades, and several approaches for the construction of the underlying dual basis exist, see e.g. [2]. In the computational mechanics community, this property has been used for different purposes, e.g. for dual mortar methods [105], [107] or for unlocking of Reissner-Mindlin shell formulations [82].

Dual spline basis functions still suffer from shortcomings when applied as test functions in the variational formulation of elastodynamics as envisioned in [100], to the extent that their use in explicit dynamics seems not straightforward: Firstly, bi-orthogonality in general holds only on the parametric domain, but is in general lost under non-affine geometric mappings. Secondly, dual spline functions with the same smoothness as their B-spline counterparts have global support on each patch, thus producing fully populated stiffness forms. Their support can be reduced, but at the price of losing continuity, leading to discontinuous functions in the fully localized case. Both are prohibitive in a finite element context. And thirdly, dual basis functions are not interpolatory at the boundaries. Therefore, the identification of a kinematically admissible set of test functions that allows the variationally consistent strong imposition of Dirichlet boundary conditions is not straightforward.

In this paper, we present an isogeometric Petrov-Galerkin method that combines the dual basis concept and standard row-sum lumping and achieves higher-order accuracy in explicit dynamics irrespective of the polynomial degree of the spline approximation. Its key ingredients are a class of "approximate" dual spline functions that was introduced in [131]. It only approximately satisfies the discrete bi-orthogonality property, but preserves all other properties of the original B-spline basis, such as C^{p-1} smoothness, polynomial reproduction and local support. We employ the approximate dual functions to discretize the test function space in the variational formulation of elastodynamics. This leads to a semidiscrete Petrov-Galerkin formulation that can be written in the format (5.1), whose consistent mass matrix $\mathbf{M}$ is not diagonal, but is, in some sense, "close" to the identity matrix. Specifically, its row-sum lumped mass preserved all polynomials up to degree p when used in a Galerkin projection. Consequently, the row-sum lumped mass matrix may be used in explicit dynamics without compromising higher-order spatial accuracy. In Fig. 5.1b, we anticipate the result of our isogeometric Petrov-Galerkin formulation with approximate dual basis functions and row-sum lumping for the classical example of the one-dimensional bar. We observe that the spectrum of our method maintains accuracy in the low and medium range of modes, which is a significant improvement over the standard IGA Galerkin formulation with mass lumping. We note that when the mass matrix is evaluated consistently without lumping, the two methods yield exactly the same spectrum shown in Fig. 5.1a.

We note that a similar approach is presented in [210]. It consists of a minimally invasive technique, based on approximate dual test functions, which can be applied in the sense of preconditioner by a simple matrix pre-multiplication. They show high-order convergent results and a straightforward application of Dirichlet boundary conditions by manipulating this transformation matrix. An additional row-summing step is required to convert the banded into a diagonal mass matrix.

The structure of our paper is as follows: In Section 5.2, we briefly review the definition and construction of approximate dual functions of B-splines. In addition, we present an iterative scheme for improving the approximate dual basis towards exactly satisfying bi-orthogonality. In Section 5.3, we derive our isogeometric Petrov-Galerkin formulation with mass lumping for higher-order accurate explicit dynamics. In Section 5.4, we present numerical examples of beam and plate problems, demonstrating that our Petrov-Galerkin scheme indeed preserves higher-order accuracy in explicit dynamics calculations. In Section 5.5, we provide a critical discussion of the potential significance of our results, highlight by means of a more involved shell benchmark that extending the demonstrated benefits to practical problems might not be immediate, and motivate potential future research directions.

5.2 Approximate dual spline basis

In this section, we briefly review the construction and the relevant properties of the approximate dual functions for univariate B-splines introduced in [131]. We also present an iterative algorithm to improve an approximate dual basis in terms of satisfying the bi-orthogonality constraint. We start this section with a brief recap of univariate B-splines and their dual bases.

5.2.1 B-spline basis functions

A B-spline function is a piecewise polynomial that is characterized by the polynomial degree, a given series of segments that we call Bézier elements, and the regularity at the interfaces of the Bézier elements. Let $\mathcal{P}^p$ denote the space of piecewise polynomials of degree $p \geq 0$ and consider a partitioning of an interval $\hat{\Omega} = [a,\, b] \subset \mathbb{R}$ into an increasing sequence of *breakpoints* that define Bézier elements:

$$a = t_0 < \ldots < t_{k-1} < t_k < \ldots < t_m = b\,. \tag{5.2}$$

Let $\mathbb{S}$ denote the space of C^{p-1} smooth splines that is:

$$\mathbb{S} := \left\{\, s : [a,\, b] \mapsto \mathbb{R} : s|_{t_{k-1},t_k} \in \mathcal{P}^p\,, s \text{ is } C^{p-1} \text{ smooth at } \hat{x} = t_1 \ldots t_{m-1} \,\right\}\,. \tag{5.3}$$

Consider B-spline functions B_i, $i = 1,\ldots,N$, of degree p with C^{p-1}-continuity defined on an open *knot vector*, $\Xi := \{\hat{x}_1,\, \ldots,\, \hat{x}_{N+p+1}\}$, which is the partition (5.2) with $p+1$ multiplicity of the first and last breakpoints and non-repeated internal knots. Such B-splines have interpolating end-conditions, reproduce polynomials in $\mathcal{P}^p$, and form a basis for $\mathbb{S}$. B-splines can for instance be defined recursively by using the Cox-de Boor formula [1]. They can be extended to multiple dimensions by constructing tensor products of univariate B-splines.

Remark 5.2.1. *In the current paper, we use B-spline functions with maximum smoothness of C^{p-1}. But dual basis functions, approximate dual basis functions and hence the explicit dynamics technology to be presented do not require maximum smoothness, but can also operate with B-splines of any continuity. In particular, the extension to (tensor-product) multi-patch discretizations seems straightforward.*

5.2.2 Dual basis functions

We consider the spline space $\mathbb{S}$ in (5.3) that is spanned by C^{p-1}-smooth B-splines of degree p, B_i, $i = 1, \ldots, N$, defined on an open knot vector $\boldsymbol{\Xi}$. Let $\hat{\Omega} \subset \mathbb{R}$ denote the parametric domain with local coordinates represented in $\boldsymbol{\Xi}$, i.e. the breakpoints in (5.2). Given an inner product $(\cdot, \cdot)_{\hat{\Omega}} : \mathbb{S} \times \mathbb{S} \mapsto \mathbb{R}$ in $\hat{\Omega}$. The functions $\bar{B}_i$, $i = 1, \ldots, N$, that satisfy the bi-orthogonality constraint:

$$\left(\bar{B}_i, B_j\right)_{\hat{\Omega}} = \delta_{ij}\,, \tag{5.4}$$

where δ_{ij} is the Kronecker delta, form the dual basis of $\mathbb{S}$, corresponding to the B-splines B_i.

Let $\mathbf{b} = \left[B_1 \ldots B_N\right]^T$ and $\bar{\mathbf{b}} = \left[\bar{B}_1 \ldots \bar{B}_N\right]^T$ denote the function vector of the B-spline basis B_i and its associated dual functions $\bar{B}_i$, respectively. The bi-orthogonality constraint (5.4) can then be expressed in matrix form:

$$\left(\bar{\mathbf{b}}\,\mathbf{b}\right)_{\hat{\Omega}} = \mathbf{I}\,, \tag{5.5}$$

where $\mathbf{I}$ is the identity matrix. We recall the Gramian matrix $\mathbf{G}$ of the B-spline basis:

$$\mathbf{G} = \left(\mathbf{b}\,\mathbf{b}\right)_{\hat{\Omega}}\,. \tag{5.6}$$

Equation (5.5) is now reformulated as:

$$\left(\bar{\mathbf{b}}\,\mathbf{b}\right)_{\hat{\Omega}} = \mathbf{I} = \mathbf{G}^{-1}\,\mathbf{G} = \mathbf{G}^{-1}\,\left(\mathbf{b}\,\mathbf{b}\right)_{\hat{\Omega}} \tag{5.7}$$

The dual functions $\bar{B}_i$, $i = 1, \ldots, N$ can then be formulated via the inverse of the Gramian matrix:

$$\bar{\mathbf{b}} = \mathbf{G}^{-1}\,\mathbf{b}\,. \tag{5.8}$$

These dual functions are linear combinations of the corresponding B-splines, thus span the same spline space $\mathbb{S}$, and also reproduce polynomials in $\mathcal{P}^p$. The duals (5.8) computed with the global Gramian matrix have global support and generally do not preserve the partition of unity and non-negativity properties of the associated B-splines. For illustration purposes, we plot quadratic C^1-continuous B-splines and their global dual functions (5.8) in Figs. 5.2a and b, respectively. For other possibilities to compute the global dual basis of spline spaces, we refer to [102], [211] and the references therein.

Alternatively, one can construct dual functions with the same minimal support as the corresponding B-splines [100], [104], [106], [107]. One approach is to compute the

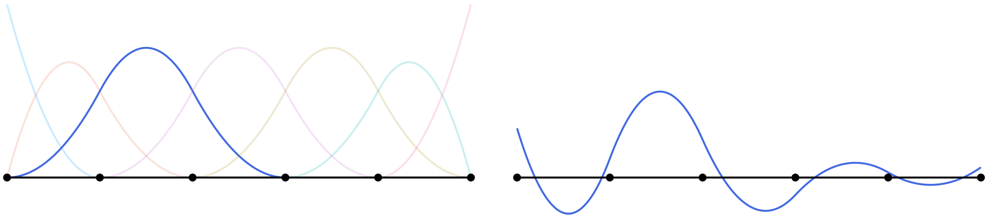

(a) C^1-continuous B-spline function.

(b) Associated C^1-continuous dual function, but with global support.

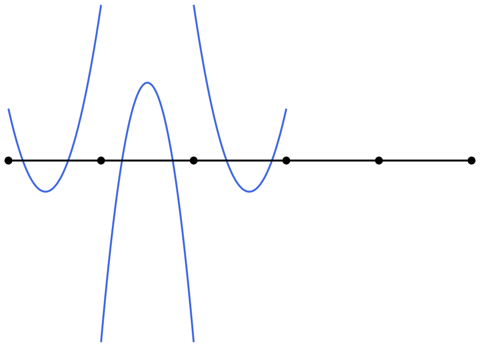

(c) Associated dual function with minimal support, but discontinuous.

Figure 5.2: Dual functions for a quadratic C^1-continuous B-spline function.

dual function of the Bernstein polynomials, using the inverse of the Gramian matrix for a Bézier element, and then to apply the Bézier extraction operator to obtain the dual of the B-spline basis [104], [107]. For illustration purposes, we plot a quadratic C^1-continuous B-spline function in Fig. 5.2a. We observe that while the global dual (5.8) is C^{p-1}-continuous, the dual basis with minimal support is discontinuous at the internal knots.

5.2.3 Approximate dual functions

In this paper, we consider approximate dual functions of B-splines originally introduced in [131]. Let $\hat{B}_i$, $i = 1, \ldots, N$, denote the approximate dual functions of C^{p-1}-continuous B-splines of degree p in the space $\mathbb{S} \subset \mathcal{P}^p$, and let $\hat{\mathbf{b}} = \left[\, \hat{B}_1 \;\ldots\; \hat{B}_N \,\right]^T$ be their function vector. The approximate dual functions $\hat{B}_i$ can again be constructed as linear combinations of the corresponding B-splines:

$$\hat{\mathbf{b}} = \hat{\mathbf{G}}^{-1}\,\mathbf{b}\,, \tag{5.9}$$

and thus span the same space $\mathbb{S}$ and reproduce polynomials in $\mathcal{P}^p$.

The approximate dual basis satisfies the bi-orthogonality constraint (5.5) “approximately”, in the sense that the matrix $\hat{\mathbf{G}}^{-1}$ is an approximate inverse of the Gramian matrix:

$$\hat{\mathbf{G}}^{-1} \approx \mathbf{G}^{-1} \,. \tag{5.10}$$

We note that the notation $\hat{\mathbf{G}}^{-1}$ is to imply that it is an approximate inverse. The approximate dual basis preserves important properties of the underlying B-spline basis, such as C^{p-1} regularity and local support. The construction of $\hat{\mathbf{G}}^{-1}$ does not require any matrix inversion, see [131] or the worked-out example in Appendix 5.A. It is a recursive computation, based on fundamental properties of B-splines such as the nestedness of spaces under knot insertion. For a 1D patch of splines, the approximate inverse matrix $\hat{\mathbf{G}}^{-1}$ is symmetric and positive definite with a bandwidth of at most $p+1$ [131].

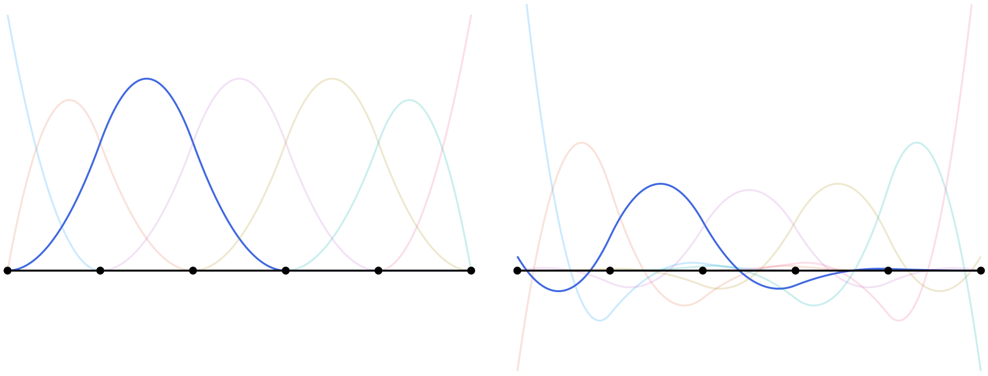

(a) C^1-continuous B-spline basis.

(b) Approximate dual basis.

Figure 5.3: Approximate dual functions for a quadratic C^1-continuous B-spline basis.

For illustration purposes, we plot the approximate dual functions (5.9) next to the corresponding quadratic C^1-continuous B-spline basis. We observe that the approximate dual functions preserve the C^{p-1}-continuity of the B-spline functions and have local support. Their support, however, is larger than that of the corresponding spline functions due to the band structure of $\hat{\mathbf{G}}^{-1}$.

Remark 5.2.2. *We note that in general, the approximate dual basis does not preserve the partition of unity and non-negativity properties of B-splines. Partition of unity, however, could be restored by scaling the approximate dual with the inverse of its function value sum.*

In this paper, we consider tensor-product extensions to multivariate dual B-spline functions. To this end, we use the same spline space $\mathbb{S}$ in every coordinate direction such that the multivariate spaces in the two-dimensional case is $\mathbb{S} \otimes \mathbb{S}$. In the parametric domain, the tensor-product structure leads to matrices with Kronecker structure due to affine mapping. We note that the approximate dual functions can also be extended to non-uniform rational B-splines (NURBS) as shown in [103].

5.2.4 An iterative approach for improving bi-orthogonality

We outline a method to iteratively improve the accuracy of the approximation (5.10) based on the predictor-multicorrector scheme introduced in [87]. We consider the linear system of equations:

$$\mathbf{G}\,\boldsymbol{u} = \boldsymbol{c}\,, \tag{5.11}$$

where $\boldsymbol{u}$ and $\boldsymbol{c}$ denote the vector of unknowns and a known right-hand side vector, respectively. Replacing the Gramian matrix $\mathbf{G}$ by an approximation $\hat{\mathbf{G}}$ with a simpler band structure leads to:

$$\hat{\mathbf{G}}\,\boldsymbol{u} = \boldsymbol{c}\,, \tag{5.12}$$

which can be iteratively solved to obtain a more accurate solution as follows:

$$\begin{cases} \boldsymbol{u}^{(0)} = \mathbf{0}\,, \\ \text{for } i = 0, \ldots, r \\ \quad \hat{\mathbf{G}}\,\Delta\,\boldsymbol{u}^{(i)} = \boldsymbol{c} - \mathbf{G}\,\boldsymbol{u}^{(i)} \\ \qquad \boldsymbol{u}^{(i+1)} = \boldsymbol{u}^{(i)} + \Delta\,\boldsymbol{u}^{(i)} \\ \text{end.} \end{cases} \tag{5.13}$$

Here, r denotes the number of iterations, which corresponds to the number of corrector passes, $r \geq 0$. This iterative scheme is based on the recurrence relation[1]:

$$\hat{\mathbf{G}}\,\boldsymbol{u}^{(i+1)} = \boldsymbol{c} - \mathbf{A}\,\hat{\mathbf{G}}\,\boldsymbol{u}^{(i)}\,, \tag{5.14}$$

where $\mathbf{A} = \mathbf{G}\,\hat{\mathbf{G}}^{-1} - \mathbf{I}$. Combining (5.13) and (5.14) results in:

$$\begin{aligned} \hat{\mathbf{G}}\,\boldsymbol{u}^{(r)} &= \boldsymbol{c} - \mathbf{A}\,\hat{\mathbf{G}}\,\boldsymbol{u}^{(r)} \\ &= \boldsymbol{c} - \mathbf{A}\left(\boldsymbol{c} - \mathbf{A}\,\hat{\mathbf{G}}\,\boldsymbol{u}^{(r-1)}\right) = \boldsymbol{c} - \mathbf{A}\boldsymbol{c} + \underbrace{\mathbf{A}\,\mathbf{A}}_{\mathbf{A}^2}\,\hat{\mathbf{G}}\,\boldsymbol{u}^{(r-1)} \\ &= \ldots = \left(\sum_{i=0}^{r}(-1)^i\,\mathbf{A}^i\right)\boldsymbol{c}\,. \end{aligned} \tag{5.15}$$

Here, $\mathbf{A}^i$ denotes the matrix $\mathbf{A}$ of power i, $i = 0, \ldots, r$. The matrix $\hat{\mathbf{G}}$ in the initial equation (5.12) can be then replaced by $\hat{\mathbf{G}}_r$:

$$\hat{\mathbf{G}}_r = \hat{\mathbf{G}}_r(r) := \left(\sum_{i=0}^{r}(-1)^i\,\mathbf{A}^i\right)^{-1}\hat{\mathbf{G}}\,, \tag{5.16}$$

---

[1] This relation appears in each loop of (5.13) when computing: $\hat{\mathbf{G}}\,\boldsymbol{u}^{(i+1)} = \hat{\mathbf{G}}\left(\boldsymbol{u}^{(i)} + \Delta\,\boldsymbol{u}^{(i)}\right) = \hat{\mathbf{G}}\,\boldsymbol{u}^{(i)} + \boldsymbol{c} - \mathbf{G}\,\boldsymbol{u}^{(i)} = \boldsymbol{c} - \left[\mathbf{G}\,\hat{\mathbf{G}}^{-1} - \mathbf{I}\right]\hat{\mathbf{G}}\,\boldsymbol{u}^{(i)} = \boldsymbol{c} - \mathbf{A}\,\hat{\mathbf{G}}\,\boldsymbol{u}^{(i)}$.

to obtain a more accurate solution for $\boldsymbol{u}$. Hence, $\hat{\mathbf{G}}_r$ is an improved approximation of the Gramian matrix $\mathbf{G}$.

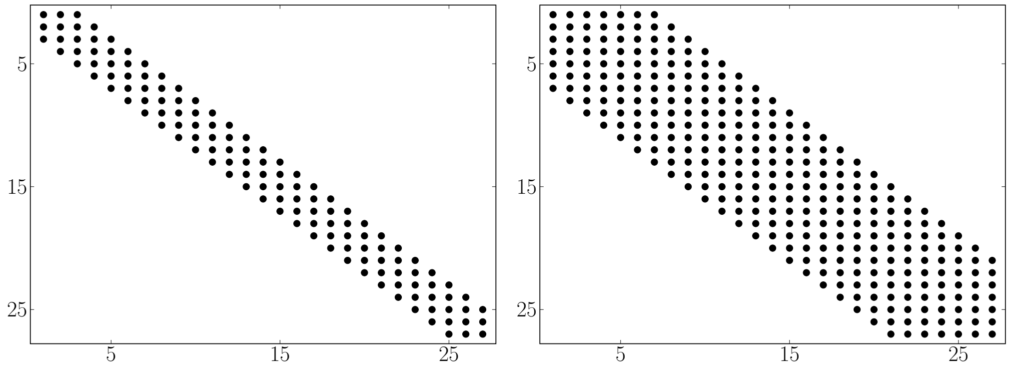

(a) $r = 0$, bandwidth = 2 (b) $r = 1$, bandwidth = 6

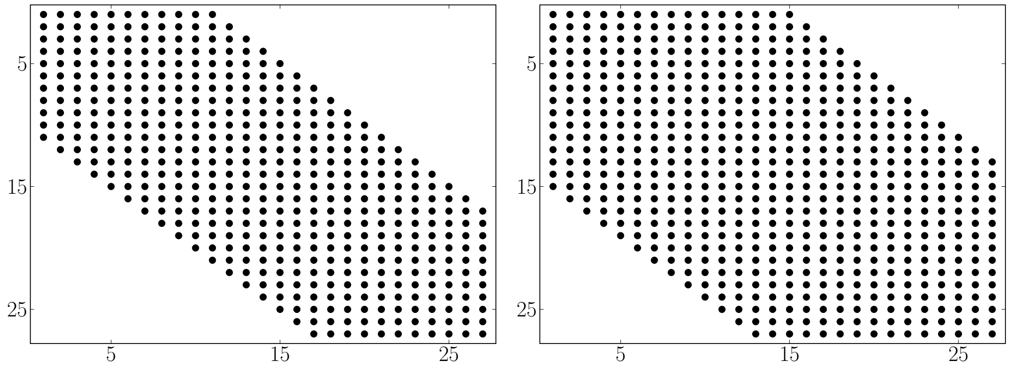

(c) $r = 2$, bandwidth = 10 (d) $r = 3$, bandwidth = 14

Figure 5.4: Structure of the approximate inverse $\hat{\mathbf{G}}_r^{-1}$ for increasing r, computed with (5.17), corresponding to the approximate dual basis of quadratic C^1-continuous B-splines in 1D on 25 Bézier elements.

p	$r = 0$		$r = 1$		$r = 2$	
	Bandwidth [−]	Support [elements]	Bandwidth [−]	Support [elements]	Bandwidth [−]	Support [elements]
2	2	7	6	11	10	15
3	3	10	9	16	15	22
4	4	13	12	21	20	29
5	5	16	15	26	25	36
p	p	$3p + 1$	$3p$	$5p + 1$	$p(2r + 1)$	$2pr + 3p + 1$

Table 5.1: Bandwidth of $\hat{\mathbf{G}}_r^{-1}$ and the support length of the approximate dual with different degrees p and numbers of iterations r.

We are interested in the approximate inverse $\hat{\mathbf{G}}_r^{-1}$:

$$\hat{\mathbf{G}}_r^{-1} = \hat{\mathbf{G}}_r^{-1}(r) := \hat{\mathbf{G}}^{-1}\left(\sum_{i=0}^{r}(-1)^i\,\mathbf{A}^i\right). \tag{5.17}$$

We note that for $r = 0$, $\hat{\mathbf{G}}_r^{-1} = \hat{\mathbf{G}}^{-1}$, i.e. no iteration is performed. On the one hand, increasing the number of iterations r increases the accuracy of the approximation $\hat{\mathbf{G}}_r^{-1} \approx \mathbf{G}^{-1}$. On the other hand, it increases the bandwidth of the iteratively improved approximate inverse $\hat{\mathbf{G}}_r^{-1}$, as illustrated in Fig. 5.4 for 1D quadratic B-splines, and hence also increasing the support of the corresponding approximate dual functions. We report the bandwidth of $\hat{\mathbf{G}}_r^{-1}$ and the maximum support of the improved approximate dual functions in terms of the Bézier elements as a function of p and r in Table 5.1. We emphasize that the computation of $\hat{\mathbf{G}}_r^{-1}$ does not require any matrix inversion and its notation is to imply that $\hat{\mathbf{G}}_r^{-1}$ is an approximate inverse of the Gramian matrix.

5.3 A Petrov-Galerkin formulation with higher-order accurate mass lumping

In this section, we motivate and describe an isogeometric Petrov-Galerkin scheme that employs standard B-splines as trial functions and the corresponding approximate dual functions as test functions. Due to the approximate bi-orthogonality of the two function spaces, it enables higher-order mass lumping via the standard row-sum technique. We discuss several further relevant aspects, such as maintaining bi-orthogonality on mapped domains, strong enforcement of boundary conditions, and computational cost in explicit dynamics.

5.3.1 Model problem: Kirchhoff plate

We consider the vibration of an undamped Kirchhoff plate given by the following fourth-order partial differential equation:

$$\rho\, d\, \ddot{u}(\boldsymbol{x},t) + \frac{E\,d^3}{12\,(1-\nu^2)}\,\Delta^2 u(\boldsymbol{x},t) = f(\boldsymbol{x},t)\,, \quad \boldsymbol{x}\in\Omega\,,\ t\in[0,T]\,, \tag{5.18}$$

with mass density ρ, plate thickness d, Young's modulus E, and Poisson's ratio ν. The spatial and time domains are given by Ω and T. To set up a well-defined initial boundary value problem, equation (5.18) needs to be complemented by suitable initial and boundary conditions. For ease of notation, we consider the case of a simply supported plate here. We thus have the following initial conditions at time $t = 0$:

$$u(\boldsymbol{x},0) = u_0(\boldsymbol{x})\,, \quad \dot{u}(\boldsymbol{x},0) = v_0(\boldsymbol{x})\,, \tag{5.19}$$

and the following boundary conditions:

$$u(\boldsymbol{x},t) = 0\,, \quad \nabla u(\boldsymbol{x},t)\cdot\boldsymbol{n} = 0 \quad \text{on } \Gamma\,, \tag{5.20}$$

where $\boldsymbol{n}$ is the outward unit normal to the boundary Γ.

Multiplying (5.18) by suitable test functions w, integrating over Ω, performing integration by parts twice, and substituting the boundary conditions (5.20) results in the following weak form: Find $u \in \mathcal{S}$ such that $\forall\, w \in \tilde{\mathcal{S}}$:

$$\rho\, d \int_\Omega \ddot{u}\, w \,\mathrm{d}\Omega + \frac{E\, d^3}{12\,(1-\nu^2)} \int_\Omega \Delta u\, \Delta w \,\mathrm{d}\Omega = \int_\Omega f\, w \,\mathrm{d}\Omega\,. \tag{5.21}$$

We assume the spaces $\mathcal{S}$ and $\tilde{\mathcal{S}}$ are sufficiently regular such that the Laplace operator Δ can be applied. In addition, we assume that all material and geometric parameters are constants.

Remark 5.3.1. *In the following sections, we will also present computational results for a straight Euler-Bernoulli beam and a Kirchhoff-Love shell. Based on the exposition for the Kirchhoff plate, we believe it is straightforward to extend our Petrov-Galerkin formulation to the one-dimensional beam and the three-dimensional shell. In the interest of conciseness of the exposition, we therefore do not repeat the derivation for these two models.*

5.3.2 Spatial discretization on geometrically mapped domains

The approximate dual basis is constructed such that the bi-orthogonality constraint is approximately satisfied in the parametric domain, see (5.9). The basis functions, however, need to be mapped from the parametric domain to the physical domain, and this mapping will not be affine in the general case. Discretizing the solution u and the test function w in (5.21) with standard B-splines and the original approximate dual functions (5.9), respectively, does not preserve the approximate bi-orthogonality in the physical domain.

To preserve the approximate bi-orthogonality in the physical domain, we discretize u with standard B-splines of degree p, $B_i(x)$, $i = 1, \ldots, N$, and w with modified approximate dual functions that are divided by the determinant of the Jacobian matrix of the mapping:

$$\tilde{B}_i(\hat{\boldsymbol{x}}) := \frac{\hat{B}_i(\hat{\boldsymbol{x}})}{C(\hat{\boldsymbol{x}})}\,, \qquad i = 1, \ldots, N\,. \tag{5.22}$$

Here, the function $C(\hat{\boldsymbol{x}})$ denotes the determinant of the Jacobian matrix. It corresponds to a geometry map $\Phi : \hat{\Omega} \to \Omega$ that maps a point $\hat{\boldsymbol{x}}$ from the parametric domain $\hat{\Omega}$ to a point $\boldsymbol{x}$ in the physical domain Ω. We assume that Φ is sufficiently smooth and invertible such that the Jacobian matrix and its inverse are well-defined.

The modified functions defined in (5.22) constitute the approximate dual basis of the standard B-spline basis in the physical domain Ω, where it approximately satisfies the bi-orthogonality constraint (5.5) in the same sense as the original approximate dual basis

(5.9) in the parametric domain $\hat{\Omega}$:

$$\begin{aligned}\left(\tilde{B}_i,\, B_j\right)_\Omega &= \int_\Omega \tilde{B}_i(\hat{\boldsymbol{x}})\, B_j(\hat{\boldsymbol{x}})\,\mathrm{d}\,\Omega = \int_{\hat{\Omega}} \frac{\hat{B}_i(\hat{\boldsymbol{x}})}{C(\hat{\boldsymbol{x}})}\, B_j(\hat{\boldsymbol{x}})\, C(\hat{\boldsymbol{x}})\,\mathrm{d}\,\hat{\Omega} \\ &= \int_{\hat{\Omega}} \hat{B}_i(\hat{\boldsymbol{x}})\, B_j(\hat{\boldsymbol{x}})\,\mathrm{d}\,\hat{\Omega} = \left(\hat{B}_i,\, B_j\right)_{\hat{\Omega}} . \end{aligned} \tag{5.23}$$

The modified functions $\tilde{B}_i$ are linearly independent due to the linear independence of the approximate dual functions $\hat{B}_i$ and preserve their local support. Their regularity, however, depends on the smoothness of the Jacobian $C(\hat{\boldsymbol{x}})$.

We are now in a position to discretize the weak form (5.18). To this end, we first write the discretized displacement solution u^h and the discretized test function w^h as:

$$\begin{aligned} u^h(\boldsymbol{x}, t) &= \left[B_1(\boldsymbol{x}) \; \ldots \; B_N(\boldsymbol{x})\right] \hat{\mathbf{u}}^h(t)\,, \\ w^h(\boldsymbol{x}) &= \left[\tilde{B}_1(\boldsymbol{x}) \; \ldots \; \tilde{B}_N(\boldsymbol{x})\right] \hat{\mathbf{w}}^h\,, \end{aligned}$$

where $\hat{\mathbf{u}}^h(t)$ and $\hat{\mathbf{w}}^h$ are the unknown time-dependent displacement coefficients and the coefficients of the discrete test function, respectively. The discrete trial space $\mathcal{S}^h$ and the discrete test space $\tilde{\mathcal{S}}^h$ are then:

$$\mathcal{S}^h := \operatorname{span}\left(B_i(\hat{\boldsymbol{x}})\right)_{i\in[1,\,N]}\,, \quad \tilde{\mathcal{S}}^h := \operatorname{span}\left(\tilde{B}_i(\hat{\boldsymbol{x}})\right)_{i\in[1,\,N]} = \operatorname{span}\left(\frac{\hat{B}_i(\hat{\boldsymbol{x}})}{C(\hat{\boldsymbol{x}})}\right)_{i\in[1,\,N]} . \tag{5.25}$$

The resulting semidiscrete formulation of (5.21) is: Find $u^h \in \mathcal{S}^h \subset \mathcal{S}$ such that $\forall\, w^h \in \tilde{\mathcal{S}}^h \subset \tilde{\mathcal{S}}$:

$$\rho\, d \int_\Omega \ddot{u}^h\, w^h\,\mathrm{d}\,\Omega + \frac{E\, d^3}{12\,(1-\nu^2)} \int_\Omega \Delta u^h\, \Delta w^h\,\mathrm{d}\,\Omega = \int_\Omega f\, w^h\,\mathrm{d}\,\Omega . \tag{5.26}$$

Figure 5.5 shows a one-dimensional example: $\mathcal{S}^h$ contains a standard quadratic B-spline patch, and $\tilde{\mathcal{S}}^h$ contains the corresponding modified approximate dual functions. For illustration purposes, we assume a geometric map based on a quarter circle with unit radius represented by NURBS. We also plot the corresponding non-constant function of the Jacobian determinant.

Remark 5.3.2. *In general, due to the Jacobian determinant* $C(\hat{\boldsymbol{x}})$ *in the denominator, the approximate dual functions* (5.22) *span a different space as the corresponding B-splines. Therefore,* $\mathcal{S}^h$ *and* $\tilde{\mathcal{S}}^h$ *represent two different spaces. Hence, the semidiscrete formulation* (5.26) *is in general a Petrov-Galerkin formulation. Only in the special case of a constant Jacobian determinant, the modified approximate dual function functions* (5.22) *span the same space as the original approximate dual functions* (5.9)*, since they are only scaled by a constant factor, and thus* (5.26) *falls back to a Galerkin formulation.*

Remark 5.3.3. *The differential operators in* (5.26) *require the following derivatives of*

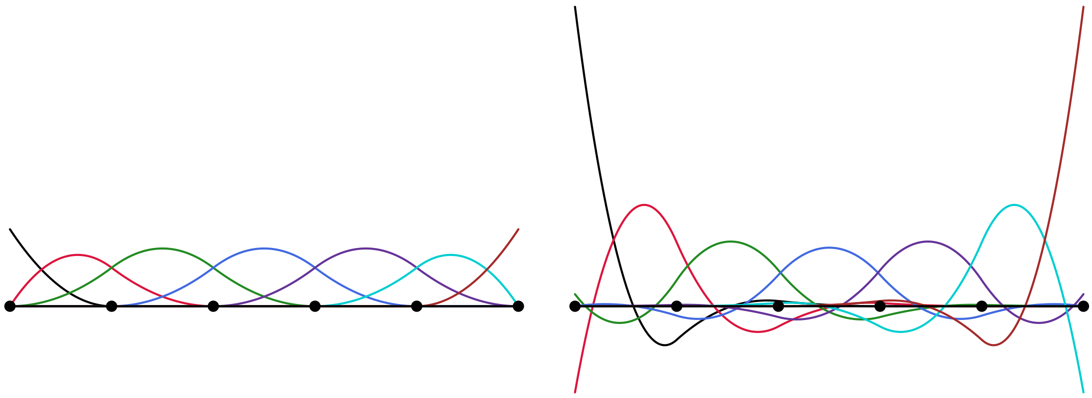

(a) $\mathcal{S}^h := \operatorname{span}\left(B_i(\hat{x})\right)_{i\in[1,7]}$

(b) $\tilde{\mathcal{S}}^h := \operatorname{span}\left(\frac{\hat{B}_i(\hat{x})}{C(\hat{x})}\right)_{i\in[1,7]}$

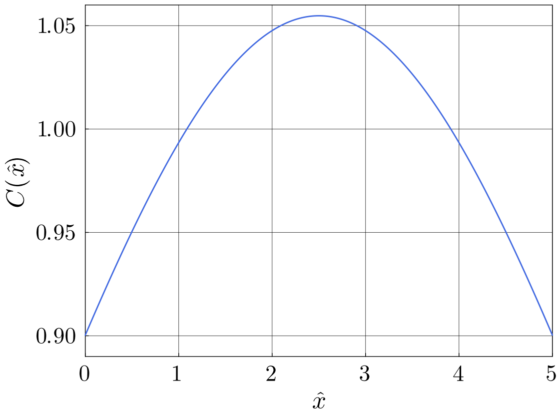

(c) Jacobian determinant function for a quarter circle.

Figure 5.5: Petrov-Galerkin discretization in space: discrete trial space $\mathcal{S}^h$ of standard B-splines and discrete test space $\tilde{\mathcal{S}}^h$ of modified approximate dual functions for a 1D patch of quadratic B-splines and a non-constant Jacobian determinant.

the modified approximate dual functions (5.22)*:*

$$\tilde{B}_{i,\alpha} = \left(\frac{\hat{B}_i}{C}\right)_{,\alpha} = \frac{1}{C}\,\hat{B}_{i,\alpha} - \frac{1}{C^2}\,\hat{B}_i\,C_{,\alpha}\,, \tag{5.27a}$$

$$\tilde{B}_{i,\alpha\beta} = \left(\frac{\hat{B}_i}{C}\right)_{,\alpha\beta} = \frac{1}{C}\,\hat{B}_{i,\alpha\beta} - \frac{1}{C^2}\,\hat{B}_{i,\alpha}\,C_{,\beta} - \frac{1}{C^2}\,\hat{B}_{i,\beta}\,C_{,\alpha} - \frac{1}{C^3}\,\hat{B}_i\,\left(C_{,\alpha\beta}\,C - 2C_{,\alpha}\,C_{,\beta}\right)\,. \tag{5.27b}$$

For the plate model considered here, the indices α *and* β *take values* $1, 2$ *and the notation* $(\cdot)_{,\alpha}$ *denotes the derivative with respect to the* α^{th} *Cartesian coordinate.*

5.3.3 Higher-order accurate mass lumping scheme

In the following, we again use of the following vector notation: $\tilde{\mathbf{b}} = \begin{bmatrix} \tilde{B}_1 \ldots \tilde{B}_N \end{bmatrix}^T$ is the vector of modified approximate dual functions, and $\hat{\mathbf{b}}$ and $\mathbf{b}$ the corresponding vectors of approximate dual functions and B-splines, respectively. Moving towards explicit dynamics, we now rethink the semidiscrete variational formulation (5.5) in the format (3.9a), bringing its second term on the right-hand side. Focusing on the left-hand side, we find the following (consistent) mass matrix $\mathbf{M}$:

$$\mathbf{M} = \rho\, d \int_{\Omega} \tilde{\mathbf{b}}\, \mathbf{b}^T \,\mathrm{d}\,\Omega = \rho\, d \int_{\hat{\Omega}} \frac{\hat{\mathbf{b}}}{C(\hat{\boldsymbol{x}})}\, \mathbf{b}^T\, C(\hat{\boldsymbol{x}}) \,\mathrm{d}\,\hat{\Omega} = \rho\, d \int_{\hat{\Omega}} \hat{\mathbf{b}}\, \mathbf{b}^T \,\mathrm{d}\,\hat{\Omega}\,. \tag{5.28}$$

integrated over the physical domain Ω and the parametric domain $\hat{\Omega}$. Employing (5.9) leads to:

$$\mathbf{M} = \rho\, d\, \hat{\mathbf{G}}^{-1} \int_{\hat{\Omega}} \mathbf{b}\, \mathbf{b}^T \,\mathrm{d}\,\hat{\Omega} = \rho\, d\, \hat{\mathbf{G}}^{-1}\, \mathbf{G} \;=\; \rho\, d\, \hat{\mathbf{I}}\,, \tag{5.29}$$

and hence to the following semidiscrete form of our model problem:

$$\rho\, d\, \hat{\mathbf{I}}\, \ddot{\boldsymbol{u}}^n \;=\; \mathbf{F}^n_{\text{ext}} \;-\; \int_{\Omega} \boldsymbol{B}(\boldsymbol{x}^n)^T\, \boldsymbol{\sigma}^n \,\mathrm{d}\Omega\,, \tag{5.30}$$

where the mass matrix, due to (5.5), corresponds to an approximation of the identity matrix, $\hat{\mathbf{I}} \approx \mathbf{I}$, scaled by a scalar that corresponds for our model problem to the density ρ times the thickness d of the plate. The approximation $\hat{\mathbf{I}}$, however, is not diagonal, and hence precludes efficient explicit dynamics, when e.g. a central difference scheme in time is applied to (5.30).

Our central idea to enable efficient higher-order accurate explicit dynamics based on (5.30) is simple: we apply standard row-sum mass lumping to diagonalize the approximate identity matrix $\hat{\mathbf{I}}$. It is straightforward to show that this leads in fact to the identity matrix $\mathbf{I}$.

Theorem: The application of row-sum lumping to the matrix $\left(\hat{B}_i,\, B_j\right)_{\hat{\Omega}}$ yields the identity matrix.

Proof: Let $P \in \mathcal{P}^p$ be a polynomial of degree p in the parametric domain $\hat{\Omega}$, and consider the spline basis B_i, $i = 1, \ldots, N$ and its approximate dual basis $\hat{B}_i$. There exists a set of coefficients u_i such that:

$$\left(\hat{B}_i,\, B_j\right)_{\hat{\Omega}}\, u_j = \left(\hat{B}_i,\, P\right)_{\hat{\Omega}}\,. \tag{5.31}$$

The spline basis B_i reproduces polynomials $P \in \mathcal{P}^p$, i.e. $\sum_{j=1}^{N} B_j\, u_j = P$. If $f = 1$, $u_j = 1$ due to the partition of unity $\sum_{j=1}^{N} B_j(\hat{x}) = 1$. We thus obtain:

$$\left(\hat{B}_i,\, B_j\right)_{\hat{\Omega}}\, 1 = \left(\hat{B}_i,\, 1\right)_{\hat{\Omega}} = 1\,. \tag{5.32}$$

Our hypothesis is that the effect of row-sum lumping does not preclude higher-order accuracy, as $\hat{\mathbf{I}}$ is already close to the true identity matrix, which is of course diagonal. We will show by way of numerical examples that this is indeed the case.

5.3.4 Computational cost

The computational cost in explicit dynamics primarily depends on the critical time step size, the number of quadrature points, and the evaluation of the internal force vector per quadrature point. We expect that the first two aspects do not differ significantly between the isogeometric Galerkin method and our isogeometric Petrov-Galerkin method. In this context, we refer to outlier removal techniques to prevent prohibitively small critical time steps [121], [122], [183] and to advanced quadrature schemes for spline discretizations that significantly reduce the number of quadrature points with respect to standard Gauss quadrature per Bézier element [133], [171], [212].

The cost of the evaluation of the internal force vector requires a more detailed analysis. Just as standard B-splines (or NURBS), the modified approximate dual basis functions can be cast into a Bézier or Lagrange extraction format per element [213], [214], whose derivation from relation (5.10) and the appoximate inverse of the Gramian matrix is straightforward. The extraction operators can be computed in an offline step, such that they do not contribute to the online cost of explicit dynamics calculations. In a Petrov-Galerkin sense, bilinear stiffness forms are not symmetric, as we are using different test and trial functions on the right-hand side. In explicit dynamics, this is not an issue per se, as the stiffness matrix is never assembled, stored, or inverted. The central difference to the standard Galerkin scheme, however, is that the support of the modified approximate dual functions is larger than the one of the standard B-splines (or NURBS). According to Table 5.1, the support of an approximate dual function is up to $3p+1$ Bézier elements in each parametric direction, as compared to $p+1$ for the corresponding B-spline. For

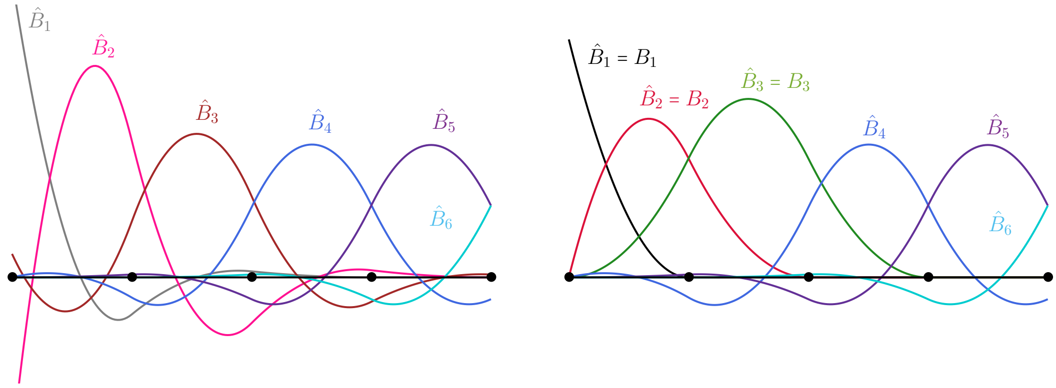

(a) Patch of approximate dual functions.

(b) Boundary functions replaced by B-splines.

Figure 5.6: Replacing approximate dual functions with support at a boundary with interpolatory B-splines, illustrated here for one end of a quadratic B-spline patch, recovers the ability to strongly impose Dirichlet constraints.

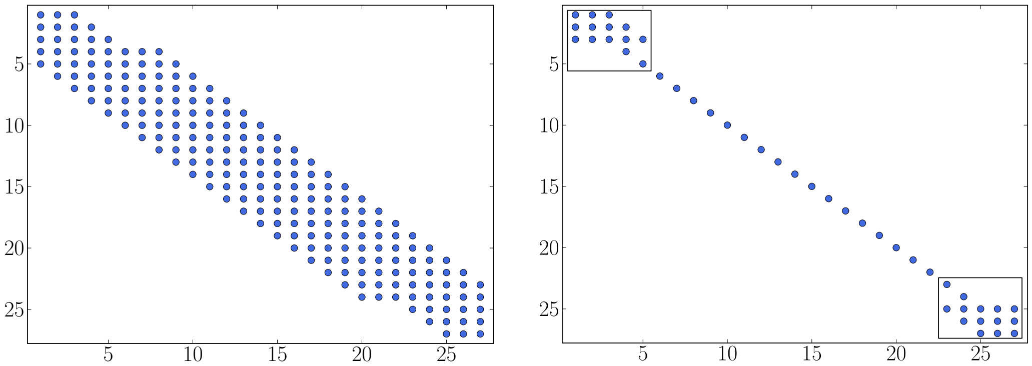

(a) Consistent mass matrix. (b) (Partially) Lumped mass matrix.

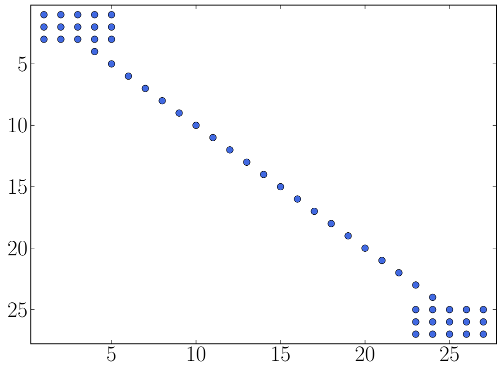

(c) Inverse of the (partially) lumped mass matrix.

Figure 5.7: Population of the consistent mass matrix, (partially) lumped mass matrix and its inverse for our Petrov-Galerkin scheme for an Euler-Bernoulli beam problem, discretized by quadratic splines on 25 Bézier elements.

two-dimensional elements, such as plates or shells, due to the increased support of the basis functions of the discrete test space, the internal force vector has eight to nine times as many entries, and we have to expect approximately eight to nine times as many basis function related operations to compute it. In practical scenarios, computationally costly routines to take into account nonlinear material behavior, such as radial return algorithms in plasticity, do not depend on the cost or number of the basis functions of the discrete test space, and hence the net increase in computational cost per quadrature point will be much lower. It remains to be seen how our Petrov-Galerkin scheme can be implemented in a competitive fashion and how much this disadvantage in computational cost then really matters in comparison with its advantage in accuracy.

5.3.5 Imposition of Dirichlet boundary conditions

In general, the approximate dual basis (5.22) does not preserve the interpolatory ends of the underlying B-spline basis. To enable the strong imposition of Dirichlet boundary conditions, we recover the interpolatory ends by simply replacing the original approximate dual functions with support at the Dirichlet boundary by the corresponding interpolatory B-splines. Figure 5.6 illustrates this simple idea for one end of a quadratic B-spline patch.

Figure 5.7 illustrates the structure of the resulting mass matrix **M** for an Euler-Bernoulli beam model computed with our Petrov-Galerkin scheme, where we use a 1D patch of quadratic basis functions and their corresponding approximate dual functions. Figure 5.7a shows the consistent mass matrix that approximates a diagonal matrix, but still exhibits the full bandwidth of non-zero entries according to Table 1. Figure 5.7b shows the non-zero entries of **M** after row-sum lumping. We note that for now, we employ the row-sum technique only in those rows that associate to approximate dual functions $\hat{B}_j$ in order not to jeopardize full accuracy of the Petrov-Galerkin scheme. In turn, a few rows that associate to interpolatory B-spline functions with support on the Dirichlet boundary remain "unlumped", as illustrated in Fig. 5.7b for our 1D example. Hence, we only require the inversion of small blocks, which limits requirements on computational and memory resources. The block structure of the inverse mass matrix is illustrated in Fig. 5.7c.

Remark 5.3.4. *If one wants to keep the modified approximate dual functions at the boundary to maintain a fully diagonal mass matrix without the need for any inversion operations or associated memory storage, one can resort to imposing Dirichlet boundary conditions weakly, for instance via the penalty method [40], [208] or Nitsche's method [215]–[217].*

5.4 Numerical examples

In this section, we demonstrate the favorable numerical behavior of our Petrov-Galerkin scheme. We will consider both explicit dynamics calculations and spectral analysis results, obtained for B-spline discretizations of degrees $p = 2$ through $p = 5$. In particular, we will compare the performance of our Petrov-Galerkin scheme with the standard isogeometric Galerkin method based on a consistent or row-sum lumped mass matrix.

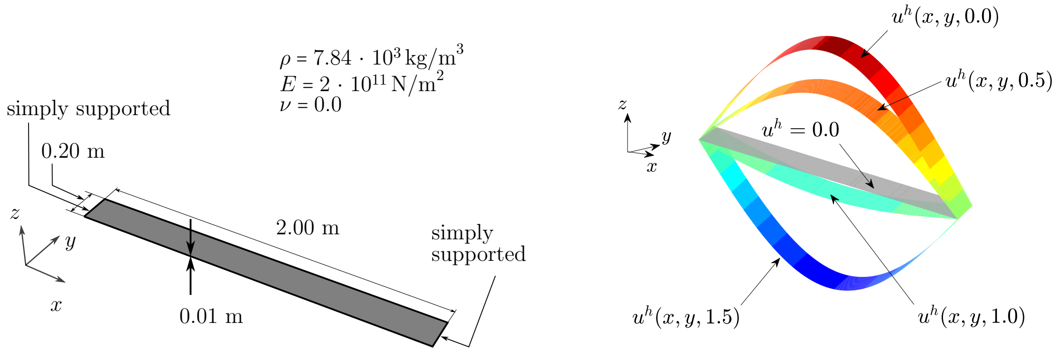

(a) Beam-like plate model

(b) Displacement snapshots

Figure 5.8: Set-up of the simply supported beam benchmark.

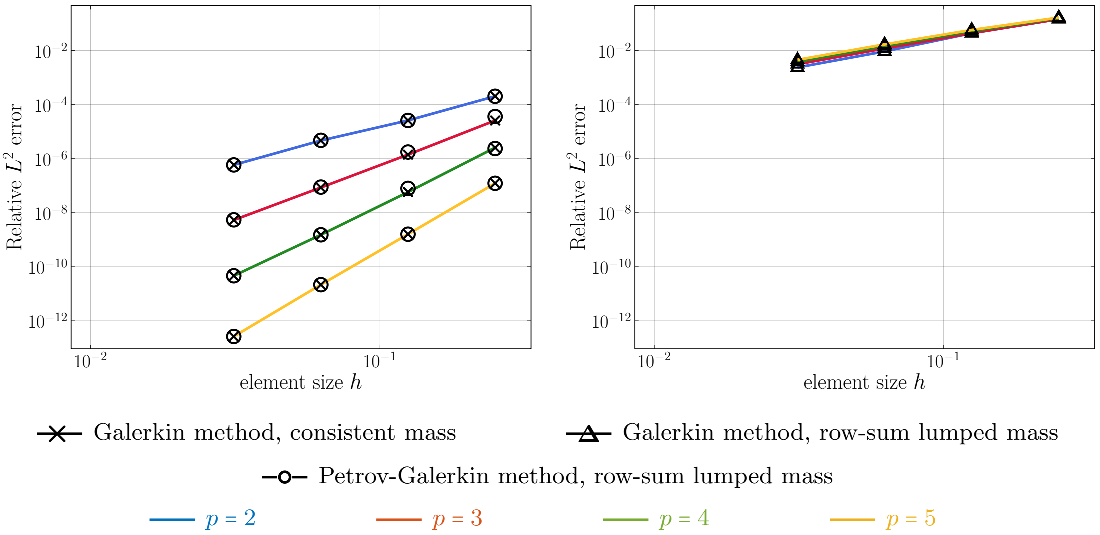

Figure 5.9: Beam-like plate: convergence of the relative L^2 error in the displacement solution at $t = 1.5$ s.

5.4.1 Simply supported beam

Our first example is the explicit dynamics calculation of a freely vibrating simply supported steel beam, which is modeled as a stretched Kirchhoff plate as illustrated in Fig. 5.8a. We assume the following analytical solution:

$$u(x, y, t) = \sin\left(\pi \frac{x}{L_x}\right) \cos\left(\left(\frac{\pi}{L_x}\right)^2 \sqrt{\frac{EI}{\rho A}}\, t\right), \tag{5.33}$$

where L_x, I and A are the longitudinal length, the moment of inertia, and the cross section area, respectively. From (5.33), we can also derive the initial and boundary conditions. We perform uniform mesh refinement in x-direction with 8, 16, 32, 64 Bézier elements, while we use one Bézier element in y-direction. We apply the central difference method [66] for explicit time integration, simulating the first 1.5 s of the vibration history. To guarantee that the time integration error is very small, we choose the following order-dependent time step size: $\Delta t = (p/\,(2\, n_{ele}))^p$ [122], [183]. Figure 5.8b illustrates the solution for quadratic splines and 16 Bézier elements at three different snapshots in time.

Figure 5.9 illustrates the convergence behavior of the relative L^2 error for the standard Galerkin method with consistent mass matrix (crosses), the standard Galerkin method with row-sum lumped mass matrix (triangles), and our Petrov-Galerkin method with lumped mass matrix (circles). On the one hand, we observe that our approach achieves the same optimal accuracy under mesh refinement as the Galerkin method with consistent mass matrix. Thus, the accuracy of our Petrov-Galerkin method based on test functions discretized by approximate dual functions is not affected by row-sum lumping.

On the other hand, we observe that the accuracy of the Galerkin method is significantly affected by row-sum lumping, limiting convergence to a maximum of second order irrespective of the polynomial degree of the spline basis.

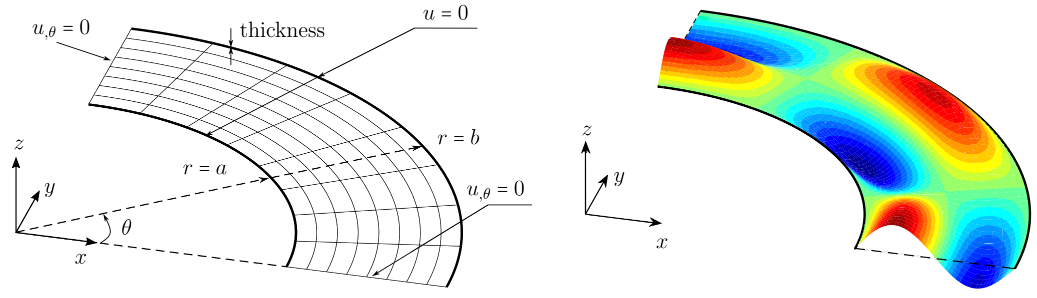

(a) Coarsest Bézier mesh with boundary conditions.

(b) Initial displacement field $u(r, \theta, 0)$.

Figure 5.10: Set-up of the annular plate benchmark.

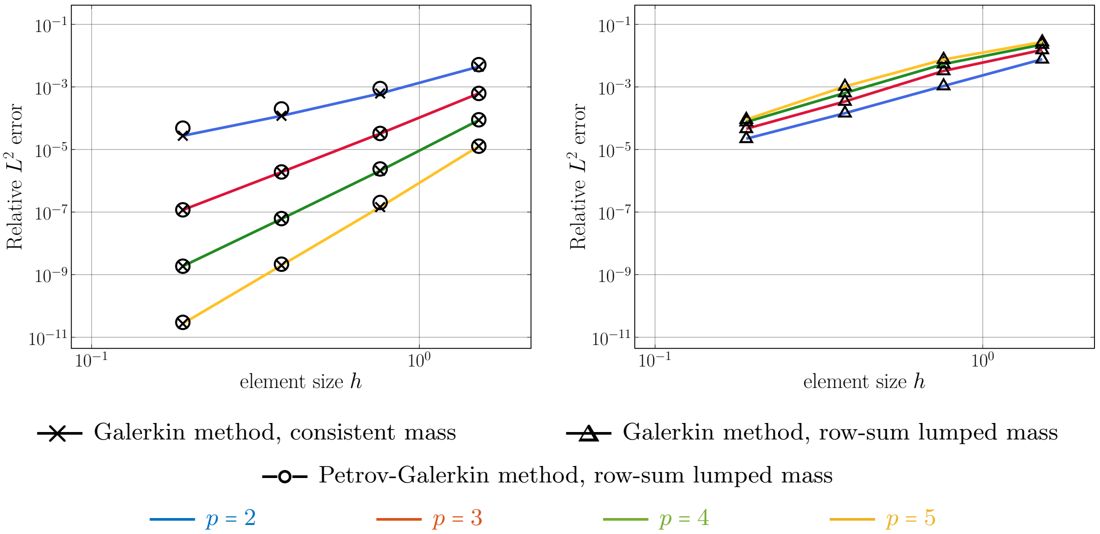

Figure 5.11: Annular plate: convergence of the relative L^2 error in the displacement solution at $t = 0.6$ s.

5.4.2 Annular plate

We now consider a quarter of a freely vibrating annular steel plate. Its set-up is illustrated in Fig. 5.10a, with thickness $d = 0.01$ m, Young's modulus $E = 2 \cdot 10^{11}\,\mathrm{N/m^2}$, Poisson's ratio $\nu = 0.0$, and mass density $\rho = 7.84 \cdot 10^3\,\mathrm{kg/m^3}$. It is simply supported along both the inner radius $r = a$ and the outer radius $r = b$. We construct the following analytical solution in polar coordinates $(r,\,\theta)$:

$$u(r,\theta,t) \;=\; J_4(r)\,\cos(4\,\theta)\,\cos\left(\sqrt{\frac{E\,d^3}{12\,(1-\nu^2)\,\rho\,d}}\,t\right), \tag{5.34}$$

where $J_4(r)$ denotes the 4th Bessel function of the first kind. We choose the second and fourth positive zeros of $J_4(r)$ as the inner and outer radii of the annulus, i.e., $a = \lambda_2 \approx 11.065$ and $b = \lambda_4 \approx 17.616$. The analytical solution (5.34) at time $t = 0$, plotted in Fig. 5.10b, represents the initial displacement field. We perform uniform mesh refinement in both radial and angular directions, using 8, 16, 32, and 64 Bézier elements. We again apply the central difference method for time integration with the same time step estimate as above.

We focus on the accuracy in space at time $t = 0.6$ s. Figure 5.11 shows the convergence behavior of the relative L^2 error for the standard Galerkin method with consistent mass matrix (crosses), the standard Galerkin method with row-sum lumped mass matrix (triangles), and our Petrov-Galerkin method with lumped mass matrix (circles). The results again confirm that our approach achieves the same optimal accuracy under mesh refinement as the Galerkin method with consistent mass matrix, whereas the accuracy of the Galerkin method is significantly affected by row-sum lumping, limiting convergence to second order irrespective of the polynomial degree of the spline basis.

5.4.3 Spectral analysis

We now use the tool of spectral analysis to elucidate the impact of lumping on the three different schemes. To this end, we recall the discrete eigenvalue problem corresponding to the semidiscrete formulation (5.26), expressed in matrix form:

$$\mathbf{K}\,\mathbf{U}_n^h \;=\; \lambda_n^h\,\mathbf{M}\,\mathbf{U}_n^h\,, \tag{5.35}$$

where $\mathbf{U}_n^h$ denotes the vector of unknown coefficients corresponding to the n^{th} discrete eigenmode U_n^h, and λ_n^h is the n^{th} discrete eigenvalue. For further details on spectral analysis and eigenvalue analysis in this context, we refer for instance to our previous papers on the topic [122], [135], [183] and the references therein.

Petrov-Galerkin vs. standard Galerkin formulations

We first consider the free transverse vibration of an unconstrained straight Euler-Bernoulli beam with the following parameters (steel, rectangular cross section): length 1.0 m, width 0.1 m, thickness 0.01 m, Young's modulus $E = 2 \cdot 10^{11}\,\text{N/m}^2$, and mass density $\rho = 7.84 \cdot 10^3\,\text{kg/m}^3$. We can obtain the exact solution in terms of eigenvalues and mode shapes from the continuous problem, given for instance in [174].

We solve the discrete eigenvalue problem (5.35) by discretizing the beam with 500 Bézier elements. We then employ our Petrov-Galerkin formulation discussed above, using B-splines and the corresponding approximate dual functions, and the standard Galerkin

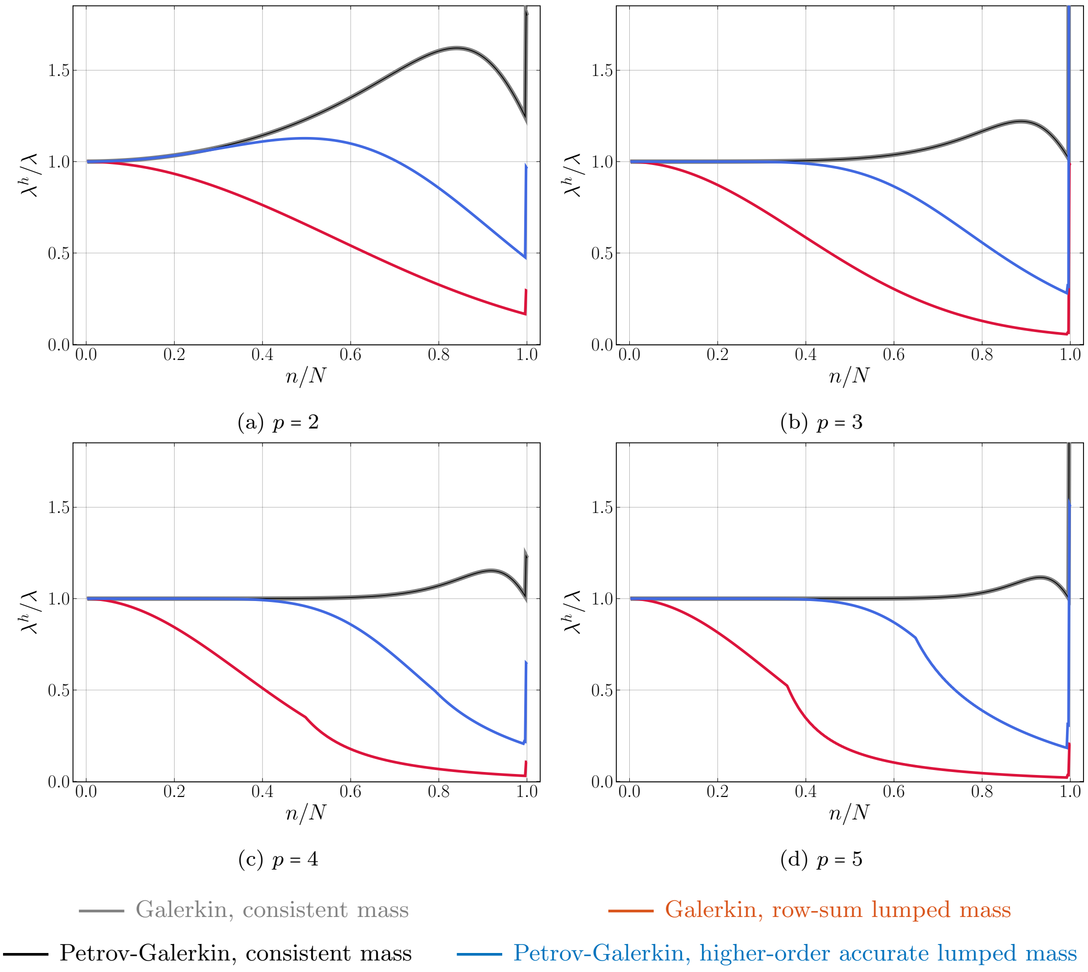

(a) $p = 2$

(b) $p = 3$

(c) $p = 4$

(d) $p = 5$

Figure 5.12: Normalized eigenvalues of a freely vibrating beam, computed on 500 Bézier elements.

formulation, using only B-splines, all for degrees $p = 2$ through 5. We then do the analysis of each formulation once with a consistent mass matrix and once with a lumped mass matrix based on the row-sum technique. Figure 5.12 plots the eigenvalues of the discrete problem in ascending order, normalized with respect to the corresponding exact eigenvalues of the continuous problem versus the normalized mode number. Figure 5.13 plots the relative L^2 error in the corresponding mode shapes, versus the normalized mode number.

We observe in all plots that the eigenvalues and mode shape errors obtained with the Petrov-Galerkin and Galerkin methods and a consistent mass matrix are identical. The reason behind this observation is that in the current example, due to the constant determinant of the Jacobian matrix, the modified approximate dual functions span the same space as the B-splines, and hence both methods need to produce the same results, when the variational formulations are evaluated and solved consistently. We now focus on the results obtain with mass lumping. In Fig. 5.12, we observe that our Petrov-Galerkin ap-

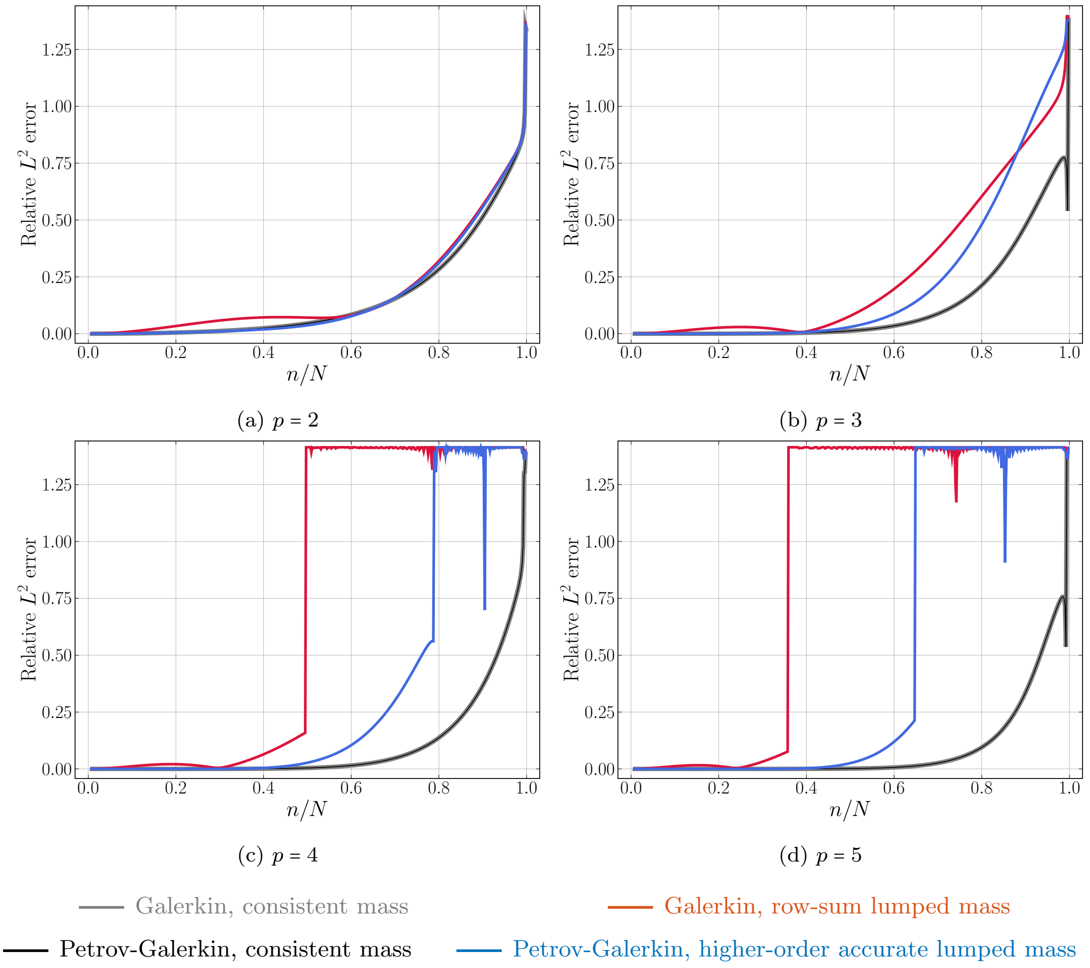

(a) $p = 2$

(b) $p = 3$

(c) $p = 4$

(d) $p = 5$

Figure 5.13: Relative L^2 error of the mode shapes of a freely vibrating beam, computed on 500 Bézier elements.

proach with lumped mass matrix leads to significantly better spectral accuracy compared to the standard Galerkin approach with lumped mass matrix. The difference between the results of the two approaches becomes more pronounced with increasing polynomial degree. For $p = 5$, for instance, we see that in our Petrov-Galerkin approach, the first 40% of the eigenvalues are close to the desired ratio of 1.0, whereas in the Galerkin approach, this is achieved by only about 5%. Figure 5.13 indicates the same trend for the error in the corresponding mode shapes. We can observe, however, that for $p = 2$, all methods, whether consistent or lumped, produce practically the same error, and a clear difference between the two methods with lumped mass matrices starts to be evident only for $p = 4$ and $p = 5$.

We then investigate the convergence of the error under mesh refinement, focusing on the tenth eigenvalue and eigenmode. We note that the lowest eigenmodes are particularly important for achieving accurate results in space. Figure 5.14 illustrates the

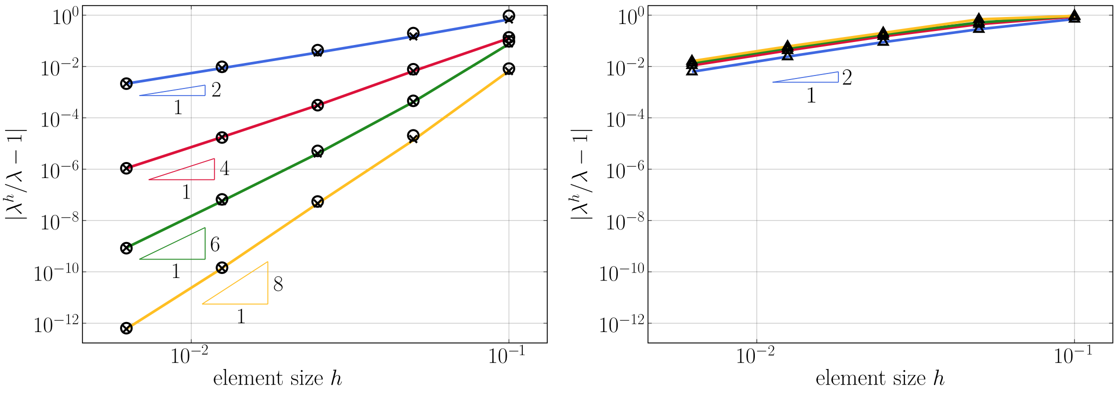

(a) Eigenvalue λ_{10}^h.

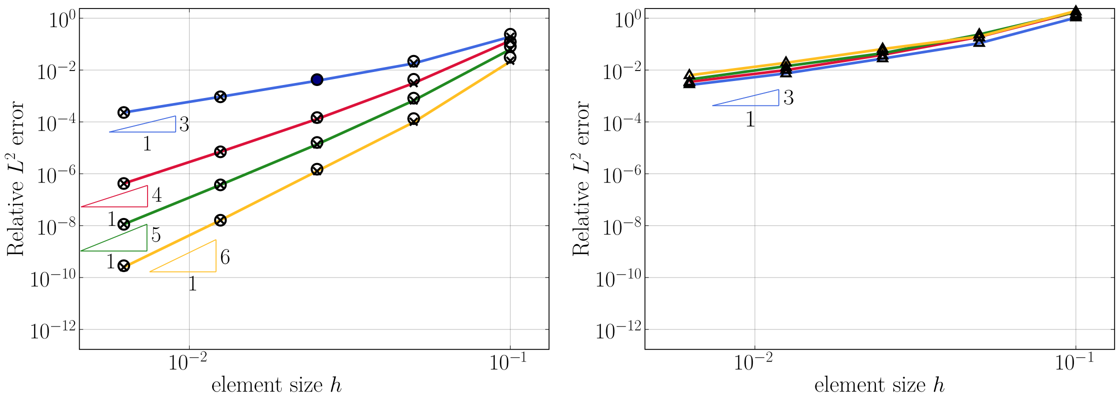

(b) Mode shape U_{10}^h.

Figure 5.14: Convergence of the relative L^2 error in the tenth eigenvalue and mode shape of a freely vibrating beam, computed on 500 Bézier elements.

convergence of the relative error of the eigenvalue (upper row) and the convergence of the L^2 error in the corresponding mode shape (lower row). We observe that the Petrov-Galerkin method with mass lumping achieves the same optimal convergence as the Galerkin method with consistent mass matrix, while the Galerkin method with mass lumping only achieves second-order convergence for all polynomial degrees. We note that the optimal convergence rate of the eigenvalue error and the L^2 error in the mode is $\mathcal{O}(2(p-1))$ and $\mathcal{O}(p+1)$, respectively [43], [66]. These results indicate that unlike in the standard Galerkin method, mass lumping in our Petrov-Galerkin method does not affect optimal convergence of analysis results.

We now investigate how these results transfer to the two-dimensional case. To this end, we repeat the same analysis for the example of a simply supported Kirchhoff plate with

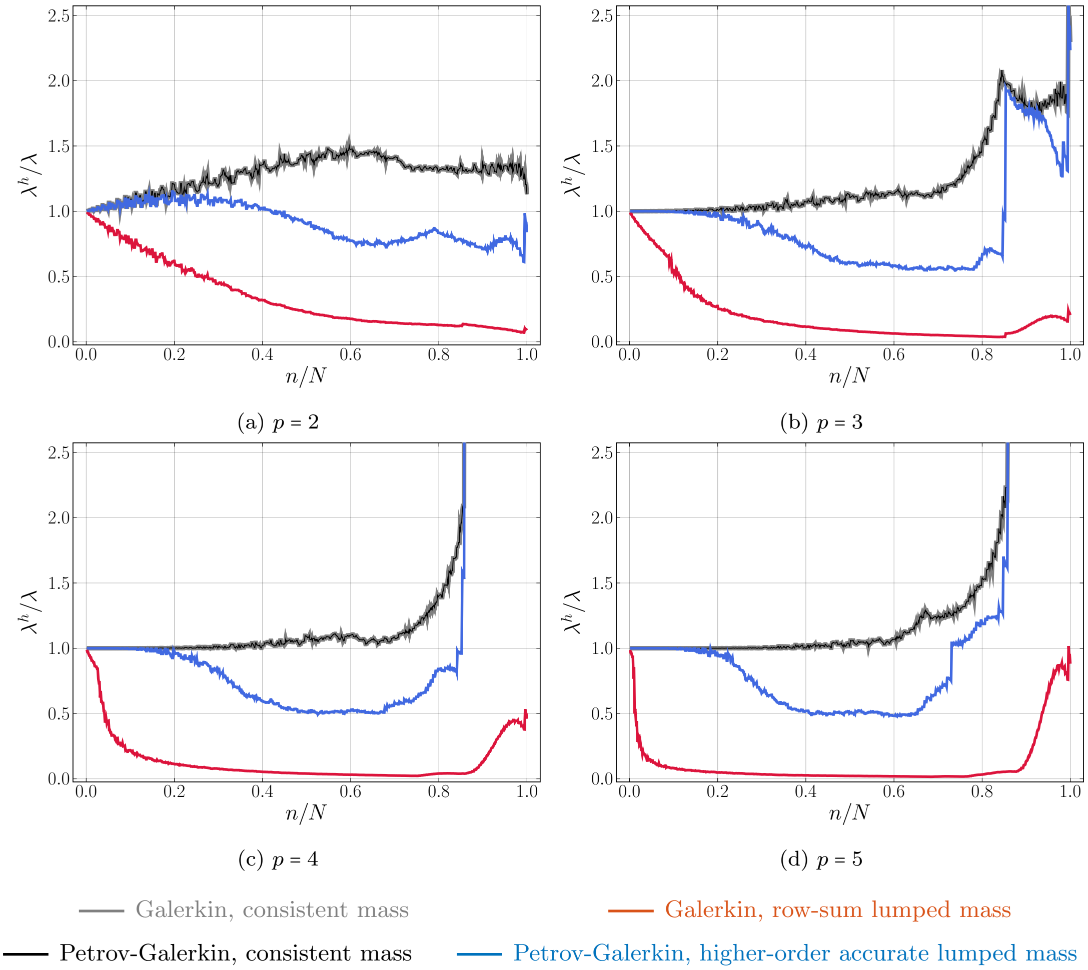
(a) $p = 2$

(b) $p = 3$

(c) $p = 4$

(d) $p = 5$

Figure 5.15: Normalized eigenvalues of a freely vibrating simply supported plate, computed on 25×25 Bézier elements.

the following parameters (square aluminium sheet): length and width 1.0 m, thickness 0.01 m, Young's modulus $E = 7 \cdot 10^{10}\ \mathrm{N/m^2}$, and mass density $\rho = 2.7 \cdot 10^3\ \mathrm{kg/m^3}$. We can obtain the exact solution in terms of eigenvalues and mode shapes from the continuous problem, given for instance in [174]. For the discrete problem (5.35), we consider meshes with 25×25 Bézier elements of degrees $p = 2$ to 5.

Figure 5.15 plots the normalized eigenvalues versus the normalized mode number. We note that some outliers at the end of the spectra lie outside the plotted range. Figure 5.16 plots the convergence of the relative error of the first eigenvalue under uniform mesh refinement. In Fig. 5.15, we can observe again significant accuracy advantages of our Petrov-Galerkin scheme with mass lumping over the standard Galerkin scheme with mass lumping in the spectrum results. Figure 5.15 confirms our observation that unlike in the standard Galerkin method, mass lumping does not affect the optimal convergence of our Petrov-Galerkin method.

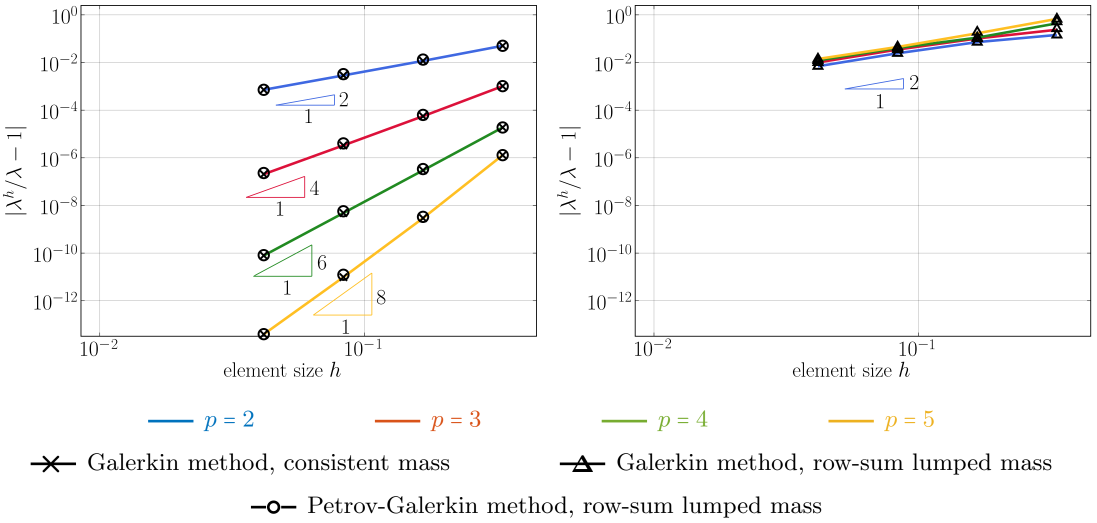

Figure 5.16: Convergence of the relative error in the first eigenvalue of a freely vibrating simply supported plate.

Iterative improvement of bi-orthogonality

To further elucidate the accuracy of our Petrov-Galerkin scheme based on approximate dual functions and mass lumping, we use the iterative approach discussed in Section 5.2.4 to gradually improve the bi-orthogonality property of the approximate dual basis. To this end, we consider again the two examples of the unconstrained Euler-Bernoulli beam in 1D and the simply supported square plate in 2D. We now employ our Petrov-Galerkin scheme with an iteratively improved mass matrix, where we use one or two corrector passes ($r = 1, 2$) before mass lumping, and compare the corresponding spectral results to those obtained with the Petrov-Galerkin scheme with a consistent mass matrix and mass lumping without improvement ($r = 0$).

For the Euler-Bernoulli beam, the normalized eigenvalues and the relative L^2 error in the corresponding mode shapes are plotted versus the normalized mode number in Figs. 5.17 and 5.18, respectively. We observe that with increasing number of corrector passes, the spectrum curves quickly approach the reference solution obtained with the consistent mass matrix. We see that the iterative improvement is particularly efficient for improving the accuracy of the mode shapes. After two corrector passes, the L^2 error curve of the Petrov-Galerkin scheme with mass lumping is practically the same as the one of the reference for polynomial degrees $p = 2$ to 4 throughout the complete spectrum, and a clear difference is only noticeable in the high modes for $p = 5$.

Figure 5.19 plots the normalized eigenvalues versus the normalized mode number for the simply supported square plate. We observe that in this case, a lumped mass matrix with one or two corrector passes can eliminate the error in the eigenvalue spectrum completely. For $p = 5$, the normalized eigenvalue curve obtained with a consistent mass matrix and the lumped mass matrix with only one corrector pass are practically indistinguishable throughout the complete spectrum. We conclude that - although we have

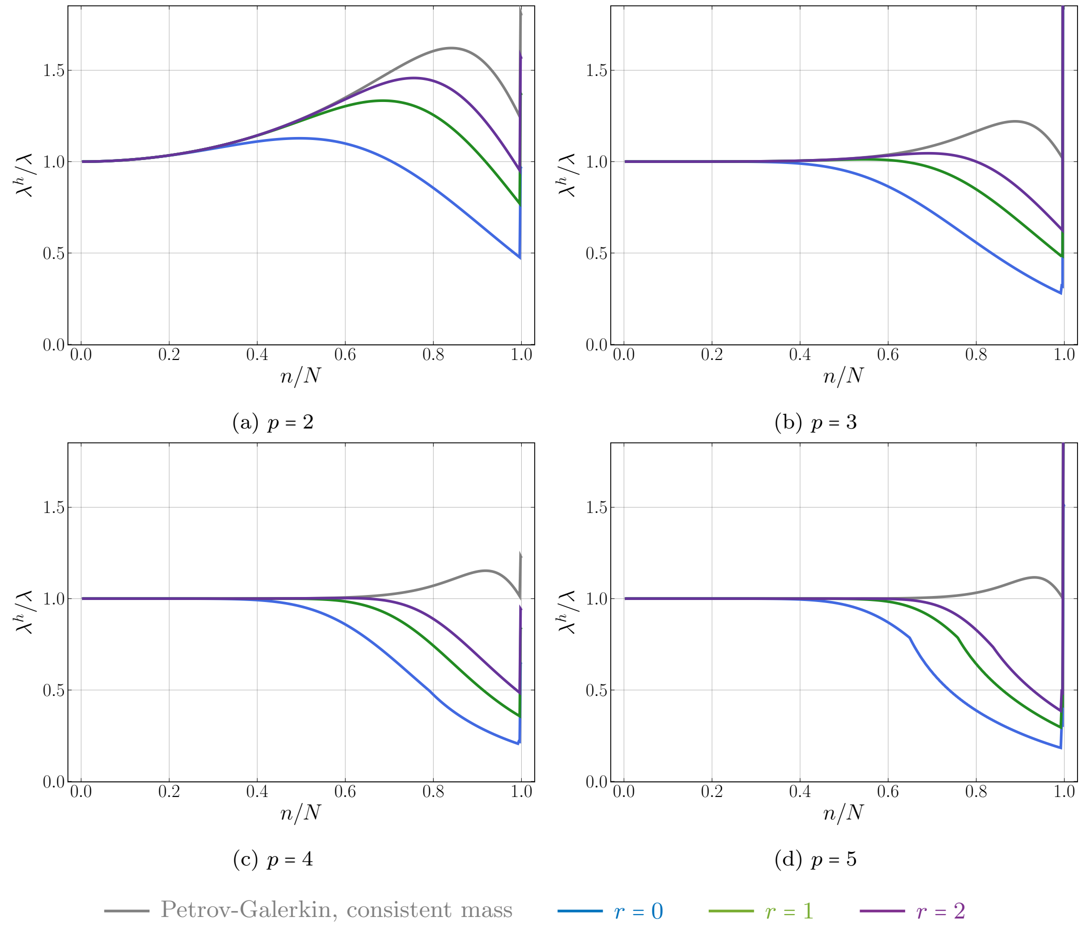

(a) $p = 2$ (b) $p = 3$

(c) $p = 4$ (d) $p = 5$

Figure 5.17: Normalized eigenvalues of the freely vibrating beam, computed with an iteratively improved approximate dual basis and a different number r of corrector passes.

not used the iterative improvement in our simple benchmark calculations here - it could represent a tool to improve spectral accuracy of the Petrov-Galerkin approach in future more challenging applications.

5.5 Discussion and outlook

5.5.1 Summary and significance of current results

In this paper, we introduced an isogeometric Petrov-Galerkin formulation that enables higher-order accurate mass lumping. It is based on B-splines to discretize the solution fields and corresponding approximate dual functions with local support to discretize the test functions. We demonstrated via convergence studies and spectral analysis for beam and plate models that our Petrov-Galerkin method leads to higher-order accurate solutions in explicit dynamics, also when the mass matrix is lumped. Our results thus

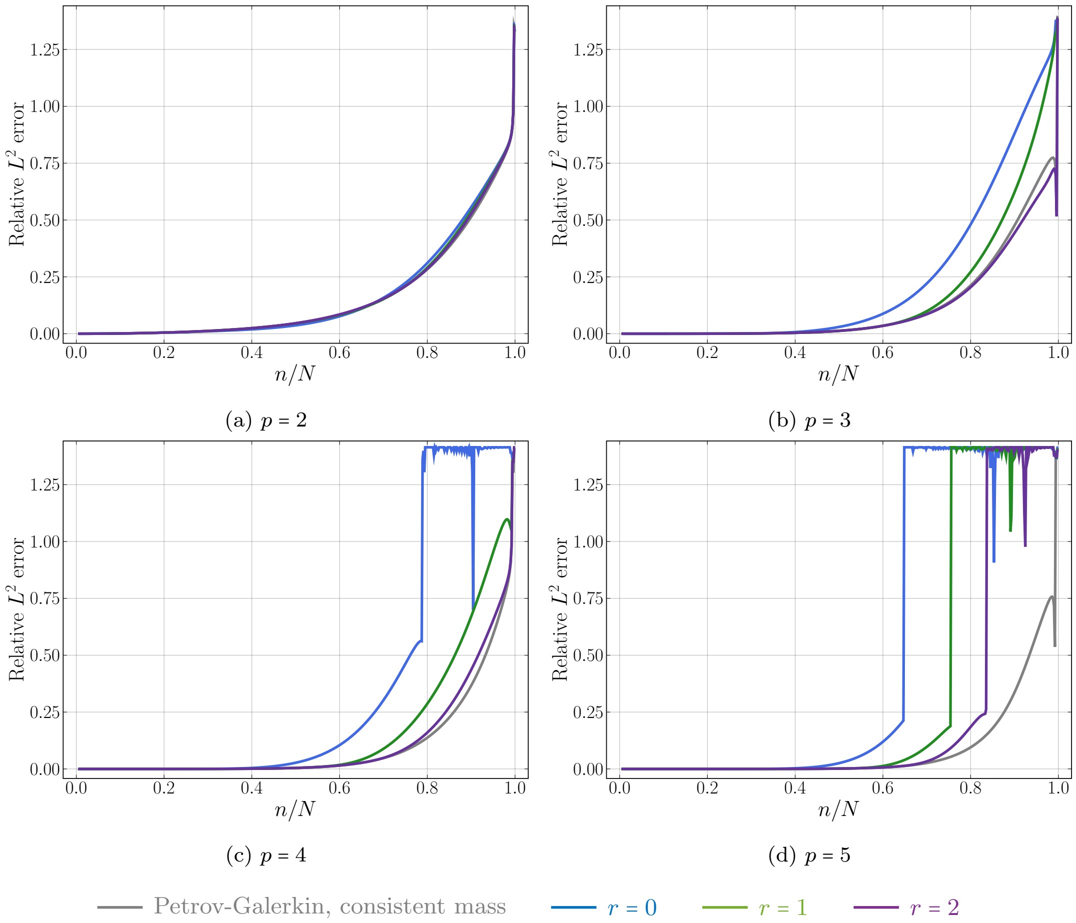

(a) $p = 2$

(b) $p = 3$

(c) $p = 4$

(d) $p = 5$

Figure 5.18: Relative L^2 error in the mode shapes of the freely vibrating beam, computed with an iteratively improved approximate dual basis and a different number r of corrector passes.

confirm that mass lumping as such does not have to be a deal-breaker for higher-order accuracy in the context of isogeometric explicit dynamics calculations, if one adequately exploits the additional opportunities of splines.

We also presented several ideas to resolve related technical issues. Firstly, we showed that the approximate bi-orthogonality property, which is in general destroyed under non-affine geometry mapping, is preserved when we use modified approximate dual functions that are divided by the Jacobian determinant. Secondly, we discussed options for the weak and strong imposition of Dirichlet boundary conditions. For the latter, we suggested to replace the few non-interpolatory approximate dual functions at the Dirichlet boundary by standard B-splines, restoring the interpolation property as a prerequisite for the strong imposition of Dirichlet boundary conditions. We also presented an algorithm for iteratively improving the approximate bi-orthogonality property of the dual basis. While its application is not necessary for securing higher-order accurate results, in particular given the additional computational cost, it establishes a rigorous link between

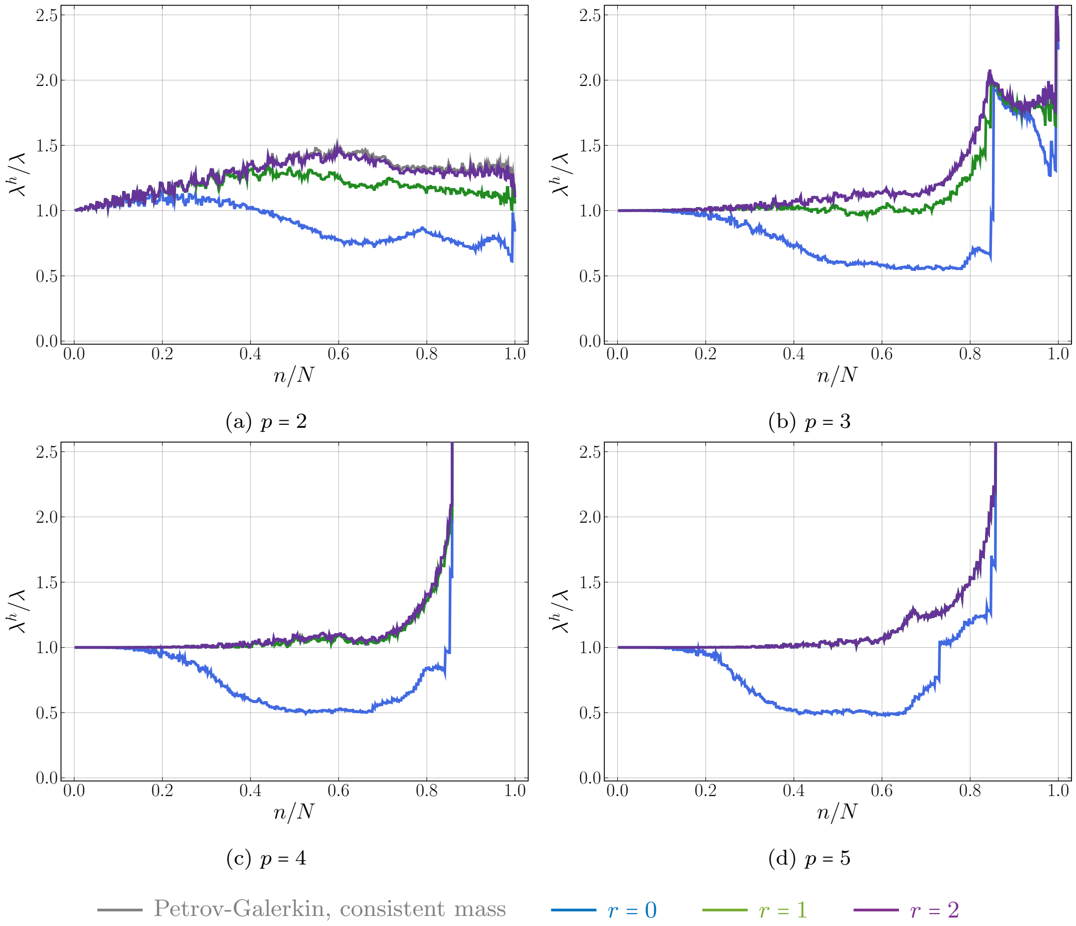

(a) $p = 2$

(b) $p = 3$

(c) $p = 4$

(d) $p = 5$

Figure 5.19: Normalized eigenvalues of the simply supported plate, computed with an iteratively improved approximate dual basis and a different number r of corrector passes.

truly dual and approximate dual basis functions and the accuracy of the associated spectra.

5.5.2 A first look at explicit dynamics of shells

To get an idea whether its advantages directly transfer to more involved explicit dynamics calculations, we employ our Petrov-Galerkin method with mass lumping to solve the test case of a pinched cylinder, whose set-up is given in Fig. 5.20. Our implementation follows the Kirchhoff-Love shell model and its isogeometric discretization presented in [48], assuming large deformation kinematics and the St. Venant-Kirchhoff constitutive model. In our Petrov-Galerkin approach, we apply B-splines to discretize the displacement solution and modified approximate dual functions to discretize the virtual displacements, while the geometry map is provided by an exact NURBS representation of the cylinder. We use the central difference method to integrate in time, with a time

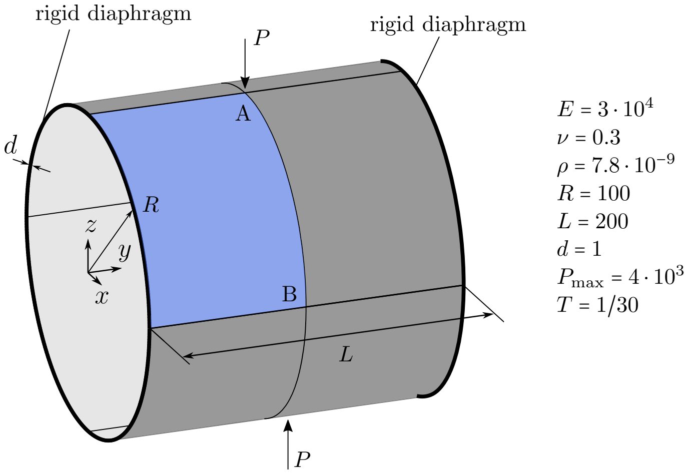

Figure 5.20: Pinched cylinder constrained by rigid diaphragms.

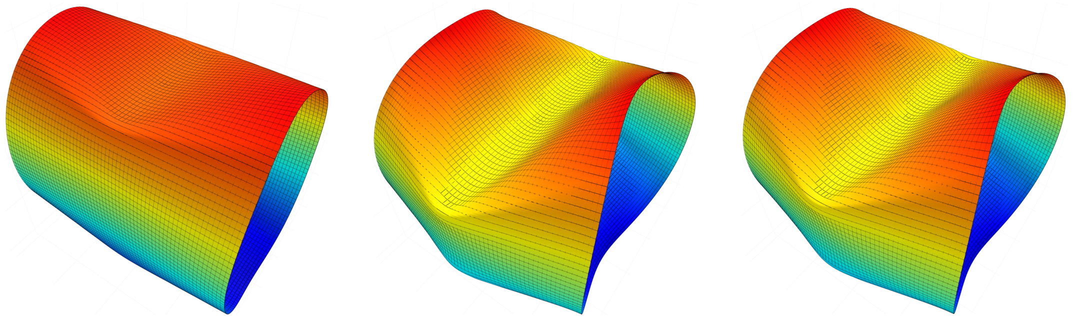

(a) $P = \frac{1}{3}P_{\max}$ (b) $P = \frac{2}{3}P_{\max}$ (c) $P = P_{\max}$

Figure 5.21: Deformed configurations of the cylinder, computed with our Petrov-Galerkin method with mass lumping.

step size of $\Delta t = 5 \cdot 10^{-8}$. The mass matrix of the Petrov-Galerkin scheme is lumped via the standard row-sum technique, except for the few rows that correspond to coefficients of the boundary B-spline functions.

The point load P is linearly increased from zero to $P_{\max}$ during the time $T = 1/30$. Using symmetry, we compute one eighth of the cylinder that we discretize with cubic, quartic and quintic splines on a mesh of 32×32 Bézier elements. This resolution is known in the literature to be adequate for this problem [208], which exhibits highly localized features in the displacement solution due to the point load and the appearance of wrinkles during deformation. In addition, this resolution guarantees that locking phenomena, in particular membrane locking, are controlled. Figure 5.21 illustrates three snapshots from the deformation history.

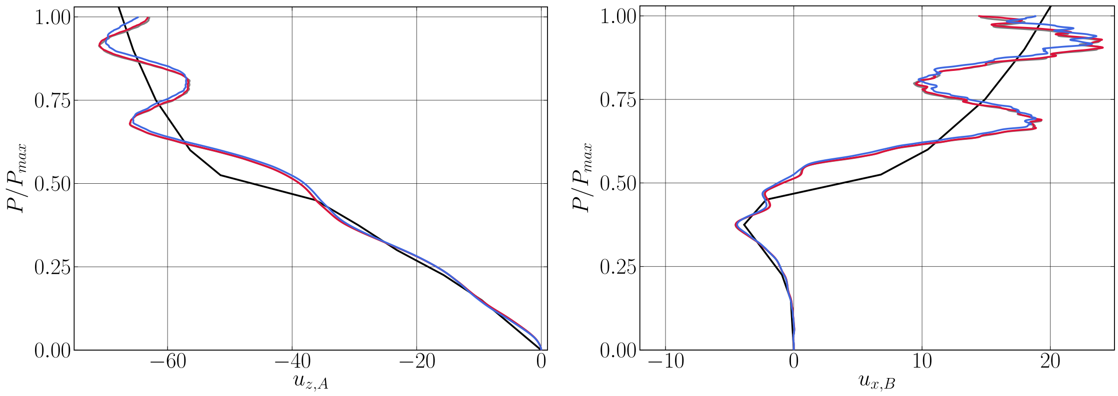

(a) $p = 3$, point A.

(b) $p = 3$, point B.

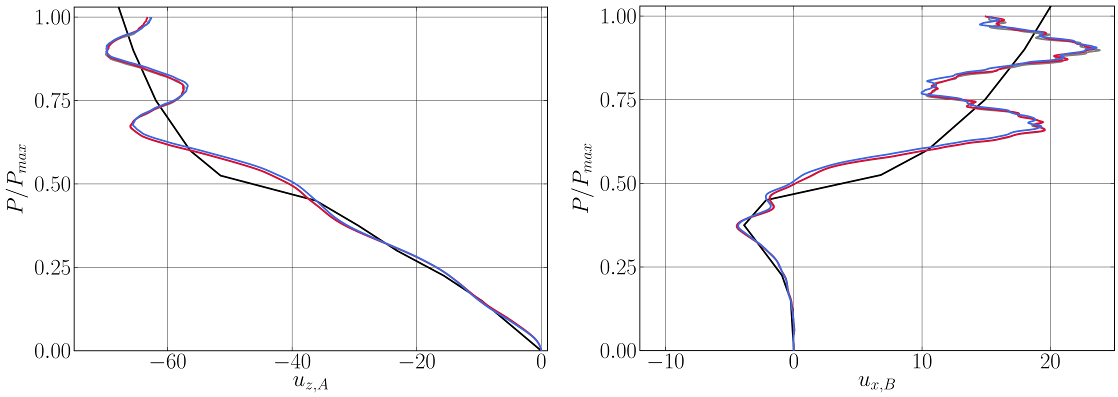

(c) $p = 4$, point A.

(d) $p = 4$, point B.

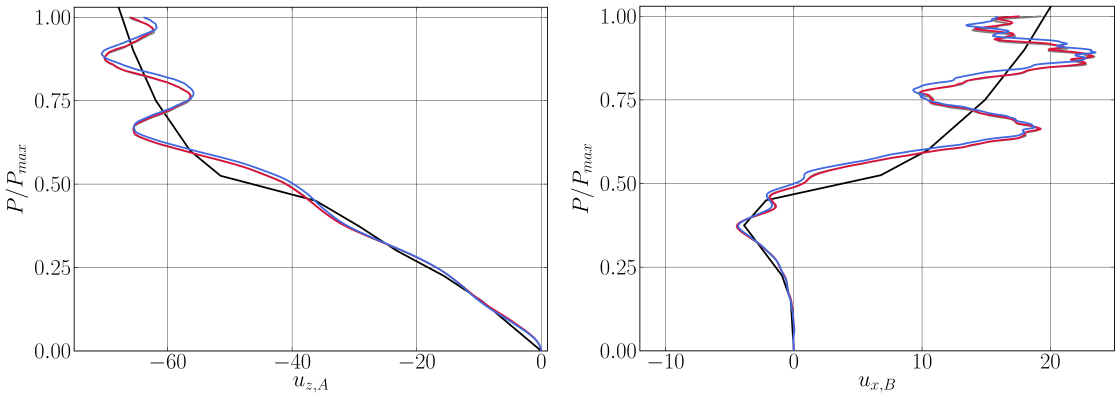

(e) $p = 5$, point A.

(f) $p = 5$, point B.

— Static solution [218] — Galerkin, consistent mass

— Galerkin, row-sum lumped mass — Petrov-Galerkin, higher-order accurate lumped mass

Figure 5.22: Load-deflection curves at point A (u_z) and at point B (u_x) of the pinched cylinder, computed with three different isogeometric schemes on a mesh of 32×32 Bézier elements.

To assess the performance of our Petrov-Galerkin method, we compare its displacement response to the results obtained with the standard Galerkin method with a consistent mass matrix and with a row-sum lumped mass matrix. We plot the load-deflection curves at points A and B, that is $u_{z,A}$ and $u_{x,B}$, in Fig. 5.22. As an additional reference, we also include the static solution (black curves), as the explicit dynamic results oscillate around the static solution after snap-through [208]. We observe that for the given mesh, all three methods lead to practically the same displacement response, irrespective of the polynomial degree considered. We note that we also tried to lower the resolution by repeating the same study on meshes with 16 × 16 Bézier elements. We found that the three methods still yield displacement results that are overall equivalent, but all deviate from the static solution, and hence are not accurate.

These results of a more involved test case confirm that our Petrov-Galerkin scheme also works here. But they also indicate that its advantages might not always be as evident in practical applications as in the simple benchmarks shown in Section 5.4 above.

5.5.3 Future research directions

From our viewpoint, there are two particularly important technical aspects that remain to be investigated. One is an in-depth performance test of our Petrov-Galerkin method in more involved scenarios, extending our initial results presented above. In particular, relevant scenarios feature typical challenges in explicit dynamics calculations, including shell elements, large deformations, contact, nonlinear material behavior, and their combinations. The other one is a detailed analysis of the computational efficiency, in particular with respect to the computational cost of a competitive matrix-free implementation that fully exploits additional technical opportunities of spline functions such as the exploitation of their tensor-product structure [219], the use of optimal quadrature rules with minimal number of points [212], and the removal of outliers [122].

The results presented in this paper open up further directions for future technical work. One is the capability of directly building interpolatory boundary basis functions and/or the required Dirichlet boundary conditions into the approximate dual space. Another one is the combination of locking preventing mechanisms with the approximate dual basis, in order to enable accurate solution fields on coarse meshes. Another challenge, for which no initial idea exists, is to extend the concept of the approximate dual basis as a test function space to trimmed Bézier elements.

Appendix 5.A

Approximate inverse of the Gramian matrix

We summarize the recursive construction of $\hat{\mathbf{G}}^{-1}$ based on [103], [131] in Algorithm 6. As discussed in Section 5.2.3, $\hat{\mathbf{G}}^{-1}$ is an approximate inverse of the Gramian matrix, $\hat{\mathbf{G}}^{-1} \approx \mathbf{G}^{-1}$.

In [131], the authors provide formulas for computing the homogeneous polynomial

Algorithm 6 Compute the approximate inverse $\hat{\mathbf{G}}^{-1}$ of the Gramian matrix based on [131]

```
Input: $p$, $N$ and $\Xi$
Output: $\hat{\mathbf{G}}^{-1}$
$\mathbf{D} = \mathbf{I}_{N\times N}$                                          ▷ Initialize
$\hat{\mathbf{G}}^{-1}$ = compute_matrix_$\mathbf{U}(v = 0, p, \Xi, N)$    ▷ Initialize. See Algorithm 7
for $v$ in $1:p$ do
    $\mathbf{U}$ = compute_matrix_$\mathbf{U}(v, p, \Xi, N)$                  ▷ See Algorithm 7
    $\mathbf{D}$ *= compute_matrix_$\mathbf{D}(v, p, \Xi, N)$                 ▷ See Algorithm 8
    $\hat{\mathbf{G}}^{-1}$ += $\mathbf{D}\,\mathbf{U}\,\mathbf{D}^T$
end for
```

Algorithm 7 Compute the diagonal matrix **U** in Algorithm 6 [131]

```
Input: Index $v$ ($v = 0, \ldots, p$), $p$, $\Xi$ and $N$
Output: $\mathbf{U}$
$c = \frac{(p+1)\ !(p-v)\ !}{(p+v+1)\ !(p+v)\ !}$
$F_v(\xi_{j+1} \ldots \xi_{j+p+v})$ according to Equation (5.1) in [131]   ▷ See (5.36) for $v = 0, \ldots, 5$
for $j$ in $1:(N - v)$ do
    $U_{jj} = c\,\frac{p+v+1}{\xi_{j+p+v+1} - \xi_j}\,F_v(\xi_{j+1} \ldots \xi_{j+p+v})$
end for
```

Algorithm 8 Compute matrix **D** in Algorithm 6 [131]

```
Input: Index $v$ ($v = 0, \ldots, p$), $p$, $\Xi$ and $N$
Output: $\mathbf{D}$
$k = p + v$
for $j$ in $1:(N + p + 1 - k)$ do
    $d_{\Xi,j} = k \,/\, (\xi_{j+k} - \xi_j)$
end for
$\boldsymbol{\Delta}_{N+p+1-k} = \begin{bmatrix} 1 & & & \\ -1 & 1 & & \\ & \ldots & \ldots & \\ & & -1 & 1 \\ & & & -1 \end{bmatrix}_{(N+p+1-k)\times(N+p-k)}$
$\mathbf{D} = \mathrm{diag}\,(\mathbf{d}_\Xi)\;\boldsymbol{\Delta}_{N+p+1-k}$
```

$F_v(x_1, \ldots, x_r)$ in Algorithm 7 with $v = 0, \ldots, 5$ as follows:

$$F_0(x_1, \ldots, x_r) = 1.0\,, \tag{5.36a}$$

$$F_1(x_1, \ldots, x_r) = r^2\,\sigma_2\,, \tag{5.36b}$$

$$2F_2(x_1, \ldots, x_r) = r^2\left(r^2 - 3r + 3\right)\sigma_2^2 - r^2\,(r-1)\,\sigma_4\,, \tag{5.36c}$$

$$6F_3(x_1, \ldots, x_r) = r^3\,(r-2)\left(r^2 - 7r + 15\right)\sigma_2^3 - 3r^2\,(r-2)\left(r^2 - 5r + 10\right)\sigma_4\,\sigma_2 -$$

$$2r^2\left(3r^2-15r+20\right)\sigma_3^2 + 2r^2(r-1)(r-2)\sigma_6\,, \tag{5.36d}$$

$$\begin{aligned}
24F_4(x_1,\ldots,x_r) = {}& r^4\left(r^4-18r^3+125r^2-384r+441\right)\sigma_2^4 - \\
& 6r^3\left(r^4-16r^3+104r^2-305r+336\right)\sigma_4\sigma_2^2 + \\
& 3r^2\left(r^4-14r^3+95r^2-322r+420\right)\sigma_4^2 + \\
& 8r^2(r-2)(r-3)\left(r^2-7r+21\right)\sigma_6\sigma_2 - \\
& 8r^3(r-3)\left(3r^2-24r+56\right)\sigma_3^2\sigma_2 + 48r^2(r-3)\left(r^2-7r+14\right)\sigma_5\sigma_3 - \\
& 6r^2(r-1)(r-2)(r-3)\sigma_8\,,
\end{aligned} \tag{5.36e}$$

$$\begin{aligned}
120F_5(x_1,\ldots,x_r) = {}& r^5(r-4)\left(r^4-26r^3+261r^2-1176r+2025\right)\sigma_2^5 - \\
& 10r^4(r-4)\left(r^4-24r^3+230r^2-999r+1674\right)\sigma_4\sigma_2^3 + \\
& 20r^3(r-4)\left(r^4-20r^3+168r^2-645r+972\right)\sigma_6\sigma_2^2 + \\
& 15r^3(r-4)\left(r^4-22r^3+211r^2-942r+1620\right)\sigma_4^2\sigma_2 - \\
& 20r^4\left(3r^4-60r^3+470r^2-1665r+2232\right)\sigma_3^2\sigma_2^2 - \\
& 30r^2(r-2)(r-3)(r-4)\left(r^2-9r+36\right)\sigma_8\sigma_2 - \\
& 20r^2(r-4)\left(r^4-18r^3+173r^2-828r+1512\right)\sigma_6\sigma_4 + \\
& 240r^3\left(r^4-19r^3+143r^2-493r+648\right)\sigma_5\sigma_3\sigma_2 + \\
& 20r^4(r-4)\left(3r^2-30r+83\right)\sigma_4\sigma_3^2 - \\
& 24r^2\left(5r^4-90r^3+655r^2-2250r+3024\right)\sigma_5^2 - \\
& 240r^2(r-3)(r-4)\left(r^2-9r+24\right)\sigma_7\sigma_3 + \\
& 24r^2(r-1)(r-2)(r-3)(r-4)\sigma_{10}\,,
\end{aligned} \tag{5.36f}$$

where σ_l are the centered moments:

$$\sigma_l = \frac{1}{r}\sum_{j=1}^{r}\left(x_j-\bar{x}\right)^l \quad \text{with} \quad \bar{x} = \frac{1}{r}\sum_{j=1}^{r} x_j\,.$$

We demonstrate the computation of $\hat{\mathbf{G}}^{-1}$ in Example 5.5.1 for a space of quadratic C^1 B-splines ($p = 2$) defined on an open knot vector $\mathbf{\Xi} = [0,0,0,1,2,3,3,3]$.

Example 5.5.1. (Computation of the approximate inverse using Algorithm 6 based on [131]). *Consider a space of quadratic C^1 B-splines ($p = 2$) on $\mathbf{\Xi} = [0,0,0,1,2,3,3,3]$. The number of B-splines is $N = 5$. The spline function vector $\mathbf{b} = [B_1\ B_2\ B_3\ B_4\ B_5]$.*

The matrix $\hat{\mathbf{G}}^{-1}$ computed with Algorithm 6 is:

$$\begin{aligned}
\hat{\mathbf{G}}^{-1} = \mathbf{U}(v=0) \quad + \quad & \mathbf{D}(v=1)\,\mathbf{U}(v=1)\,\mathbf{D}^T(v=1) \quad + \\
& \mathbf{D}(v=1)\,\mathbf{D}(v=2)\,\mathbf{U}(v=2)\,\mathbf{D}^T(v=2)\,\mathbf{D}^T(v=1)\,.
\end{aligned}$$

For $v = 0$, we compute the diagonal matrix $\mathbf{U}$ *using Algorithm 7 and obtain:*

$$\mathbf{U}(v=0) = \begin{bmatrix} 3.0 & & & & \\ & 1.5 & & & \\ & & 1.0 & & \\ & & & 1.5 & \\ & & & & 3.0 \end{bmatrix}.$$

For $v = 1$, we compute the values of the homogeneous polynomial F_1 using the equivalent formulas in (5.36) *and obtain $F_1 = 2, 6, 6, 2$ for the entries U_{11}, U_{22}, U_{33} and U_{44} of* $\mathbf{U}$, *respectively. The diagonal matrix* $\mathbf{U}$ *is then:*

$$\mathbf{U}(v=1) = \begin{bmatrix} 1/6 & & & \\ & 3/4 & & \\ & & 3/4 & \\ & & & 1/6 \end{bmatrix}.$$

Matrix $\mathbf{D}$, *computed with Algorithm 8, is:*

$$\mathbf{D}(v=1) = \begin{bmatrix} 3.0 & & & & \\ & 1.5 & & & \\ & & 1.0 & & \\ & & & 1.5 & \\ & & & & 3.0 \end{bmatrix} \begin{bmatrix} 1 & & & \\ -1 & 1 & & \\ & -1 & 1 & \\ & & -1 & 1 \\ & & & -1 \end{bmatrix} = \begin{bmatrix} 3.0 & & & \\ -1.5 & 1.5 & & \\ & -1.0 & 1.0 & \\ & & -1.5 & 1.5 \\ & & & -3.0 \end{bmatrix}.$$

For $v = 2$, analogously, we obtain:

$$\mathbf{U}(v=2) = \begin{bmatrix} 1/36 & & \\ & 13/144 & \\ & & 1/36 \end{bmatrix} \quad \text{and} \quad \mathbf{D}(v=2) = \begin{bmatrix} 2.0 & & \\ -4/3 & 4/3 & \\ & -4/3 & 4/3 \\ & & -2.0 \end{bmatrix}.$$

The matrix $\hat{\mathbf{G}}^{-1}$ is then:

$$\hat{\mathbf{G}}^{-1} = \begin{bmatrix} 11/2 & -19/12 & 2/9 & & \\ -19/12 & 265/72 & -7/6 & 13/36 & \\ 2/9 & -7/6 & 65/27 & -7/6 & 2/9 \\ 0 & 13/36 & -7/6 & 265/72 & -19/12 \\ 0 & 0 & 2/9 & -19/12 & 11/2 \end{bmatrix}.$$

6 Isogeometric locking-free explicit dynamics of shells with a Petrov-Galerkin mixed formulation built on an approximate dual spline basis

This chapter is reproduced from:

T.-H. Nguyen, R. R. Hiemstra, and D. Schillinger. *Isogeometric locking-free explicit dynamics of shells with a Petrov-Galerkin mixed formulation built on an approximate dual spline basis*, Submitted to Int. J. Numer. Methods Eng. 2023 *(under review).*

Abstract

In this paper, we combine an isogeometric Petrov-Galerkin approach that uses approximate dual spline functions to enable higher-order accurate mass lumping with the Hellinger-Reissner principle to eliminate the effect of membrane locking for Kirchhoff-Love shells. The resulting variational mixed formulation consists of the equations of motion and a strain projection equation. We discretize all test functions with an approximate dual spline basis that satisfies approximate bi-orthogonality in the mapped domain with respect to a trial space of B-splines. For the equations of motion, we apply row-sum lumping of the mass matrix, maintaining higher-order spatial accuracy in explicit dynamics calculations. For the strain projection equation, we also apply row-sum lumping to the projection matrix, which leads to an inexpensive explicit solve equivalent to what is obtained for the equations of motion. In addition, we show that row-sum lumping of the projection matrix preserves higher-order spatial accuracy. Moving towards an effective isogeometric analysis framework for explicit dynamics of shells, we combine our approach with optimal quadrature rules that minimize the number of popint evaluations and outlier removal techniques that increase robustness and critical time step sizes. We demonstrate the performance of our approach in terms of spatial accuracy via convergence studies and spectral analysis of curved beam and shell benchmarks.

6.1 Introduction

In structural dynamics, particularly in crash and metal forming simulations, explicit methods are widely applied. Current commercial codes such as LS-Dyna, Pam-Crash, or Radioss rely on three key ingredients to achieve highly efficient explicit transient calculations: (1) low memory requirements; (2) an efficient solver; and (3) relatively large critical time step sizes. In commercial codes, these ingredients are typically achieved by combining classical C^0 finite elements using lowest-order linear basis functions with specific mass lumping techniques [66]. Various lumping techniques exist, such as row-summing [44], [220], diagonal scaling [89], manifold-based methods [90], and lumping by nodal quadrature [91]–[93], [172]. While row-summing is very easy to implement, the lumped mass matrix is not necessarily positive-definite, as negative or zero diagonal values are possible. In contrast, diagonal scaling and the manifold-based schemes guarantee the positive definiteness of the lumped mass matrix, but might deliver sub-optimal convergence rates [94], [95]. For lumping by nodal quadrature, given the proper choice of basis functions and quadrature rules, optimal convergence as well as a positive-definite lumped mass matrix can be obtained [95]. Employing Lagrangian basis functions with Gauss-Lobatto-Legendre quadrature points as interpolation nodes and using the Gauss-Lobatto-Legendre quadrature rule results in a diagonal matrix. This is also known as the spectral element method [92], [96], [97]. The *hp*-collocation method [93] which employs the Gauss-Lobatto Lagrange test functions and Gauss-Lobatto points as collocation points also falls in this category.

A lumped mass matrix enables a significant reduction in memory usage and computational cost, as only a matrix-vector multiplication needs to be performed per explicit time step. In terms of accuracy, however, lumping schemes are generally restricted to second-order accuracy irrespective of the polynomial degree of the basis functions [43], [44]. Therefore, only for lower-order elements, optimal accuracy in space can be preserved. For higher-order elements, optimal accuracy is typically not maintained. Exceptions are if additional accuracy conditions of the quadrature rule are satisfied [91], or the spectral element method based on nodal quadrature is applied [95]. There are various attempts at improving the accuracy of the lumped mass matrix such as the explicit predictor-multicorrector scheme presented in [66], [86], [87], which, nevertheless, results in a mass matrix that is no longer diagonal, but has a band structure.

Isogeometric analysis (IGA) [30], [51] constitutes an opportunity for higher-order accurate explicit dynamics calculations. It offers a well-behaved discrete spectrum of eigenfrequencies and eigenmodes [43], a feature that cannot be achieved in finite element analysis based on nodal basis functions [176]. Standard row-sum lumping, however, destroys the higher-order spatial accuracy of IGA. Therefore, a focus of recent work has been on the design of suitable lumping schemes that maintain spatial accuracy. In [98], the authors construct a set of transformed spline basis functions that are interpolatory at the Greville points and lumped the resulting Galerkin consistent mass matrix using the row-sum lumping technique. It is shown that the spectral accuracy and convergence obtained with these transformed basis functions are improved, however, not optimal. In [99], the authors develop preconditioners for this type of mass lumping scheme. The improved mass matrix potentially achieves better accuracy in explicit dynamics, however, is no longer diagonal, but has a banded structure.

Another idea to obtain a diagonal mass matrix without lumping is to exploit the bi-orthogonality of a dual spline basis. When the corresponding dual basis functions are used as test functions, the inner product with the spline functions yields a diagonal matrix. In [100], the authors construct such dual space for non-uniform rational B-splines, based on their Bernstein-Bézier representation and apply it to obtain a diagonal mass matrix for explicit dynamics calculations. The resulting formulation is an isogeometric Petrov-Galerkin formulation, which results in good spectral properties and the same optimal convergence behavior as the standard Galerkin method based on a consistent mass matrix. However, it relies on dual functions that are discontinuous, and requires the inverse of the geometric mapping, which is not trivial for curved multidimensional geometries. In [188], we have recently developed another isogeometric Petrov-Galerkin formulation based on B-splines and their corresponding smooth approximate dual functions with local support to discretize the solution fields and the test functions, respectively. Its main feature is that row-sum lumping to the resulting mass matrix, which is only approximately diagonal due to the approximate bi-orthogonality, can be applied without loosing spatial accuracy. Our approach thus preserves higher-order spatial accuracy with optimal rates of convergence in explicit dynamics. In [132], we further specified our approach, verifying our lumping approach from a numerical analysis viewpoint and solving important technical issues such as the treatment of Dirichlet boundary conditions that can be built directly into the discretization space.

In this work, we extend our isogeometric Petrov-Galerkin approach to higher-order accurate explicit dynamics calculations of shell structures, with an emphasis on how to leverage the properties of the approximate dual basis to obtain an efficient discrete mixed formulation that mitigates locking. For an overview of existing approaches to mitigate locking and the extensive pertinent literature, we refer the interested to [64] and [135]. Here, we develop an isogeometric Petrov-Galerkin mixed formulation based on the Hellinger-Reissner principle that enables higher-order spatial accuracy in explicit dynamics. We specify our approach for the isogeometric Kirchhoff-Love shell [48], which is typically prone to membrane locking. Our formulation considers the displacement and strain fields as two independent variable fields, where we discretize the latter with a basis of one degree lower than the former. The resulting system of equations contains a sub-system of discrete equations of motion and a sub-system of discrete strain projection equations. For the discrete system of equations of motion, we apply row-sum lumping of the mass matrix, maintaining higher-order spatial accuracy. For the discrete system of strain projection equations, we also apply row-sum lumping to the projection matrix, which leads to an inexpensive explicit solve equivalent to what is obtained for the system of equations of motion. We note that for standard nodal finite elements based on lowest-order linear basis functions, similar approaches based on a locking-free mixed formulation for thin structures and lumping of the system matrices have been explored, see e.g. [221], [222] and the references therein. Moving towards an effective isogeometric analysis framework for explicit dynamics of shells, we combine our approach with optimal (reduced) quadrature rules that minimize the number of point evaluations [133] as well as an outlier removal technique that increase robustness and maximize the critical time step size [122].

The structure of our paper is as follows: In Section 6.2, we briefly review the isogeometric Kirchhoff-Love shell formulation and the explicit scheme for structural dynamics. In Section 6.3, we review the construction and relevant properties of the approximate dual functions of B-splines on arbitrarily mapped surfaces, including the enforcement of Dirichlet boundary conditions and outlier removal. In Section 6.4, we specify our isogeometric Petrov-Galerkin mixed formulation with lumping of the system matrices for higher-order accurate and locking-free explicit dynamics of Kirchhoff-Love shells. In Section 6.5, we present linear and geometrically nonlinear numerical examples of curved beam and shell problems, demonstrating via spectral analysis and convergence studies that our approach eliminates membrane locking and achieves higher-order spatial accuracy in explicit dynamics. In Section 6.6, we summarize our results and draw conclusions.

6.2 Preliminaries

In this section, we briefly review the fundamentals of general continuum elastodynamics, the explicit scheme for structural dynamics, the Hellinger-Reissner principle, and the Kirchhoff-Love shell model [48], [64], which form the starting points for the new developments in the remainder of this work.

6.2.1 Finite-strain elastodynamics of a solid continuum

Consider a three-dimensional physical domain $\Omega \subset \mathbb{R}^3$ of a solid continuum. The local equilibrium equation at each point $\mathbf{X} \in \Omega$ in the reference configuration and time $t > 0$, the constitutive law of the Saint Venant-Kirchhoff material model, and the Green-Lagrange strain tensor, $\mathbf{E}$, are:

$$\begin{cases} \operatorname{Div}\left(\mathbf{F}\,\mathbf{S}\right) + \rho\mathbf{b} - \rho\ddot{\boldsymbol{u}} = 0\,, & (6.1\text{a}) \\ \mathbf{S} = \mathbb{C} : \mathbf{E}\,, & (6.1\text{b}) \\ \mathbf{E} = \dfrac{1}{2}\left(\mathbf{F}^T\mathbf{F} - \mathbf{I}\right)\,, & (6.1\text{c}) \end{cases}$$

where $\mathbf{S}$ denotes the second Piola-Kirchhoff stress tensor and $\boldsymbol{u} = \boldsymbol{u}(\mathbf{X}, t)$ the displacement vector, and $\mathbf{F}$ the deformation gradient that depends on $\boldsymbol{u}$:

$$\mathbf{F} = \mathbf{I} + \frac{d\boldsymbol{u}}{d\mathbf{X}} = \mathbf{F}(\boldsymbol{u})\,, \tag{6.2}$$

with $\mathbf{I}$ is the identity matrix. Furthermore, the tensor $\mathbb{C}$ is the fourth order material tensor, ρ is the mass density in the reference configuration that is assumed to be constant in space and time, and $\mathbf{b}$ is the body force.

At time $t = 0$, the required initial conditions are:

$$\boldsymbol{u}(\boldsymbol{X}, t = 0) = \boldsymbol{u}_0(\boldsymbol{X})\,, \tag{6.3a}$$

$$\frac{\partial}{\partial t}\,\boldsymbol{u}(\boldsymbol{X}, t = 0) = \mathbf{v}_0(\boldsymbol{X})\,. \tag{6.3b}$$

Along the boundary of Ω, denoted as Γ, we consider either Dirichlet (on Γ_D) or Neumann (on Γ_N) conditions:

$$\boldsymbol{u}(\boldsymbol{X}, t) = \boldsymbol{u}_D \quad \text{on } \Gamma_D\,, \tag{6.4a}$$

$$(\mathbf{F} \cdot \mathbf{S}) \cdot \boldsymbol{\nu} = \mathbf{h} \quad \text{on } \Gamma_N\,, \tag{6.4b}$$

where $\boldsymbol{\nu}$ denotes the outward facing unit normal vector.

6.2.2 Finite element discretization and explicit time integration

Finite element discretizations of transient problems governed by (6.1a) generate semidiscrete systems of the following type:

$$\mathbf{M}\,\ddot{\boldsymbol{u}}^n \;=\; \mathbf{F}^n_{\text{ext}} \;-\; \int_\Omega \boldsymbol{B}(\boldsymbol{x}^n)^T\, \boldsymbol{\sigma}^n \,\mathrm{d}\Omega\,, \tag{6.5}$$

where $\mathbf{M}$ is the mass matrix, $\mathbf{F}_{\text{ext}}$ the vector of external forces, $\boldsymbol{B}$ the discrete gradient operator, and $\boldsymbol{\sigma}$ the Cauchy stress. The superscript n is the time index that indicates that a variable is evaluated at time instant t^n.

In this work, we employ the explicit central difference method [66], [111], [189] for time integration. To remain stable, its time step size, Δt, is bounded from below by the critical time step size, Δt_{crit}, that is inversely proportional to the maximum eigenfrequency, ω_{max}, of the discretization:

$$\Delta t \le \Delta t_{\text{crit}} = \frac{2}{\omega_{\text{max}}}\,. \tag{6.6}$$

Hence, Δt_{crit} can be estimated by finding the maximum eigenvalue of the discrete system, or alternatively an accurate approximation, for instance, via the power iteration method [46], [202] or via nodal and element estimates [111], [116], [209], [223]. In this work, we apply the element estimate of Δt_{crit}, where we solve a local generalized eigenvalue problem at the element level to estimate the element critical time step size, which is assumed to be smaller than Δt_{crit} of the global system. We note that the aforementioned methods for time step estimate are generally applied to linear systems. For nonlinear systems, a common practical approach is to transfer the linear result to a nonlinear one by multiplying it with a safety factor [208].

Remark 6.2.1. *An alternative to the explicit central difference method is the fourth-order Runge Kutta method that leads to higher-order convergence in time. In this work, we focus on the spatial accuracy obtained with our approach. Hence, we apply the central difference method and choose a small time step such that the accuracy in time is ensured.*

6.2.3 The Hellinger-Reissner principle

The idea of the Hellinger-Reissner principle is to consider the displacement and either stress or strain as the second variable field [224], [225]. The result is a two-field variational formulation that corresponds to a *saddle-point* problem.

We illustrate one possibility for its derivation in the context of finite-strain elastostatics of a solid continuum, whose strong form corresponds to (6.1) with $\ddot{\boldsymbol{u}} = 0$. The constitutive law (6.1b) is assumed to be strongly satisfied at each point in Ω. The weighted residual method is then applied to the strong form of the equilibrium equation (6.1a) and the strain-displacement relation (6.1c), where both the displacements $\boldsymbol{u}$ and the strains $\mathbf{E}$ are considered independent variable fields. To help differentiate between displacement-based strains and the independent variable field, we formulate the displacement-based strains in terms of a strain operator $\mathscr{E}$:

$$\mathscr{E} \cdot \boldsymbol{u} = \frac{1}{2} \left[\mathbf{F}^T(\boldsymbol{u}) \mathbf{F}(\boldsymbol{u}) - \mathbf{I} \right] . \tag{6.7}$$

The resulting variational formulation with displacements and strains as variable fields is [226]:

$$\int_{\Omega} \left[- (\mathbb{C} : \mathbf{E}) : (\mathscr{E} \cdot \boldsymbol{w}) + \rho \boldsymbol{b} \cdot \boldsymbol{w} \right] \, \mathrm{d}\Omega + \int_{\Omega} \delta\mathbf{E} \cdot (\mathbf{E} - \mathscr{E} \cdot \boldsymbol{u}) \, \mathrm{d}\Omega + \int_{\Gamma_N} \boldsymbol{w} \cdot \mathbf{h} \, \mathrm{d}\Omega \; = \; 0 \, , \tag{6.8}$$

which can be split into two equations as follows:

$$\begin{cases} \displaystyle\int_{\Omega} - (\mathbb{C} : \mathbf{E}) : (\mathscr{E} \cdot \boldsymbol{w}) + \rho \boldsymbol{b} \cdot \boldsymbol{w} \, \mathrm{d}\Omega + \int_{\Gamma_N} \boldsymbol{w} \cdot \mathbf{h} \, \mathrm{d}\Omega \; = \; 0 & \text{(6.9a)} \\ \displaystyle\int_{\Omega} \delta\mathbf{E} \cdot (\mathbf{E} - \mathscr{E} \cdot \boldsymbol{u}) \, \mathrm{d}\Omega = 0 \, . & \text{(6.9b)} \end{cases}$$

Here, $\boldsymbol{w}$ and $\delta\mathbf{E}$ are the test functions corresponding to $\boldsymbol{u}$ and $\mathbf{E}$, respectively. We note that the Neumann boundary condition (6.4)b is directly substituted in (6.8).

6.2.4 The Kirchhoff-Love shell model

The Kirchhoff-Love shell model can be derived directly from the three-dimensional equations of a solid continuum reviewed above [64], [227]. Key assumptions are that cross sections remain straight, unstretched, and normal to the midsurface in the deformed state. Due to these assumptions, the shell can be represented by its midsurface with linear strain distribution through the thickness and negligible transverse shear strains. Therefore, the coefficients E_{i3}, $i = 1, 2, 3$, of the strain tensor $\mathbf{E}$ are zero, $E_{i3} = 0$. One can formulate the remaining in-plane covariant strain coefficients as a sum of a constant part due to membrane action and a linear part due to bending action as follows:

$$E_{\alpha\beta} = \varepsilon_{\alpha\beta} + \theta^3 \, \kappa_{\alpha\beta} \, , \qquad \text{with} \;\; \alpha, \beta = 1, 2 \;\; \text{and} \;\; -0.5d \leq \theta^3 \leq 0.5d \, , \tag{6.10}$$

where d is the shell thickness, and $\varepsilon_{\alpha\beta}$, $\kappa_{\alpha\beta}$ and θ^3 are the membrane strains, the change in curvature due to bending and the coordinate in the thickness direction, respectively.

We briefly review the derivation of $\varepsilon_{\alpha\beta}$, $\kappa_{\alpha\beta}$, following [48], [64]. We first recall the representation of the shell continuum by its midsurface in the reference and deformed configuration:

$$\boldsymbol{x} = \theta^\alpha \, \boldsymbol{a}_\alpha + \theta^3 \, \boldsymbol{a}_3 \, , \qquad \mathbf{X} = \theta^\alpha \, \boldsymbol{A}_\alpha + \theta^3 \, \boldsymbol{A}_3 \, , \qquad \text{with} \quad \alpha = 1, 2 \tag{6.11}$$

respectively. Here, θ^α are the in-plane curvilinear coordinates, $\boldsymbol{a}_\alpha$ the base vectors on the middle surface and $\boldsymbol{a}_3$ its unit normal that is the normalized cross product of $\boldsymbol{a}_\alpha$. The base vector $\boldsymbol{A}_\alpha$ and $\boldsymbol{A}_3$ are denoted by capital letters to point out that they refer to the reference configuration. To emphasize that the base vectors $\boldsymbol{a}_\alpha$ depend on the displacements $\boldsymbol{u}$, we recall:

$$\boldsymbol{a}_\alpha(\boldsymbol{u}) = \boldsymbol{A}_\alpha + \boldsymbol{u}_{,\alpha}(\theta^3 = 0) \, . \tag{6.12}$$

The base vectors at an arbitrary point of the shell continuum are then:

$$\boldsymbol{g}_\alpha = \boldsymbol{x}_{,\alpha} = \boldsymbol{a}_\alpha + \theta^3 \, \boldsymbol{a}_{3,\alpha} \, , \qquad \boldsymbol{G}_\alpha = \boldsymbol{X}_{,\alpha} = \boldsymbol{A}_\alpha + \theta^3 \, \boldsymbol{A}_{3,\alpha} \, . \tag{6.13}$$

The corresponding metric coefficients are:

$$g_{\alpha\beta} = \boldsymbol{g}_\alpha \cdot \boldsymbol{g}_\beta = \underbrace{\boldsymbol{a}_\alpha \cdot \boldsymbol{a}_\beta}_{a_{\alpha\beta}} - 2\theta^3 \, \boldsymbol{a}_{\alpha,\beta} \cdot \boldsymbol{a}_3 + \left(\theta^3\right)^2 \, \boldsymbol{a}_{3,\alpha} \, \boldsymbol{a}_{3,\beta} \approx a_{\alpha\beta} - 2\theta^3 \, \boldsymbol{a}_{\alpha,\beta} \cdot \boldsymbol{a}_3 \, , \tag{6.14a}$$

$$\begin{aligned} G_{\alpha\beta} = \boldsymbol{G}_\alpha \cdot \boldsymbol{G}_\beta &= \underbrace{\boldsymbol{A}_\alpha \cdot \boldsymbol{A}_\beta}_{A_{\alpha\beta}} - 2\theta^3 \, \boldsymbol{A}_{\alpha,\beta} \cdot \boldsymbol{A}_3 + \left(\theta^3\right)^2 \, \boldsymbol{A}_{3,\alpha} \, \boldsymbol{A}_{3,\beta} \\ &\approx A_{\alpha\beta} - 2\theta^3 \, \boldsymbol{A}_{\alpha,\beta} \cdot \boldsymbol{A}_3 \, , \end{aligned} \tag{6.14b}$$

where the quadratic terms with respect to θ^3 are neglected based on the assumption of thin shells. The in-plane covariant strain coefficients, $E_{\alpha\beta}$, are then:

$$E_{\alpha\beta} = \frac{1}{2} \left(g_{\alpha\beta} - G_{\alpha\beta}\right) = \frac{1}{2} \left(a_{\alpha\beta} - A_{\alpha\beta}\right) + \theta^3 \left(\boldsymbol{A}_{\alpha,\beta} \cdot \boldsymbol{A}_3 - \boldsymbol{a}_{\alpha,\beta} \cdot \boldsymbol{a}_3\right) \, , \tag{6.15}$$

which leads to the following expression for $\varepsilon_{\alpha\beta}$ and $\kappa_{\alpha\beta}$ in (6.10):

$$\varepsilon_{\alpha\beta} = \frac{1}{2} (\underbrace{a_{\alpha\beta}}_{a_{\alpha\beta}(\boldsymbol{u})} - A_{\alpha\beta}) = \varepsilon_{\alpha\beta}(\boldsymbol{u}) \, , \tag{6.16a}$$

$$\kappa_{\alpha\beta} = \boldsymbol{A}_{\alpha,\beta} \cdot \boldsymbol{A}_3 - \underbrace{\boldsymbol{a}_{\alpha,\beta} \cdot \boldsymbol{a}_3}_{\boldsymbol{a}_{\alpha,\beta}(\boldsymbol{u}) \cdot \boldsymbol{a}_3(\boldsymbol{u})} = \kappa_{\alpha\beta}(\boldsymbol{u}) \, . \tag{6.16b}$$

We note that $\varepsilon_{\alpha\beta}$ and $\kappa_{\alpha\beta}$ depend on the displacement $\boldsymbol{u}$ since the base vectors $\boldsymbol{a}_\alpha$ and $\boldsymbol{a}_3$ depend on $\boldsymbol{u}$ (see (6.12)).

As discussed above, the strain tensor $\mathbf{E}$ of Kirchhoff-Love shells consists of only three non-zero in-plane coefficients. Accordingly, the stress tensor $\mathbf{S}$ also has three non-zero coefficients $S^{\alpha\beta}$. Using Voigt notation for $\mathbf{S}$ and $\mathbf{E}$, equation (6.1b) becomes:

$$\mathbf{S} = \begin{bmatrix} S^{11} \\ S^{22} \\ S^{12} \end{bmatrix} = \underbrace{\frac{E}{1-\nu^2} \begin{bmatrix} 1 & \nu & 0 \\ \nu & 1 & 0 \\ 0 & 0 & \frac{1-\nu}{2} \end{bmatrix}}_{\mathbf{C}} \begin{bmatrix} E_{11} \\ E_{22} \\ 2E_{12} \end{bmatrix} = \mathbf{C}\,\mathbf{E}\,, \tag{6.17}$$

where E and ν are the Young's modulus and Poisson's ratio, respectively, and $\mathbf{C}$ a material matrix. Inserting (6.10) into (6.17), one can separate the stresses in a membrane and a bending part. Integrating these counterparts through the shell thickness, we obtain the stress resultants $\mathbf{n}$ for normal forces and $\mathbf{m}$ for bending moments as follows:

$$\mathbf{n} = \begin{bmatrix} n^{11} \\ n^{22} \\ n^{12} \end{bmatrix} = d\,\mathbf{C} \begin{bmatrix} \varepsilon_{11} \\ \varepsilon_{22} \\ 2\varepsilon_{12} \end{bmatrix} = d\,\mathbf{C}\,\boldsymbol{\varepsilon}\,, \qquad \mathbf{m} = \begin{bmatrix} m^{11} \\ m^{22} \\ m^{12} \end{bmatrix} = \frac{d^3}{12}\mathbf{C} \begin{bmatrix} \kappa_{11} \\ \kappa_{22} \\ 2\kappa_{12} \end{bmatrix} = \frac{d^3}{12}\mathbf{C}\,\boldsymbol{\kappa}\,. \tag{6.18}$$

We note that all strains and stresses in (6.17) and (6.18) are expressed in a local Cartesian coordinate system.

For Kirchhoff-Love shell boundary value problems, the Dirichlet boundary conditions (on Γ_D) generally include prescribed displacements and rotations around Γ_D that are:

$$\boldsymbol{u} = \boldsymbol{u}_D \qquad \text{on } \Gamma_D\,, \tag{6.19a}$$

$$\omega_{\Gamma_D} = \omega_D \qquad \text{on } \Gamma_D\,, \tag{6.19b}$$

respectively. In general, the Neumann boundary conditions (on Γ_N) consists of the prescribed tractions and bending moments that are:

$$\mathbf{n} = \mathbf{n}_N \qquad \text{on } \Gamma_N\,, \tag{6.20a}$$

$$\mathbf{m} = \mathbf{m}_N \qquad \text{on } \Gamma_N\,, \tag{6.20b}$$

respectively.

6.3 Approximate dual spline bases

In this section, we review the modified approximate dual functions introduced in [188]. In addition, we discuss the strong enforcement of Dirichlet boundary conditions recently introduced in [132], and the integration of our approach of strongly removing outliers [122].

6.3.1 Construction and computation

We start with a brief review of the construction and relevant properties of the original approximate dual functions for univariate B-splines introduced in [131]. Let $\mathbb{S} \subset \mathcal{P}^p$

denote the space of C^{p-1} smooth splines that is:

$$\mathbb{S} := \left\{ s : [a,\, b] \mapsto \mathbb{R} : s|_{t_{k-1},t_k} \in \mathcal{P}^p \,, s \text{ is } C^{p-1} \text{ smooth at } \hat{x} = t_1 \ldots t_{m-1} \right\} , \tag{6.21}$$

where $\mathcal{P}^p$ denotes the space of piecewise polynomials of degree $p \geq 0$, and the interval $[a,\, b] \subset \mathbb{R}$ is partitioned into an increasing sequence of *breakpoints* that define Bézier elements:

$$a = t_0 < \ldots < t_{k-1} < t_k < \ldots < t_m = b\,. \tag{6.22}$$

Consider B-spline functions B_i, $i = 1, \ldots, N$, of degree p with C^{p-1}-continuity defined on an open *knot vector*, $\boldsymbol{\Xi} := \{\hat{x}_1, \ldots, \hat{x}_{N+p+1}\}$, which is the partition (6.22) with $p+1$ multiplicity of the first and last breakpoints and non-repeated internal knots. Let $\hat{\Omega} \subset \mathbb{R}$ denote the parametric domain with local coordinates represented in $\boldsymbol{\Xi}$, i.e. the breakpoints in (6.22). Given an inner product $(\cdot,\, \cdot)_{\hat{\Omega}} : \mathbb{S} \times \mathbb{S} \mapsto \mathbb{R}$ in $\hat{\Omega}$. We recall the bi-orthogonality constraint expressed in matrix form:

$$\int_{\hat{\Omega}} \bar{\mathbf{b}}\, \mathbf{b}^T \, \mathrm{d}\hat{\Omega} = \mathbf{I}\,, \tag{6.23}$$

where $\mathbf{I}$ is the identity matrix, $\mathbf{b} = \left[\, B_1 \, \ldots \, B_N \,\right]^T$ and $\bar{\mathbf{b}} = \left[\, \bar{B}_1 \, \ldots \, \bar{B}_N \,\right]^T$ denote the function vector of the B-spline basis B_i and its associated dual functions $\bar{B}_i$, respectively. Equation (6.23) can be reformulated in terms of the Gramian matrix, $\mathbf{G} = (\mathbf{b}\,, \mathbf{b})_{\hat{\Omega}}$, as follows:

$$\left(\bar{\mathbf{b}}\, \mathbf{b}\right)_{\hat{\Omega}} = \mathbf{I} = \mathbf{G}^{-1}\, \mathbf{G} = \mathbf{G}^{-1} \, (\mathbf{b}\, \mathbf{b})_{\hat{\Omega}} \,. \tag{6.24}$$

Let $\hat{B}_i$, $i = 1, \ldots, N$, denote the approximate dual functions of C^{p-1}-continuous B-splines of degree p in the space $\mathbb{S}$, and $\hat{\mathbf{b}} = \left[\, \hat{B}_1 \, \ldots \, \hat{B}_N \,\right]^T$ be their function vector. The approximate dual functions $\hat{B}_i$ can be constructed as linear combinations of the corresponding B-splines [131] as follows:

$$\hat{\mathbf{b}} = \hat{\mathbf{G}}^{-1}\, \mathbf{b}\,. \tag{6.25}$$

$\hat{B}_i$ satisfies the bi-orthogonality constraint (6.23) "approximately", in the sense that the matrix $\hat{\mathbf{G}}^{-1}$ is an approximate inverse of the Gramian matrix:

$$\hat{\mathbf{G}}^{-1} \approx \mathbf{G}^{-1}\,. \tag{6.26}$$

We note that the notation $\hat{\mathbf{G}}^{-1}$ is to imply that it is an approximate inverse, and its construction does not require any matrix inversion [131]. It is a recursive computation, based on fundamental properties of B-splines such as the nestedness of spaces under knot insertion. For a 1D patch of splines, the approximate inverse matrix $\hat{\mathbf{G}}^{-1}$ is symmetric and positive definite with a bandwidth of at most $p+1$ [131]. Since $\hat{B}_i$ constructed with

(6.25) are linear combinations of B-splines, they span the same space $\mathbb{S}$ and reproduce polynomials in $\mathcal{P}^p$. They preserve important properties of the underlying B-spline basis, such as C^{p-1} regularity and local support. For more detail regarding the computation of $\hat{\mathbf{G}}^{-1}$ and in-depth discussions of these approximate dual functions, we refer to [103], [131], [188].

Remark 6.3.1. *The approximation* (6.26) *can be iteratively improved based on a predictor-multicorrector scheme, see [188]*

For multivariate spline spaces, we consider tensor-product extensions to multivariate dual B-spline functions in this work. To this end, we use the same spline space $\mathbb{S}$ in every coordinate direction such that the multivariate space in the two-dimensional case is $\mathbb{S} \otimes \mathbb{S}$. In the parametric domain, the tensor-product structure leads to matrices with Kronecker structure due to affine mapping. We note that the approximate dual functions can also be extended to non-uniform rational B-splines (NURBS) as shown in [103].

6.3.2 Geometric mapping

For general non-affine geometric mappings, the approximation (6.26), and thus the approximate bi-orthogonality, is not preserved when mapped from the parametric domain to the physical domain. To tackle this problem, in [188], we introduced a modification of the original approximate dual functions, $\hat{B}_i$, by a multiplication with the inverse of the determinant of the Jacobian matrix of the mapping, $C(\hat{\mathbf{x}})$. Hence, the modified approximate dual functions are:

$$\tilde{B}_i(\hat{\boldsymbol{x}}) := \frac{\hat{B}_i(\hat{\boldsymbol{x}})}{C(\hat{\boldsymbol{x}})}\,, \qquad i = 1, \ldots, N\,. \tag{6.27}$$

As shown in [188], $\tilde{B}_i$ approximately satisfy the bi-orthogonality constraint (6.23) in the physical domain in the same sense as $\hat{B}_i$ in the parametric domain. $\tilde{B}_i$ are linearly independent due to the linear independence of the approximate dual functions $\hat{B}_i$ and preserve their local support. Their regularity, however, depends on the smoothness of the Jacobian $C(\hat{\boldsymbol{x}})$. For practical scenarios, we can assume that the underlying geometric mapping is assumed to be sufficiently smooth and invertible such that the Jacobian matrix and its inverse are well-defined.

For illustration, we consider a quarter circle with unit radius represented by NURBS. In Fig. 6.1, we plot the modified approximate dual functions (6.27) next to the corresponding quadratic C^1-continuous B-splines. We also plot the corresponding non-constant function of the Jacobian determinant. We observe that the modified approximate dual functions have local support and preserve the C^{p-1}-continuity of the B-spline functions.

6.3.3 Dirichlet boundary conditions

The strong enforcement of Dirichlet boundary conditions is not straightforward, since the dual basis (6.27) generally does not preserve the interpolatory property of open-knot

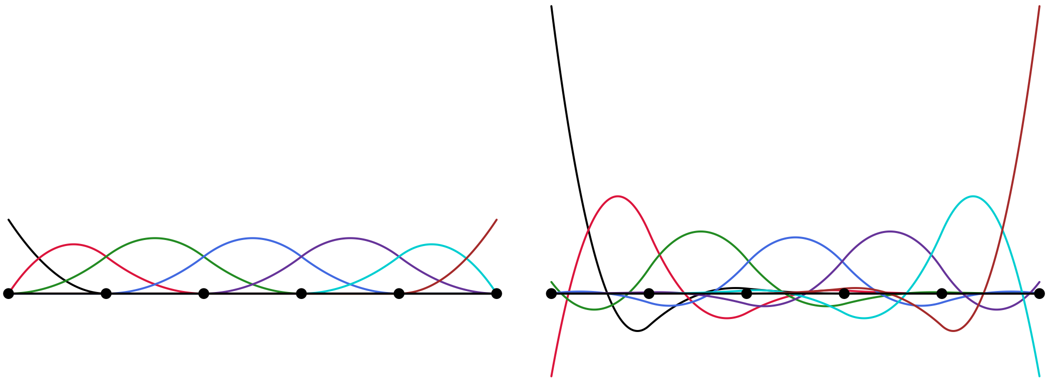

(a) B-splines

(b) Modified approximate dual functions

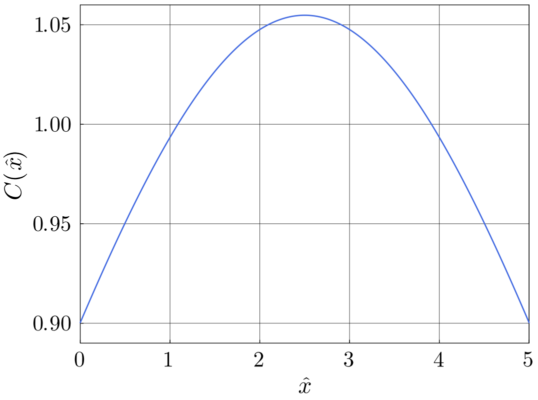

(c) Jacobian determinant function for a quarter circle.

Figure 6.1: Standard B-splines and modified approximate dual functions for a 1D patch of quadratic B-splines and a non-constant Jacobian determinant (from [188]).

B-splines at the ends of the spline patch (see e.g. Fig. 6.1). In this work, we rely on the methodology recently introduced in [132] that directly builds the Dirichlet boundary conditions into the basis of the original approximate dual functions, before modification by multiplication with the inverse of the Jacobian determinant. The underlying idea of this methodology is to reduce the degrees of freedom of the approximate dual basis by solving a minimization problem that includes homogeneous Dirichlet boundary conditions as linear constraints. This approach yields a basis that satisfies homogeneous Dirichlet boundary conditions and preserves the approximate bi-orthogonality property for all functions. In homogeneous Dirichlet boundary conditions can be easily imposed by adding any additional basis functions at the boundary that is linear independent, e.g. the interpolatory standard B-splines at the ends. Since it is multiplied by a known coefficient and moved to the right-hand side, it does not appear in the system matrix and hence the missing bi-orthogonality for that particular function does not affect our method. For an in-depth discussion, we refer the interested reader to [132].

We illustrate the effect of Dirichlet boundary condition enforcement on the approxi-

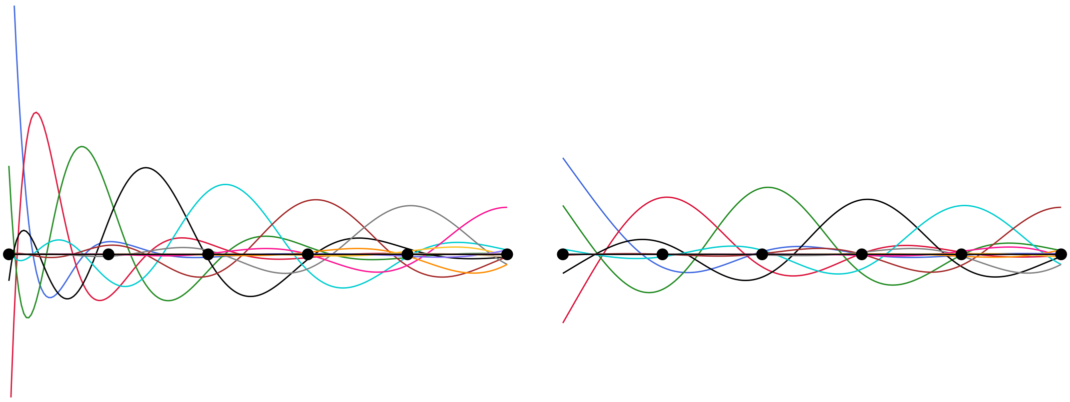

(a) Unconstrained

(b) Unconstrained, outliers removed

Figure 6.2: Half a patch of unconstrained approximate dual functions (Neumann boundary at the left end). The basis is computed for quintic C^4 B-splines ($p = 5$) defined on an open knot vector with 10 Bézier elements.

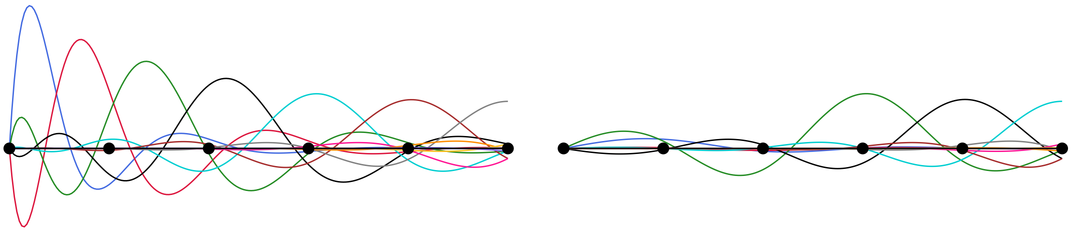

(a) Pinned at left end

(b) Pinned at left end, outliers removed

Figure 6.3: Half a patch of constrained approximate dual functions (pinned Dirichlet boundary at the left end). The basis is computed for quintic C^4 B-splines ($p = 5$) defined on an open knot vector with 10 Bézier elements.

mate dual basis for a one-dimensional patch of splines that could for instance be used to discretize a beam. In Fig. 6.2a, the basis is unconstrained at the left end, suitable for a Neumann boundary. We observe that the basis is not interpolatory at the left end. In Fig. 6.3a, the basis is constrained at the left end to represent a pin. In Fig. 6.4a to represent a fully fixed support.

6.3.4 Outlier removal

To increase the efficiency of our explicit scheme, we extend the outlier removal technique proposed in [122] to our approximate dual basis. The main idea is to directly build ad-

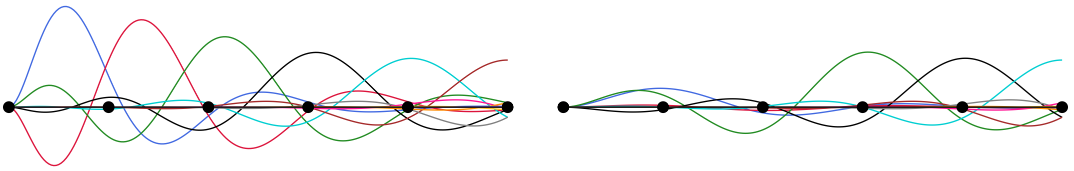

(a) Fully fixed at left end

(b) Fully fixed at left end, outliers removed

Figure 6.4: Half a patch of constrained approximate dual functions (fully fixed Dirichlet boundary at the left end). The basis is computed for quintic C^4 B-splines ($p = 5$) defined on an open knot vector with 10 Bézier elements.

ditional boundary constraints into the discrete space, such that these spurious modes and their corresponding overestimated frequencies are removed from the discrete spectrum. In practice, the resulting maximum eigenfrequency is significantly reduced, which in turn increases the critical time step size as a consequence of (6.6). Analogously to the imposition of Dirichlet boundary conditions, we build these additional constraints into the approximate dual basis before modification, using the same type of minimization problem, where the additional outlier conditions at the boundary are added as linear constraints. For further details on the constrained minimization procedure, we refer the interested reader to [122] and [132].

We illustrate the effect of outlier removal on the approximate dual basis for a one-dimensional patch of splines, given a Neumann and Dirichlet boundary conditions for a beam. In Fig. 6.2b, the basis is unconstrained at the left end, suitable for a Neumann boundary. In Figs. 6.3b and 6.4b, the basis is constrained at the left end to represent a pin and a fully fixed support, respectively. We can see that the new basis without outliers consists of fewer basis functions, but maintains the same approximation power [122]. The removed degrees of freedom can be associated with the removed outlier modes that do not contribute to the accuracy of the analysis results. We note that we will apply the outlier removal approach in all numerical examples shown in this paper. We note that there are also methods to impose outlier removal constraints weakly at boundaries [121] and across patch interfaces [183].

6.4 Variational formulation, isogeometric discretization and lumping

In this section, we derive an isogeometric Petrov-Galerkin mixed formulation based on the Hellinger-Reissner principle that considers the displacements and strains as two independent variable fields. For a Kirchhoff shell formulation, discretizing the latter with a basis of one degree lower than the former removes membrane locking [80], [135], [205]. To discretize this formulation, we employ standard B-splines as trial functions and the corresponding modified approximate dual functions as test functions. In the context of explicit dynamics, our formulation enables higher-order accurate lumping of the mass matrix due to their approximate bi-orthogonality. In addition, we also apply row-sum lumping to the projection matrix, eliminating the need for solving a system for strain projection. We also discuss implications on the computational cost of our explicit dynamics scheme with regards to lumping, outlier removal and (reduced) quadrature.

6.4.1 Variational mixed formulation

Consider the strong form (6.1). We apply the Hellinger-Reissner principle and the weighted residual method, as discussed in Section 6.2.3. In particular, we multiply (6.1a) and (6.1c) by suitable test functions, $\boldsymbol{w}$ and $\delta\mathbf{E}$, respectively, integrate over Ω, performe integration by parts with the first term of (6.1a), and, purely for ease of notation, assume homogeneous Neumann conditions to obtain the following weak form: Find $\mathbf{E} \in \mathcal{S}$, $\boldsymbol{u} \in \mathcal{V}$ such that:

$$\begin{cases} \displaystyle\int_\Omega \rho \ddot{\boldsymbol{u}} \cdot \boldsymbol{w} \, \mathrm{d}\Omega + \int_\Omega (\mathbb{C} : \mathbf{E}) : (\mathscr{E} \cdot \boldsymbol{w}) \, \mathrm{d}\Omega = \int_\Omega \boldsymbol{w} \cdot \rho \boldsymbol{b} \, \mathrm{d}\Omega \qquad \forall \boldsymbol{w} \in \tilde{\mathcal{V}}, & \text{(6.28a)} \\ \displaystyle\int_\Omega \delta\mathbf{E} \cdot \mathbf{E} \, d\Omega - \int_\Omega \delta\mathbf{E} \cdot (\mathscr{E} \cdot \boldsymbol{u}) \, \mathrm{d}\Omega = 0 \qquad \forall \delta\mathbf{E} \in \tilde{\mathcal{S}}, & \text{(6.28b)} \end{cases}$$

where we consider the strains, $\mathbf{E}$, and displacement, $\boldsymbol{u}$, as two independent variable fields. Here, the strain operator $\mathscr{E}$ is defined in (6.7). We assume that the spaces, $\mathcal{S}$, $\mathcal{V}$, $\tilde{\mathcal{S}}$, and $\tilde{\mathcal{V}}$, are sufficiently regular for all differential operators in (6.28). In addition, we assume that all material and geometric parameters are constants.

For Kirchhoff-Love shells, one can employ the simplified stress and strain (6.17) and formulate them with their membrane and bending counterparts (6.10). After integrating over the shell thickness, the weak form (6.28) for Kirchhoff-Love shells becomes: Find $(\boldsymbol{\varepsilon}, \boldsymbol{\kappa}) \in \mathcal{S} \times \mathcal{S}$, $\boldsymbol{u} \in \mathcal{V}$ such that:

$$\begin{cases} \displaystyle\int_{\Omega_A} \rho \, d \, \ddot{\boldsymbol{u}} \cdot \boldsymbol{w} \, \mathrm{d}\Omega + \int_{\Omega_A} \mathbf{n} \cdot (\mathscr{E}_\varepsilon \cdot \boldsymbol{w}) \, \mathrm{d}\Omega + \cdot \int_{\Omega_A} \mathbf{m} \cdot (\mathscr{E}_\kappa \cdot \boldsymbol{w}) \, \mathrm{d}\Omega \\ \displaystyle\qquad\qquad = \int_{\Omega_A} \boldsymbol{w} \cdot \rho \, d \, \boldsymbol{b} \, \mathrm{d}\Omega \qquad \forall \boldsymbol{w} \in \tilde{\mathcal{V}}, & \text{(6.29a)} \\ \displaystyle\int_{\Omega_A} d \, \delta\boldsymbol{\varepsilon} \cdot \boldsymbol{\varepsilon} \, \mathrm{d}\Omega + \int_{\Omega_A} \frac{d^3}{12} \delta\boldsymbol{\kappa} \cdot \boldsymbol{\kappa} \, \mathrm{d}\Omega - \int_{\Omega_A} d \, \delta\boldsymbol{\varepsilon} \cdot (\mathscr{E}_\varepsilon \cdot \boldsymbol{u}) \, \mathrm{d}\Omega \\ \displaystyle\qquad\qquad - \int_{\Omega_A} \frac{d^3}{12} \delta\boldsymbol{\kappa} \cdot (\mathscr{E}_\kappa \cdot \boldsymbol{u}) \, \mathrm{d}\Omega = 0 \qquad \forall \, (\delta\boldsymbol{\varepsilon}, \delta\boldsymbol{\kappa}) \in \tilde{\mathcal{S}} \times \tilde{\mathcal{S}}, & \text{(6.29b)} \end{cases}$$

where Ω_A is the domain of the shell middle surface, $\mathbf{n}$ and $\mathbf{m}$ are the stress resultants corresponding to the independent variable fields $\boldsymbol{\varepsilon}$ and $\boldsymbol{\kappa}$, respectively. Analogous to (6.7), we define strain operators corresponding to the displacement-based membrane strains and changes in curvature in (6.16) as:

$$\mathscr{E}_\varepsilon \cdot \boldsymbol{u} = \frac{1}{2}\big(\underbrace{a_{\alpha\beta}}_{a_{\alpha\beta}(\boldsymbol{u})} - A_{\alpha\beta} \big)\,, \tag{6.30a}$$

$$\mathscr{E}_\kappa \cdot \boldsymbol{u} = \boldsymbol{A}_{\alpha,\beta} \cdot \boldsymbol{A}_3 - \underbrace{\boldsymbol{a}_{\alpha,\beta} \cdot \boldsymbol{a}_3}_{\boldsymbol{a}_{\alpha,\beta}(\boldsymbol{u}) \cdot \boldsymbol{a}_3(\boldsymbol{u})}\,, \tag{6.30b}$$

with α, $\beta = 1, 2$. One can split (6.29b) in two subequations for the membrane strains and the changes in curvature, and neglect the factor with respect to the shell thickness d. Equation (6.29) then becomes:

$$\left\{ \begin{aligned} &\int_{\Omega_A} \rho\, d\, \ddot{\boldsymbol{u}} \cdot \boldsymbol{w} \,\mathrm{d}\Omega + \int_{\Omega_A} \mathbf{n} \cdot (\mathscr{E}_\varepsilon \cdot \boldsymbol{w}) \,\mathrm{d}\Omega + \int_{\Omega_A} \mathbf{m} \cdot (\mathscr{E}_\kappa \cdot \boldsymbol{w}) \,\mathrm{d}\Omega \\ &\qquad\qquad = \int_{\Omega_A} \boldsymbol{w} \cdot \rho\, d\, \boldsymbol{b} \,\mathrm{d}\Omega \qquad\qquad \forall \boldsymbol{w} \in \tilde{\mathcal{V}}\,, && (6.31\text{a}) \\ &\int_{\Omega_A} \delta\boldsymbol{\varepsilon} \cdot \boldsymbol{\varepsilon} \,\mathrm{d}\Omega - \int_{\Omega_A} \delta\boldsymbol{\varepsilon} \cdot (\mathscr{E}_\varepsilon \cdot \boldsymbol{u}) \,\mathrm{d}\Omega = 0 \qquad\qquad \forall \delta\boldsymbol{\varepsilon} \in \tilde{\boldsymbol{\mathcal{S}}}\,, && (6.31\text{b}) \\ &\int_{\Omega_A} \delta\boldsymbol{\kappa} \cdot \boldsymbol{\kappa} \,\mathrm{d}\Omega - \int_{\Omega_A} \delta\boldsymbol{\kappa} \cdot (\mathscr{E}_\kappa \cdot \boldsymbol{u}) \,\mathrm{d}\Omega = 0 \qquad\qquad \forall \delta\boldsymbol{\kappa} \in \tilde{\boldsymbol{\mathcal{S}}}\,. && (6.31\text{c}) \end{aligned} \right.$$

6.4.2 Isogeometric Petrov-Galerkin discretization

To eliminate membrane locking in the Kirchhoff-Love shell formulation [80], [135], [205], we discretize the trial functions regarding the strains, $\boldsymbol{\varepsilon}$, $\boldsymbol{\kappa}$ and the displacements $\boldsymbol{u}$ with standard smooth B-splines of degree $p-1$ and p, respectively:

$$\begin{aligned} \boldsymbol{\varepsilon}^h(\boldsymbol{x},t) &= \big[N_1(\boldsymbol{x}) \;\ldots\; N_m(\boldsymbol{x})\big]\, \hat{\boldsymbol{\varepsilon}}^h(t)\,, \\ \boldsymbol{\kappa}^h(\boldsymbol{x},t) &= \big[N_1(\boldsymbol{x}) \;\ldots\; N_m(\boldsymbol{x})\big]\, \hat{\boldsymbol{\kappa}}^h(t)\,, \\ \boldsymbol{u}^h(\boldsymbol{x},t) &= \big[B_1(\boldsymbol{x}) \;\ldots\; B_n(\boldsymbol{x})\big]\, \hat{\mathbf{u}}^h(t)\,, \end{aligned} \tag{6.32}$$

where we denote basis functions of reduced degree $p-1$ as N_i, $i = 1, \ldots, m$, and basis functions of degree p as B_j, $j = 1, \ldots, n$. Following our discussion in Section 6.3.2, we discretize the test functions, $\delta\boldsymbol{\varepsilon}$, $\delta\boldsymbol{\kappa}$, and $\boldsymbol{w}$, with their corresponding modified approximate dual functions (6.27), $\tilde{N}_i$ and $\tilde{B}_j$:

$$\begin{aligned} \delta\boldsymbol{\varepsilon}^h(\boldsymbol{x}) &= \big[\tilde{N}_1(\boldsymbol{x}) \;\ldots\; \tilde{N}_m(\boldsymbol{x})\big]\, \delta\hat{\boldsymbol{\varepsilon}}^h\,, \\ \delta\boldsymbol{\kappa}^h(\boldsymbol{x}) &= \big[\tilde{N}_1(\boldsymbol{x}) \;\ldots\; \tilde{N}_m(\boldsymbol{x})\big]\, \delta\hat{\boldsymbol{\kappa}}^h\,, \\ \boldsymbol{w}^h(\boldsymbol{x}) &= \big[\tilde{B}_1(\boldsymbol{x}) \;\ldots\; \tilde{B}_n(\boldsymbol{x})\big]\, \hat{\mathbf{w}}^h\,, \end{aligned} \tag{6.33}$$

respectively, where

$$\tilde{N}_i(\hat{\boldsymbol{x}}) := \frac{\hat{N}_i(\hat{\boldsymbol{x}})}{C(\hat{\boldsymbol{x}})}\,, \qquad \tilde{B}_i(\hat{\boldsymbol{x}}) := \frac{\hat{B}_i(\hat{\boldsymbol{x}})}{C(\hat{\boldsymbol{x}})}\,. \tag{6.34}$$

The resulting semidiscrete formulation is: Find $\left(\boldsymbol{\varepsilon}^h, \boldsymbol{\kappa}^h\right) \in \mathcal{S}^h \times \mathcal{S}^h$, $\boldsymbol{u}^h \in \mathcal{V}^h$ such that:

$$\begin{cases} \displaystyle\int_{\Omega_A} \rho\, d\, \ddot{\boldsymbol{u}}^h \cdot \boldsymbol{w}^h \,\mathrm{d}\Omega + \int_{\Omega_A} \mathbf{n}^h \cdot \left(\mathscr{E}_\varepsilon \cdot \boldsymbol{w}^h\right) \mathrm{d}\Omega + \int_{\Omega_A} \mathbf{m}^h \cdot \left(\mathscr{E}_\kappa \cdot \boldsymbol{w}^h\right) \mathrm{d}\Omega & \\ \displaystyle\qquad\qquad\qquad\qquad = \int_{\Omega_A} \boldsymbol{w}^h \cdot \rho\, d\, \boldsymbol{b} \,\mathrm{d}\Omega \qquad \forall \boldsymbol{w}^h \in \tilde{\mathcal{V}}^h\,, & \text{(6.35a)} \\ \displaystyle\int_{\Omega_A} \delta\boldsymbol{\varepsilon}^h \cdot \boldsymbol{\varepsilon}^h \,\mathrm{d}\Omega - \int_{\Omega_A} \delta\boldsymbol{\varepsilon}^h \cdot \left(\mathscr{E}_\varepsilon \cdot \boldsymbol{u}^h\right) \mathrm{d}\Omega = 0 \qquad \forall \delta\boldsymbol{\varepsilon}^h \in \tilde{\mathcal{S}}^h\,, & \text{(6.35b)} \\ \displaystyle\int_{\Omega_A} \delta\boldsymbol{\kappa}^h \cdot \boldsymbol{\kappa}^h \,\mathrm{d}\Omega - \int_{\Omega_A} \delta\boldsymbol{\kappa}^h \cdot \left(\mathscr{E}_\kappa \cdot \boldsymbol{u}^h\right) \mathrm{d}\Omega = 0 \qquad \forall \delta\boldsymbol{\kappa}^h \in \tilde{\mathcal{S}}^h\,, & \text{(6.35c)} \end{cases}$$

where the discrete normal forces and bending moments, $\mathbf{n}^h$ and $\mathbf{m}^h$, following from (6.18), are:

$$\mathbf{n}^h = d\,\mathbf{C}\boldsymbol{\varepsilon}^h\,, \qquad \mathbf{m}^h = \frac{d^3}{12}\mathbf{C}\boldsymbol{\kappa}^h\,. \tag{6.36}$$

One can express (6.35) in the following matrix equations, using the format (6.5) for explicit dynamics:

$$\begin{cases} \mathbf{M}\,\ddot{\boldsymbol{u}}^h = \mathbf{F}_{\text{ext}} - \mathbf{F}_{\text{int}}\left(\boldsymbol{\varepsilon}^h, \boldsymbol{\kappa}^h\right)\,, & \text{(6.37a)} \\ \underbrace{\begin{bmatrix} \mathbf{M}_\varepsilon & \\ & \mathbf{M}_\kappa \end{bmatrix}}_{\mathbf{M}_E} \begin{bmatrix} \hat{\boldsymbol{\varepsilon}}^h \\ \hat{\boldsymbol{\kappa}}^h \end{bmatrix} = \begin{bmatrix} \mathbf{F}_\varepsilon(\boldsymbol{u}^h) \\ \mathbf{F}_\kappa(\boldsymbol{u}^h) \end{bmatrix}\,. & \text{(6.37b)} \end{cases}$$

The mass matrix $\mathbf{M}$ corresponds to the first term of (6.35a), the external force vector $\mathbf{F}_{\text{ext}}$ is its right-hand side, and the internal force vector $\mathbf{F}_{\text{int}}$ is its second and third terms that are the membrane and bending parts, respectively. Equation (6.37b) represents the collection of both (6.35b) and (6.35c), after bringing the second term in each equation to the right-hand side. We note that the matrices $\mathbf{M}_\varepsilon$ and $\mathbf{M}_\kappa$ are equivalent, since we use the same spline basis to discretize $\boldsymbol{\varepsilon}$ and $\boldsymbol{\kappa}$, as well as $\delta\boldsymbol{\varepsilon}$ and $\delta\boldsymbol{\kappa}$ (see (6.32) and (6.33)).

6.4.3 Projection of strain fields

In the semidiscrete formulation (6.37) (or (6.35)), we observe that (6.37a) corresponds to the equations of motion and (6.37b) corresponds to the L^2 projection of the displacement-based strain fields, $\mathscr{E}_\varepsilon \cdot \boldsymbol{u}^h$ and $\mathscr{E}_\kappa \cdot \boldsymbol{u}^h$, onto the space $\mathcal{S}^h$ of the independent strain variable fields, $\boldsymbol{\varepsilon}^h$ and $\boldsymbol{\kappa}^h$. In explicit dynamics calculations, updating the internal force vector, $\mathbf{F}_{\text{int}}$, in (6.37a) at each time step requires the solution of this projection to interpolate $\boldsymbol{\varepsilon}^h$ and $\boldsymbol{\kappa}^h$. As discussed in [188], discretizing the trial and test functions, $\boldsymbol{\varepsilon}^h$ and $\delta\boldsymbol{\varepsilon}^h$, with the standard B-splines and the modified approximate dual functions (6.34), respectively, results in $\mathbf{M}_\varepsilon$ that is an approximation of the identity matrix $\mathbf{I}$. Row-sum lumping $\mathbf{M}_\varepsilon$ indeed yields the identity matrix $\mathbf{I}$ [132], [188], which also holds for $\mathbf{M}_\kappa$, since these two

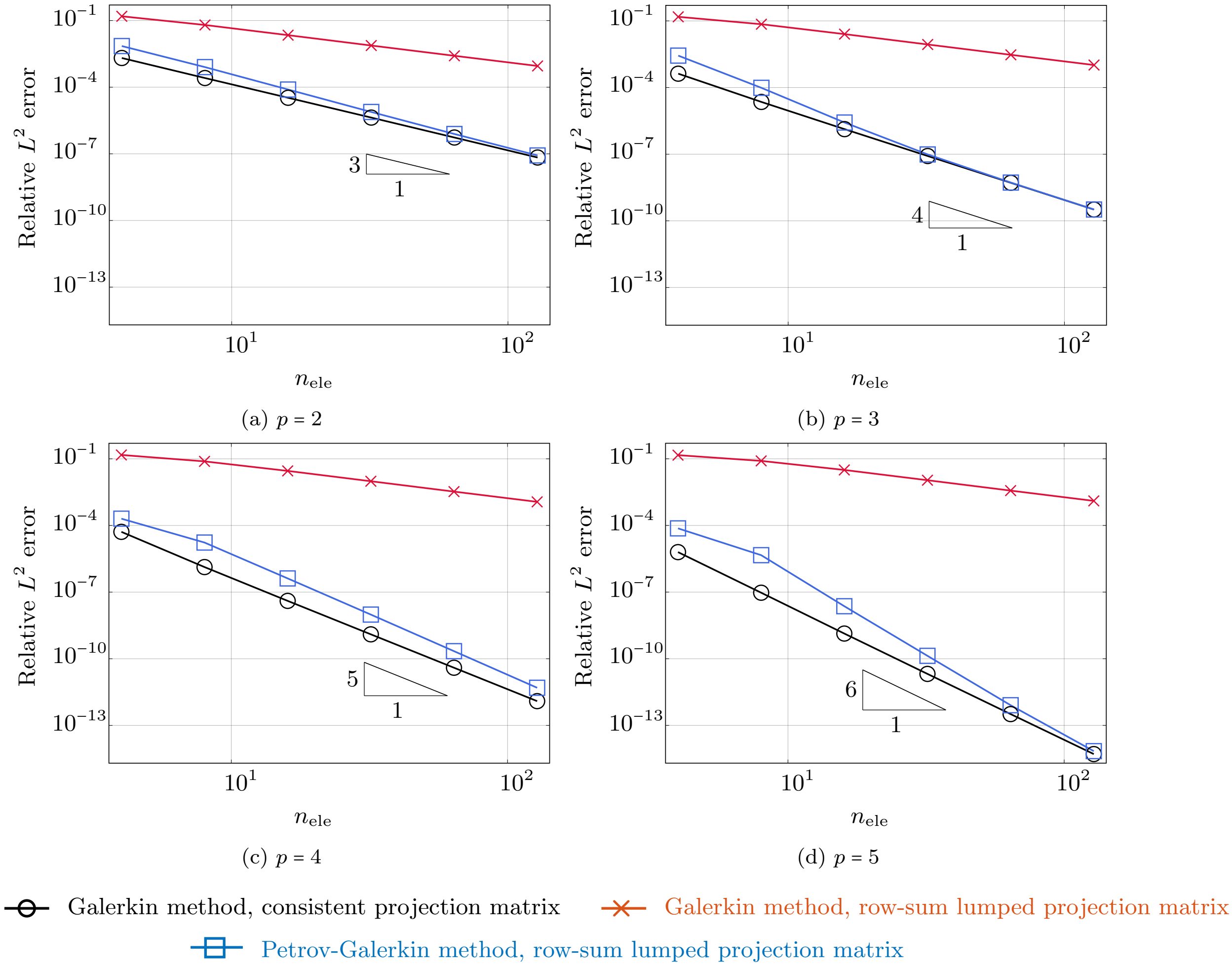

(a) $p = 2$

(b) $p = 3$

(c) $p = 4$

(d) $p = 5$

Figure 6.5: Convergence of the relative L^2 error in the projected function $f(x)$ on a quarter circle NURBS-curve, computed with different approaches.

matrices are the same. This necessarily means that row-sum lumping $\mathbf{M}_E$ yields the identity matrix $\mathbf{I}$, and (6.37b) then becomes:

$$\mathbf{I}\begin{bmatrix}\hat{\boldsymbol{\varepsilon}}^h \\ \hat{\boldsymbol{\kappa}}^h\end{bmatrix} = \begin{bmatrix}\mathbf{F}_\varepsilon(\boldsymbol{u}^h) \\ \mathbf{F}_\kappa(\boldsymbol{u}^h)\end{bmatrix} \qquad \text{or} \qquad \begin{bmatrix}\hat{\boldsymbol{\varepsilon}}^h \\ \hat{\boldsymbol{\kappa}}^h\end{bmatrix} = \begin{bmatrix}\mathbf{F}_\varepsilon(\boldsymbol{u}^h) \\ \mathbf{F}_\kappa(\boldsymbol{u}^h)\end{bmatrix}. \tag{6.38}$$

Hence, we observe in (6.38) that the need for solving (6.37b) to update $\mathbf{F}_{\text{int}}$ is indeed eliminated. We note that (6.38) also eliminates the static condensation step in reformulating the mixed formulation to the displacement-based formulation.

Remark 6.4.1. *When using the standard Galerkin method,* $\mathbf{M}_E$ *can also be row-sum lumped to avoid solving a system for strain projection* (6.37b) *[221], [222]. While the computational cost becomes comparable to our approach, the accuracy is severely affected* *(to be illustrated in the following).*

To illustrate the approximation power of the Petrov-Galerkin approach, we plot the convergence of the relative L^2 error in the projection of a function $f(x) = \sin(x)\,\cos(x)$ on a quarter circle NURBS-curve, computed with quadratic, cubic, quartic, and quintic discretizations in Fig. 6.5. We compare the accuracy and convergence behavior obtained with the standard Galerkin method with consistent projection matrix (black), the Galerkin method with row-sum lumped projection matrix (red), and our Petrov-Galerkin method with row-sum lumped projection matrix (blue). We observe that the Petrov-Galerkin approach leads to results that are several orders of magnitude more accurate than the Galerkin approach with lumped strain projection. It achieves the same optimal convergence rate as the Galerkin method with consistent projection matrix, but at a slightly higher error level. We also see that the accuracy of the projection with the Galerkin method is significantly affected by row-sum lumping, limiting the convergence rate to second order irrespective of the polynomial degree of the spline basis.

6.4.4 Higher-order accurate mass lumping

In addition to lumping the strain projection matrix, we adopt the higher-order accurate mass lumping scheme introduced in [132], [188] when using our Petrov-Galerkin mixed formulation. Hence, we row-sum lump the mass matrix $\mathbf{M}$ of (6.37a), which again yields the identity matrix. This eliminates the need for matrix inversion and preserves higher-order spatial accuracy in explicit dynamics [132], [188]. When it comes to strong Dirichlet boundary conditions, we use the new boundary treatment recently introduced in [132], which preserves the approximate bi-orthogonality for the complete system and allows row-sum lumping of the entire mass matrix without compromising higher-order accuracy.

6.4.5 Computational cost

The computational cost in explicit dynamics primarily depends on the critical time step size, the number of quadrature points, and the evaluation of the internal force vector per quadrature point. We expect that the first two aspects do not differ significantly between the isogeometric Galerkin method and our isogeometric Petrov-Galerkin method. In this work, we will remove spurious outlier modes, see Section 6.3.4 [122], to increase the critical time step size. We will show that it allows a time step that is four or five times larger than without outlier removal, which directly translates in an equivalent speed-up. As for the number of quadrature points, we refer to advanced quadrature schemes for spline discretizations that significantly reduce the number of quadrature points with respect to standard Gauss quadrature per Bézier element [133], [171], [212]. In this work, we will apply the optimal rules presented in [133] that provide the minimum number of points at full accuracy. We will use these rules in the sense of reduced quadrature, using the rule that corresponds to the spline basis of one degree lower, which was shown to maintain full accuracy in [133].

For explicit dynamics computations based on mixed formulations such as (6.37) (or (6.35)), given a lumped mass matrix, an important additional factor that affects the computational cost is the solution of the strain projection equation (6.37b). One can mitigate this cost factor via lumping of the projection matrix $\mathbf{M}_E$ on the left-hand side (see e.g. [221], [222]). For the standard Galerkin method, however, the lumping of the projection matrix impedes higher-order accuracy, see the L^2 projection example shown in Section 6.4.3. In this work, we apply the modified approximate dual functions as test functions, which enables higher-order accurate row-sum lumping, without compromising higher-order accuracy. Approximate dual test functions in conjunction with row-sum lumping eliminates the need for solving the system of projection equations. Instead, we obtain an explicit expression of the strain fields, which can be directly employed in the evaluation of the internal force vector in the equations of motion. The discrete equations of motion themselves can be solved explicitly, without loss of accuracy, due to the same combined mechanism of approximate dial functions with subsequent row-sun lumping that leads to a diagonal mass matrix, as already demonstrated in [132], [188]. In the framework of the current mixed formulations, applying this mechanism to both systems is therefore crucial to ensure that the solution costs of all components are of the same order, and that the cost and memory advantages of the lumped mass matrix are not spoiled by a potentially higher-order solution cost of the strain projection system, with a system matrix to be stored.

As for the cost of the evaluation of the internal force vector, we need to have a closer look at the Petrov-Galerin scheme, as already outlined in [188]. Just as standard B-splines (or NURBS), the modified approximate dual basis functions can be cast into a Bézier or Lagrange extraction format per element [213], [214]. In a Petrov-Galerkin sense, bilinear stiffness forms are not symmetric, as we are using different test and trial functions on the right-hand side. In explicit dynamics, this is not an issue per se, as the stiffness matrix is never assembled, stored, or inverted. The central difference to the standard Galerkin scheme, however, is that the support of the approximate dual functions is up to $3p + 1$ Bézier elements in each parametric direction, as compared to only $p + 1$ for the corresponding B-spline. For two-dimensional elements, such as plates or shells, due to the increased support of the basis functions of the discrete test space, the internal force vector has eight to nine times as many entries, and we have to expect approximately eight to nine times as many basis function related operations to compute it. In practical scenarios, computationally costly routines to take into account nonlinear material behavior, such as radial return algorithms in plasticity, do not depend on the cost or number of the basis functions of the discrete test space, and hence the net increase in computational cost per quadrature point will be much lower. This aspect will require further attention in future studies, when production-level implementations of our Petrov-Galerkin type method will be available.

6.5 Numerical examples

In this section, we demonstrate the favorable numerical behavior of our Petrov-Galerkin scheme. We first illustrate that the Hellinger-Reissner mixed formulation eliminates the effect of membrane locking via spectral analysis of an Euler-Bernoulli circular ring and via convergence studies for the three examples of the shell obstacle course, using B-spline discretizations of degrees $p = 2$ through 5. We then demonstrate the higher-order accuracy of our approach in explicit dynamics via examples of a curved beam and a pinched cylinder. We compare the performance of our Petrov-Galerkin scheme with the standard Galerkin method based on consistent or row-sum lumped mass and projection matrices. We note that for conciseness, we refer to the entire system, including mass and projection matrices, when we talk about mass lumping in the following.

6.5.1 Spectral analysis of an Euler-Bernoulli ring

Based on studies in [135], we leverage spectral analysis of a slender Euler-Bernoulli circular ring to assess membrane locking. We note that the simplified version for one-dimensional problems of the mixed formulation for Kirchhoff-Love shells (6.35) is the Euler-Bernoulli mixed beam formulation (see e.g. [135]), which we employ for this example. To this end, we recall the discrete eigenvalue problem corresponding to the semidiscrete formulation (6.35a), expressed in matrix form:

$$\mathbf{K}\,\mathbf{U}_n^h = (\omega_n^h)^2\,\mathbf{M}\mathbf{U}_n^h\,, \tag{6.39}$$

where $\mathbf{U}_n^h$ denotes the vector of unknown coefficients corresponding to the n^{th} discrete eigenmode U_n^h, and ω_n^h the n^{th} discrete eigenfrequency. We note that the final stiffness matrix $\mathbf{K}$ of the eigenvalue problem based on the Hellinger-Reissner mixed formulation is obtained using static condensation. For more details of its derivation and spectral analysis in this context, we refer for instance to our previous paper [135] and the references therein.

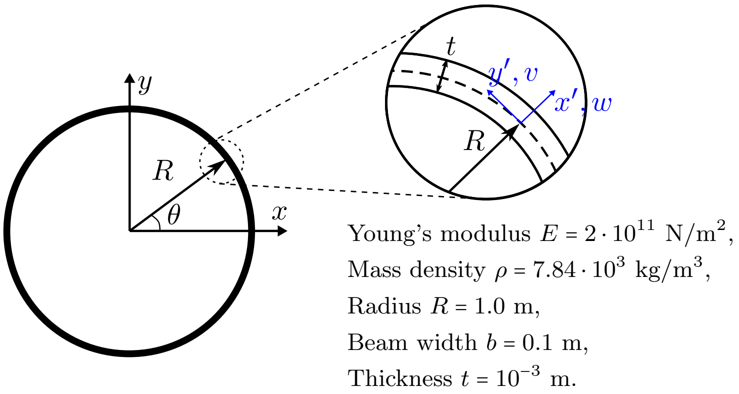

Figure 6.6: Closed circular steel ring modeled as a curved Euler-Bernoulli beam.

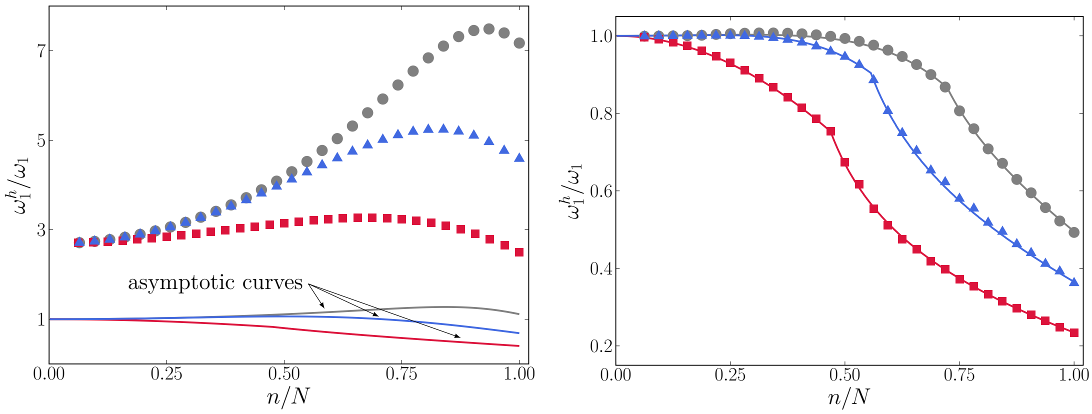

(a) Displacement-based formulation, $N = 32$

(b) Mixed formulation, $N = 32$

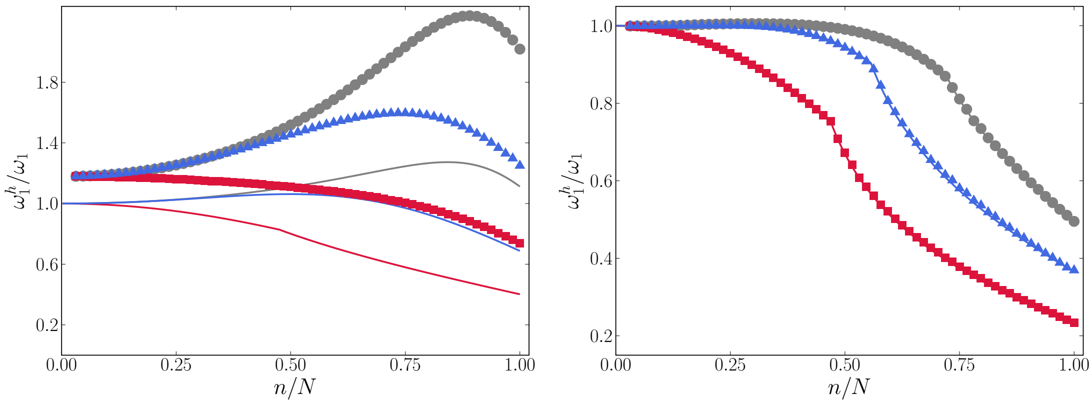

(c) Displacement-based formulation, $N = 64$

(d) Mixed formulation, $N = 64$

● Galerkin, consistent mass

■ Galerkin, row-sum lumped mass

▲ Petrov-Galerkin, higher-order accurate lumped mass

— asymptotic spectrum (2048 ele)

Figure 6.7: Normalized eigenfrequency ω_1^h (associated with transverse modes) of the ring computed with quadratic B-splines. The continuous lines show the asymptotic curves of each method and case computed with 2,048 elements ($N = 1,024$).

Fig. 6.6 illustrates the studied ring that is assumed to be undamped and unconstrained, for which an analytical solution of its eigenvalue problem exists [174], [228]. Based on the results shown in [135], we consider only the accuracy of the discrete eigenfrequencies corresponding to the transverse modes that are affected by membrane locking. We compute the spectrum using periodic uniform B-splines and their corresponding modified approximate dual functions. We strongly enforce the periodicity as a boundary constraint in both of these bases, as discussed in Section 6.3.3. To isolate the effect of locking and unlocking on the spectral accuracy, we always perform a consistent strain projection and use the full quadrature rule. We compare the discrete eigenfrequencies, normalized by the exact one, ω_1^h/ω_1, and plotted as a function of the normalized mode

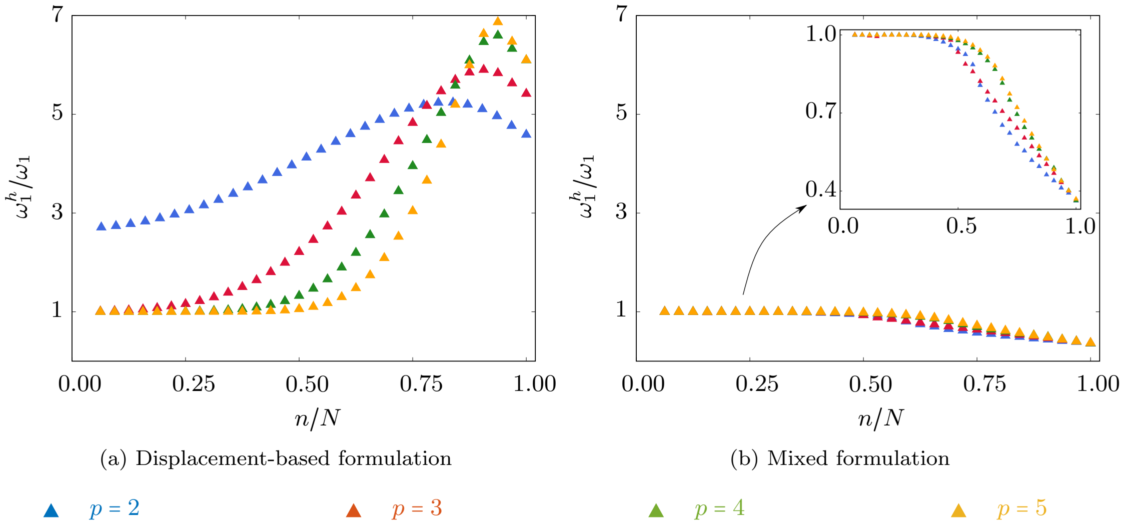

(a) Displacement-based formulation

(b) Mixed formulation

Figure 6.8: Petrov-Galerkin method with lumped mass matrix: normalized eigenfrequency (associated with transverse modes) of the ring computed on a mesh of 64 elements ($N = 32$) for increasing polynomial degrees $p = 2$ to 5.

number, n/N, obtained with the Hellinger-Reissner mixed formulation and the standard displacement-based formulation. We employ for each formulation the standard Galerkin consistent mass matrix (circles), the standard Galerkin row-sum lumped mass matrix (squares), and our Petrov-Galerkin row-sum lumped mass matrix (triangles).

We start by comparing the spectrum obtained with the displacement-based and the mixed formulations using quadratic spline functions, plotted on the left and right columns in Fig. 6.7, respectively. We adopt the locking indicator introduced in [135], and hence, include the asymptotic curve of each case that is computed on a mesh of 2,048 elements. On the one hand, we observe that the transverse frequencies obtained with the displacement-based formulation show significant error levels with the spectrum being far away from the asymptotic reference, irrespective of the mass lumping scheme. This error level can be reduced by refining the mesh, as illustrated in Fig. 6.7c. On the other hand, using the mixed formulation leads to a spectrum that matches well with its asymptotic curve in all cases, irrespective of the mesh size. We conclude that membrane locking affects the Galerkin and our Petrov-Galerkin methods in terms of spectral accuracy in the same way. The locking effect does not depend on mass lumping and can be eliminated by using the Hellinger-Reissner mixed formulation.

In [135], we reported the diverging frequencies corresponding to high modes with increasing polynomial degree as another effect of membrane locking. Focusing on this effect, we carry out a p-refinement study on a fixed mesh of 64 Bézier elements, using quadratic, cubic, quartic, and quintic basis functions. We compare the spectra computed with the displacement-based (left) and the mixed formulation (right) in Fig. 6.8. We observe that for the dsiplacement-based formulation, the frequencies corresponding to high modes, obtained with our Petrov-Galerkin approach, also diverge with increasing polynomial degree, as observed for the Galerkin method in [135]. Using the mixed formulation removes this divergence and the error of these frequencies remains at the same level. We conclude that our Petrov-Galerkin approach behaves in the same way as the Galerkin method, exhibiting a distinct locking effect on the high modes, which can be removed by using the mixed formulation.

6.5.2 Shell obstacle course

To illustrate that our Petrov-Galerkin mixed formulation with mass lumping of the projection matrix effectively removes membrane locking and achieves comparable accuracy to the Galerkin mixed formulation with a consistent mass matrix in the projection, we consider the three elastostatic benchmarks of the shell obstacle course [229]. We note that to ensure that we isolate locking and unlocking and exclude the influence of other potential error sources, we apply the full instead of a reduced quadrature rule [133].

Scordelis-Lo roof

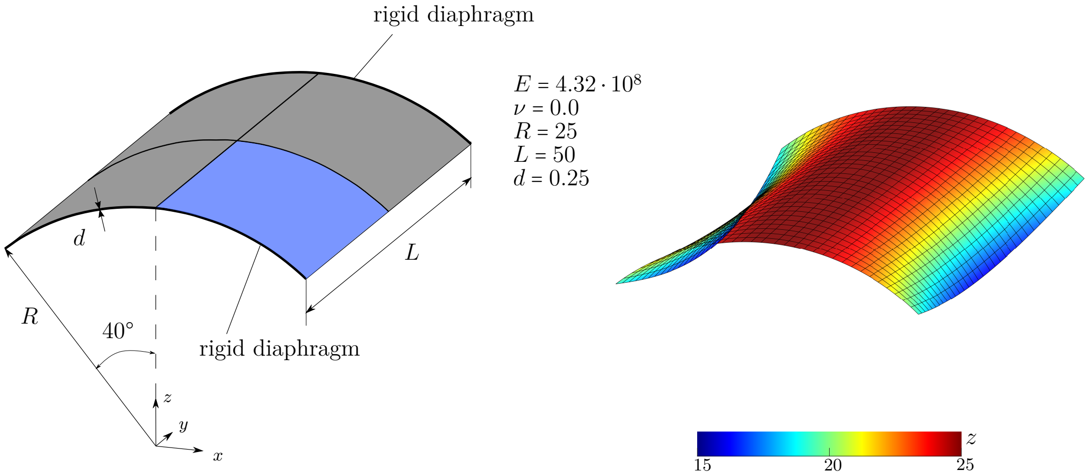

Figure 6.9: Scordelis-Lo roof constrained by rigid diaphragms and subjected to its self-weight of 90.0 per unit area. The deformations are illustrated with displacements scaled by a factor of 10.

The first example is the Scordelis-Lo roof subjected to its self-weight of 90.0 per unit area, illustrated in Fig. 6.9a. For discretization, we exploit the symmetry and model only a quarter of the structure marked in blue. Fig. 6.9b illustrates the deformed configuration, computed with our Petrov-Galerkin mixed formulation and cubic splines on a 16×16 mesh.

For quadratic and cubic basis functions, we first plot the convergence of the normalized displacement at the midpoint of the free edge in Fig. 6.10, where reference solutions exist, see e.g. [48], [229]. We observe that the Galerkin displacement-based formulation leads to less accurate results on coarse meshes, likely a result of membrane locking. This effect is reduced with increasing polynomial degree and eliminated when using the mixed

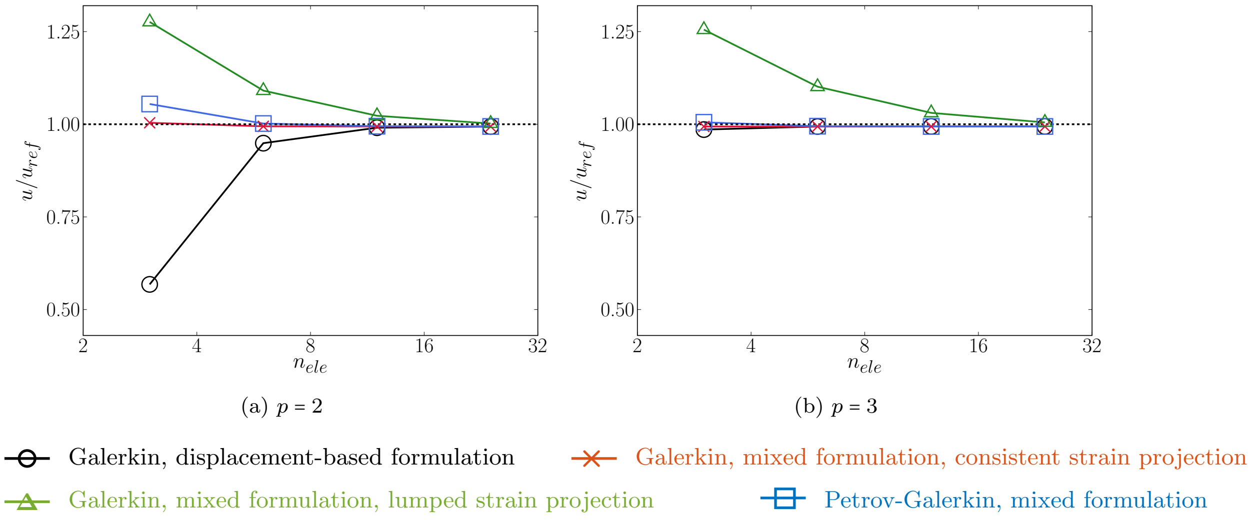

(a) $p = 2$

(b) $p = 3$

Figure 6.10: **Scordelis-Lo roof**: Convergence of the normalized vertical displacement at the midpoint of the free edge, computed with different formulations.

formulation. Consistent with the observations above, we see that the Galerkin mixed formulation using a lumped mass matrix in the strain projection results in significantly larger errors in the deformation.

We then carry out uniform h-refinement using the sequence of 3, 6, 12, and 24 elements per edge and smooth B-splines of degree $p = 2$ through 5. In Fig. 6.11, we plot the convergence of the relative error in the H^2 semi-norm in the stress resultant m^{12}. As a reference, we compute an overkill solution with the Galerkin mixed formulation on a mesh of 128×128 Bézier elements, using smooth B-splines of degree $p = 7$. We compare the error obtained with the Galerkin displacement-based formulation (black), the Galerkin mixed formulation with either a consistent (red) or lumped (green) mass matrix in the strain projection, and our Petrov-Galerkin mixed formulation (blue) with a lumped mass matrix in the strain projection. Focusing on the two Galerkin methods, we observe in Fig. 6.11 that the displacement-based formulation shows a slightly higher error level on coarse meshes, but converges to the same error level at the optimal rate of $\mathcal{O}(p-1)$ [137], [138] when the mesh is refined. We can also see that the error difference on coarse meshes is reduced with increasing polynomial degree. These observations indicate the well-known effect of membrane locking on the accuracy and convergence behavior. Comparing the red and the green curves, i.e. the results obtained with the Galerkin mixed formulation with a consistent and lumped mass matrix in the strain projection, respectively, we see that the latter leads to significantly larger errors and a linear convergence, irrespective of the polynomial degree. This is consistent with the observations above and illustrates the dominating impact of mass lumping in the strain projection on the accuracy and convergence of the corresponding discretization. Focusing on our Petrov-Galerkin mixed formulations (blue) and the Galerkin mixed formulation

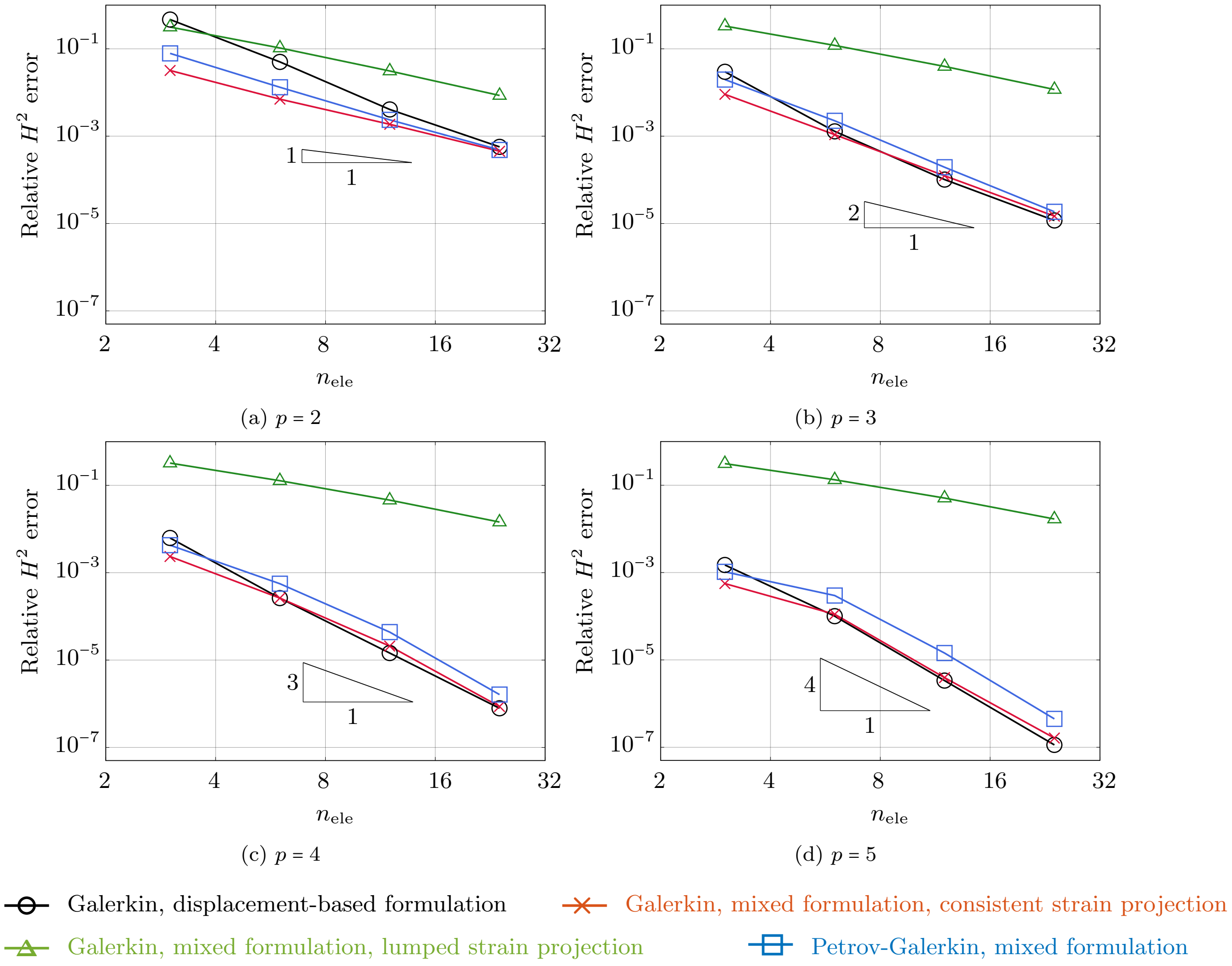

(a) $p = 2$

(b) $p = 3$

(c) $p = 4$

(d) $p = 5$

Figure 6.11: **Scordelis-Lo roof**: Convergence of the relative error in H^2 semi-norm in the stress resultant m^{12}, computed with different formulations.

with a consistent mass matrix in the strain projection (red), we observe that the former shows a slightly higher error level than the latter, nevertheless, has the same order of magnitude and converges to the same error when the mesh is refined.

Pinched cylinder

The second example is a pinched cylinder subjected to two opposite unit loads in the middle, illustrated in Fig. 5.20a. We again exploit the symmetry and model only one-eighth of the structure marked in blue. Figure 5.20b illustrates the deformed configuration, computed with our Petrov-Galerkin mixed formulation and cubic splines on a 16 × 16 mesh.

For quadratic and cubic basis functions, we plot the convergence of the normalized

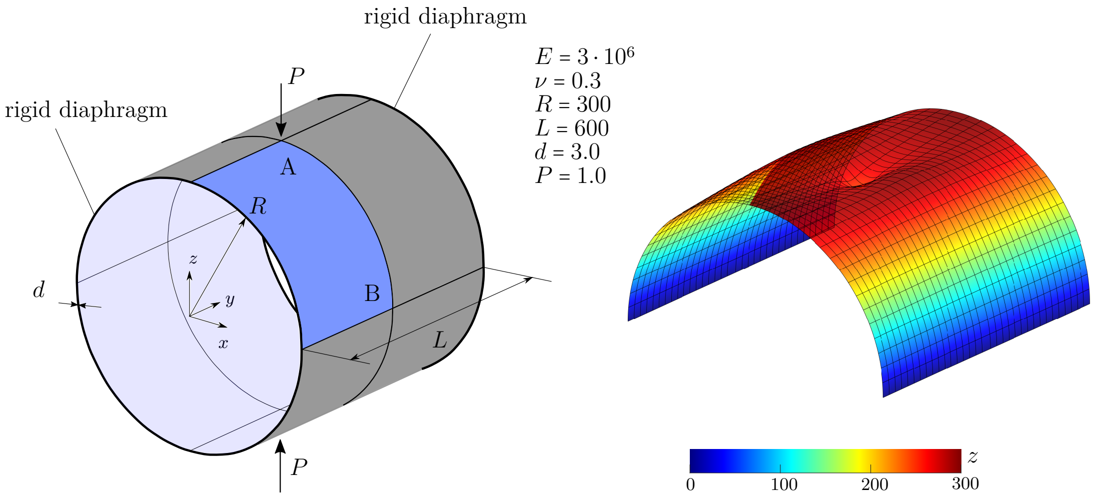

Figure 6.12: Pinched cylinder constrained by rigid diaphragms. The deformations are illustrated with displacements scaled by a factor of $3 \cdot 10^6$.

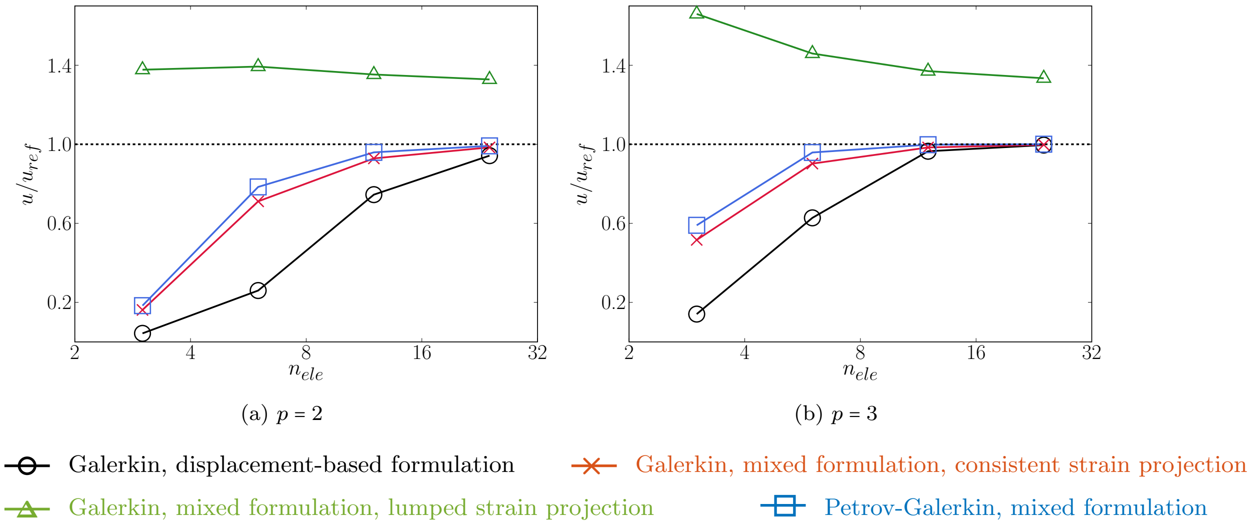

(a) $p = 2$

(b) $p = 3$

Figure 6.13: **Pinched cylinder**: Convergence of the normalized displacement under the load, computed with different formulations.

displacement at point A under the pinching load in Fig. 6.13, for which reference solutions exist, see e.g. [48], [229]. We also observe less accurate results on coarse meshes when using the Galerkin displacement-based formulation (black), likely due to membrane locking. Increasing the polynomial degree or using the mixed formulation improves the accuracy and the convergence. We see that, in contrast to the Scordelis-Lo roof above, the cylinder requires finer meshes to achieve the same accuracy. Focusing on the results obtained with the Galerkin mixed formulation with a lumped mass matrix in the strain

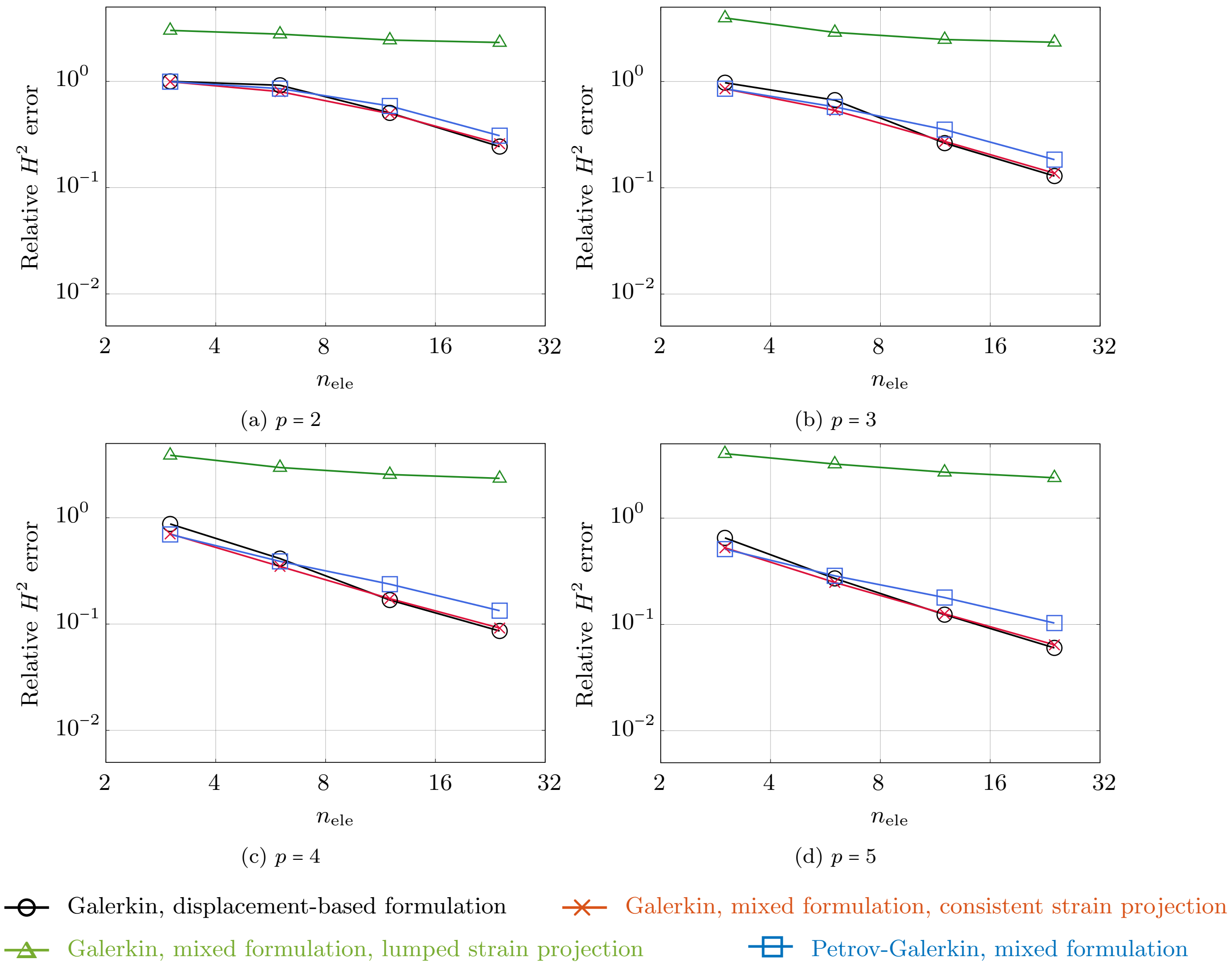

(a) $p = 2$

(b) $p = 3$

(c) $p = 4$

(d) $p = 5$

Figure 6.14: **Pinched cylinder**: Convergence of the relative error in H^2 semi-norm in the stress resultant m^{12}, computed with different formulations.

projection (green), we again observe significantly larger errors in the displacements. The results do not seem to converge to the reference value when the mesh is refined, but to a larger value.

We also carry out the same uniform h-refinement study as above and plot the convergence of the relative error in the H^2 semi-norm in the stress resultant m^{12} in Fig. 6.14. We use an overkill solution computed with the Galerkin mixed formulation on a mesh of 128×128 Bézier elements, using smooth B-splines of degree $p = 7$. We again compare the four aforementioned approaches. Focusing on the Galerkin mixed formulation with either a consistent (red) or a lumped (green) mass matrix in the strain projection, we observe the same dominating error due to mass lumping, which leads to significantly larger errors. Our Petrov-Galerin mixed formulation (blue) exhibits a slightly increased error level under refinement compared to the Galerkin mixed formulation with a consistent mass matrix in the strain projection (red).

Hemispherical shell

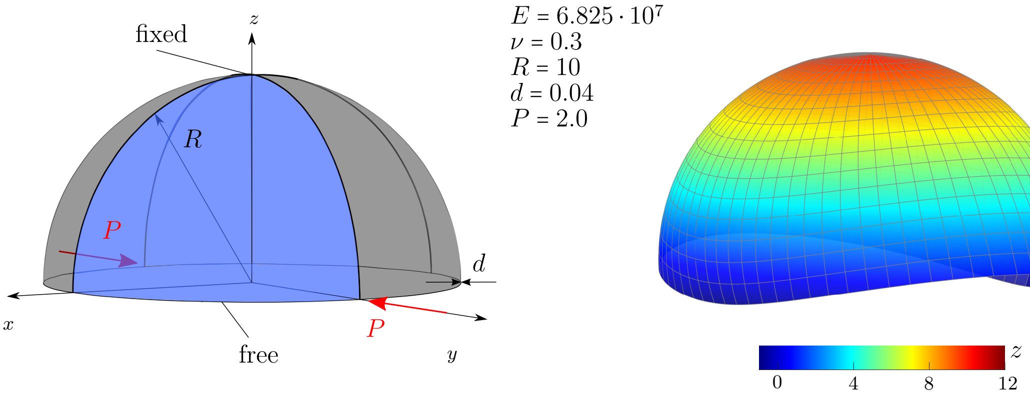

Figure 6.15: Hemispherical shell fixed at the top. The deformations are illustrated with displacements scaled by a factor of 20.

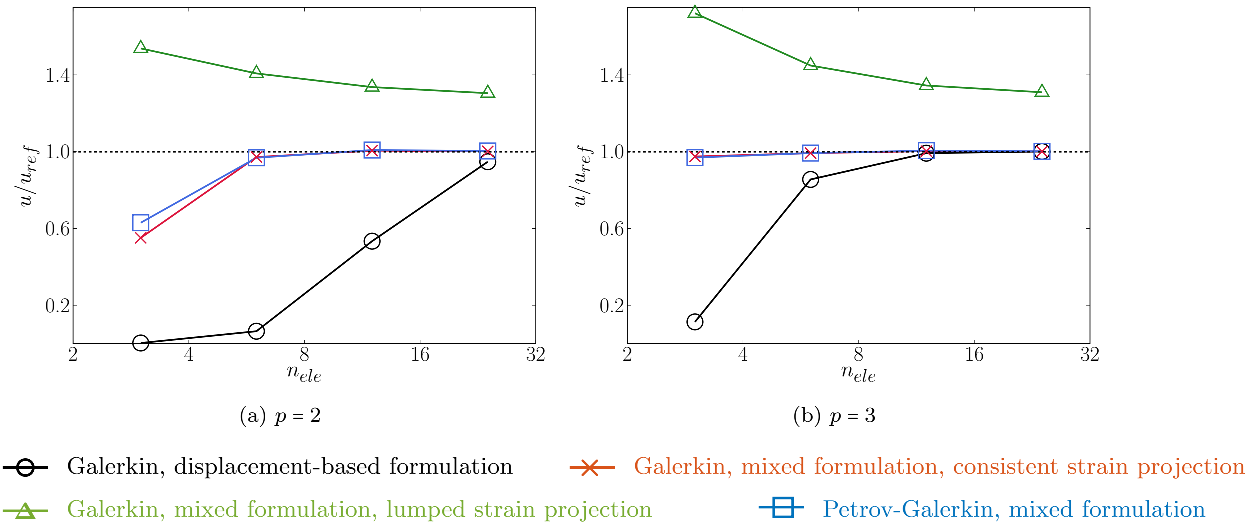

(a) $p = 2$

(b) $p = 3$

Figure 6.16: **Hemispherical shell**: Convergence of the normalized radial displacement under the load, computed with different formulations.

The third example is a hemispherical shell subjected to two opposite loads in the xy-plane, illustrated in Fig. 6.15a. We also exploit the symmetry and model only a quarter of the structure marked in blue. Figure 6.15b illustrates the deformed configuration,

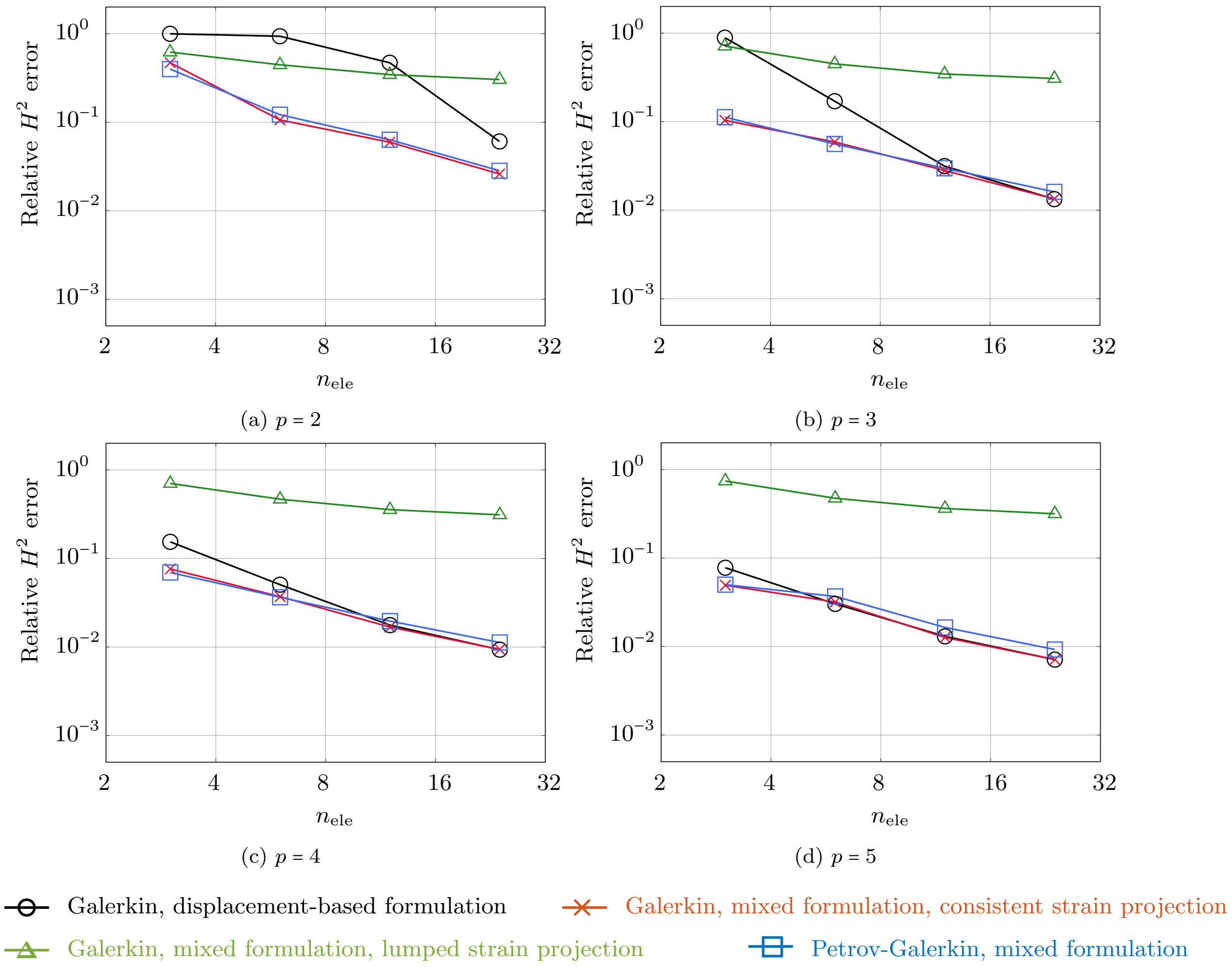

(a) $p = 2$

(b) $p = 3$

(c) $p = 4$

(d) $p = 5$

Figure 6.17: **Hemispherical shell**: Convergence of the relative error in H^2 semi-norm in the stress resultant m^{12}, computed with different formulations.

computed with our Petrov-Galerkin mixed formulation and cubic splines on a 16 × 16 mesh.

For quadratic and cubic basis functions, we again plot the convergence of the normalized radial displacement at the pinched point under the load in Fig. 6.16, where reference solutions exist, see e.g. [48], [229]. Similarly to the Scordelis-Lo roof and the pinched cylinder, we observe that the Galerkin displacement-based formulation (black) leads to less accurate results on coarse meshes, likely due to membrane locking. This locking effect is reduced with increasing polynomial degree and eliminated when using the mixed formulation. Consistent with the observations above, we see that using the Galerkin mixed formulation with a lumped mass matrix in the strain projection (green) leads to significantly overestimated displacement that does not seem to converge to the reference value when the mesh is refined.

We again carry out uniform h-refinement as above and plot the convergence of the relative error in the H^2 semi-norm in the stress resultant m^{12} in Fig. 6.17. As a reference, we again compute an overkill solution as above. We observe that in contrast to the Scordelis-Lo roof and the pinched cylinder, the Galerkin displacement-based formulation (black) leads to larger errors on coarse meshes than the mixed formulation with a consistent mass matrix in the strain projection (red). Particularly in the case of quadratic spline functions, we see a pre-asymptotic plateau, which indicates a typical effect of membrane locking. This effect is reduced with increasing polynomial degree or eliminated when using the mixed formulation. Focusing on the results obtained with the Galerkin mixed formulation with a lumped mass matrix in the strain projection (green), we again observe significantly larger errors that do not seem to converge to the reference value. Focusing on our Petrov-Galerkin mixed formulation (blue), we see that it leads to approximately the same error as the Galerkin mixed formulation with a consistent mass matrix in the strain projection (red).

6.5.3 A vibrating curved Euler-Bernoulli beam

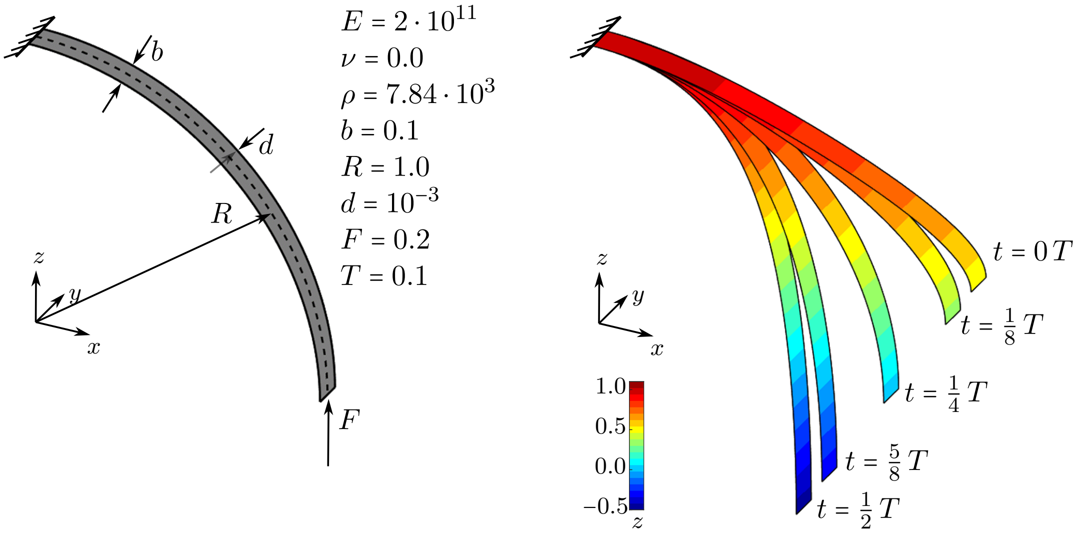

(a) Beam-like plate model

(b) Displacement snapshots

Figure 6.18: Beam-like shell model (circular cantilever). The displacements in (b) are scaled by a factor of 5.

Our first example in explicit dynamics is a vibrating circular beam that is modeled by a shell and subjected to a constant unit force at the free end, as illustrated in Fig 6.18a. Assuming small deformations, we can construct the following analytical solution from

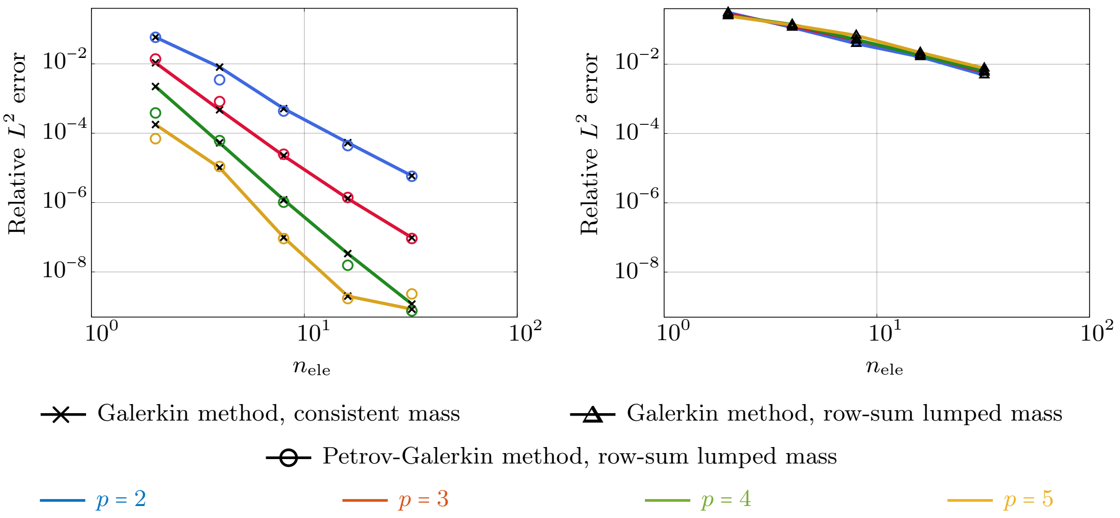

Figure 6.19: Circular beam-like shell: convergence of the relative L^2 error in the displacement solution at $t = T$.

Euler-Bernoulli beam theory:

$$\mathbf{u}(\theta,t)=\begin{pmatrix}\frac{F}{2}\left(\frac{R^3}{EI}-\frac{R}{EA}\right)\sin^2(\theta)\\ 0\\ \frac{F}{2}\left(\frac{R^3}{EI}+\frac{R}{EA}\right)\theta-\frac{F}{4}\left(\frac{R^3}{EI}-\frac{R}{EA}\right)\sin(2\theta)\end{pmatrix}\cos\left(\frac{2\pi}{T}\,t\right), \tag{6.40}$$

from which the initial and boundary conditions directly follow. We perform uniform mesh refinement in the arc length direction, using a sequence of 2, 4, 8, 16 and 32 elements and one Bézier element in y-direction, using smooth splines of degrees $p = 2$ through 5. We apply the central difference method for explicit time integration, simulating a full period of $T = 0.1$ s of the vibration history. We estimate the critical time step $\Delta t_{\text{crit}} = 6 \cdot 10^{-6}$ after removing the outliers on the finest mesh of 32 elements with quintic basis functions, which increases by almost a factor of four compared to the critical time step without outlier removal. We choose a time step of $\Delta t = 4 \cdot 10^{-6}$ s. To reduce the computational cost, we apply reduced quadrature [133], as discussed in Section 6.4.5. Figure 6.18b illustrates the solution snapshots obtained with our Petrov-Galerkin mixed formulation using quadratic spline functions and 16 Bézier elements at five different time instants.

Figure 6.19 illustrates the convergence behavior of the relative L^2 error in the displacements for the Galerkin mixed formulation with a consistent mass matrix (crosses), the Galerkin mixed formulation with a row-sum lumped mass matrix (triangles), and our Petrov-Galerkin method with a lumped mass matrix (circles). In general, we do not observe any pre-asymptotic plateau, but the errors converge right away on coarse meshes, asserting the expected behavior of locking-free discretizations. On the one hand, we observe that our approach achieves the same optimal accuracy under mesh refinement as the Galerkin method with a consistent mass matrix. Thus, the accuracy of our Petrov-Galerkin method based on test functions discretized by modified approximate dual functions is not affected by row-sum mass lumping. On the other hand, we observe that the accuracy of the Galerkin method is significantly affected by mass lumping, limiting its convergence to second order irrespective of the polynomial degree of the spline basis.

6.5.4 Explicit dynamics of a pinched cylindrical shell

We now focus on the explicit dynamics simulation of the pinched cylinder illustrated in Fig. 5.20, involving finite deformations, with the following parameters: Young's modulus $E = 3 \cdot 10^4$, Poisson's ratio $\nu = 0.3$, mass density $\rho = 7.8 \cdot 10^{-9}$, radius $R = 100$, length $L = 200$, and thickness $d = 1$. The pinching force is linearly increased from zero to $P_{\text{max}} = 4 \cdot 10^3$ during a simulation time of $T = 1/30$ s. We estimate the critical time step of $\Delta t_{\text{crit}} = 1 \cdot 10^{-6}$ s after removing the outliers on a fine mesh of 32 elements with quintic splines, which is increased by almost five times compared to the one without outlier removal. We subsequently choose a time step of $\Delta t = 2 \cdot 10^{-7}$ s, with a safety factor of 5 for this geometrically nonlinear problem, as discussed in Section 6.2.2. We apply the reduced quadrature rule discussed above.

To assess our Petrov-Galerkin mixed formulation, we compare its displacement response with the one obtained with the Galerkin mixed formulation and a row-sum lumped mass matrix. In Fig. 6.20, we plot the deformed configuration for half the cylinder, when P_{max} is reached, obtained with quadratic, cubic, quartic, and quintic basis functions on a mesh of 20 × 20 Bézier elements. As a reference, we also show the solution commonly used in the literature [208], which is obtained with the Galerkin displacement-based formulation and a consistent mass matrix on a much finer mesh of 32 × 32 Bézier elements. This resolution is known to be adequate for this problem and guarantees that membrane locking is controlled. We observe that our Petrov-Galerkin approach with mass lumping (right column) leads to accurate and stable results that agree well with the reference solutions (left column). While it seems to deliver an accurate solution for $p = 2$, the Galerkin method with a row-sum lumped mass matrix (middle column) leads to diverging and unstable solutions for larger polynomial degrees.

In Fig. 6.21, we plot the load-deflection curve at point A under the pinching load (see Fig. 5.20) obtained with different mesh sizes. We compare our Petrov-Galerkin mixed formulation (blue) with the Galerkin mixed formulation (red), both with mass lumping, computed with cubic (left column) and quintic basis functions (right column). We also include the reference solution obtained with the Galerkin displacement-based formulation with a consistent mass matrix on a 32 × 32 mesh (gray) as well as the quasi-static solution (black). We observe that on the one hand, the load-deflection curves obtained with our Petrov-Galerkin mixed formulation agrees well with the reference solutions when the mesh is refined. For 24 × 24 elements, it shows larger deformations before snap-through, but oscillates afterwards around the quasi-static solution. The Galerkin mixed formulation with lumping yields good results yields accurate results for cubics on the coarsest mesh, but the displacements response quickly diverges with mesh

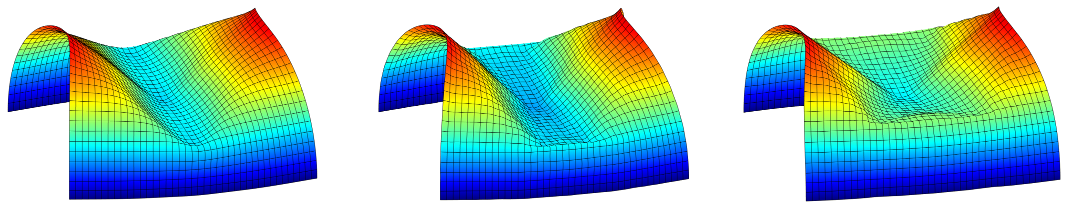

(a) $p = 2$

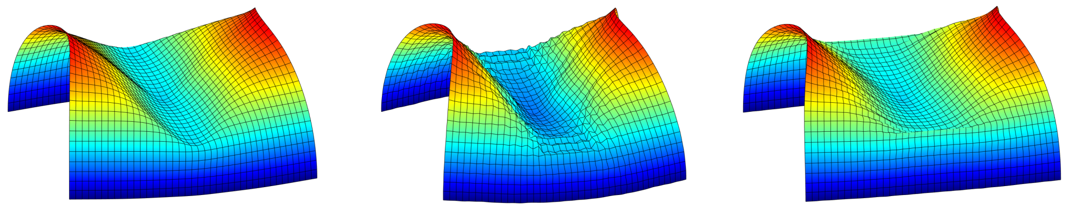

(b) $p = 3$

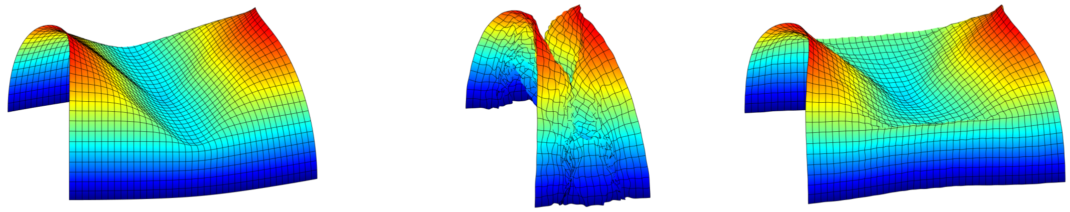

(c) $p = 4$

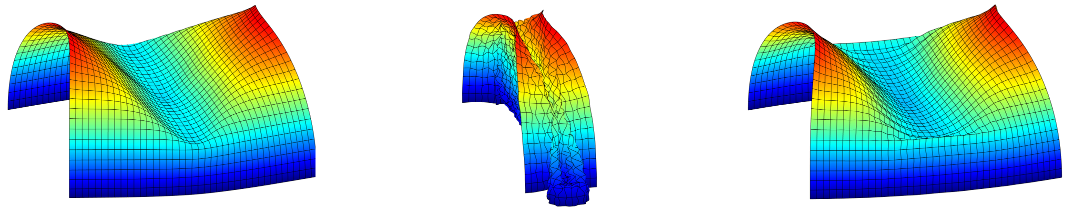

(d) $p = 5$

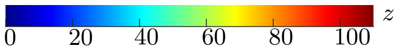

left: Galerkin, standard formulation, consistent mass, 32×32 elements

middle: Galerkin, mixed formulation, row-sum lumped mass

right: Petrov-Galerkin, mixed formulation, higher-order accurate lumped mass

Figure 6.20: Deformed configurations of the cylinder, computed with two different isogeometric schemes (middle and right columns), computed on a mesh of 20×20 Bézier elements, obtained at $P_{\max}$.

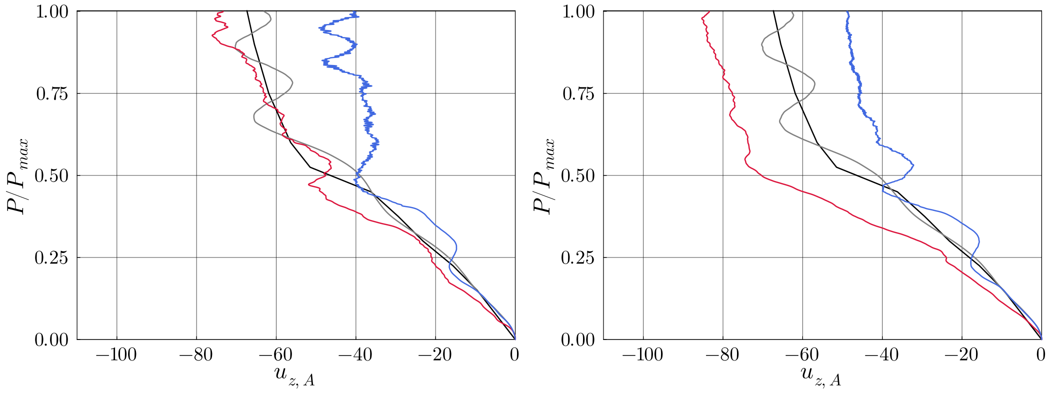

(a) $p = 3,\ 6 \times 6$ elements

(b) $p = 5,\ 6 \times 6$ elements

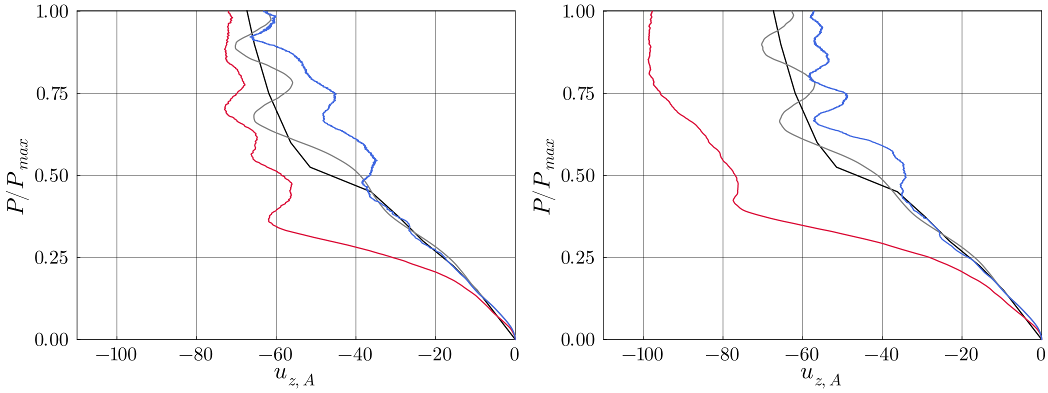

(c) $p = 3,\ 12 \times 12$ elements

(d) $p = 5,\ 12 \times 12$ elements

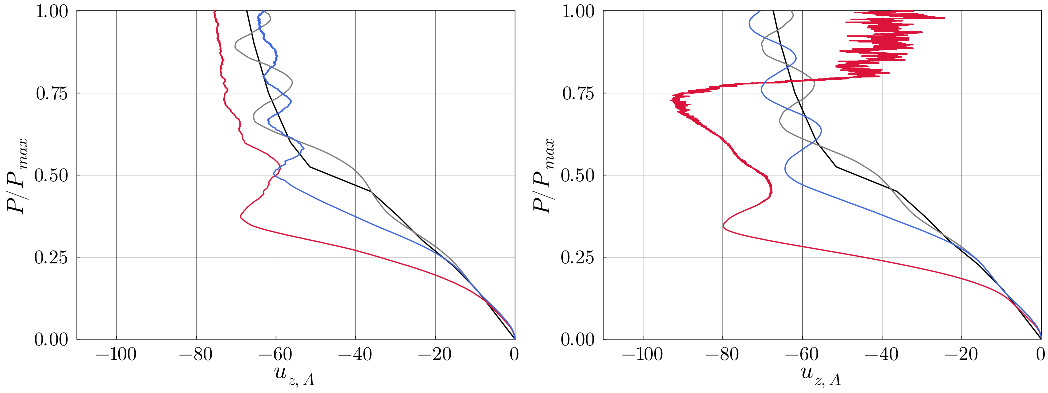

(e) $p = 3,\ 24 \times 24$ elements

(f) $p = 5,\ 24 \times 24$ elements

—— Static solution [218] —— Galerkin, displacement-based formulation, consistent mass, 32×32 elements

—— Galerkin, mixed formulation, row-sum lumped mass

—— Petrov-Galerkin, mixed formulation, higher-order accurate lumped mass

Figure 6.21: Load-deflection curves at **point A** (u_z) of the pinched cylinder, computed with two different isogeometric schemes.

refinement and for quintics overall. This observation is consistent with the results seen in Fig. 6.20 above. For $p = 5$ and a mesh of 24×24 Bézier elements, see Fig. 6.21f, the computation obviously turns unstable.

As we did not observe the robustness issues for the Galerkin mixed formulation with a consistent mass matrix in the strain projection, we conclude that in the case of nonlinear transient problems, the error induced by lumping of the strain projection matrix could become so dominant that the analysis becomes unstable. In contrast, when mass lumping is used, our Petrov-Galerkin method remains robust and accurate, and thus performs significantly better, particularly for higher-order discretizations, than the Galerkin method.

6.6 Summary and conclusions

In this paper, we described a Petrov-Galerkin mixed formulation based on the Hellinger-Reissner principle that considers the displacements and strains as two independent variable fields. When discretized with B-spline trial functions and associated modified approximate dual splines as test functions, it enables higher-order accurate lumping of both the mass matrix and the strain projection matrix, which opens the door for efficient higher-order accurate explicit dynamics simulations. The corresponding methodological groundwork has been worked out for the mass matrix alone in two recent papers [132], [188]. In addition, when used in the context of a Kirchhoff-Love shell model, it allows for an effective elimination of membrane locking by discretizing the strains with basis functions of one degree lower than the basis functions used for the displacements. We combined our approach with outlier removal, increasing the critical time step size, and employed a reduced quadrature rule.

We demonstrated via spectral analysis of a curved beam and convergence studies for several shell examples that our Petrov-Galerkin approach leads to locking-free, higher-order accurate and stable solutions in explicit dynamics, when both the mass and the projection matrix are lumped. For geometrically nonlinear shells, our results illustrate that our Petrov-Galerkin approach with lumping of the mass and projection matrices is robust and accurate irrespective of the polynomial degree of the discretization, in contrast to the Galerkin method with corresponding lumping, which became unstable for meshes beyond $p = 2$. Our results thus confirm that lumping of both the mass matrix and the projection matrix can be achieved without loss of accuracy and robustness in the context of isogeometric explicit dynamics calculations. On the one hand, our method thus enables robust locking-free analysis of beam and shell models. On the other hand, our method enables the solution of the discrete equations of motion and the discrete projection equations with the same computational complexity. Due to lumping, both systems can be solved with a complexity of $\mathcal{O}(n)$ and $\mathcal{O}(k)$, where n and k denote the number of discrete equations of motion and the number of discrete projection equations. In contrast, if the system matrix of the projection equations could not be lumped, the complexity of a Cholesky solver would be at best $\mathcal{O}(k^{3/2})$, and hence the cost of the strain projection would quickly dominate the solution time for large meshes.

Based on the current first study, there are various aspects that need to be explored and investigated further. One is an in-depth performance test of our Petrov-Galerkin approach for isogeometric shells in more involved scenarios that feature typical challenges in explicit dynamics calculations, including very large deformations, contact, nonlinear material behavior, and their combinations. Another one is a detailed analysis of the computational efficiency, in particular with respect to the computational cost of a competitive matrix-free implementation that fully exploits additional technical opportunities of spline functions such as the exploitation of their tensor-product structure [219]. Another question, for which no initial idea exists, is to extend the concept of the approximate dual basis as a test function space to trimmed Bézier elements.

7 Nonlinear dynamic analysis of shear- and torsion-free rods using isogeometric discretization, outlier removal and robust time integration

This chapter is reproduced from:

T.-H. Nguyen, B. A. Roccia, R. R. Hiemstra, C. G. Gebhardt, and D. Schillinger. *Nonlinear dynamic analysis of shear- and torsion-free rods using isogeometric discretization, outlier removal and robust time integration*, Submitted to Computational Mechanics, 2023 *(under review).*

Abstract

In this paper, we present a discrete formulation of nonlinear shear- and torsion-free rods based on [134] that uses isogeometric discretization and robust time integration. Omitting the director as an independent variable field, we reduce the number of degrees of freedom and obtain discrete solutions in multiple copies of the Euclidean space $\left(\mathbb{R}^3\right)$, which is larger than the corresponding multiple copies of the manifold $\left(\mathbb{R}^3 \times S^2\right)$ obtained with standard Hermite finite elements. For implicit time integration, we choose a hybrid form of the mid-point rule and the trapezoidal rule that preserves the linear angular momentum exactly and approximates the energy accurately. In addition, we apply a recently introduced approach for outlier removal [122] that reduces high-frequency content in the response without affecting the accuracy, ensuring robustness of our nonlinear discrete formulation. We illustrate the efficiency of our nonlinear discrete formulation for static and transient rods under different loading conditions, demonstrating good accuracy in space, time and the frequency domain. Our numerical example coincides with a relevant application case, the simulation of mooring lines.

7.1 Introduction

Nonlinear rods have a plethora of applications in science and engineering, for example, in the analysis of DNA molecules [230]–[232], the dynamics of cables [233], [234], the mechanical analysis of Möbius bands [235], or the stability of elastic knots [236], [237], among others. The shear-free model of rods is based on the assumption of cross-sections that remain flat and perpendicular to the tangent vector associated with the curve that describes the rod axis [238], [239]. In the context of linear rods, the Euler-Bernoulli and Rayleigh models are well-established [240], [241]. For nonlinear rods, one of the most widely used models is the so-called Kirchhoff rod, which can be considered a generalization of the Rayleigh model [242]–[244].

In general, it is not possible to formulate the governing equation of non-shearable rods through a truly unconstrained variational statement, particularly in dynamics problems, due to the non-integrable nature of vanishing shear deformations [238], [239]. In [245], Romero and Gebhardt developed an unconstrained variational formulation for this type of rod, but rely on certain simplification hypotheses. Recently, in [134], Gebhardt and Romero introduced a new unconstrained structural model for nonlinear initially straight rods that do not exhibit shear and torsion. This model provides a variational formulation for shear- and torsion-free rods and is a special case of the static and dynamic variational principles for nonlinear Kirchhoff rods developed in [245]. Moreover, it can be considered as the non-shearable counterpart of the torsion-free beam model introduced in [246].

Among the several approaches to solve the governing equations of non-shearable rods, we can mention classical nodal and isogeometric finite elements [247]–[251]. One of the key advantages of isogeometric finite elements is the higher-order smoothness of spline basis functions, which naturally fulfills the C^1 continuity required by the rod formulation. As a consequence, they have broad applications in the analysis of beam and shell structures, see e.g. [45]–[49], [252]–[254]. For the recently developed nonlinear rod formulation in [134], the spatial discretization scheme applied so far is the one based on nodal finite elements. It relies on cubic Hermite functions to represent the discrete rod configuration, which in turn is decomposed into nodal positions and nodal directors. We refer to this scheme hereinafter as the standard discretization scheme. The discrete solutions obtained lie in the manifold $\left(\mathbb{R}^3 \times S^2\right)^n$, where n is the number of discrete nodes. This discretization scheme establishes the first attempt to numerically solve the shear- and torsion-free Kirchhoff rod.

In this paper, we investigate an alternative spatial discretization scheme in the context of isogeometric analysis (IGA). In particular, we discretize the rod configuration in terms of the position of control points, without considering the director as an independent variable field. Hence, the number of degrees of freedom can be reduced and the discrete solution lies in multiple copies of the Euclidean space $\mathbb{R}^3$ which is a larger space than the corresponding multiple copies of the manifold $\left(\mathbb{R}^3 \times S^2\right)$ of the standard scheme. We utilize the higher-order smoothness of spline functions that naturally fulfill the C^1 continuity required by the rod formulation (and beyond). We demonstrate, via static benchmarks of two- and three-dimensional cantilever rods, that isogeometric discretizations and the standard scheme achieve a comparable level of accuracy. Moreover, we illustrate for a geometrically nonlinear cantilever rod bent to a circle that the convergence behavior is comparable to optimal convergence in the linear problem, but sub-optimal in the H^1 semi-norm and the L^2 norm.

For time integration in our dynamic computations, we employ the same implicit integration scheme as [134], which is a hybrid combination of the midpoint and trapezoidal rules. This type of implicit scheme has been shown to achieve second-order accuracy, approximately preserve the energy, and exactly preserves the linear angular momentum [255], [256]. We show, via dynamic benchmarks of two- and three-dimensional rods, that the isogeometric discretization scheme is less robust than the standard one. We improve its robustness via the strong approach of outlier removal introduced in [122]. We illustrate, via an example of an unconstrained rod subjected to out-of-plane vanishing forces, that the mass term associated to the inertia is irregular. Hence, the configuration-dependent mass matrix of the studied formulation behaves irregularly and, therefore, cannot be simplified to a constant matrix. Finally, we test our rod formulation for the nonlinear behavior of swinging rods under conservative, non-conservative, and pulsating forces. Our results indicate that our discrete isogeometric scheme is an efficient tool for such nonlinear computations.

The structure of the paper is as follows: In Section 7.2, we briefly review the nonlinear rod formulation. In addition, we derive the external forces induced by a surrounding flow, considered in our numerical examples. In Section 7.3, we discuss discretization in space with isogeometric finite elements, the resulting semi-discrete formulation, and differences when compared to the standard discretization scheme based on Hermite functions. We also briefly recap the implicit time integration scheme that is applied in our transient computations. In Section 7.4, we numerically demonstrate the robustness of isogeometric discretizations for two- and three-dimensional benchmarks and improve it via a strong approach for outlier removal. In Section 7.5, we apply the isogeometric nonlinear rod formulation to a swinging rubber rod subjected to different loading conditions, which can be considered as a relevant application case for the simulation of mooring lines. In Section 7.6, we summarize our results and draw conclusions.

7.2 Nonlinear shear- and torsion-free rods

In this section, we briefly review the formulation of nonlinear shear- and torsion-free rods in a continuous setting introduced in [134]. We then describe and derive the external forces induced by a surrounding flow that are considered in the numerical examples of this work. We start with a brief recap of required fundamental equations and definitions in differential geometry that are later utilized for the rod formulation.

7.2.1 Preliminaries

Consider an arbitrary regular one-parameter curve $\boldsymbol{\varphi} = \boldsymbol{\varphi}(s)$ in the ambient space $\mathbb{R}^3$, where $s \in [0, L]$ is the arc-length coordinate. Since $\boldsymbol{\varphi}$ is regular, its first derivative with respect to s, denoted as $\boldsymbol{\varphi}'$, is non-zero, i.e. $\boldsymbol{\varphi}' \neq \mathbf{0}$. The Frenet-Serret moving frame associated with the curve $\boldsymbol{\varphi}$ is then:

$$\mathbf{d} := \frac{\boldsymbol{\varphi}'}{|\boldsymbol{\varphi}'|}, \qquad \mathbf{t} := \frac{\boldsymbol{\varphi}''}{|\boldsymbol{\varphi}''|}, \qquad \mathbf{b} := \frac{\boldsymbol{\varphi}' \times \boldsymbol{\varphi}''}{|\boldsymbol{\varphi}' \times \boldsymbol{\varphi}''|}, \tag{7.1}$$

where $(\cdot)'$ denotes the first derivative with respect to the arc-length s, i.e. $(\cdot)' = \partial(\cdot)/\partial s$, and $|\cdot| : \mathbb{R}^3 \to \mathbb{R}_{\geq 0}$ denotes the Euclidean vector norm. We refer to $\mathbf{d}$ as the director of the curve $\boldsymbol{\varphi}$. We note that $\mathbf{t}$, and thus also $\mathbf{b}$, is ill-defined at points where $|\boldsymbol{\varphi}''| = 0$, while the director $\mathbf{d}$ is well-defined everywhere along the curve $\boldsymbol{\varphi}$.

The director $\mathbf{d}$ lives in the unit sphere $S^2 := \left\{\mathbf{d} \in \mathbb{R}^3 \,|\, \mathbf{d} \cdot \mathbf{d} = 1\right\}$ that is a nonlinear, smooth, compact, two-dimensional manifold [257], [258]. The tangent bundle associated with S^2 is also a manifold, which is given by $TS^2 := \left\{(\mathbf{d}, \mathbf{c}) \in S^2 \times \mathbb{R}^3, \mathbf{d} \cdot \mathbf{c} = 0\right\}$. We recall that the covariant derivative of a smooth vector field $\mathbf{v} : S^2 \to TS^2$ along a vector field $\mathbf{w} : S^2 \to TS^2$ is a vector field in TS^2 evaluated at $\mathbf{d}$, given by:

$$\nabla_{\mathbf{w}} \mathbf{v} := (\mathbf{I} - \mathbf{d} \otimes \mathbf{d})\, D\mathbf{v} \cdot \mathbf{w}, \tag{7.2}$$

where $\mathbf{I}$ denotes the identity matrix, and $D\mathbf{v}$ the derivative of $\mathbf{v}$. The covariant derivative $\nabla_{\mathbf{w}} \mathbf{v}$ is the projection of $D\mathbf{v}$ in the direction of $\mathbf{w}$ onto the tangent plane at $\mathbf{d}$ [257], [258].

For the rod formulation [134] considered in this work, we are particularly interested in the covariant derivative of $\boldsymbol{\varphi}'$ in the direction of $\mathbf{d}'$. Applying (7.2), this covariant derivative takes the following form [134]:

$$\nabla_{\mathbf{d}'} \boldsymbol{\varphi}' = \underbrace{(\mathbf{I} - \mathbf{d} \otimes \mathbf{d})}_{\mathcal{P}_{\mathbf{d}}} \boldsymbol{\varphi}'', \tag{7.3}$$

where $\mathbf{d}'$ is computed by taking the derivative of (7.1), i.e., $\mathbf{d}' = \frac{1}{|\boldsymbol{\varphi}'|} \mathcal{P}_{\mathbf{d}} \boldsymbol{\varphi}''$. We refer to $\mathcal{P}_{\mathbf{d}}$ as the orthogonal projection operator.

7.2.2 Strong and weak forms

Let the curve $\boldsymbol{\varphi}$ now be the configuration of Kirchhoff rods, dependent on the arc-length s and time t, $\boldsymbol{\varphi} = \boldsymbol{\varphi}(s, t)$, $(s, t) \in [0, L] \times [0, T]$, that are initially straight, shear-, torsion-free, and transversely isotropic [134]. Next, let us consider the following set for the rod configurations:

$$\mathcal{D} := \left\{\boldsymbol{\varphi} \in \left[C^2(0, L)\right]^3, \left|\boldsymbol{\varphi}'\right| > 0, \boldsymbol{\varphi}(0, t) = \mathbf{0}, \boldsymbol{\varphi}'(0, t) = \mathbf{E}_3\right\}, \tag{7.4}$$

where $C^2(0, L)$ is the space of C^2 continuous functions on $(0, L)$, $\mathbf{E}_i$, $i = 1, 2, 3$, are the canonical Cartesian basis of $\mathbb{R}^3$. For simplicity, we adopt here the clamped boundary condition at $s = 0$.

We recall, from [134], the strong form of the equations of motion governing the space-time evolution for the Kirchhoff rod:

$$\mathbf{n}' + \left(\frac{1}{|\boldsymbol{\varphi}'|} \mathbf{d} \times \nabla_{\mathbf{d}'} \mathbf{m} \right)' = A_\rho \ddot{\boldsymbol{\varphi}} + \left(\frac{1}{|\boldsymbol{\varphi}'|} \mathbf{d} \times I_\rho \nabla_{\dot{\mathbf{d}}} \dot{\mathbf{d}} \right)' - \mathbf{f}^{\mathrm{ext}} , \tag{7.5}$$

where $\mathbf{n}$ and $\mathbf{m}$ are the stress measures, defined as:

$$\mathbf{n} = EA\boldsymbol{\epsilon} , \qquad \mathbf{m} = EI\boldsymbol{\kappa} , \tag{7.6}$$

respectively, which are conjugated with the following strain measures:

$$\boldsymbol{\epsilon} := \boldsymbol{\varphi}' - \mathbf{d} , \qquad \boldsymbol{\kappa} := \mathbf{d} \times \mathbf{d}' . \tag{7.7}$$

Here, A_ρ and I_ρ are the mass per unit length and the inertia density, respectively, i.e. $A_\rho = \rho A$ and $I_\rho = \rho I$, where ρ is the mass density, A the cross-section area and I the moment of inertia of the rod. $\mathbf{f}^{\mathrm{ext}}$ is the external generalized forces, and the dot notation in the superscript denotes the derivative with respect to time t, i.e. $\dot{(\cdot)} = \partial(\cdot)/\partial t$. We note that since the director $\mathbf{d}$ is well-defined along the rod $\boldsymbol{\varphi} \in \mathcal{D}$ (see also (7.4)), as discussed in the previous subsection, the strain measures (7.7) are also well-defined at every point of the rod.

At time $t = 0$, we require the following initial conditions:

$$\boldsymbol{\varphi} = \boldsymbol{\varphi}_0 \qquad \text{on } (s, t) \in [0, L] \times [0] , \tag{7.8a}$$

$$\dot{\boldsymbol{\varphi}} = \mathbf{v}_0 \qquad \text{on } (s, t) \in [0, L] \times [0] . \tag{7.8b}$$

Additionally, we require at all times the following boundary conditions, for instance, clamped-free ends:

$$\text{on } (s, t) \in [0] \times [0, T] : \quad \boldsymbol{\varphi} = \mathbf{0} , \qquad \boldsymbol{\varphi}' = \mathbf{E}_3 , \tag{7.9a}$$

$$\text{on } (s, t) \in [L] \times [0, T] : \quad \mathbf{n} + \frac{1}{|\boldsymbol{\varphi}'|} \mathbf{d} \times \left(\nabla_{\mathbf{d}'} \mathbf{m} - I_\rho \nabla_{\dot{\mathbf{d}}} \dot{\mathbf{d}} \right) = \mathbf{0} , \tag{7.9b}$$

$$\frac{1}{|\boldsymbol{\varphi}'|} \mathbf{d} \times \mathbf{m} = \mathbf{0} . \tag{7.9c}$$

According to [134], the weak form corresponding to (7.5) is then:

$$\int_0^S \delta\boldsymbol{\varphi} \cdot \left(\mathcal{M}\left(\boldsymbol{\varphi}'\right) \hat{\nabla}_{\dot{\boldsymbol{\varphi}}} \dot{\boldsymbol{\varphi}} + \mathcal{B}\left(\boldsymbol{\varphi}', \boldsymbol{\varphi}''\right)^T \boldsymbol{\sigma} - \mathbf{f}^{\mathrm{ext}} \right) \mathrm{d}s = 0 , \tag{7.10}$$

where the mass operator, $\mathcal{M}$, and the linearized strain operator, $\mathcal{B}$, are given by:

$$\mathcal{M} = \mathcal{M}\left(\boldsymbol{\varphi}'\right) := A_\rho \mathbf{I} + (\cdot)'^T I_\rho \frac{1}{|\boldsymbol{\varphi}'|^2} \mathcal{P}_{\mathbf{d}} (\cdot)' \tag{7.11}$$

$$\mathcal{B} = \mathcal{B}\left(\boldsymbol{\varphi}', \boldsymbol{\varphi}''\right) := \begin{bmatrix} \mathbf{I} - \frac{1}{|\boldsymbol{\varphi}'|} \mathcal{P}_{\mathbf{d}} & \mathbf{0} \\ -\frac{1}{|\boldsymbol{\varphi}'|^2} \left[\boldsymbol{\varphi}''\right]_\times \mathcal{H}_{\mathbf{d}} & \frac{1}{|\boldsymbol{\varphi}'|} \left[\mathbf{d}\right]_\times \end{bmatrix} \begin{bmatrix} (\cdot)' \\ (\cdot)'' \end{bmatrix} . \tag{7.12}$$

Here, $\boldsymbol{\sigma} := [\mathbf{n} \quad \mathbf{m}]^T$, $\mathcal{H}_{\mathbf{d}}$ is the Householder operator[1], $\mathcal{H}_{\mathbf{d}} := \mathbf{I} - 2\,\mathbf{d} \otimes \mathbf{d}$, and $[\mathbf{a}]_\times$ denotes the skew-symmetric matrix of a vector $\mathbf{a} = [a_1 \quad a_2 \quad a_3]^T$, i.e.:

$$[\mathbf{a}]_\times = \begin{bmatrix} 0 & -a_3 & a_2 \\ a_3 & 0 & -a_1 \\ -a_2 & a_1 & 0 \end{bmatrix}.$$

The field covariant derivative $\hat{\nabla}_{(\cdot)}(\cdot)$ is the extension of the covariant derivative (7.2).

7.2.3 Simplified model of a force field induced by a surrounding flow

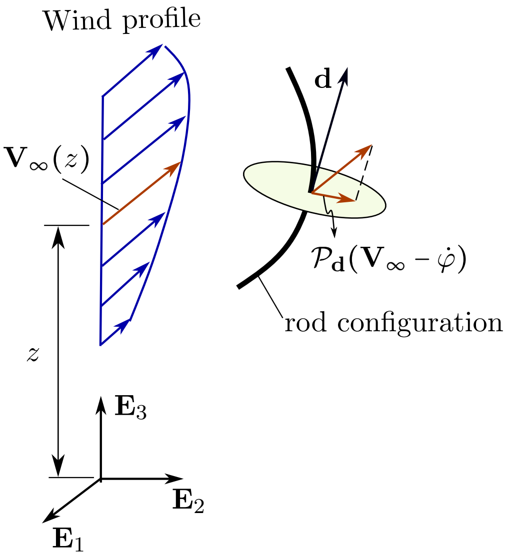

Figure 7.1: Schematic of a wind profile.

For the numerical examples included in subsequent sections, we consider forces induced by a surrounding flow such as wind and water. Fig. 7.1 illustrates the schematic of an exemplary wind profile acting on a rod configuration. We consider a simplified model of such forces [259] that consist of three counterparts: the resulting force due to the accelerated surrounding flow by the moving rod, which we refer to as the added mass force, the tangential drag force, and the normal drag force. To this end, the resulting force $\mathbf{F}_f$ per unit length at an arbitrary point of the rod is expressed as follows:

$$\mathbf{F}_f = C_1 \mathbf{a}_N + C_2 \left|\mathbf{V}_N\right| \mathbf{V}_N + C_3 \left|\mathbf{V}_T\right| \mathbf{V}_T\,, \tag{7.13}$$

where $\mathbf{a}_N$ is the normal component of the relative flow acceleration with respect to the rod, $\mathbf{V}_N$ and $\mathbf{V}_T$ the normal and tangential component of the relative flow velocity,

---

[1] The Householder operator is also known as a Householder reflection or elementary reflector.

respectively, and the coefficients C_1, C_2 and C_3 are given by:

$$\begin{aligned} C_1 &= \frac{1}{4}\pi\, C_M \rho_f\, \varnothing^2\,, \\ C_2 &= \frac{1}{2} C_N \rho_f\, \varnothing\,, \\ C_3 &= \frac{1}{2} C_T \rho_f\, \varnothing\,, \end{aligned} \tag{7.14}$$

where ρ_f is the mass density of the surrounding flow, and $\varnothing$ is the diameter of the cylindrical cross-section of the rod. The coefficients C_M, C_N, and C_T depend on the Reynolds number and are commonly determined experimentally [259].

To determine the forces acting on a rod segment of length ds due to the added mass, normal and tangential counterparts, it is necessary to describe the relative flow acceleration and velocity in terms of the ambient motion of the fluid and the rod. Considering the kinematic description of the rod given in the previous subsection, the quantities $\mathbf{a}_N$, $\mathbf{V}_N$, and $\mathbf{V}_T$ can be expressed as follows:

$$\begin{aligned} \mathbf{a}_N &= \mathcal{P}_{\mathbf{d}}\, \mathbf{a}, \\ \mathbf{V}_N &= \mathcal{P}_{\mathbf{d}} \mathbf{V}, \quad \text{and} \\ \mathbf{V}_T &= (\mathbf{d} \otimes \mathbf{d})\, \mathbf{V}, \end{aligned} \tag{7.15}$$

where $\mathbf{V} = \mathbf{V}_\infty - \dot{\boldsymbol{\varphi}}$, and $\mathbf{a} = \mathbf{a}_\infty - \ddot{\boldsymbol{\varphi}}$. The magnitude and direction of the free-stream velocity $\mathbf{V}_\infty(z,t)$ is a function of the height z above the ground level (or below the sea level if ocean structures are considered) and time t. The free-stream acceleration is the time derivative of the free-stream velocity, i.e., $\mathbf{a}_\infty(z,t) = \frac{\partial}{\partial t}\mathbf{V}_\infty(z,t)$. Inserting (7.15) into (7.13) and integrating along the rod, we obtain the resultant forces as follows:

$$\begin{aligned} \mathbf{F}_f = C_1 & \int_0^S \mathcal{P}_{\mathbf{d}}\, (\mathbf{a}_\infty - \ddot{\boldsymbol{\varphi}})\, ds \\ + C_2 & \int_0^S \left|\mathcal{P}_{\mathbf{d}}\, (\mathbf{V}_\infty - \dot{\boldsymbol{\varphi}})\right| \mathcal{P}_{\mathbf{d}}\, (\mathbf{V}_\infty - \dot{\boldsymbol{\varphi}})\, ds \\ + C_3 & \int_0^S \left|(\mathbf{d} \otimes \mathbf{d})\, (\mathbf{V}_\infty - \dot{\boldsymbol{\varphi}})\right| (\mathbf{d} \otimes \mathbf{d})\, (\mathbf{V}_\infty - \dot{\boldsymbol{\varphi}})\, ds. \end{aligned}$$

We note that coefficients C_i, $i = 1, 2, 3$, are assumed to be independent of the position along the rod.

7.3 Isogeometric discrete rod model and implicit time integration

In this section, we first discuss an alternative spatial discretization scheme of the rod formulation (7.10), reviewed in the previous section. We employ isogeometric discretizations, which utilize the higher-order continuity of smooth spline functions fulfilling the C^1-continuity required by the considered rod formulation. We show that this alternative discretization scheme yields different semi-discrete formulations, reduces the number of degrees of freedom, and leads to a larger solution space than the standard one based on nodal finite elements using cubic Hermite functions. We then numerically demonstrate, via a geometrically nonlinear rod bent to a circle, that the isogeometric discretizations show optimal convergence in H^2 semi-norm, and sub-optimal in H^1 semi-norm and L^2 norm. In addition, we briefly review the implicit time integration scheme employed in this work. We close this section with a discussion of applying the strong approach of outlier removal [122] to improve the robustness of isogeometric discretizations.

7.3.1 Spatial discretizations

The rod formulation (7.10) requires discretizations of at least C^1-continuity. To fulfill this, the standard discretization scheme based on nodal finite element employs cubic Hermite functions and discretizes both the nodal spatial position and nodal director as two variable fields [134]. In this work, we want to utilize the higher-order continuity of smooth spline functions that allow lower polynomial degree and one can omit the director as a variable field. Thus, we discretize the rod configuration, $\boldsymbol{\varphi}(s,t) \in \mathcal{D}$, and its variation, $\delta\boldsymbol{\varphi}(s,t)$, by a weighted finite sum of m B-splines, $N_i(s)$, with continuity C^r and polynomial degree p [1], [2], where r is the continuity order, $1 \leq r \leq p-1$, as follows:

$$\boldsymbol{\varphi}(s,t) \approx \boldsymbol{\varphi}_h(s,t) = \sum_i^m N_i(s)\,\mathbf{x}_i(t) = \mathbf{N}\,\mathbf{q}, \tag{7.16a}$$

$$\delta\boldsymbol{\varphi}(s) \approx \delta\boldsymbol{\varphi}_h(s) = \sum_i^m N_i(s)\,\delta\mathbf{x}_i = \mathbf{N}\,\delta\mathbf{q}. \tag{7.16b}$$

Here, $\boldsymbol{\varphi}_h = \boldsymbol{\varphi}_h(s,t) \in \mathbb{R}^3$ denotes the discrete rod configuration in space, $\mathbf{x}_i \in \mathbb{R}^3$ is the time-dependent position of the i^{th} control point, $\mathbf{q} = \mathbf{q}(t) \in (\mathbb{R}^3)^m$ is the vector of unknown time-dependent coefficients, and $\delta\boldsymbol{\varphi}_h(s)$, $\delta\mathbf{x}_i$, and $\delta\mathbf{q}$ their variations, respectively. The discrete director $\mathbf{d}$ and strain/stress measures follow directly from their definitions in (7.1) and (7.6)-(7.7), respectively.

Introducing (7.16) into the variational formulation (7.10), we obtain the following semi-discrete formulation:

$$\begin{aligned}&\text{Find } \mathbf{q}(t) \in \mathbb{R}^{3m}, t \in [0,T], \text{ such that:}\\ &\int_0^S \delta\mathbf{q} \cdot \left(\mathbf{M}(\mathbf{q})\,\nabla_{\dot{\mathbf{q}}}\,\dot{\mathbf{q}} + \mathbf{B}(\mathbf{q})^T \boldsymbol{\sigma}_h - \mathbf{N}^T\,\mathbf{f}^{\text{ext}}\right) \mathrm{d}s = \mathbf{0} \quad \forall\,\delta\mathbf{q} \in \mathbb{R}^{3m}.\end{aligned} \tag{7.17}$$

Here, the mass matrix $\mathbf{M}$ and the matrix $\mathbf{B}$, resulting from the operators (7.11) and (7.12), respectively, are:

$$\mathbf{M} = \mathbf{M}(\mathbf{q}) = \underbrace{A_\rho\,\mathbf{N}^T\,\mathbf{I}\,\mathbf{N}}_{\mathbf{M}_1} + \underbrace{I_\rho\,\frac{1}{|\boldsymbol{\varphi}_h'|^2}\left(\mathbf{N}'\right)^T\,\mathbf{P}_{\mathbf{d}}\,\mathbf{N}'}_{\mathbf{M}_2} \tag{7.18}$$

$$\mathbf{B} = \mathbf{B}(\mathbf{q}) := \begin{bmatrix} \mathbf{I} - \frac{1}{|\varphi_h'|}\mathbf{P_d} & \mathbf{0} \\ -\frac{1}{|\varphi_h'|^2}\left[\varphi_h''\right]_\times \mathbf{H_d} & \frac{1}{|\varphi_h'|}\left[\mathbf{d}_h\right]_\times \end{bmatrix} \begin{bmatrix} \mathbf{N}' \\ \mathbf{N}'' \end{bmatrix}, \tag{7.19}$$

with $\mathbf{P_d} = \mathbf{I} - \mathbf{d}_h \otimes \mathbf{d}_h$, and $\mathbf{H_d} = \mathbf{I} - 2\,\mathbf{d}_h \otimes \mathbf{d}_h$. The discrete stress measures $\boldsymbol{\sigma}_h$ are:

$$\boldsymbol{\sigma}_h = \begin{bmatrix} \mathbf{n}_h \\ \mathbf{m}_h \end{bmatrix} = \begin{bmatrix} EA\,\boldsymbol{\epsilon}_h \\ EI\,\boldsymbol{\kappa}_h \end{bmatrix} = \begin{bmatrix} EA\left(\varphi_h' - \mathbf{d}_h\right) \\ EI\,\mathbf{d}_h \times \mathbf{d}_h \end{bmatrix}. \tag{7.20}$$

The term $\mathbf{M}(\mathbf{q})\,\nabla_{\dot{\mathbf{q}}}\,\dot{\mathbf{q}}$ in (7.17), derived in [134], takes the following form:

$$\begin{aligned} \mathbf{M}(\mathbf{q})\,\nabla_{\dot{\mathbf{q}}}\,\dot{\mathbf{q}} = \mathbf{M}\,\ddot{\mathbf{q}} - 2\,I_\rho\,\frac{1}{|\varphi_h'|^2}\left(\mathbf{N}'\right)^T \left[\frac{1}{|\varphi_h'|}\left(\mathbf{d}_h \cdot \dot{\varphi}_h'\right)\mathbf{P_d} + \mathbf{d}_h \odot \mathbf{d}_h\right]\dot{\mathbf{q}} \\ + 2\,I_\rho\,\frac{1}{|\varphi_h'|^3}\left(\mathbf{N}'\right)^T \left[\mathbf{P_d} \odot \left(\dot{\varphi}_h' \otimes \mathbf{d}_h\right)\right]\dot{\varphi}_h', \end{aligned} \tag{7.21}$$

where $\odot$ denotes the symmetric product between two vectors $\mathbf{a}_1$, $\mathbf{a}_2$, or two second-order tensors $\mathbf{A}_1$, $\mathbf{A}_2$, that is:

$$\mathbf{a}_1 \odot \mathbf{a}_2 = \frac{1}{2}\left(\mathbf{a}_1 \otimes \mathbf{a}_2 + \mathbf{a}_2 \otimes \mathbf{a}_1\right), \tag{7.22a}$$

$$\mathbf{A}_1 \odot \mathbf{A}_2 = \frac{1}{2}\left(\mathbf{A}_1\,\mathbf{A}_2 + \mathbf{A}_2^T\,\mathbf{A}_1^T\right). \tag{7.22b}$$

7.3.2 Isogeometric versus classical nodal finite elements

The isogeometric discretization scheme and the standard one based on nodal finite element using cubic Hermite functions both are based on the isoparametric concept. When the former applies cubic C^1 B-splines, the basis functions of these two schemes span the same function space. However, they belong to two different classes of finite element methods. While the standard scheme employs classical nodal finite elements, the isogeometric scheme is in the context of isogeometric analysis, where we deal with control points instead of element nodes [30]. Moreover, the former requires two variable fields that are the nodal spatial position and the nodal director [134], while the latter only considers the positions of the control points as a variable field. Hence, the isogeometric scheme can reduce the number of degrees of freedom (dofs). In particular, a discretization with n_e elements using C^r B-splines of degree p leads to $3\left[n_e\,(p-r)+r+1\right]$ dofs[2]. Applying B-splines with maximum continuity C^{p-1} leads to $3(n_e+p)$ dofs, while the standard scheme leads to $5(n_e+1)$ dofs. For example, employing B-splines of minimum required polynomial degree of $p=2$, that are C^1 continuous, leads to a smaller number of dofs of $3(n_e+2)$ for the same number of elements. Using cubic C^1 B-splines that are in the same function space as cubic Hermite functions, however, leads to more dofs of

---

[2] The number of basis functions is $m_k - p - 1$, where m_k is the number of knots in the knot vector. We assume that the C^r B-splines of degree p are defined on an open knot vector with interior knots repeated $(p-r)$-times.

$6(n_e+1)$ for the same number of elements. Due to the different variable fields of these two schemes, they lead to different solution spaces. Particularly, using the standard scheme results in a discrete solution in the manifold $\varphi_h \in \left(\mathbb{R}^3 \times S^2\right)^m$ since the director belongs to a unit sphere S^2. This necessary means that the standard scheme also preserves the manifold structure of the continuous rod. Isogeometric discretizations, however, lead to a solution in the Euclidean space $\varphi_h \in \left(\mathbb{R}^3\right)^N$, which is a larger space but does not ensure the underlying manifold structure of the rod.

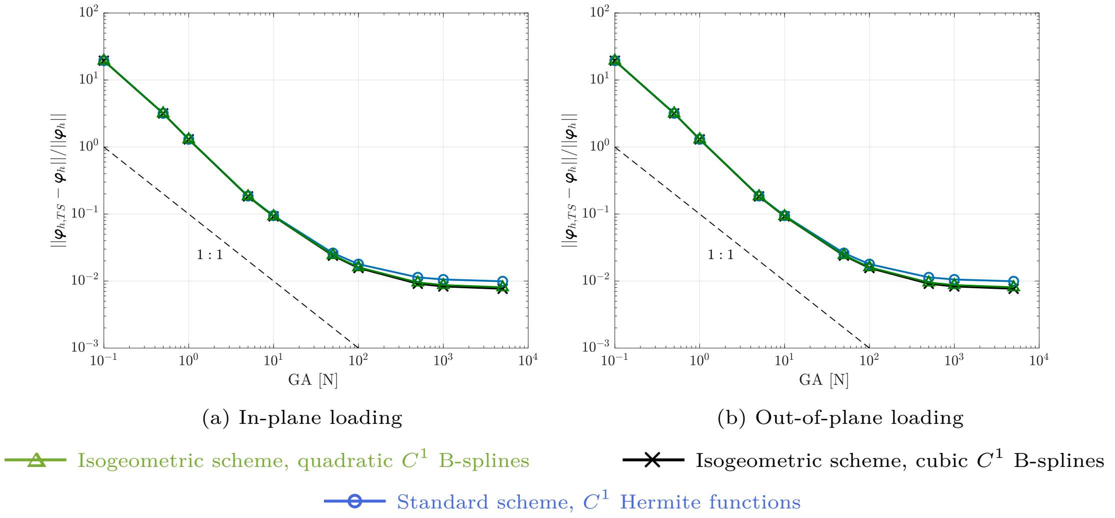

(a) In-plane loading

(b) Out-of-plane loading

Figure 7.2: Convergence of the relative error between the geometrically exact beam and the nonlinear rod model [134], computed with different discretizations on a mesh of 40 elements, obtained at the last load step.

We now numerically demonstrate that the isogeometric scheme, with a possibly smaller number of dofs, and the standard one approximately achieve the same accuracy via two- and three-dimensional static benchmarks from [134, Sec. 5.1]. We consider an initially straight, transversely isotropic, clamped rod of 40 m with an axial stiffness of $EA = 100$ N, bending stiffness of $EI = 200$ Nm^2, and subjected to an in-plane and out-of-plane loading. We compare the response obtained with isogeometric discretizations using quadratic and cubic C^1 B-splines, with classical nodal finite elements using cubic C^1 Hermite functions, and with a geometrically exact beam model including shear and torsion deformations using linear C^0 Lagrange polynomials. The results of the last two approaches are provided by [134]. For the first two approaches, we discretize the rod with the same number of 40 uniform elements with the force divided into 55 uniform load steps. The number of dofs of the isogeometric scheme using quadratic, cubic B-splines, and the standard scheme is 126, 246, and 205, respectively. We have chosen a tolerance of 10^{-10} for the Newton-Raphson scheme, which required up to 6 iterations in all cases. We obtained visually indistinguishable snapshots when compared to the standard scheme (see [134, Fig. 1, 4]) in all cases. In Fig. 7.2, we compare the difference between the geometrically exact beam formulation and the isogeometric beam formulation with the one between the former and the standard Hermite scheme. To this end, we plot the relative L^2 error between the deformed rod obtained with the geometrically exact beam and the one obtained with the isogeometric (black and green curves), and the standard scheme (blue), as a function of the shear stiffness GA employed in the geometrically exact beam model. In [134], the authors employed this convergence study to point out that the geometrically exact beam model converges to the model using their rod formulation when GA increases, since the normal directors tend to become tangent to the deformed rod axis with increasing GA. We adopt this study to illustrate that the isogeometric scheme results in the same behavior as the standard one, as observed in Fig. 7.2 for both the in-plane and out-of-plane loading cases, irrespective of the spline basis employed in the isogeometric scheme. We note that the constant error level between the geometrically exact beam and the nonlinear rod of [134] at large values of GA is due to shear and torsion deformations considered in the former but not in the latter.

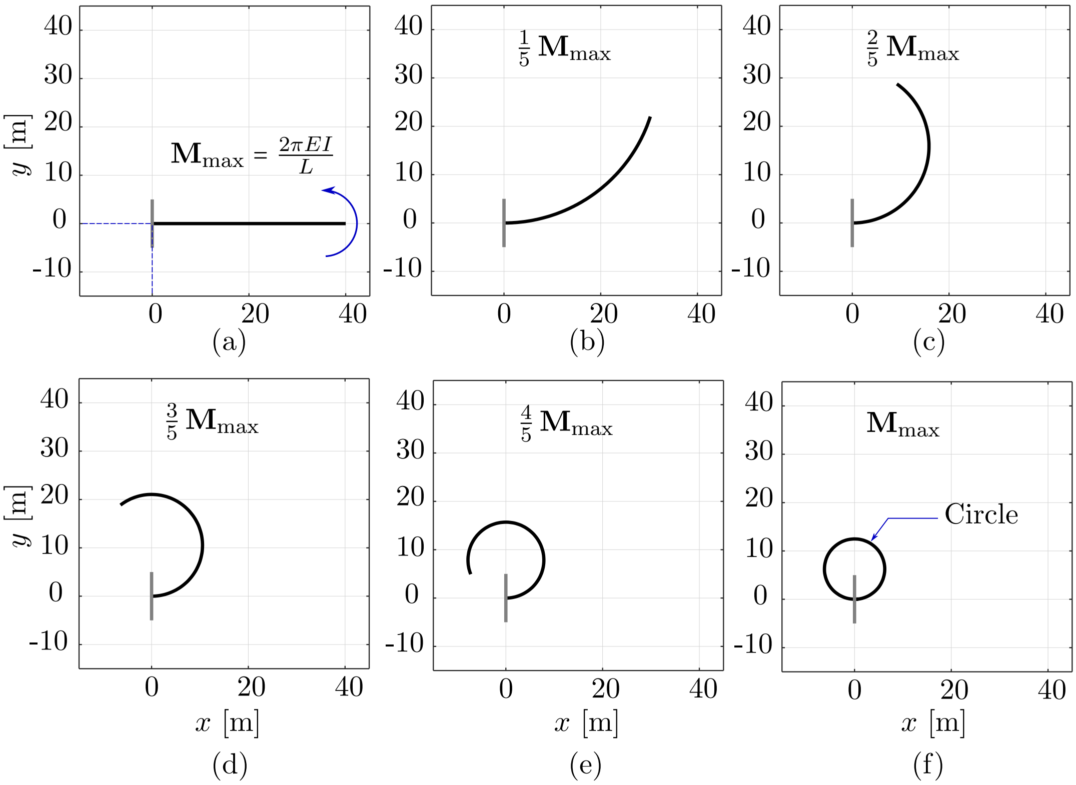

Figure 7.3: Deformed configurations of a clamped rod bent to a circle at different load steps, computed with quadratic C^1 B-splines ($p = 2$) and a mesh of 40 elements.

To study the convergence behavior of the isogeometric scheme with mesh refinement, we consider a geometrically nonlinear benchmark of planar roll-up. Fig. 7.3a illustrates the initial rod subjected to a bending moment $M_{\max} = \frac{2EI\pi}{L}$ Nm at its free end, where L is the rod initial length. We choose the same material parameters and value of L as in the static benchmarks above. We illustrate the deformed rod in a sequence of six load

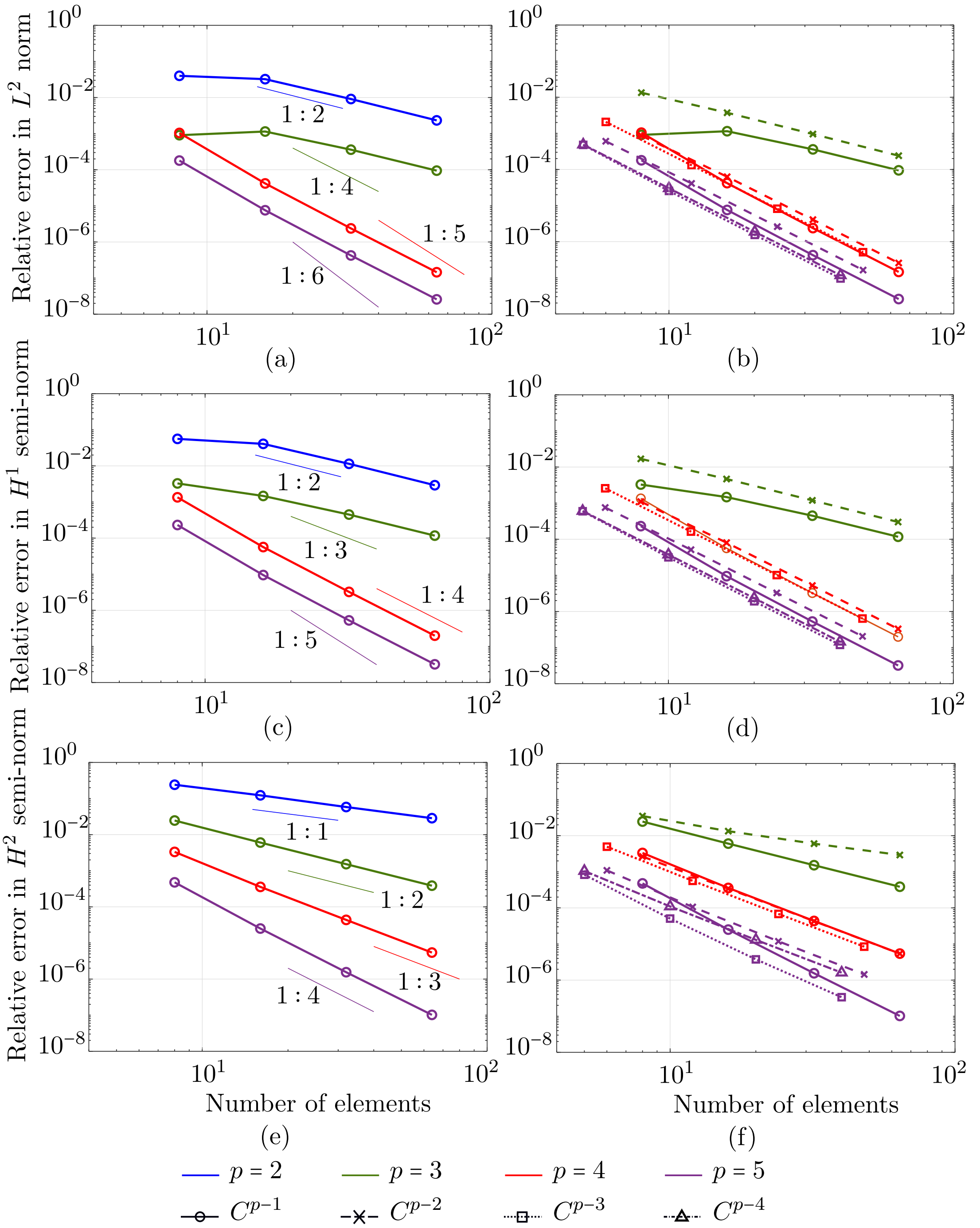

Figure 7.4: Convergence of relative errors of the clamped rod bent to a circle computed with C^{p-1} B-splines of different degrees p (left column) and with C^r B-splines, $1 \leq r \leq p-1$ (right column). The rate shown in figures on the right colum is the optimal rate of linear fourth-order problems [138].

steps, obtained with the isogeometric scheme using quadratic C^1 B-splines ($p = 2$) in Fig. 7.3. We observe that, as expected, the deformed rod closes a circle in the last load step. In the left column of Fig. 7.4, we demonstrate the convergence of the relative error in L^2 norm, H^1, and H^2 semi-norm, obtained with C^{p-1} B-splines of different polynomial degrees p, compared to the exact circle in the last load step. We included the optimal convergence rate of linear fourth-order problems using isogeometric discretizations based on [138]. We observe the same optimal convergence behavior obtained in H^2 semi-norm as the linear case for all degrees (see Fig. 7.4e). The error in the H^1 semi-norm (see Fig. 7.4c), however, converges with the same optimal rate of linear cases only when using even degrees, but with one order lower when using odd degrees. Focusing on the error in the L^2 norm, we see that the convergence rate is smaller than this optimal rate for all $p \geq 3$ (see Fig. 7.4a). Furthermore, cubic C^2 B-splines illustrate the same convergence rate as quadratic, and quintic functions the same as quartic ones. The different convergence behavior between even and odd degrees is well-known in isogeometric collocation methods [260], [261], however, to our best knowledge, is not yet established for nonlinear problems.

To investigate the impact of the smoothness of spline basis functions on the convergence behavior of isogeometric discretizations, we compute the relative error obtained with C^r B-splines of different polynomial degrees $p \geq 3$, where $1 \leq r \leq p-1$, and illustrate this on the right column of Fig. 7.4. Different markers correspond to different continuous orders r. We can see that the continuity of B-splines does not affect the convergence rate in both the L^2 norm and the H^1 semi-norm for this planar roll-up example. Focusing on the error in the H^2 semi-norm, reducing the continuity of B-spline basis functions decreases the convergence rate in cases of odd degrees (see the green and purple curves in Fig. 7.4f), however, does not affect this rate in the case of even degree ($p = 4$, red curve in Fig. 7.4f). Furthermore, based on empirical results, we observe that increasing or decreasing the number of quadrature points also does not affect the convergence behavior of the discretizations employed in this example. Further numerical investigations of a linear simply supported nonlinear rod subjected to sinusoidal loads shows the same optimal convergence behavior as in the linear cases for all error norms, polynomial degrees, and continuity. Hence, we suggest that the convergence behavior in the planar roll-up example results from the nonlinearity captured by the rod formulation [134]. We note that, in [134], the authors showed that using cubic Hermite functions with solutions in the manifold $\left(\mathbb{R}^3 \times S^2\right)^m$ results in the same optimal convergence behavior in the energy norm as obtained for linear problems. Therefore, we assume that the manifold structure of the discrete solution space might affect the convergence of the corresponding discretizations. A mathematical error estimate for the considered nonlinear rod formulation [134] is outside the scope of this work and is postponed to future work.

7.3.3 Time integration scheme

For time integration of our numerical examples in subsequent sections, we apply the same implicit scheme as in [134], which is a hybrid combination of the midpoint and trapezoidal rules. This implicit scheme achieves second-order accuracy, approximately preserves energy, and exactly preserves the linear and angular momenta [134], [262], which we also verify via an example of an elastic pendulum in Appendix 7.A.

Remark 7.3.1. *The mass matrix* (7.18) *of the considered rod formulation [134] is configuration-dependent due to its second counterpart* $\mathbf{M}_2$. *Thus, an explicit time integration scheme would not be applicable.*

Consider the semi-discrete formulation (7.17) in space evaluated at time instant $t_{n+\frac{1}{2}} \in [t_n, t_{n+1}]$:

$$\int_0^S \delta\mathbf{q} \cdot \left(\mathbf{M}(\mathbf{q})\,\nabla_{\dot{\mathbf{q}}}\,\dot{\mathbf{q}} + \mathbf{B}(\mathbf{q})^T\,\boldsymbol{\sigma}_h - \mathbf{N}^T\,\mathbf{f}^{\text{ext}}\right)_{n+\frac{1}{2}} \mathrm{d}s = \mathbf{0}\,. \tag{7.23}$$

We approximate the inertial term $\left(\mathbf{M}(\mathbf{q})\,\nabla_{\dot{\mathbf{q}}}\,\dot{\mathbf{q}}\right)_{n+\frac{1}{2}}$ using an extended version of the midpoint rule as follows:

$$\begin{aligned}\left(\mathbf{M}(\mathbf{q})\,\nabla_{\dot{\mathbf{q}}}\,\dot{\mathbf{q}}\right)_{n+\frac{1}{2}} \approx\; & \frac{\mathbf{M}\left(\mathbf{q}_{n+1}\right)\dot{\mathbf{q}}_{n+1} - \mathbf{M}\left(\mathbf{q}_n\right)\dot{\mathbf{q}}_n}{\Delta t} \\ & + \left\{2\,I_\rho\,\frac{1}{\left|\boldsymbol{\varphi}_h'\right|^3}\left(\mathbf{N}'\right)^T\left[\mathbf{P}_{\mathbf{d}} \odot \left(\dot{\boldsymbol{\varphi}}_h' \otimes \mathbf{d}_h\right)\right]\dot{\boldsymbol{\varphi}}_h'\right\}_{n+\frac{1}{2}}\,,\end{aligned} \tag{7.24}$$

where Δt is the time step. The internal term
$\left(\mathbf{B}(\mathbf{q})^T\,\boldsymbol{\sigma}_h\right)_{n+\frac{1}{2}}$ is approximated by using the trapezoidal rule as follows:

$$\left(\mathbf{B}(\mathbf{q})^T\,\boldsymbol{\sigma}_h\right)_{n+\frac{1}{2}} \approx \frac{\mathbf{B}\left(\mathbf{q}_{n+1}\right)^T\,\boldsymbol{\sigma}_{h,n+1} + \mathbf{B}\left(\mathbf{q}_n\right)^T\,\boldsymbol{\sigma}_{h,n}}{2}\,. \tag{7.25}$$

We also approximate $\mathbf{q}_{n+\frac{1}{2}}$ and $\dot{\mathbf{q}}_{n+\frac{1}{2}}$ using the trapezoidal and midpoint rules, respectively, as follows:

$$\mathbf{q}_{n+\frac{1}{2}} \approx \frac{\mathbf{q}_{n+1} + \mathbf{q}_n}{2}\,, \qquad \dot{\mathbf{q}}_{n+\frac{1}{2}} \approx \frac{\mathbf{q}_{n+1} - \mathbf{q}_n}{\Delta t}\,, \tag{7.26}$$

and $\dot{\mathbf{q}}_{n+1}$ as:

$$\dot{\mathbf{q}}_{n+1} \approx \frac{2}{\Delta t}\left(\mathbf{q}_{n+1} - \mathbf{q}_n\right) - \dot{\mathbf{q}}_n\,. \tag{7.27}$$

Introducing the approximations (7.24)-(7.27) into (7.23) leads to a system of discrete nonlinear equations in space and time:

$$\mathbf{g}\left(\mathbf{q}_{n+1}\right) = \mathbf{0}\,, \tag{7.28}$$

which can be normalized and solved using, for instance, the Newton-Raphson method, for $\mathbf{q}_{n+1}$. $\dot{\mathbf{q}}_{n+1}$ can be then obtained using (7.27). The configuration-independent external forces are evaluated at time instant $t_{n+\frac{1}{2}}$, while the configuration-dependent forces induced by a surrounding flow, discussed in Section 7.2.3, are approximated using the midpoint rule along with the approximations (7.26)-(7.27). We note that solving (7.28) using the Newton-Raphson method requires each term in (7.24)-(7.25) and force terms in cases of configuration-dependent forces to be linearized. We derive this and their resulting counterparts to the tangent stiffness matrix in Appendix 7.B.

7.3.4 Outlier removal

Algorithm 9 Implicit time integration scheme employing the strong approach of outlier removal of [122].

```
Input: $\mathbf{q}_0$, $\dot{\mathbf{q}}_0$ (initial conditions)
Output: $\mathbf{q}(t)$, $\dot{\mathbf{q}}(t)$
$\mathbf{C} = \mathcal{C}(p, n_{ele}$, continuity $C^r$, boundary conditions)   ▷ Extraction operator of [122]
$n = 0$   ▷ index of the time step
for $t$ in $\Delta t : \Delta t : T$ do
    $\mathbf{q}(t) = \mathbf{q}_n$, $\dot{\mathbf{q}}(t) = \dot{\mathbf{q}}_n$
    $\mathbf{q}_{n+1} = \mathbf{q}_n$   ▷ inital guess for Newton-Raphson scheme
    $\Delta\mathbf{q}_{n+1} = 1.0$   ▷ initialize
    while $\Delta\mathbf{q}_{n+1} \geq 10^{-10}$ do
        $\mathbf{r} = -\mathbf{g}(\mathbf{q}_{n+1})$   ▷ residual vector, see also Eq. (7.28)
        $\mathbf{K} = \frac{\partial\mathbf{g}}{\partial\mathbf{q}_{n+1}}$   ▷ Tangent stiffness matrix, see also Appendix 7.B
        $\mathbf{r} = \mathbf{C}^T\mathbf{r}$, $\mathbf{K} = \mathbf{C}^T\mathbf{K}\mathbf{C}$   ▷ Removing outliers
        $\Delta\mathbf{q}_{n+1} = \mathbf{K}^{-1}\mathbf{r}$
        $\mathbf{q}_{n+1} += \Delta\mathbf{q}_{n+1}$
        $\dot{\mathbf{q}}_{n+1} \approx \frac{2}{\Delta t}(\mathbf{q}_{n+1} - \mathbf{q}_n) - \dot{\mathbf{q}}_n$   ▷ Eq. (7.27)
    end while
    $n += 1$
end for
```

Our empirical results, discussed in the next section, indicate that the response obtained with isogeometric discretizations consists of high-frequency contents, which lead to unstable computations. Based on this observation, we propose to improve the robustness of these discretizations via the strong approach of outlier removal introduced in [122], which entirely removes the spurious outlier modes corresponding to the highest frequencies. The motivation to remove the outliers is based on the fact that in nonlinear dynamic analysis, the modes are coupled. Thus, when the outliers are excited at a time instance, other high-frequency modes might be excited at that time instance and later ones as well. We note that the modes mentioned here and throughout this work in the context of nonliner analysis are the ones corresponding to a linearized problem at a time instance.

To remove outliers, the fundamental idea of [122] is to enforce additional boundary constraints arising from higher-order eigenvalue problems into the space of B-spline basis functions. A new subspace of spline basis functions, that are linear combinations of the original ones, is constructed via multiplication with the so-called extraction operator $\mathcal{C}$. The operator $\mathcal{C}$ is computed by finding a basis for the null space of a matrix including boundary constraints, and thus leads to new basis functions that strongly satisfy these constraints. For more details regarding the algorithm computing $\mathcal{C}$, we refer to [122]. We note that there exist other approaches to remove outliers, either strongly [123] or weakly [121], [124]. For an overview of these approaches, we refer to [122], [183] and references therein.

The outlier removal approach [122] affects only the basis functions associated with the boundary conditions and preserves important properties of B-splines, such as non-negativity and minimum local support. We employ the strong approach of outlier removal by applying the extraction operator $\mathcal{C}$ to both the right- and left-hand sides of the semi-discrete formulation (7.17) at each time step. The operator $\mathcal{C}$ is computed once before the integration procedure and remains constant during the time integration. We note that in our computations, the essential boundary conditions are strongly enforced via $\mathcal{C}$. We illustrate the implicit time integration scheme including the outlier removal approach in Algorithm 9.

7.4 Robustness of isogeometric discretizations

In this section, we numerically demonstrate, via two- and three-dimensional benchmark, that the isogeometric discretization scheme is less robust than the standard one based on nodal finite elements using cubic Hermite functions. We then discuss important factors, such as the high-frequency contents of the response and round-off errors due to floating-point arithmetic, which may negatively affect the robustness of the employed discretization scheme. We show that employing the strong approach of outlier removal [122], discussed in the previous section, improves the robustness of isogeometric schemes. In addition, we discuss the influence of the configuration-dependent mass matrix (7.18) on the accuracy of the response.

7.4.1 Two- and three-dimensional benchmarks

We consider the two dynamic benchmarks of [134, Sec. 5.2] and compare the responses obtained with isogeometric discretizations, using cubic C^1 and C^2 B-splines, against the standard scheme. In all cases, the rod is uniformly discretized into 20 elements, which leads to 126, 69, and 105 dofs using these three approaches, respectively. We also include the solution obtained with the geometrically exact beam model including shear and torsion using linear C^0 Lagrange polynomials as a reference, which is provided by [134].

The first example consists of an initially straight, transversely isotropic, clamped rob

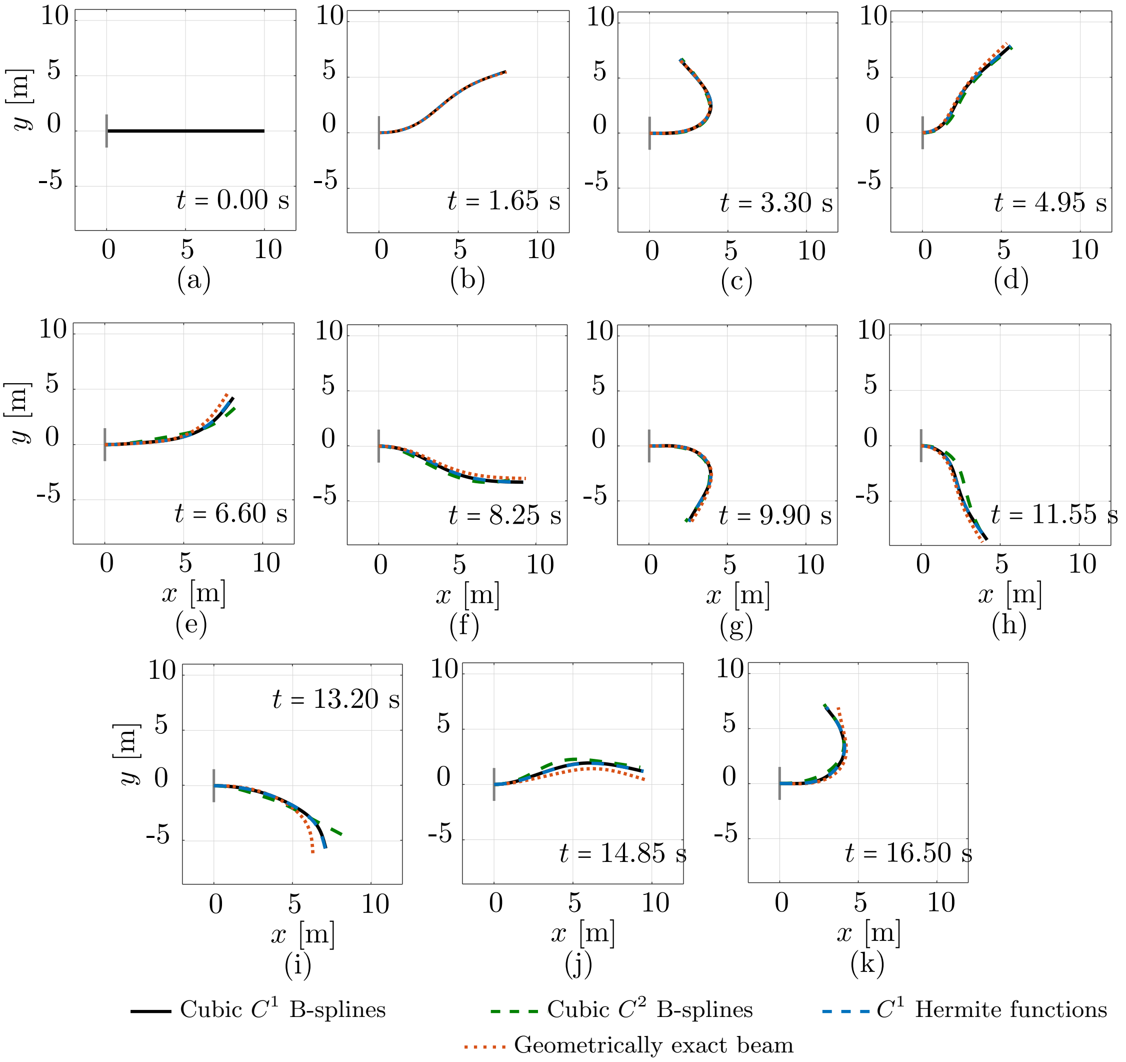

(a) (b) (c) (d) (e) (f) (g) (h) (i) (j) (k)

Figure 7.5: Deformed configurations of a clamped rod subjected to an in-plane loading at different time steps, computed with different discretizations and a geometrically exact beam model.

subjected to the following in-plane vanishing load at its free end:

$$\mathbf{F}(t) = \begin{cases} \frac{t}{0.5\,t_c} & \mathbf{F}_c\,, \quad 0 \leq t \leq 0.5\,t_c\,, \\ \frac{2}{t_c}\,(t_c - t) & \mathbf{F}_c\,, \quad 0.5\,t_c < t \leq t_c\,, \\ 0 & \mathbf{F}_c\,, \quad t > t_c\,, \end{cases} \tag{7.29}$$

where t_c and $\mathbf{F}_c$ are chosen to be $t_c = 0.5$ s and $\mathbf{F}_c = (0,\,30,\,0)$ N, respectively. Thus, the rod deforms in the xy-plane. The rod has an initial length of 10 with an initial director of (1, 0, 0), a circular cross-section with a diameter of 0.01 m, Young's modulus $E = 2 \cdot 10^{11}$ N/m^2, and mass density $\rho = 7900$ kg/m^3. We choose the same time step

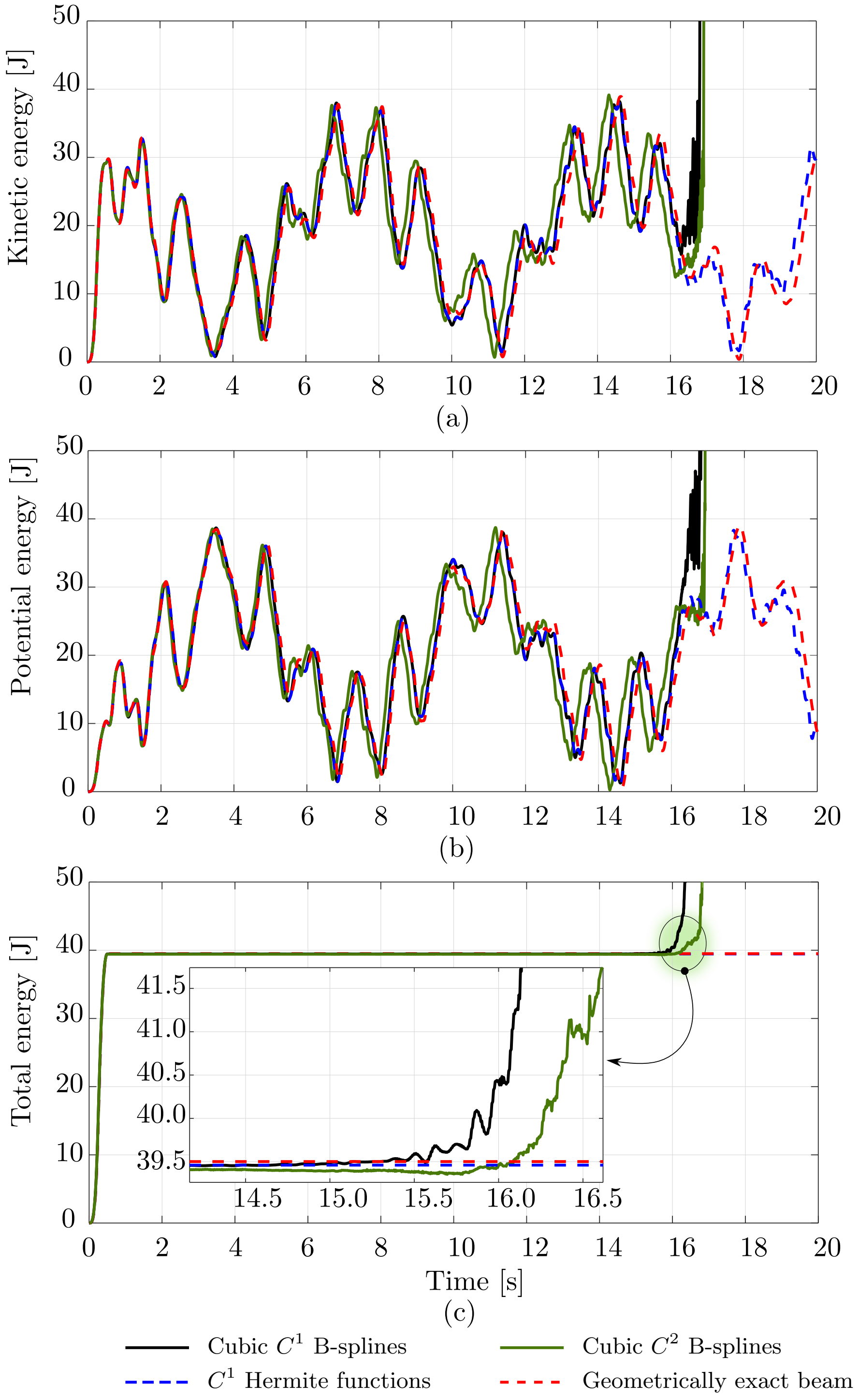

Figure 7.6: The energy of a clamped rod subjected to a vanishing in-plane loading, computed with different discretizations and a geometrically exact beam model.

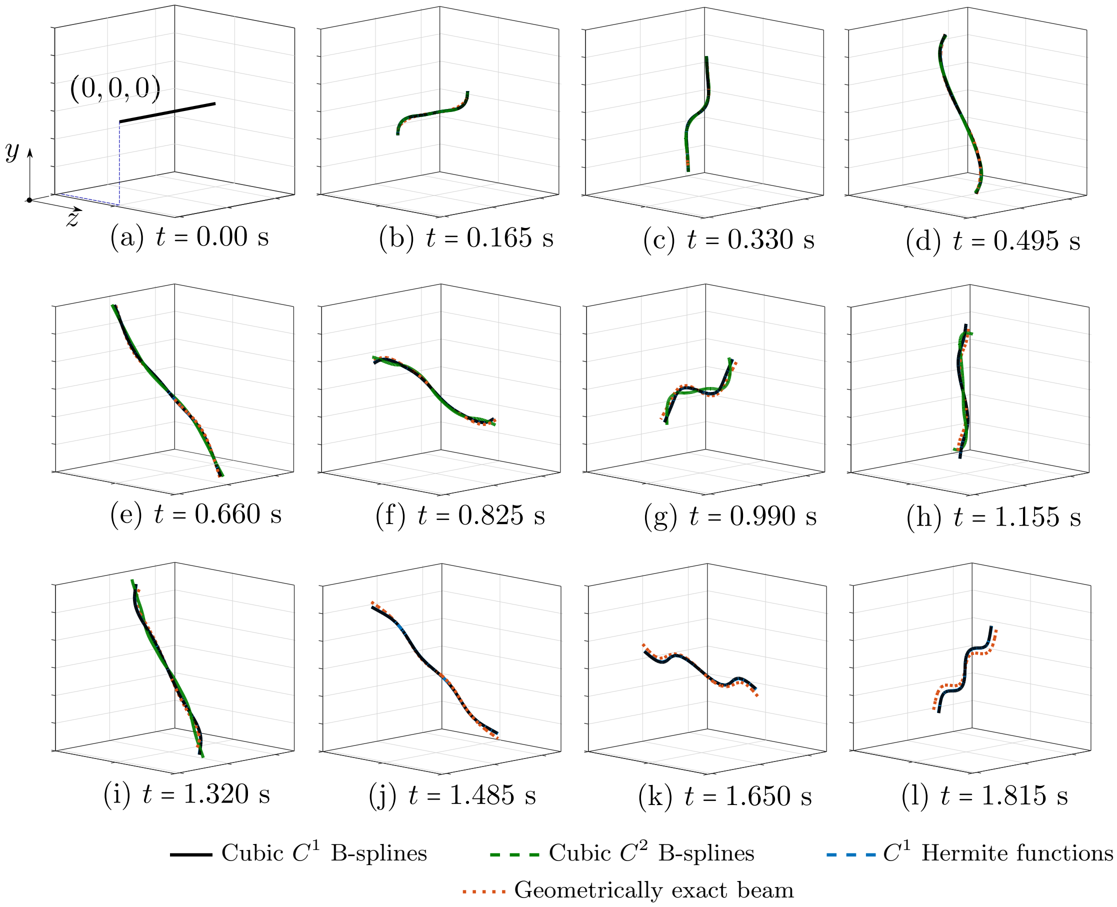

(a) $t = 0.00$ s (b) $t = 0.165$ s (c) $t = 0.330$ s (d) $t = 0.495$ s

(e) $t = 0.660$ s (f) $t = 0.825$ s (g) $t = 0.990$ s (h) $t = 1.155$ s

(i) $t = 1.320$ s (j) $t = 1.485$ s (k) $t = 1.650$ s (l) $t = 1.815$ s

Figure 7.7: Deformed configurations of an unconstrained rod subjected to a vanishing out-of-plane loading at different time steps, computed with different discretizations and a geometrically exact beam model.

of $\Delta t = 0.005$ s, a simulation time of 20 s, and a tolerance of 10^{-10} for the Newton-Raphson scheme, as done in [134]. Fig. 7.5 illustrates the deformed configurations in a sequence of eleven load steps, obtained with cubic C^1 (black curves) and C^2 (green dashed curves) B-splines, with the standard scheme using cubic C^1 Hermite functions (blue dashed curves), and with the geometrically exact beam model using linear C^0 Lagrange polynomials (red dotted curves). We note that for this example, after 16.5 s, the computations using isogeometric discretizations become unstable and the Newton scheme does not converge anymore, while the one using the standard scheme remained stable during the computation time of 20 s. Nevertheless, we observe that during the first 16.5 s the isogeometric scheme using cubic C^1 splines and the standard one result in virtually identical responses, since their basis functions span the same space and have the same approximation power. Comparing these results to the one obtained with the geometrically exact beam, we see that the difference between these two models increases progressively in time. This may result from the fact that the geometrically exact beam model includes torsion and shear, while the employed nonlinear rod formulation does not, as discussed in [134]. Focusing on the responses obtained with cubic C^2 B-splines (green dashed curves), we can see that these differ from those obtained with cubic C^1 B-splines at certain time steps.

Remark 7.4.1. *For this benchmark, computations using the isogeometric scheme with quadratic C^1 B-splines become unstable already after* 3.5 *s. Thus, in this work, we did not apply quadratic B-splines for any dynamic benchmark.*

To gain better insights, we illustrate the time history of the kinetic, potential, and total energy resulting from the aforementioned approaches in Fig. 7.6. We observe that, starting around 4 s, there is a phase shift between the responses obtained with cubic C^2 and C^1 B-splines (Fig. 7.6a,b). In particular, using cubic C^2 B-splines leads to a smaller phase than C^1 B-splines. This phase shift, thus, leads to different responses between these two approaches observed in Fig. 7.5. Focusing on the responses around 16 s, before the energy, obtained with isogeometric discretizations, shoots up, indicating unstable computations, we see that high-frequency modes are excited and lead to fluctuations in the response. Due to a smaller phase, we expect that this generally occurs earlier when using cubic C^2 B-splines than C^1 splines. This necessary means that increasing the continuity of spline basis functions reduces the robustness of the corresponding discretizations. Nevertheless, before the computations become unstable, the isogeometric scheme approximately preserves the same total energy as the standard one and the geometrically exact beam model (Fig. 7.6c). We conclude that it is less robust than the standard one based on nodal finite elements [134]. Using discretizations with splines of higher continuity reduces the phase of the responses and, hence, may reduce their robustness.

The second benchmark is an unconstrained rod of the same length and material as the clamped rod studied above. The rod has a smaller cross-section with a diameter of 0.005 m and is subjected to the vanishing load (7.29), with $t_c = 0.5$ s and $\mathbf{F}_c$ given by:

$$\begin{aligned} &\mathbf{F}_c = (-30, -30, 0)\,\mathrm{N} \quad \text{at } s = 0\,, \qquad &&\mathbf{F}_c = (30, 30, 0)\,\mathrm{N} \quad \text{at } s = L\,, \\ &\mathbf{F}_c = (0, 0, -24)\,\mathrm{N} \quad \text{at } s = L/20\,, \qquad &&\mathbf{F}_c = (0, 0, 24)\,\mathrm{N} \quad \text{at } s = 19\,L/20\,. \end{aligned}$$

Consequently, the rod deforms freely in three-dimensional space. For this benchmark, we also choose the same time step $\Delta t = 0.001$ s, a simulation time of 2 s, and a tolerance of 10^{-10} for the Newton-Raphson scheme, as done in [134]. Fig. 7.7 illustrates the deformed configurations in a sequence of twelve load steps obtained with the aforementioned approaches. For this example, after 1.35 s the computation using cubic C^2 B-splines becomes unstable and the Newton scheme does not converge anymore, while that using cubic C^1 B-splines remains stable during the simulation time of 2 s. We have similar observations as in the case of the clamped rod above: both the isogeometric scheme using cubic C^1 B-splines and the standard one show the same accuracy, while the former using C^2 B-splines leads to distinct responses. This is also demonstrated for the energy in Fig. 7.8 and the three components of the angular momentum in Fig. 7.9. We also observe a phase shift in the case of cubic C^2 B-splines, before the high-frequency

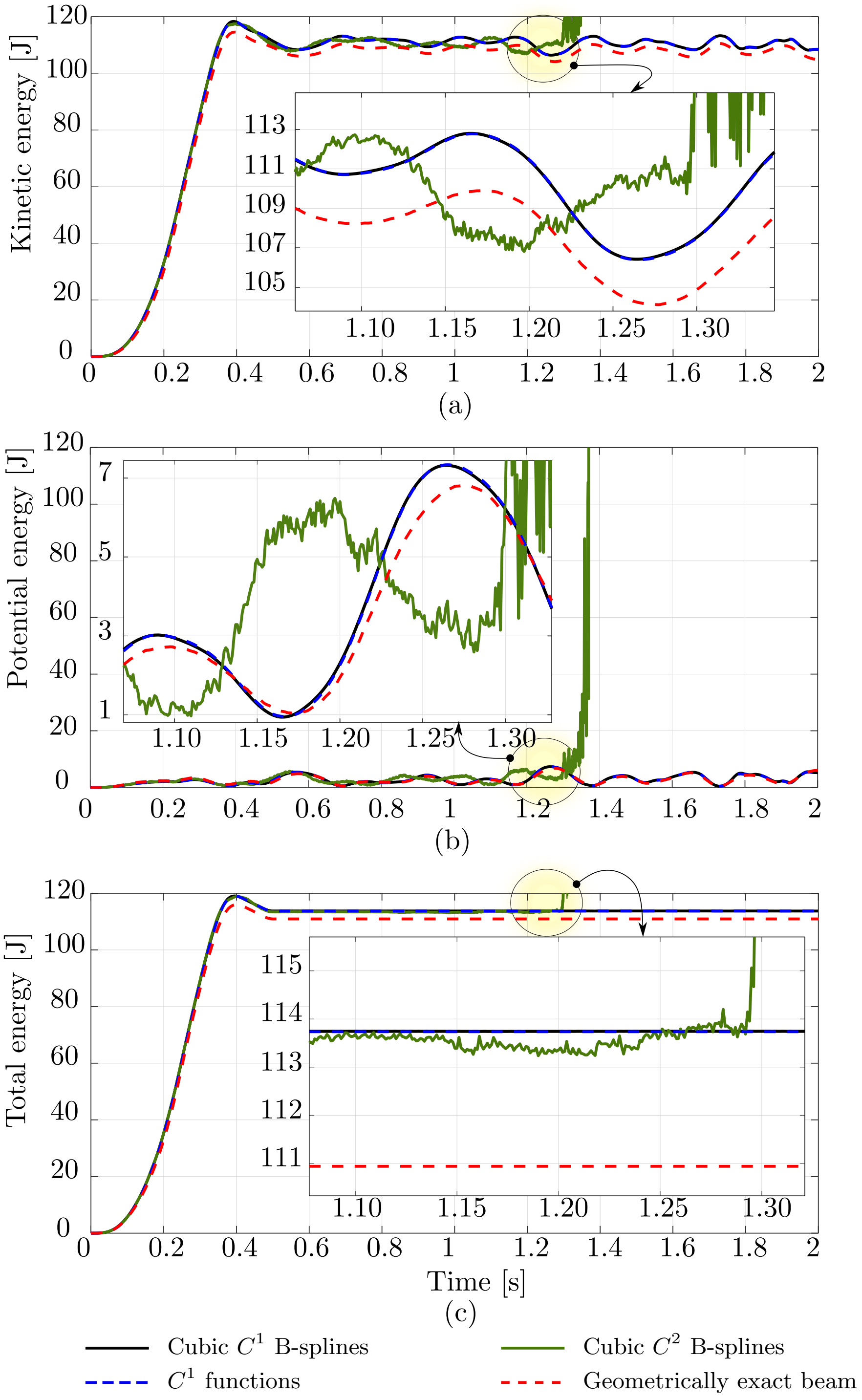

Figure 7.8: The energy of an unconstrained rod subjected to a vanishing out-of-plane loading, computed with different discretizations and a geometrically exact beam model.

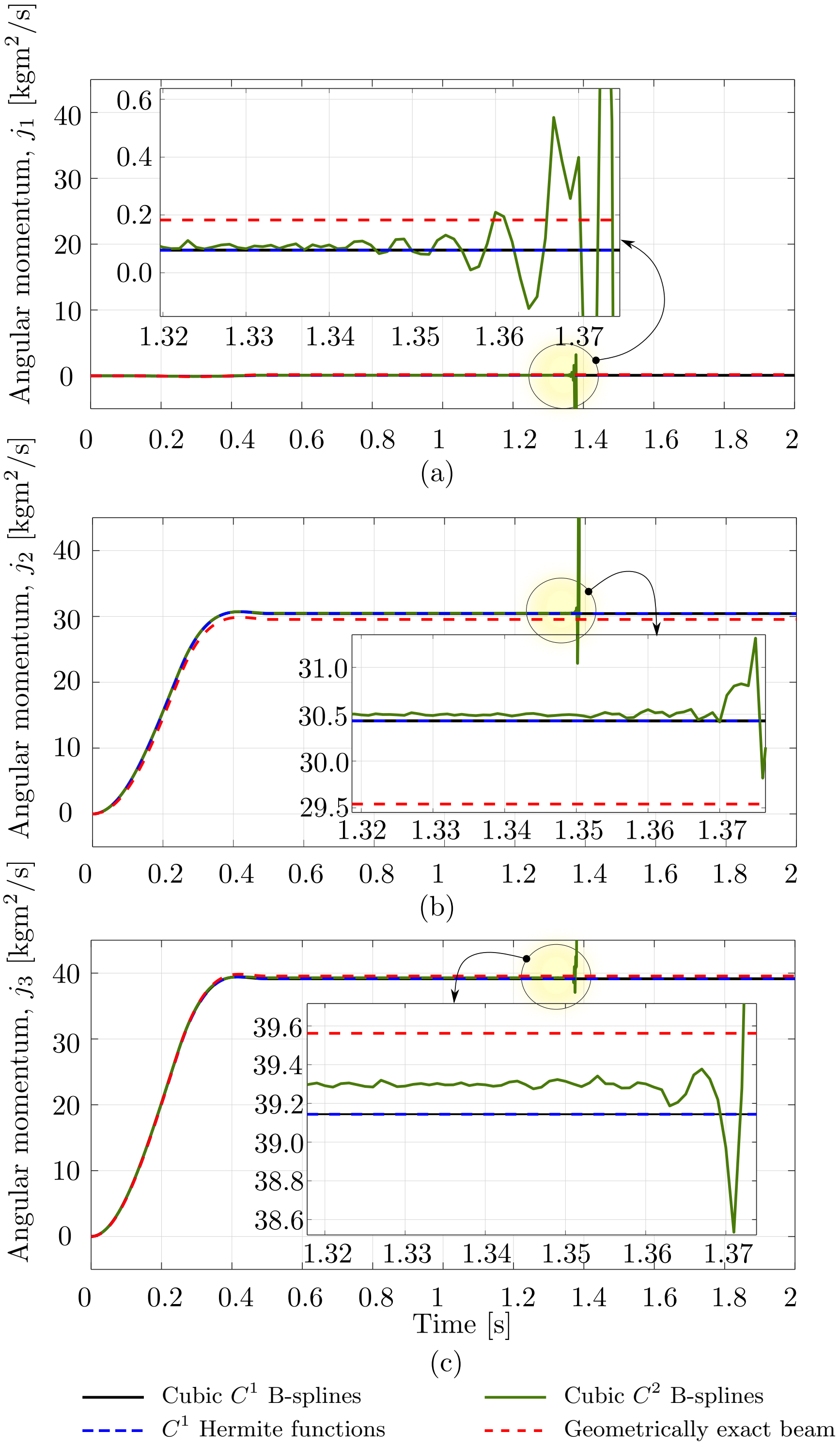

(a)

(b)

(c)

Figure 7.9: Three components of the linear angular momentum of an unconstrained rod subjected to a vanishing out-of-plane loading, computed with different discretizations and a geometrically exact beam model.

modes affect the response and the computation becomes unstable. We see that, for this benchmark, using smoother splines of C^2 also leads to less robust computation than using C^1, as discussed in the first benchmark of a clamped rod.

7.4.2 Robustness improvement with outlier removal

The results discussed in the previous subsection indicate that excited high-frequency contents in the response reduce the robustness of isogeometric discretizations. To gain better insights, we perform the Fast Fourier Transformation (FFT) of the kinetic energy in the case of the clamped rod studied in the previous subsection, subjected to half of the load during a longer simulation time, $T = 100$ s. To avoid noises in the transformed signal, we consider the energy as long as it is smaller than a threshold of 40 J. Fig. 7.10 illustrates the FFT of the kinetic energy obtained with cubic C^1 B-splines (blue circles), where we can observe that not only one, but almost all high-frequency modes are excited.

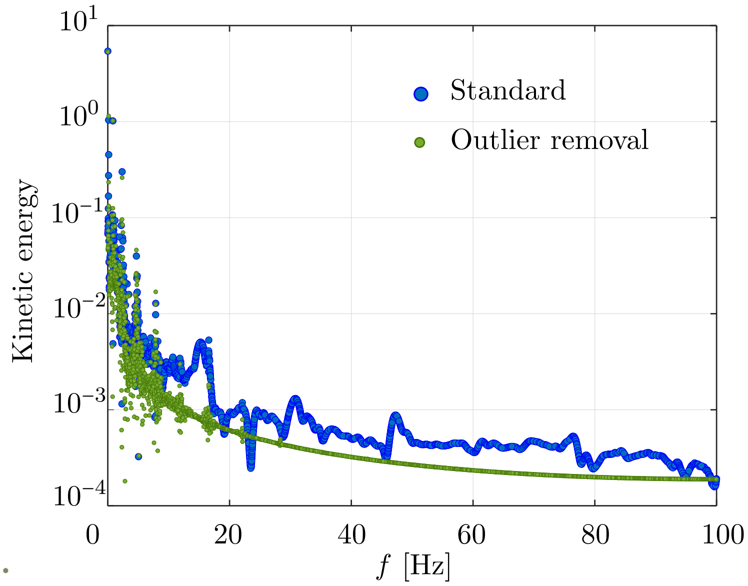

Figure 7.10: Fast Fourier transformation of the kinetic energy for the clamped rod in Fig. 7.5, subjected to a half of the load during a longer time period of 100 s.

As discussed in Section 7.3.4, we employ the strong approach of outlier removal [122] to remove the high-frequency contents in the response, such that the computations become more robust. In Fig. 7.10, we include the kinetic energy (green circles) with the outliers removed. We observe that almost all high-frequency contents are removed, as expected. Fig. 7.11 shows the kinetic, potential, and total energy of the clamped rod studied in the previous subsection. Here, we present a comparison among the energy obtained with isogeometric discretizations using cubic C^1 and C^2 B-splines, employing outlier removal, (black and green curves, respectively), the energy obtained with the standard scheme [134] (blue dashed curve), and the geometrically exact beam model (red dashed curve).

n_{ele}	cubic Hermite functions	cubic C^1 B-splines, standard	cubic C^1 B-splines, outlier removal
Δt = 0.0025 s			
2	1.000000000000000	1.000000000000002	1.000000000000001
4	1.000000000000002	1.000000000000001	0.999999999999972
8	0.999999999999988	1.000000000000044	1.000000000000038
16	0.999999999999940	1.000000000000002	0.999999999999941
32	0.999999999999979	0.999999999999240	1.000000000000137
Δt = 0.005 s			
2	0.999999999999999	0.999999999999999	1.000000000000000
4	1.000000000000006	0.999999999999998	0.999999999999997
8	1.000000000000005	0.999999999999981	0.999999999999984
16	1.000000000000013	1.000000000000125	0.999999999999771
32	0.999999999999995	1.000000000000421	1.000000000000139
Δt = 0.01 s			
2	0.999999999999997	0.999999999999992	0.999999999999997
4	1.000000000000004	1.000000000000003	1.000000000000003
8	0.999999999999998	1.000000000000004	0.999999999999982
16	0.999999999999999	1.000000000000045	0.999999999999932
32	1.000000000000020	0.999999999999663	1.000000000000187

Table 7.1: Determinant of $\tilde{\mathbf{A}}$ in Eq. (7.34).

We observe that, as expected, the outlier removal approach improves the robustness of the isogeometric scheme. We see that in the case using cubic C^2 B-splines (green curves), other remaining high-frequency modes are excited, as illustrated in the inset figure in Fig. 7.11c. Hence, we expect that in this case, the computation will become unstable at a later time, which might occur in the case using cubic C^1 B-splines as well. Moreover, we can see that the phase shift between cubic C^1 and C^2 B-splines is not affected by the outlier removal approach. We thus assume that this phase shift results from the different continuity of the spline basis functions. To investigate the effect of the time step on the robustness, we also include the results obtained with cubic C^1 B-splines using a smaller time step of Δt = 0.0025 s (purple curve) in Fig. 7.11. We see that decreasing the time step also improves the robustness of the discretization scheme. Focusing on the accuracy of the results, we observe that neither employing the outlier removal approach nor decreasing the time step, negatively affects the accuracy of the responses. We conclude that the robustness of the isogeometric scheme can be improved using the strong approach of outlier removal or by decreasing the time step, without compromising the obtained accuracy.

To gain a better understanding of how outlier modes and time step size affect the robustness of the discretization scheme, we consider the free vibration of a linear one-dimensional fourth-order problem such as an unconstrained Euler-Bernoulli beam. The

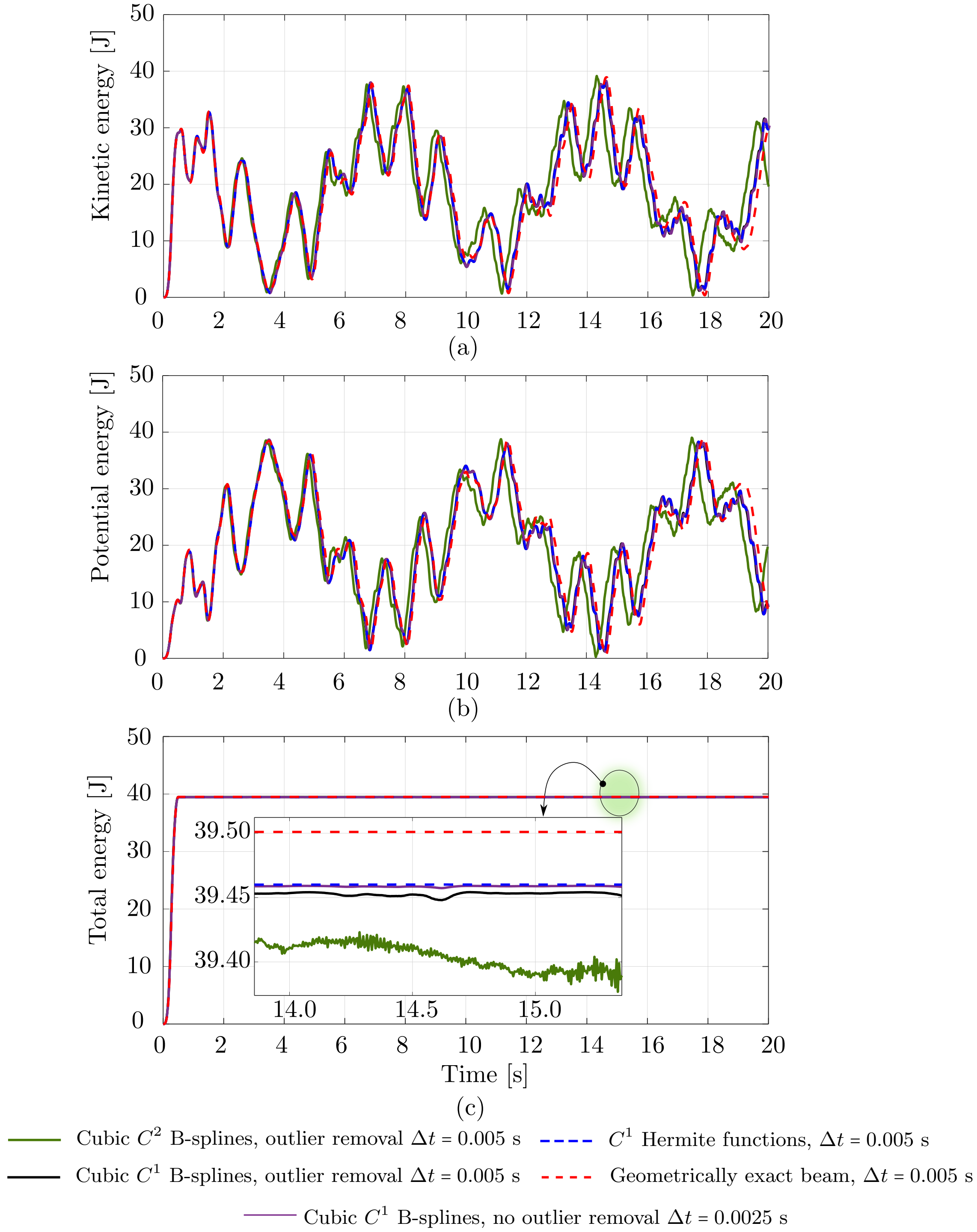

(a)

(b)

(c)

Figure 7.11: The energy of the clamped rod subjected to a vanishing in-plane loading in Fig. 7.5, computed with different basis functions, time steps, with and without outlier removal.

semi-discrete equations of motion, in matrix form, are:

$$\mathbf{M}\,\ddot{\mathbf{u}} + \mathbf{K}\,\mathbf{u} = \mathbf{0}\,, \tag{7.30}$$

where $\mathbf{M}$, $\mathbf{K}$, and $\mathbf{u}$ are the global mass matrix, global stiffness matrix, and the unknown displacement vector of the control points, respectively. Employing the implicit time integration scheme discussed in Section 7.3.3, the inertial and internal elastic terms are approximated at the time instant $t_{n+\frac{1}{2}}$ as follows:

$$\mathbf{M}\,\ddot{\mathbf{u}}_{n+\frac{1}{2}} \approx \frac{\mathbf{M}\,\dot{\mathbf{u}}_{n+1} - \mathbf{M}\,\dot{\mathbf{u}}_{n}}{\Delta\,t}\,, \tag{7.31}$$

$$\mathbf{K}\,\mathbf{u}_{n+\frac{1}{2}} \approx \frac{\mathbf{K}\,\mathbf{u}_{n+1} + \mathbf{K}\,\mathbf{u}_{n}}{2}\,. \tag{7.32}$$

Inserting these approximations into (7.30) and applying (7.27) to approximate $\dot{\mathbf{u}}_{n+1}$, we obtain the following system of equations:

$$\begin{aligned}
\underbrace{\begin{bmatrix} \Delta\,t\,\mathbf{K} & 2\,\mathbf{M} \\ -2\,\mathbf{I} & \Delta\,t\,\mathbf{I} \end{bmatrix}}_{\mathbf{A}_L} \begin{bmatrix} \mathbf{u}_{n+1} \\ \dot{\mathbf{u}}_{n+1} \end{bmatrix} &= \underbrace{\begin{bmatrix} -\Delta\,t\,\mathbf{K} & 2\,\mathbf{M} \\ -2\,\mathbf{I} & -\Delta\,t\,\mathbf{I} \end{bmatrix}}_{\mathbf{A}_R} \begin{bmatrix} \mathbf{u}_{n} \\ \dot{\mathbf{u}}_{n} \end{bmatrix} \\
\begin{bmatrix} \mathbf{u}_{n+1} \\ \dot{\mathbf{u}}_{n+1} \end{bmatrix} &= \underbrace{\mathbf{A}_L^{-1}\,\mathbf{A}_R}_{\tilde{\mathbf{A}}} \begin{bmatrix} \mathbf{u}_{n} \\ \dot{\mathbf{u}}_{n} \end{bmatrix}.
\end{aligned} \tag{7.33}$$

In linear cases, the stiffness and mass matrices, and thus $\tilde{\mathbf{A}}$, do not depend on the configuration, and remain constant during the time integration. Consequently, we can compute the response at time step t_{n+1} in terms of the initial conditions as follows:

$$\begin{bmatrix} \mathbf{u}_{n+1} \\ \dot{\mathbf{u}}_{n+1} \end{bmatrix} = \underbrace{\tilde{\mathbf{A}} \ldots \tilde{\mathbf{A}}}_{(n+1)\text{ times}} \begin{bmatrix} \mathbf{u}_{0} \\ \dot{\mathbf{u}}_{0} \end{bmatrix} = \tilde{\mathbf{A}}^{n+1} \begin{bmatrix} \mathbf{u}_{0} \\ \dot{\mathbf{u}}_{0} \end{bmatrix}. \tag{7.34}$$

The requirement for (7.34) to have an unique solution is that the matrix $\tilde{\mathbf{A}}$ is a convergent matrix [263]. This necessarily requires $\left|\det\left(\tilde{\mathbf{A}}\right)\right| < 1$. Table 7.1 illustrates the determinant of $\tilde{\mathbf{A}}$ computed with cubic Hermite functions, and cubic C^1 B-splines with and without outlier removal, using different time steps and meshes. We observe that the determinant is either smaller or larger than 1.0 with a tolerance in the range of $\left[10^{-13},\, 10^{-15}\right]$, i.e. machine accuracy. Such a problem can be attributed, in principle, to round-off errors due to floating-point arithmetic, where the numerical deviation from 1.0 highly depends on the time step, mesh size, and basis functions, i.e. on the time integration and spatial discretization schemes. We can also see that neither using cubic Hermite functions, employing outlier removal, nor reducing the time step, guarantees that $\left|\det\left(\tilde{\mathbf{A}}\right)\right| < 1$. Hence, there is no indication that one discretization scheme ensures the existence of the solution at an arbitrary time step t_{n+1} for (7.34), and the other schemes do not. For nonlinear problems, since $\tilde{\mathbf{A}}$ is configuration-dependent, it is not trivial to identify parameters and calibrate them in order to ensure $\left|\det\left(\tilde{\mathbf{A}}\right)\right| < 1$. In addition, there might be other factors that are decisive for the existence of the solution at t_{n+1}, and thus for the robustness of the discretization scheme. This requires further study and investigation, which we postpone to future work.

7.4.3 On the influence of the configuration-dependent mass matrix

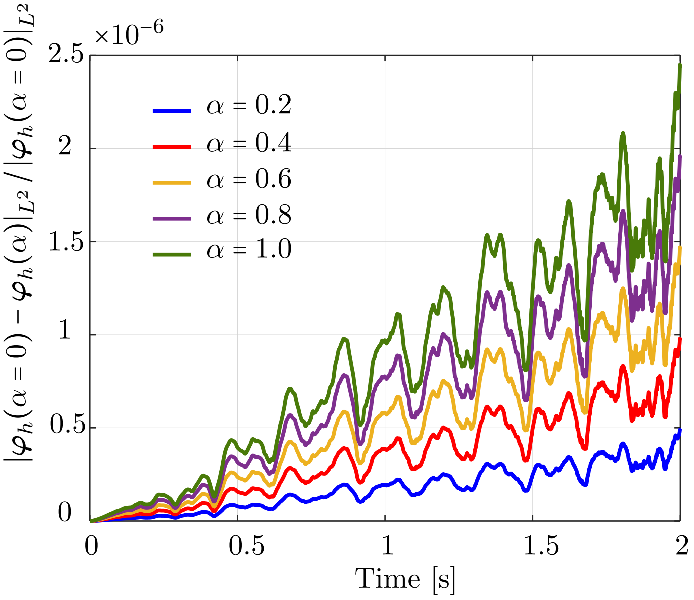

Figure 7.12: The relative change of the deformed configuration of an unconstrained rod computed with different scaling factors α.

We now briefly discuss the behavior of the configuration-dependent mass matrix (7.18), and whether this counterpart can be omitted. We recall that the mass matrix (7.18), $\mathbf{M}$, consists of two counterparts, $\mathbf{M}_1$ and the rotational counterpart $\mathbf{M}_2$. While $\mathbf{M}_1$ does not depend on the current rod configuration and remains constant, $\mathbf{M}_2$ is configuration-dependent. In most of the common nonlinear dynamic analyses, $\mathbf{M}_2$ is considered a small perturbation and thus is neglected, which results in a constant configuration-independent mass matrix.

To investigate the effect of $\mathbf{M}_2$ on the system response and whether $\mathbf{M}_2$ behaves as a regular perturbation, we consider the unconstrained rod benchmark studied in Section 7.4.1, computed with the isogeometric discretization scheme using cubic C^1 B-splines. In particular, we scale $\mathbf{M}_2$ by a factor $\alpha \in [0, 1]$. The mass matrix (7.18) then becomes:

$$\mathbf{M} = \mathbf{M}_1 + \alpha \mathbf{M}_2 \,. \tag{7.35}$$

Fig. 7.12 illustrates the relative change in the L^2 norm of the deformed rod, $\boldsymbol{\varphi}_h$, during the simulation time of 2 s. Different colors correspond to different values of α. We observe that this relative change increases in time and with increasing α. This observation implies that, for the studied rod, $\mathbf{M}_2$ does not behave as a regular perturbation, and thus should not be neglected. Mathematical proof and analysis of this counterpart of the mass matrix is out of the scope of this paper and is postponed to future works.

7.5 Application to a swinging rubber rod

In this section, we apply the nonlinear rod formulation [134], discretized with isogeometric discretizations, to a swinging rubber rod, which can represent for instance a sort of mooring line in a offshore wind turbine or a oil platform. We consider conservative and non-conservative forces such as gravity, forces induced by surrounding wind or water, and pulsating forces. We demonstrate that our rod formulation is able to represent the rod nonlinear behavior that is a combination of elastic vibrations and rigid body oscillations around a static position and shape, which deforms differently at different force frequencies. Based on our results in the previous section, we spatially discretize the swinging rod with cubic C^1 B-splines ($p = 3$) and improve its robustness with the strong approach of outlier removal. We start with benchmarking our approach via an example of a swinging rod under gravitational loading [264], [265].

7.5.1 Benchmarking

We consider an initially straight rod of length $L = 1.0$ m, with a circular cross-section, a radius of $5 \cdot 10^{-3}$ m, Young's modulus $E = 2 \cdot 10^{11}$ N/m^2, and mass density $\rho = 1100$ kg/m^3. The rod is subjected merely to gravitational loading [264], which we simulate with a direction of $(0,\ -1,\ 0)$ while the initial director of the rod is $(1,\ 0,\ 0)$. Thus, the rod deforms in the xy-plane. We choose a time step of $\Delta t = 0.01$ s, a simulation time of 2.4 s, and a tolerance of 10^{-10} for the Newton-Raphson scheme.

Fig. 7.13 illustrates the deformed configuration of the studied rod at twelve time steps, and Fig. 7.14 shows the time evolution of the horizontal ($u_x(t)$ in blue) and the vertical displacement ($u_y(t)$ in red) at the rod free-end. We observe in Fig. 7.13 that the swinging rod behaves similarly to an elastic pendulum, and thus has a stable equilibrium configuration when it is aligned with the $y-$axis and its free-end is located at $(x, y, z) = (0, -1, 0)$ m. Due to the highly nonlinear nature captured by the current formulation, the rod exhibits large elastic rotations and displacements in time. Comparing these results with those of [264, Fig. 8, 9], we observe an apparent difference after 2.0 s, for instance, the deformed configuration at $t = 2.4$ s clearly distinguishes from that in [264, Fig. 8]. We further compare the energy obtained with our approach, illustrated in Fig. 7.15, with that in [264, Fig. 10]. We see that the total energy and its counterparts show approximately the same time history as the reference, with an exception of around 2.4 s. While the reference and our results both consist of high-frequency contents around this time, the reference energy does not jump to a large value as ours. This is consistent with different deformed configurations after 2.0 s observed in Fig. 7.13. We conclude that despite the absence of outliers in our computation, our approach is less robust than the scheme using classical nodal finite elements with cubic Hermite functions applied in [264]. Nevertheless, it leads to the same behavior for the swinging rod, given that the computation is stable.

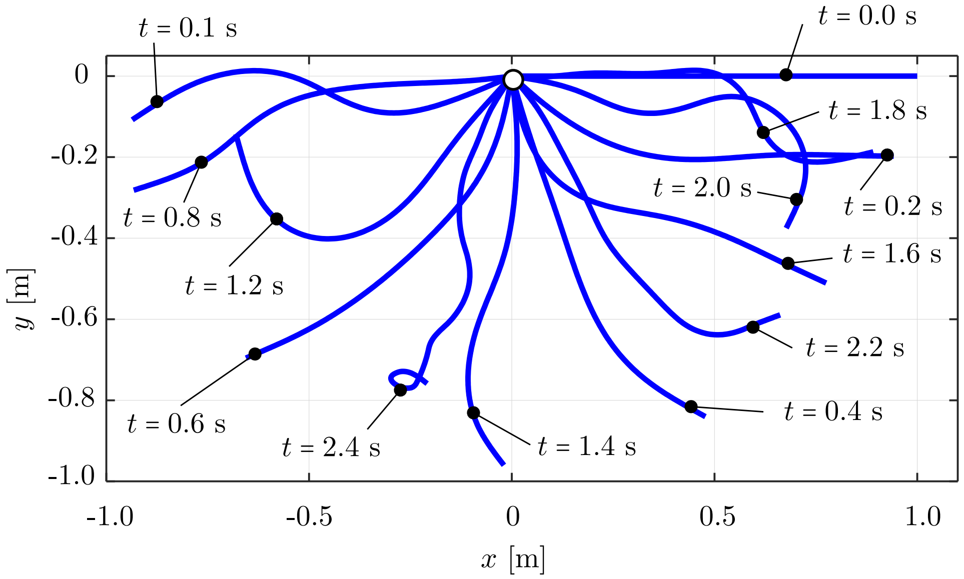

Figure 7.13: Deformed configurations of a swinging rubber rod due to gravity, computed with cubic C^1 B-splines ($p = 3$) and outliers removed.

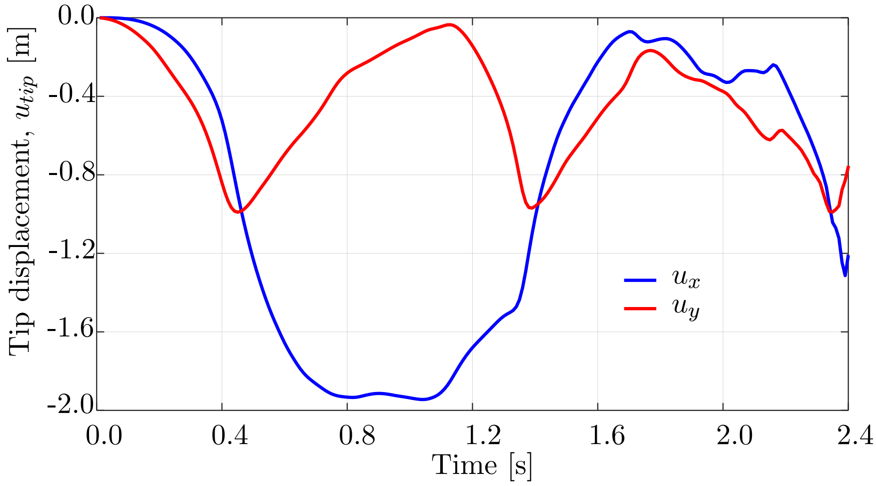

Figure 7.14: The tip displacements of the swinging rubber rod in Fig. 7.13.

7.5.2 Dynamic response to wind forces

We now consider the same rod as in the previous benchmark, subjected to an additional wind field with a wind profile illustrated in Fig. 7.16. The wind velocity has constant values but changing direction along the z−axis, that is:

$$\mathbf{v}_{wind}(z) = v_0\,\mathbf{d}_{wind}(z) = v_0\left[\mathbf{E}_1\cos\left(\beta_0 - 2\,\beta_0\,\frac{z}{L}\right) + \mathbf{E}_2\sin\left(\beta_0 - 2\,\beta_0\,\frac{z}{L}\right)\right], \tag{7.36}$$

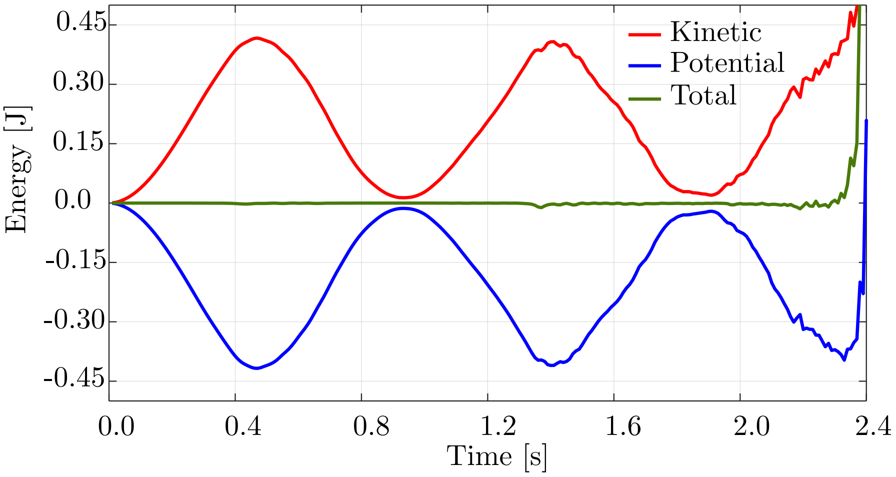

Figure 7.15: The energy of the swinging rubber rod in Fig. 7.13.

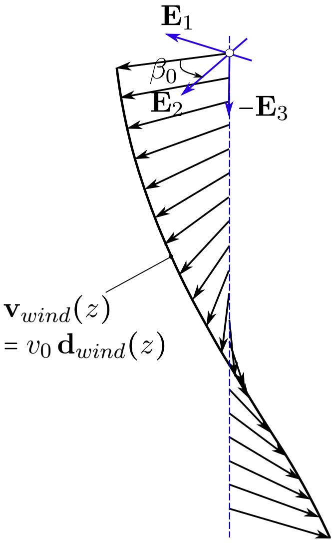

Figure 7.16: A wind profile with constant amplitude and rotating direction around the z-axis.

where v_0 is the constant value of the wind velocity, $\mathbf{d}_{wind}$ is the director of the wind velocity, β_0 is the angle of $\mathbf{d}_{wind}$ with respect to the $y-$axis at $z = 0$, and L is the initial length of the rod. For this example, we choose $v_0 = 10$ m/s, $\beta_0 = 45°$, a simulation time of 30 s, and an initial angle of the rod with respect to the $x-$axis of $-15°$, that is an initial rod director of $\mathbf{d} = (\cos(\pi/12),\ 0,\ -\sin(\pi/12))$. We apply the same discretization as in the previous benchmark. Fig. 7.17 illustrates the motion sequence of the swinging rod under the considered loading. Due to the three-dimensional wind profile, the rod shows out-of-plane deformations. Focusing on the configurations at $t = 8.75$ s and $t = 10$

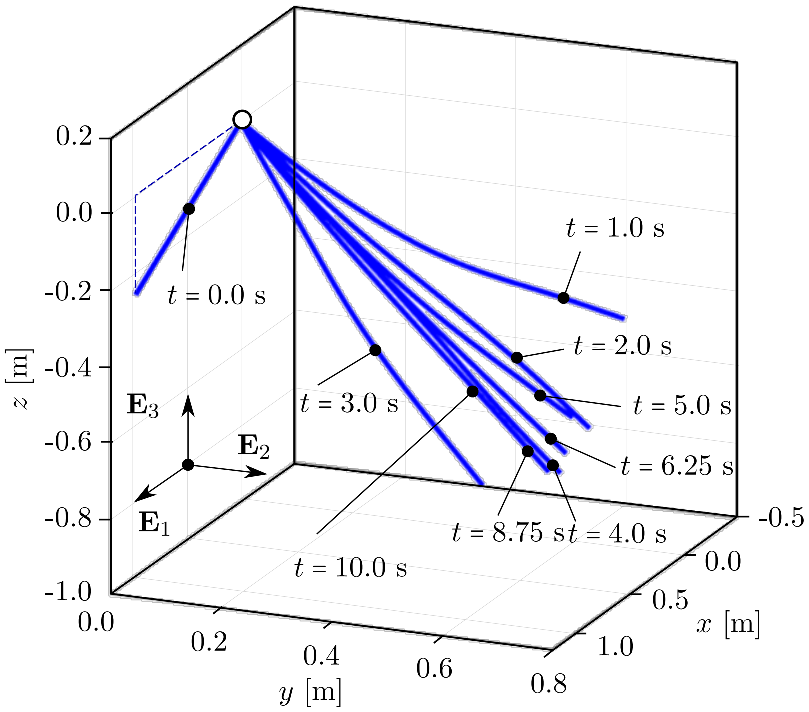

Figure 7.17: Deformed configurations of a swinging rubber rod due to gravity and the wind profile in Fig. 7.16, computed with cubic C^1 B-splines ($p = 3$) and outliers removed.

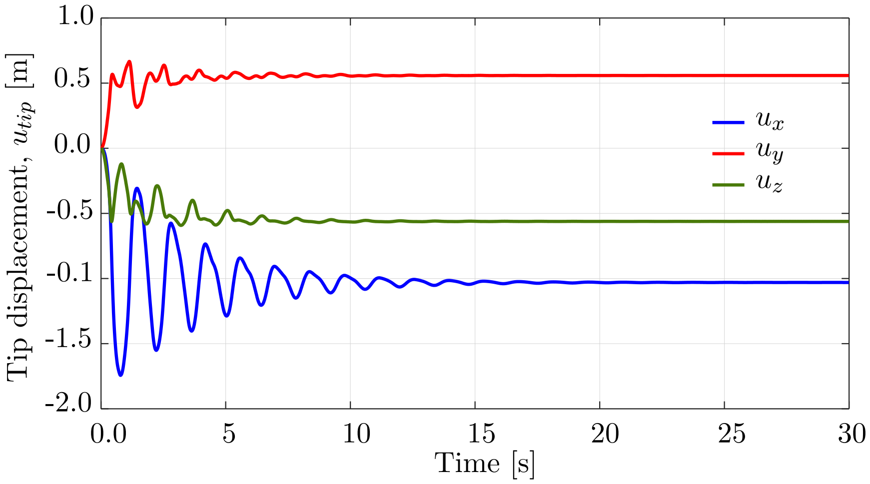

Figure 7.18: The tip displacements of the swinging rubber rod in Fig. 7.17.

s, which are no longer visually distinguishable, we assume that the rod has approximately reached a steady state configuration. This behavior is also illustrated in the time history of the rod tip displacement, demonstrated in Fig. 7.18, and of the energy of the system, demonstrated in Fig. 7.19. We observe that after about 15 s, all displacement

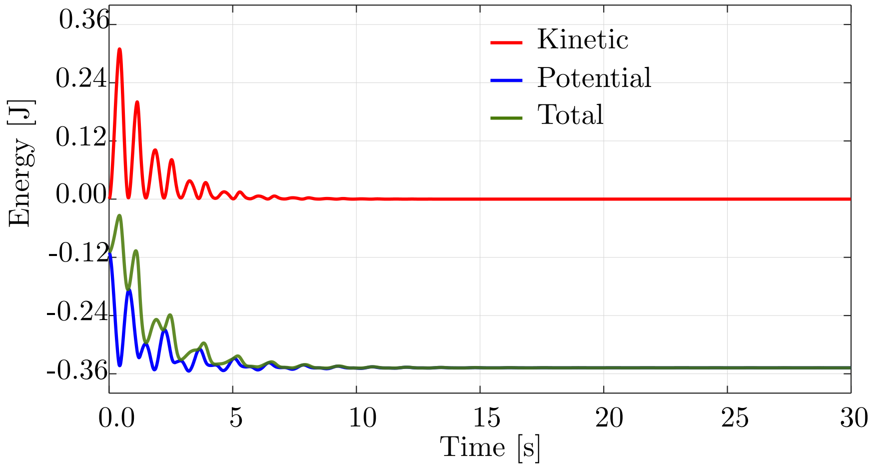

Figure 7.19: The energy of the swinging rubber rod in Fig. 7.17.

components remain approximately constant, which is consistent with approximately zero kinetic energy at this time, i.e. the rod reaches an equilibrium configuration. Comparing this with the behavior of the rod in the previous benchmark without wind force, we can see that the wind force dampens the motion of the rod to an equilibrium configuration. This damping characteristic, generally of aerodynamic forces, can be seen when it is approximated by a Taylor expansion as follows:

$$\mathbf{F}_f = \left.\frac{\partial \mathbf{F}_f}{\partial \mathbf{q}}\right|_{\mathbf{q}=\mathbf{0}} \mathbf{q} + \left.\frac{\partial \mathbf{F}_f}{\partial \dot{\mathbf{q}}}\right|_{\dot{\mathbf{q}}=\mathbf{0}} \dot{\mathbf{q}} + \left.\frac{\partial \mathbf{F}_f}{\partial \ddot{\mathbf{q}}}\right|_{\ddot{\mathbf{q}}=\mathbf{0}} \ddot{\mathbf{q}} + \ldots, \tag{7.37}$$

where the first term gives rise to the lift/thrust forces, the second term contains the so-called damping forces, and the third term is related to the added mass forces. An aerodynamic damping matrix can then be defined as $\mathbf{D}_{\text{fluid}} = -\left.\frac{\partial \mathbf{F}_f}{\partial \dot{\mathbf{q}}}\right|_{\dot{\mathbf{q}}=\mathbf{0}}$, which is a function of the free-stream velocity, among other parameters. The aerodynamic damping strongly depends on the magnitude of the free-stream velocity $V_\infty = |\mathbf{V}_\infty|$. When V_∞ is below a critical velocity V_∞^C (subcritical condition), the damping is positive and the surrounding flow absorbs the energy of the structure. When $V_\infty = V_\infty^C$ (critical condition), the damping is zero and then the surrounding flow does not absorb or supply the structure energy. When $V_\infty > V_\infty^C$ (supercritical condition), the damping becomes negative and the surrounding flow supplies energy to the structure, i.e. favoring the emergence of fluid-structure interaction instabilities such as aeroelastic flutter. For the swinging rod studied here, we are in a subcritical condition since the rod oscillation is damped out over time. Focusing on the robustness of the employed discretization scheme, we observe that the wind force also dampens out the high-frequency modes, and thus improves its robustness. We conclude that, given the subcritical condition, employing damping forces is another approach to improve the robustness, particularly of the isogeometric discretization scheme studied in this paper.

7.5.3 Dynamic response to pulsating forces

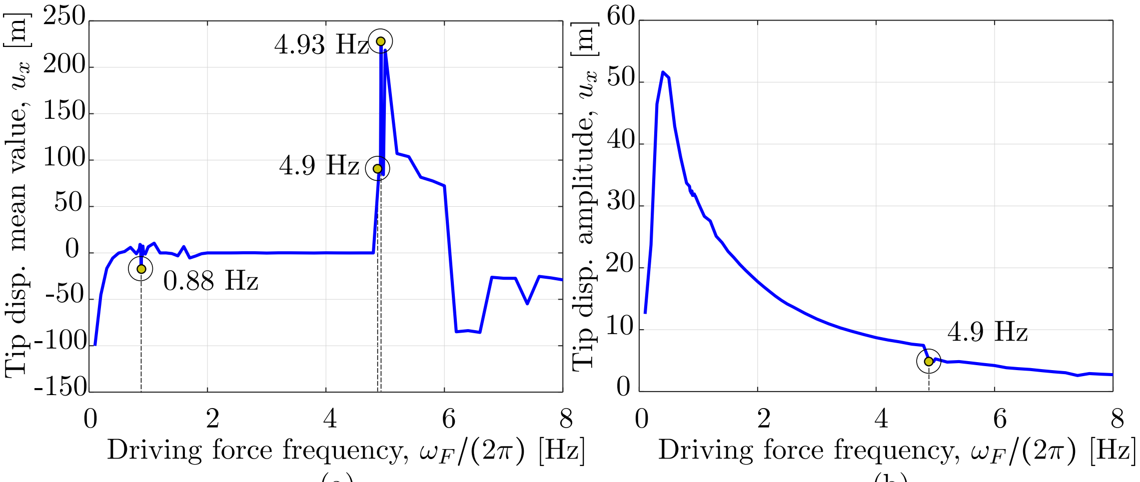

(a) (b)

Figure 7.20: The mean value and the amplitude of the horizontal tip displacement u_x of an aluminum swinging rod at steady state, computed with cubic C^1 B-splines ($p = 3$) and outliers removed.

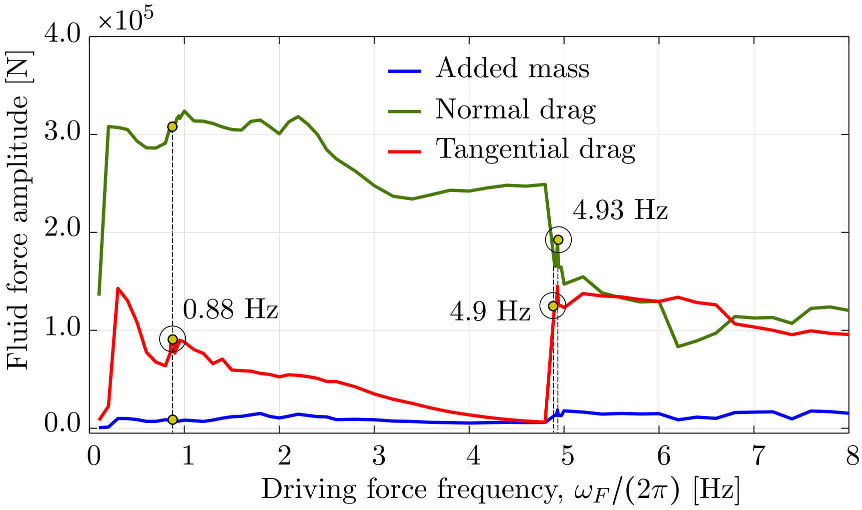

Figure 7.21: The amplitude of three force components induced by surrounding water at rest, integrated over the aluminium swinging rod at steady state.

Our last example is a long rod submerged in water, which simulates a sort of mooring line used in offshore wind engineering. To this end, we consider a combination of the gravitational field, the surrounding water at rest, and a horizontal pulsating force applied at the free end of the swinging rod. We choose a sinusoidal pulsating force that is:

$$\boldsymbol{F}(t) = A_F \sin\left(\frac{\omega_F}{2\pi} t\right) \boldsymbol{E}_1 , \tag{7.38}$$

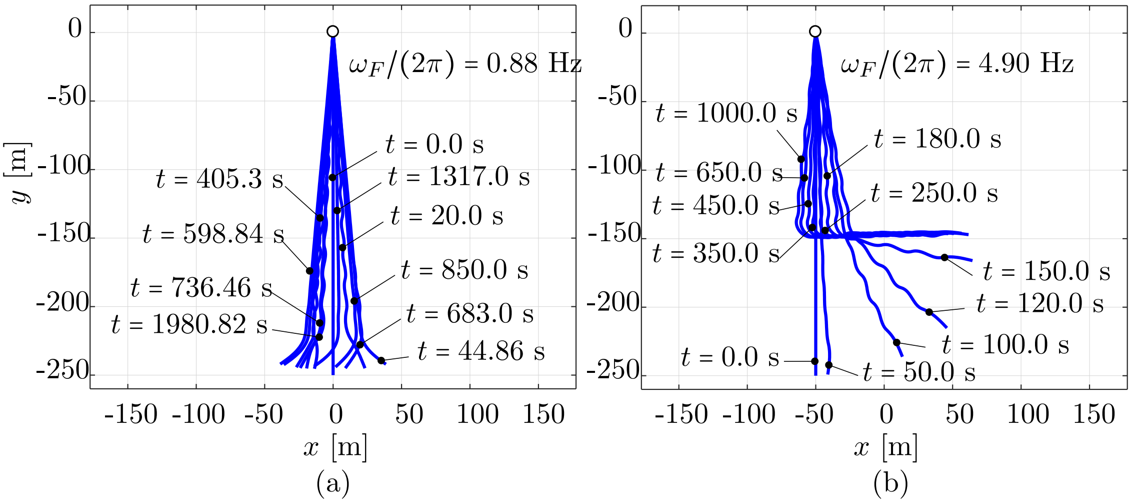

Figure 7.22: Deformed configurations of an aluminum swinging rod at force frequencies of 0.88 Hz and 4.90 Hz, computed with cubic C^1 B-splines ($p = 3$) and outliers removed.

where A_F and ω_F are the force amplitude and angular frequency, respectively. For this example, we choose an amplitude $A_f = 350.0$ kN, and different frequencies $(\omega_F/2\pi)$ ranging from 0.1 Hz to 8 Hz. The surrounding water is at rest, i.e. $\mathbf{V}_\infty = \mathbf{0}$ and $\mathbf{a}_\infty = \mathbf{0}$, and the mass density of the surrounding water is $\rho_f = 1000$ kg/m^3. In this example, we consider an aluminium rod with an initial director $\mathbf{d} = (1,\ 0,\ 0)$, a length of 250 m, a circular cross-section with a radius of 0.02 m, Young's modulus $E = 7 \cdot 10^{10}$ N/m^2, and mass density $\rho = 2700$ kg/m^3. We simulate the gravitational field with a direction of $(0,\ -1,\ 0)$, which allows the rod to deform only in the xy-plane. We compute this example for 1000 s and 2000 s such that a steady state is observed during the last 100 s, which is identified as the response becomes periodic in time.

Fig. 7.20 illustrates the mean value and the amplitude of the horizontal displacement u_x at the free tip of the studied swinging rod after it reaches the steady state, as a function of the force frequencies $(\omega_F/2\pi)$. We observe that the mean value of the tip displacement (Fig. 7.20a), which corresponds to the position, around which the rod oscillates, i.e. the static equilibrium position, jumps at force frequencies smaller than 2.0 Hz and those larger than 5.0 Hz. It means that the equilibrium position and configuration change abruptly when the force frequency changes, which indicates a nonlinear behavior of the rod in different frequency ranges. Focusing on the amplitude of the tip displacement in Fig. 7.20b, we can see that after a steep increase at low frequencies, it decreases with increasing force frequency and slightly jumps downwards around 4.9 Hz. This relation between the amplitude and the force frequency can be explained based on the linear theory. Consider a damped harmonic oscillator of mass m, spring stiffness k, and damping coefficient b, subjected to a sinusoidal pulsating force, $f_0 \sin(\Omega t)$, of frequency Ω and amplitude f_0. It is well-known from classical vibration theory that the

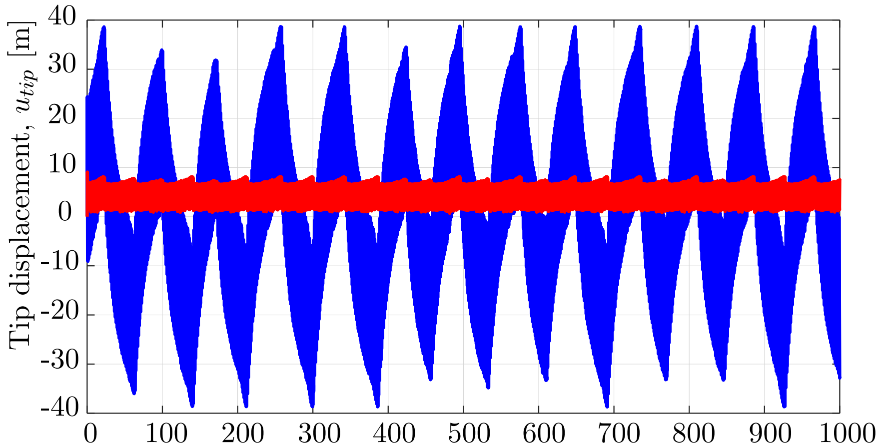

(a) $\omega_F/(2\pi) = 0.88$ Hz

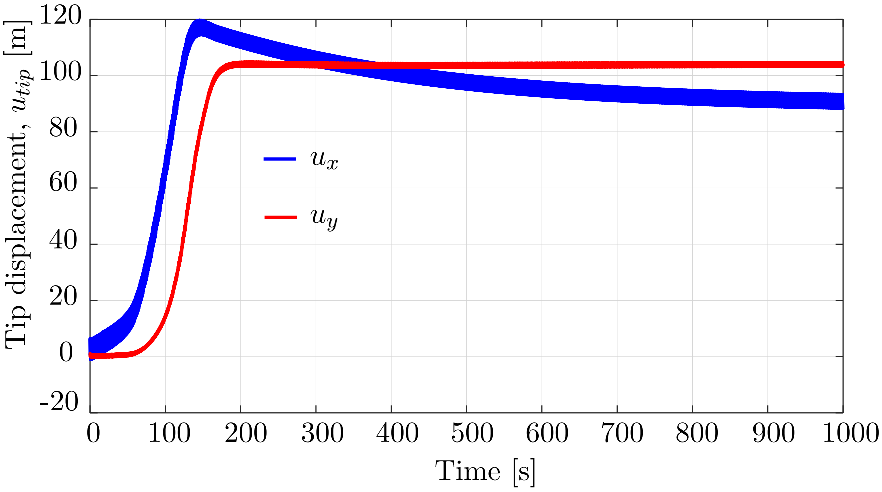

(b) $\omega_F/(2\pi) = 4.90$ Hz

Figure 7.23: The tip displacements of an aluminum swinging rod computed for force frequencies of 0.88 Hz and 4.90 Hz.

response amplitude of this linear system is:

$$A = \frac{f_0}{\sqrt{m(\Omega^2 - \omega_0^2)^2 + b^2\Omega^2}} \tag{7.39}$$

where $\omega_0 = \sqrt{k/m}$ is the natural frequency of the system. We can see that for the cases of $\Omega < \omega_0$, increasing Ω increases the amplitude A, and for the cases of $\Omega > \omega_0$, increasing Ω decreases A. Since the studied nonlinear rod can be considered as a damped (by considering the surrounding flow) distributed-parameter elastic pendulum subjected to a pulsating force at its free end, a similar relation between the amplitude and the force frequency is expected for both linear and the nonlinear cases. This supports our observation in Fig. 7.20b, except for the jump at 4.9 Hz, which associates with the highest positive peak of the mean value in Fig. 7.20a.

To gain better insights into the rod behavior, in Fig. 7.22, we plot some deformed configurations at different times for 0.88 Hz and 4.9 Hz, i.e. before and close to the frequency value where the amplitude jumps. We observe that for both two frequencies, the rod behavior is a combination of elastic vibrations and rotations as a rigid body that oscillates around a static equilibrium position. While this equilibrium position is along the vertical axis in the case of 0.88 Hz (Fig. 7.22a), it, as well as the equilibrium configuration, changes in the case of 4.9 Hz (Fig. 7.22b), since the lower part of the rod is bent to a horizontal segment, and the rod then oscillates around the new deformed position. This behavior together with the amplitude jump is also observed in the time history of the tip displacement, illustrated in Fig. 7.23 for 0.88 Hz and 4.9 Hz. We can also see that both two displacement components oscillate over time, while their mean value jumps to a value around 100 m in the case of 4.9 Hz. This is further reflected in the relation between the pulsating force frequency and the amplitude of forces induced by the surrounding flow, illustrated in Fig. 7.21. In Fig. 7.21, we illustrate the amplitude A_f^ω of three components of the resulting force induced by the surrounding flow (added mass, normal drag, and tangential drag), integrated over the rod length once the rod reaches the steady state, that is:

$$A_f^\omega(\omega_F) = \max_{\text{steady state}} \left[f_f^t(t) \right] - \min_{\text{steady state}} \left[f_f^t(t) \right] ,$$

where the integrated force $f_f^t(t)$ is:

$$f_f^t(t) = \int_0^L \left| \mathbf{F}_f(s,t) \right| ds \, ,$$

as a function of the pulsating force frequency. We observe that the amplitude of the normal and tangential drag forces also jumps approximately at 4.9 Hz. In particular, the normal drag drops, while the tangential drag jumps upwards, which is consistent with the fact that the lower part of the rod is bent to a horizontal segment, i.e. only the upper part is mainly affected by the norm drag, while the tangential drag is the dominating force in the lower part. Regarding the robustness of the applied discretization scheme, we did not obtain unstable computations and results containing high-frequency contents. We conclude that different nonlinear behaviors of the swinging rod can be represented and studied using the rod formulation [134], together with the isogeometric discretization scheme, improved using outlier removal, and with an energy-momentum preserving implicit time integration scheme. This has been shown to be a sufficiently robust approach for studying nonlinear structures such as swinging rods modeling mooring lines, which can be further investigated for complex behaviors such as parametric resonances and chaotic behavior in future works.

7.6 Summary and conclusions

In this paper, we explored the application of the nonlinear formulation [134] for rods that exhibit only axial and bending deformations, using isogeometric spatial discretizations. Our results illustrate different convergence rates for odd and even polynomial degrees, which is known from other isogeometric discretization methods, see e.g. [201], [266] and the references therein. We suggest that the manifold structure of the solution space might be one key factor affecting the convergence rate of the corresponding discretization scheme. We demonstrated computationally via dynamic benchmarks of two- and three-dimensional rods that isogeometric discretizations are less robust than the standard scheme using Hermite functions. Increasing the smoothness of spline basis functions leads to a phase shift and reduces the robustness. We showed that robustness can be improved via a strong approach of outlier removal [122] without compromising the accuracy. Alternatively, reducing the time step or employing forces with damping characteristics leads to more robust computations. We have shown that the robustness is closely related to round-off errors due to floating-point arithmetic. In addition, we demonstrated computationally via an unconstrained rod subjected to out-of-plane vanishing forces that the configuration-dependent mass matrix does not behave as a regular perturbation and thus cannot be simplified to a constant matrix. Lastly, we applied our nonlinear transient formulation to a swinging rubber rod subjected to gravity, forces induced by a surrounding flow such as wind and water, and a pulsating force of different frequencies. Our results also show that the isogeometric discretization scheme is robust and reliable for such an analysis.

The results presented in this work open up several directions for future works. One open question is the accuracy and convergence behavior of the discretization scheme in nonlinear problems. Another question is the irregular behavior of the configuration-dependent mass term that, to our best knowledge, is not yet proved analytically. This is particularly interesting for choosing and developing an efficient and robust time integration scheme. It is also desirable to employ our nonlinear formulation with the isogeometric discretization scheme in highly nonlinear problems with complex loads and geometries.

Appendix 7.A

An elastic pendulum

To benchmark our implementation regarding the time integration scheme and to verify that the chosen implicit time integration scheme achieves second-order accuracy, approximately preserves energy, and exactly preserves the linear angular momentum [134], [262], discussed in Section 7.3.3, we consider the dynamics of a two degrees-of-freedom elastic pendulum, illustrated in Fig. 7.24. Its configuration space is $\mathcal{D}_{\text{pen}} = \mathbb{R} \times SO(2)$, where $SO(2)$ is the special orthogonal group in two dimensions. For this pendulum, the two degrees of freedom are the angular rotation with respect to the vertical axis, $\theta(t)$,

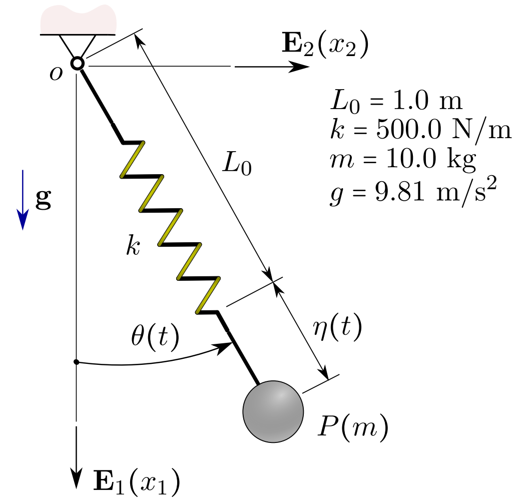

Figure 7.24: Schematic of an elastic pendulum with two degrees of freedom.

and the axial deformation of the spring, $\eta(t)$. Unit vectors $\mathbf{E}_1$ and $\mathbf{E}_2$ are the first two canonical Cartesian bases of $\mathbb{R}^3$, L_0, k, m, and g are the spring's natural length, spring stiffness, mass, and gravitational acceleration, respectively. We consider a simulation time of 30 s and a time step $\Delta t = 0.005$ s.

	t = 7.5 s	t = 15 s	t = 22.5 s	t = 30 s
Total energy	26.824953231727577	26.824943982990575	26.824999851284034	26.824976045230380
Angular momentum	−0.605000000000103	−0.605000000000105	−0.605000000000100	−0.605000000000120

Table 7.2: Total energy and the linear angular momentum of an elastic pendulum illustrated in Fig. 7.25.

We first consider the case of no gravitational acceleration ($g = 0$) and no external load with the following initial conditions:

$$\theta(t = 0) = 0\,, \qquad \eta(t = 0) = 0.1\,, \tag{7.40a}$$

$$\dot{\theta}(t = 0) = -0.5\,, \qquad \dot{\eta}(t = 0) = 0.25\,. \tag{7.40b}$$

Fig. 7.25a-b illustrates the time evolution of the energy and the third component of the angular momentum, j_3. We note that for the studied pendulum, the first and second components of the angular momentum are zero, and thus are not illustrated here. We observe that both the total energy and j_3 are virtually constant over the simulation time. Table 7.2 shows their values at four snapshots. We can see that the total energy is approximately preserved, while the angular momentum is exactly preserved up to a tolerance of the machine accuracy. Fig. 7.25c-d shows the second precision quotient of the response during the simulation time, which is computed to verify the implementation

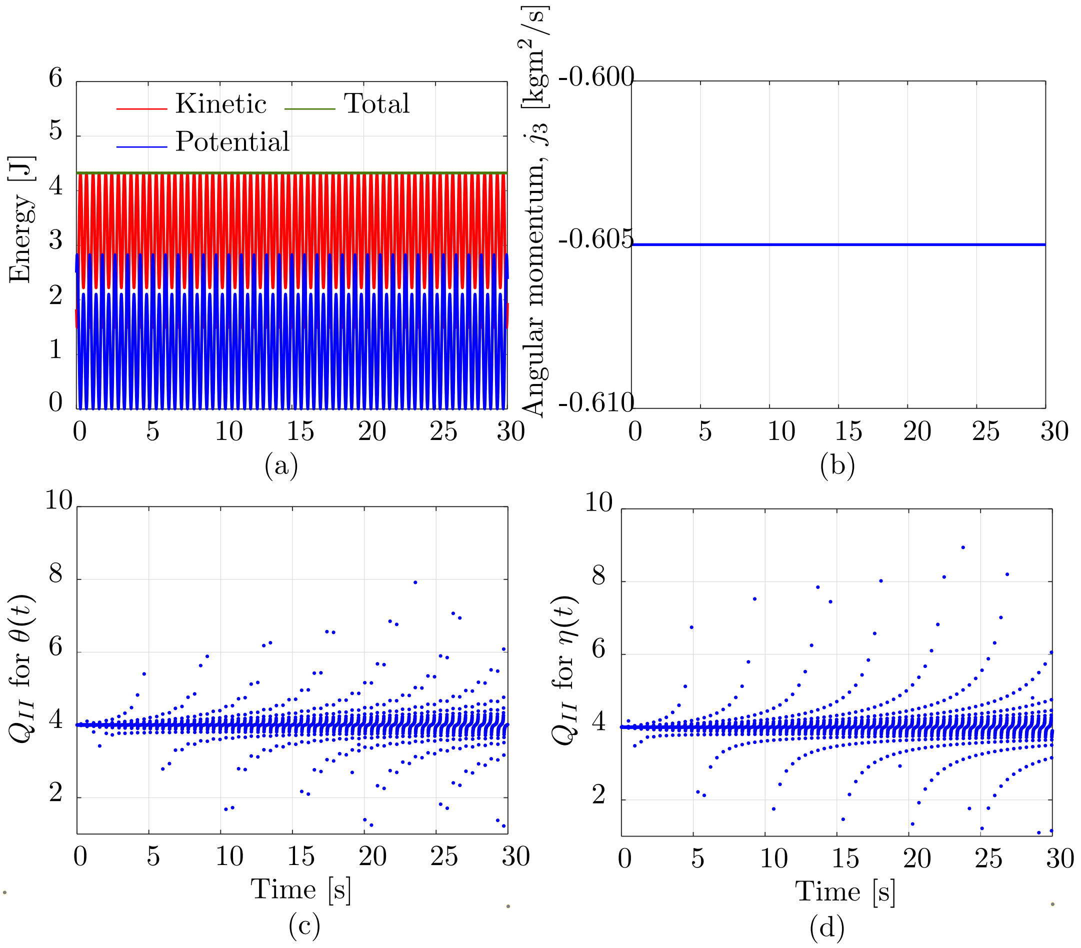

(a) (b) (c) (d)

Figure 7.25: Energy, the third component of angular momentum and the second precision quotient of the elastic pendulum in Fig. 7.24 with the initial conditions (7.40).

correctness of a numerical integration scheme and is defined as [267]:

$$Q_{II} = Q_{II}(t) = \frac{\left\| \mathbf{u}_{\Delta t} - \mathbf{u}_{\Delta t/2} \right\|}{\left\| \mathbf{u}_{\Delta t/2} - \mathbf{u}_{\Delta t/4} \right\|} , \tag{7.41}$$

where $\mathbf{u} = \mathbf{u}(t)$ is a time-dependent variable, and its subscripts, Δt, $\Delta t/2$, ..., denote the time step employed to compute $\mathbf{u}$. For well-implemented time integration schemes, the precision quotient Q_{II} is approximately 2^q, where q is the order of accuracy of the integration scheme [267]. For our implicit scheme, $q = 2$. We note that our choice of the second precision quotient instead of the first precision quotient is due to the lack of an analytical solution for the studied elastic pendulum [267]. We observe in Fig. 7.25c-d the expected value of $2^2 = 4$ for Q_{II}, which verifies the correctness of our implementation.

We then consider the load case consisting of the gravitational field and the following

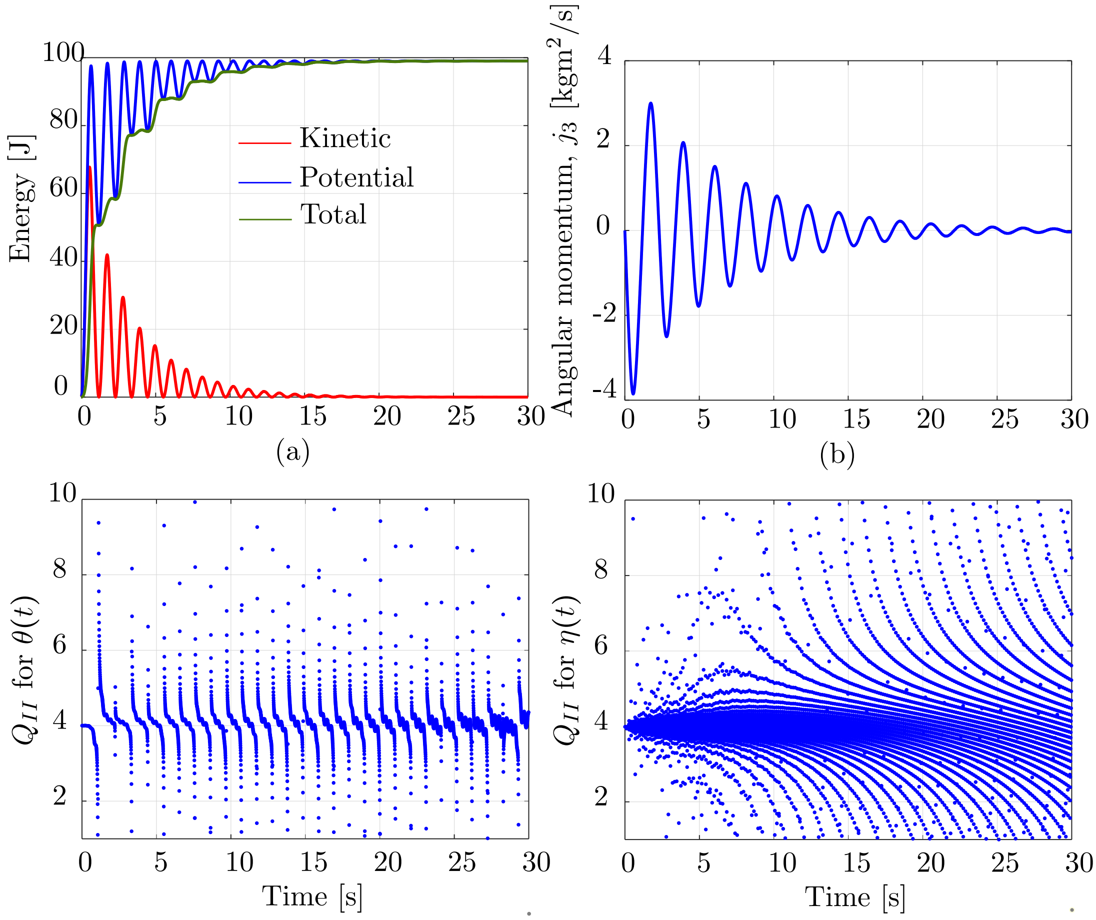

(a) (b)

(c) (d)

Figure 7.26: Energy, the third component of angular momentum and the second precision quotient of the elastic pendulum in Fig. 7.24, subjected to gravity and a parabolic wind profile, with the initial conditions (7.43).

parabolic wind profile:

$$\mathbf{v}_w(x_1\,t) = x_1^2\left(1.0 + 0.1\,\sin\left(\frac{1}{50}\,\frac{\sqrt{k/m}}{2\,\pi}\,t\right)\right)\mathbf{E}_2\,. \tag{7.42}$$

We choose the following initial conditions of the pendulum:

$$\theta(t = 0) = \pi/2\,, \qquad \eta(t = 0) = 0.0\,, \tag{7.43a}$$

$$\dot{\theta}(t = 0) = 0.0\,, \qquad \dot{\eta}(t = 0) = 0.0\,. \tag{7.43b}$$

We observe in Fig. 7.26a-b that the total energy and angular momentum are no longer preserved due to the presence of external forces, as expected. We can also see that after approximately 17 s, the pendulum does not contain any kinetic energy, i.e. it approximately achieves a static equilibrium state. The second precision quotient Q_{II}, illustrated in Fig. 7.26c-d, also implies a second-order accurate time integration scheme in this case. We conclude that the chosen implicit time integration scheme approximately preserves the total energy, exactly preserves the angular momentum, and is second-order accurate.

Appendix 7.B

Linearization

Preliminaries

We recall the semi-discrete formulation for the rod motions in Section 7.3.1, that is:

$$\mathbf{g}_d = \int_0^S \left(\mathbf{M}(\mathbf{q})\, \nabla_{\dot{\mathbf{q}}}\, \dot{\mathbf{q}} + \mathbf{B}(\mathbf{q})^T \boldsymbol{\sigma}_h - \mathbf{N}^T \mathbf{f}^{\text{ext}} \right) \mathrm{d}s = \mathbf{0}\,. \tag{7.44}$$

Analogously, the variational formulation that describes the equilibrium of the rod is:

$$\mathbf{g}_s = \int_0^S \left(\mathbf{B}(\mathbf{q})^T \boldsymbol{\sigma}_h - \mathbf{N}^T \mathbf{f}^{\text{ext}} \right) \mathrm{d}s = \mathbf{0}\,. \tag{7.45}$$

We employ a standard approach based on a Taylor expansion of (7.45) and (7.44) to obtain the tangent stiffness matrix associated with $\mathbf{g}_s$ and $\mathbf{g}_d$, respectively. To this end, Taylor's approximation for a vector function $\mathbf{g}(\mathbf{q}, \dot{\mathbf{q}}, \ddot{\mathbf{q}})$ is given by:

$$\begin{aligned}\mathbf{g}(\mathbf{q}+\Delta\mathbf{q}, \dot{\mathbf{q}}+\Delta\dot{\mathbf{q}}, \ddot{\mathbf{q}}+\Delta\ddot{\mathbf{q}}) = {} & \mathbf{g}(\mathbf{q}, \dot{\mathbf{q}}, \ddot{\mathbf{q}}) + \mathrm{D}\,\mathbf{g}(\mathbf{q}, \dot{\mathbf{q}}, \ddot{\mathbf{q}}) \cdot (\Delta\mathbf{q}, \Delta\dot{\mathbf{q}}, \Delta\ddot{\mathbf{q}}) \\ & + \mathrm{D}^2\,\mathbf{g}(\mathbf{q}, \dot{\mathbf{q}}, \ddot{\mathbf{q}}) : ((\Delta\mathbf{q}, \Delta\dot{\mathbf{q}}, \Delta\ddot{\mathbf{q}}) \otimes (\Delta\mathbf{q}, \Delta\dot{\mathbf{q}}, \Delta\ddot{\mathbf{q}})) \\ & + O\left(\|\Delta\mathbf{q}\|^3, \|\Delta\dot{\mathbf{q}}\|^3, \|\Delta\ddot{\mathbf{q}}\|^3, ..., \|\Delta\dot{\mathbf{q}}\|^2 \|\Delta\ddot{\mathbf{q}}\|, ... \right),\end{aligned} \tag{7.46}$$

where $\mathrm{D}^i(\cdot)$, $i = 1, 2, ...$, is a $(i+1)$-order tensor of type $(0, i)$, and $(:)$ denotes the double-contraction tensor operation. Assuming that the higher-order terms are negligible, we obtain:

$$\begin{aligned}\mathbf{g}(\mathbf{q}+\Delta\mathbf{q}, \dot{\mathbf{q}}+\Delta\dot{\mathbf{q}}, \ddot{\mathbf{q}}+\Delta\ddot{\mathbf{q}}) \approx {} & \mathbf{g}(\mathbf{q}, \dot{\mathbf{q}}, \ddot{\mathbf{q}}) + \partial_{\mathbf{q}}\,\mathbf{g}(\mathbf{q}, \dot{\mathbf{q}}, \ddot{\mathbf{q}}) \cdot \Delta\mathbf{q} \\ & + \partial_{\dot{\mathbf{q}}}\,\mathbf{g}(\mathbf{q}, \dot{\mathbf{q}}, \ddot{\mathbf{q}}) \cdot \Delta\dot{\mathbf{q}} + \partial_{\ddot{\mathbf{q}}}\,\mathbf{g}(\mathbf{q}, \dot{\mathbf{q}}, \ddot{\mathbf{q}}) \cdot \Delta\ddot{\mathbf{q}}\,,\end{aligned} \tag{7.47}$$

where $\partial_{\mathbf{q}}(\cdot)$, $\partial_{\dot{\mathbf{q}}}(\cdot)$, and $\partial_{\ddot{\mathbf{q}}}(\cdot)$ denote partial derivatives with respect to $\mathbf{q}$, $\dot{\mathbf{q}}$, and $\ddot{\mathbf{q}}$, respectively. Introducing (7.45) into (7.47) yields:

$$\begin{aligned}\mathbf{g}_s(\mathbf{q}+\Delta\mathbf{q}) & \approx \mathbf{g}_s(\mathbf{q}) + \partial_{\mathbf{q}} \left[\int_0^S \left(\mathbf{B}(\mathbf{q})^T \boldsymbol{\sigma}_h - \mathbf{N}^T \mathbf{f}^{\text{ext}} \right) \mathrm{d}s \right] \cdot \Delta\mathbf{q} \\ & \approx \mathbf{g}_s(\mathbf{q}) + \left[\int_0^S \partial_{\mathbf{q}} \left(\mathbf{B}(\mathbf{q})^T \boldsymbol{\sigma}_h - \mathbf{N}^T \mathbf{f}^{\text{ext}} \right) \mathrm{d}s \right] \cdot \Delta\mathbf{q}\,,\end{aligned} \tag{7.48}$$

and (7.44) into (7.47):

$$\begin{aligned}\mathbf{g}_d(\mathbf{q}+\Delta\mathbf{q},\dot{\mathbf{q}}+\Delta\dot{\mathbf{q}},\ddot{\mathbf{q}}+\Delta\ddot{\mathbf{q}}) &\approx \mathbf{g}_d(\mathbf{q},\dot{\mathbf{q}},\ddot{\mathbf{q}}) + \partial_{\mathbf{q}}\,[\ldots]\cdot\Delta\mathbf{q} + \partial_{\dot{\mathbf{q}}}\,[\ldots]\cdot\Delta\dot{\mathbf{q}} + \partial_{\ddot{\mathbf{q}}}\,[\ldots]\cdot\Delta\ddot{\mathbf{q}} \\ &\approx \mathbf{g}_d(\mathbf{q},\dot{\mathbf{q}},\ddot{\mathbf{q}}) + \left[\int_0^S \partial_{\mathbf{q}}\,(\ldots)\,\mathrm{d}s\right]\cdot\Delta\mathbf{q} \\ &\quad + \left[\int_0^S \partial_{\dot{\mathbf{q}}}\,(\ldots)\,\mathrm{d}s\right]\cdot\Delta\dot{\mathbf{q}} + \left[\int_0^S \partial_{\ddot{\mathbf{q}}}\,(\ldots)\,\mathrm{d}s\right]\cdot\Delta\ddot{\mathbf{q}}\,.\end{aligned} \tag{7.49}$$

In tensor notation, derivatives with respect to a vector can be expressed as [3] $\partial_{\mathbf{q}}(\cdot) = \partial_{q^i}(\cdot)\otimes\mathbf{G}_i$, where $\mathbf{q} = (q^1, q^2, \ldots, q^{3m})^T$, and $\{\mathbf{G}_1, \ldots, \mathbf{G}_{3m}\}$ is an orthonormal basis for $\mathbb{R}^{3m}$. We consider the three following tangent matrices resulting from (7.48) and (7.49):

$$\begin{aligned}\mathbf{K}_S &= \partial_{q^i}(\mathbf{B}(\mathbf{q})^T\mathbf{a})|_{\mathbf{a}=\boldsymbol{\sigma}_h}\otimes\mathbf{G}_i + \mathbf{B}(\mathbf{q})^T\partial_{q^i}(\boldsymbol{\sigma}_h)\otimes\mathbf{G}_i\,,\\ \mathbf{K}_F &= \partial_{q^i}(\mathbf{N}^T\mathbf{f}^{\text{ext}})\otimes\mathbf{G}_i + \partial_{\dot{q}^i}(\mathbf{N}^T\mathbf{f}^{\text{ext}})\otimes\mathbf{G}_i + \partial_{\ddot{q}^i}(\mathbf{N}^T\mathbf{f}^{\text{ext}})\otimes\mathbf{G}_i\,,\\ \mathbf{K}_M &= \partial_{q^i}(\mathbf{M}(\mathbf{q})\,\nabla_{\dot{\mathbf{q}}}\dot{\mathbf{q}})\otimes\mathbf{G}_i + \partial_{\dot{q}^i}(\mathbf{M}(\mathbf{q})\,\nabla_{\dot{\mathbf{q}}}\dot{\mathbf{q}})\otimes\mathbf{G}_i + \partial_{\ddot{q}^i}(\mathbf{M}(\mathbf{q})\,\nabla_{\dot{\mathbf{q}}}\dot{\mathbf{q}})\otimes\mathbf{G}_i\,,\end{aligned} \tag{7.50}$$

where $\mathbf{a}\in\mathbb{R}^{3m}$ is a constant vector, $\mathbf{K}_S$, $\mathbf{K}_F$ and $\mathbf{K}_M$ are the so-called *static tangent stiffness matrix*, *force tangent stiffness matrix* and *mass tangent stiffness matrix*, respectively.

Static tangent stiffness matrix

The static tangent stiffness matrix $\mathbf{K}_S$ consists of two terms: the first term resulting from the derivative of the operator $\mathbf{B}(\mathbf{q})$ (geometric stiffness), and the second arising from the derivative of vector $\boldsymbol{\sigma}_h$ (elastic stiffness), i.e., $\mathbf{K}_S = \mathbf{K}_S^g + \mathbf{K}_S^e$. We first recall the discrete stress and strain measures from Section 7.3.1, which are:

$$\boldsymbol{\sigma}_h = \begin{Bmatrix}\mathbf{n}_h\\ \mathbf{m}_h\end{Bmatrix} = \begin{bmatrix}EA\,\boldsymbol{\epsilon}_h\\ EI\,\boldsymbol{\kappa}_h\end{bmatrix} = \underbrace{\begin{bmatrix}EA\,\mathbf{I}_3 & \mathbf{0}_3\\ \mathbf{0}_3 & EI\,\mathbf{I}_3\end{bmatrix}}_{\mathbf{C}(E,A,I)}\begin{Bmatrix}\boldsymbol{\epsilon}_h\\ \boldsymbol{\kappa}_h\end{Bmatrix}\,. \tag{7.51}$$

Considering the discrete linearized strain operator $\mathbf{B}(\mathbf{q}) = \begin{bmatrix}\mathbf{B}_{11} & \mathbf{0}\\ \mathbf{B}_{21} & \mathbf{B}_{22}\end{bmatrix}$ in (7.19), we

---

[3] We note that Einstein's summation is implied.

compute the derivative of the sub-operators $\mathbf{B}_{11}$, $\mathbf{B}_{21}$, and $\mathbf{B}_{22}$, as follows:

$$\begin{aligned}
\partial_{q^i}\left[\mathbf{B}_{11}^T(\mathbf{q})\mathbf{a}\right]|_{\mathbf{a}=\mathbf{n}_h} &= \partial_{q^i}\left[\mathbf{N}'^T\left(\mathbf{I}-\left|\boldsymbol{\varphi}'_h\right|^{-1}\mathbf{P}_\mathbf{d}\right)\mathbf{a}\right]\Big|_{\mathbf{a}=\mathbf{n}_h} = \mathbf{N}'^T\mathbf{A}_1\,\partial_{q^i}(\boldsymbol{\varphi}'_h)\,,\\
\partial_{q^i}\left[\mathbf{B}_{21}^T(\mathbf{q})\mathbf{a}\right]|_{\mathbf{a}=\mathbf{m}_h} &= \partial_{q^i}\left[\mathbf{N}'^T\left(\left|\boldsymbol{\varphi}'_h\right|^{-2}\mathbf{H}_\mathbf{d}[\boldsymbol{\varphi}''_h]_\times\right)\mathbf{a}\right]\Big|_{\mathbf{a}=\mathbf{m}_h}\\
&= \mathbf{N}'^T\mathbf{A}_2\,\partial_{q^i}(\boldsymbol{\varphi}'_h)+\mathbf{N}'^T\mathbf{A}_3\,\partial_{q^i}(\boldsymbol{\varphi}''_h)\,,\\
\partial_{q^i}\left[\mathbf{B}_{22}^T(\mathbf{q})\mathbf{a}\right]|_{\mathbf{a}=\mathbf{m}_h} &= \partial_{q^i}\left[\mathbf{N}''^T\left(\left|\boldsymbol{\varphi}'_h\right|^{-1}[\mathbf{d}_h]_\times\right)\mathbf{a}\right]\Big|_{\mathbf{a}=\mathbf{m}_h} = \mathbf{N}''^T\mathbf{A}_4\,\partial_{q^i}(\boldsymbol{\varphi}'_h)\,,
\end{aligned} \tag{7.52}$$

where:

$$\begin{aligned}
\mathbf{A}_1 &= \frac{1}{\left|\boldsymbol{\varphi}'_h\right|^2}\left[2\mathbf{d}_h\odot\mathbf{n}_h-3(\mathbf{d}_h\cdot\mathbf{n}_h)\mathbf{d}_h\otimes\mathbf{d}_h+(\mathbf{d}_h\cdot\mathbf{n}_h)\,\mathbf{I}\right]\,,\\
\mathbf{A}_2 &= -\frac{2}{\left|\boldsymbol{\varphi}'_h\right|^3}\left[2\left([\boldsymbol{\varphi}''_h]_\times\mathbf{m}_h\odot\mathbf{d}_h\right)+([\boldsymbol{\varphi}''_h]_\times\mathbf{m}_h\cdot\mathbf{d}_h)(2\mathbf{H}_\mathbf{d}-\mathbf{I})\right]\,,\\
\mathbf{A}_3 &= -\frac{1}{\left|\boldsymbol{\varphi}'_h\right|^2}\mathbf{H}_\mathbf{d}\,[\mathbf{m}_h]_\times\,,\\
\mathbf{A}_4 &= \frac{1}{\left|\boldsymbol{\varphi}'_h\right|^2}[\mathbf{m}_h]_\times\,\mathbf{H}_\mathbf{d}\,.
\end{aligned} \tag{7.53}$$

Applying the spatial approximation of $\boldsymbol{\varphi}(s,t)$ introduced in (7.16), we obtain:

$$\begin{aligned}
\partial_{q^i}(\boldsymbol{\varphi}'_h) &= \partial_{q^i}\left(\frac{d}{ds}(\mathbf{N}\mathbf{q})\right) = \mathbf{N}'\partial_{q^i}\,(\mathbf{q}) = \mathbf{N}'\mathbf{G}_i\,,\\
\partial_{q^i}(\boldsymbol{\varphi}''_h) &= \mathbf{N}''\mathbf{G}_i\,.
\end{aligned} \tag{7.54}$$

Introducing (7.54) into (7.52), we obtain the first counterpart of $\mathbf{K}_S$, $\mathbf{K}_S^g$, that is:

$$\begin{aligned}
\mathbf{K}_S^g &= \partial_{q^i}(\mathbf{B}(\mathbf{q})^T\mathbf{a})|_{\mathbf{a}=\boldsymbol{\sigma}_h}\otimes\mathbf{G}_i\\
&= \left[\mathbf{N}'^T(\mathbf{A}_1+\mathbf{A}_2)\mathbf{N}'+\mathbf{N}'^T\mathbf{A}_3\,\mathbf{N}''+\mathbf{N}''^T\mathbf{A}_4\mathbf{N}'\right]\overbrace{\mathbf{G}_i\otimes\mathbf{G}_i}^{\mathbf{I}_{3m}}\\
&= \begin{bmatrix}\mathbf{N}'^T & \mathbf{N}''^T\end{bmatrix}\begin{bmatrix}\mathbf{A}_1+\mathbf{A}_2 & \mathbf{A}_3\\ \mathbf{A}_4 & \mathbf{0}_3\end{bmatrix}\begin{bmatrix}\mathbf{N}'\\ \mathbf{N}''\end{bmatrix},
\end{aligned} \tag{7.55}$$

where $\mathbf{I}_{3m}$ is the identity matrix of dimension $3m\times 3m$.

The second counterpart, $\mathbf{K}_S^e$, employing (7.51), can be computed as follows:

$$\mathbf{K}_S^e = \mathbf{B}(\mathbf{q})^T\partial_\mathbf{q}(\boldsymbol{\sigma}_h) = \mathbf{B}(\mathbf{q})^T\partial_\mathbf{q}\left(\mathbf{C}\begin{Bmatrix}\boldsymbol{\epsilon}_h\\ \boldsymbol{\kappa}_h\end{Bmatrix}\right)\,. \tag{7.56}$$

We recall $(\boldsymbol{\delta\epsilon},\delta\boldsymbol{\kappa})^T = \mathcal{B}(\boldsymbol{\varphi}',\boldsymbol{\varphi}'')\,\delta\boldsymbol{\varphi}$. Thus, the derivative $\partial_\mathbf{q}(\boldsymbol{\epsilon}_h,\boldsymbol{\kappa}_h)^T$, directly related to the discretized strain operator $\mathbf{B}(\mathbf{q})$, is:

$$\partial_{\mathbf{q}}\left(\begin{Bmatrix}\boldsymbol{\epsilon}_h\\ \boldsymbol{\kappa}_h\end{Bmatrix}\right) = \mathbf{B}(\mathbf{q})\,\underbrace{\partial_{\mathbf{q}}(\mathbf{q})}_{\mathbf{I}}\,. \tag{7.57}$$

$\mathbf{K}_S^e$ then takes the following form:

$$\mathbf{K}_S^e = \mathbf{B}(\mathbf{q})^T\mathbf{C}\,\mathbf{B}(\mathbf{q})\,, \tag{7.58}$$

where the constitutive matrix $\mathbf{C}$ is assumed to be constant. The static tangent stiffness matrix $\mathbf{K}_S$ is then:

$$\mathbf{K}_S = \mathbf{K}_S^g + \mathbf{K}_S^e = \begin{bmatrix}\mathbf{N}'^T & \mathbf{N}''^T\end{bmatrix}\begin{bmatrix}\mathbf{A}_1+\mathbf{A}_2 & \mathbf{A}_3\\ \mathbf{A}_4 & \mathbf{0}_3\end{bmatrix}\begin{bmatrix}\mathbf{N}'\\ \mathbf{N}''\end{bmatrix} + \mathbf{B}(\mathbf{q})^T\mathbf{C}\,\mathbf{B}(\mathbf{q})\,. \tag{7.59}$$

Force tangent stiffness matrix

We now derive the force tangent stiffness matrix $\mathbf{K}_F$ that is required for our computations in this work. We consider two different types of forces: (i) follower forces for two-dimensional study cases, and (ii) forces induced by a surrounding flow described in Section 7.2.3.

Follower forces in two-dimensional studies

In two-dimensional cases, the motion of the rod is confined in a single plane at all times (see Fig. 7.27). Thus, we can define a lumped follower force as follows:

$$\mathbf{f}_f = f_0\,(\mathbf{E}_2 \times \mathbf{d}_h)\,, \tag{7.60}$$

where f_0 is the magnitude of the force and is assumed to be constant, and $\mathbf{E}_2$ is the unit normal to the plane of motion. According to (7.50), the tangent stiffness matrix $\mathbf{K}_F$ resulting from $\mathbf{f}_f$ is:

$$\begin{aligned}\mathbf{K}_F &= \partial_{q^i}\left(\mathbf{N}^T f_0\,(\mathbf{E}_2\times\mathbf{d}_h)\right)\otimes\mathbf{G}_i\\ &= \frac{f_0}{|\boldsymbol{\varphi}_h'|}\mathbf{N}^T\,[\mathbf{E}_2]_\times\,\mathbf{P}_\mathbf{d}\mathbf{N}'\,\underbrace{\mathbf{G}_i\otimes\mathbf{G}_i}_{\mathbf{I}_{3m}} = \frac{f_0}{|\boldsymbol{\varphi}_h'|}\mathbf{N}^T\,[\mathbf{E}_2]_\times\,\mathbf{P}_\mathbf{d}\mathbf{N}'\,.\end{aligned} \tag{7.61}$$

We note that since the configuration space of Kirchhoff rods employed in this work requires only the specification of $\boldsymbol{\varphi}(s,t)$ and the director $\mathbf{d}$, a modeling of three-dimensional follower forces is generally not possible.

Force induced by a surrounding flow

As mentioned in Section 7.2.3, we consider a simplified model for a force induced by a surrounding flow, that consists of three counterparts: an added mass force, a tangential

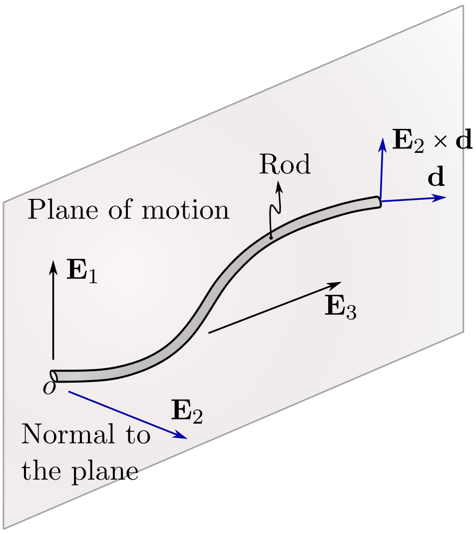

Figure 7.27: Schematic for a two-dimensional follower force.

drag force, and a normal drag force. In this subsection, we derive the tangent stiffness matrix corresponding to each counterpart. To simplify the involved algebra for this derivation, we consider the resulting expression of the semi-discrete formulation after employing the implicit time integration scheme described in Section 7.3.3. We note that the derivation of the tangent stiffness matrices can be alternatively performed with the equations of motion and/or the semi-discrete equations, and thus is independent of the numerical scheme applied.

The chosen implicit scheme in this work (see also Section 7.3.3) evaluates $\mathbf{g}_d$ at the time instant $t_{n+\frac{1}{2}}$, and thus also the force term, i.e. $(\mathbf{N}^T\mathbf{f}^{\text{ext}})_{n+\frac{1}{2}}$. The term associated with the force is then:

$$\begin{aligned}\int_0^S \left[(\mathbf{N}^T\mathbf{F}_f)_{n+\frac{1}{2}}\right]\mathrm{d}s = C_1 &\int_0^S \left[(\mathbf{N}^T\mathbf{P}_{\mathbf{d}}\mathbf{a}_h)_{n+\frac{1}{2}}\right]\mathrm{d}s\\ + C_2 &\int_0^S \left[(\mathbf{N}^T\left|\mathbf{P}_{\mathbf{d}}\mathbf{V}_h\right|\mathbf{P}_{\mathbf{d}}\mathbf{V}_h)_{n+\frac{1}{2}}\right]\mathrm{d}s\\ + C_3 &\int_0^S \left[(\mathbf{N}^T\left|(\mathbf{d}_h\otimes\mathbf{d}_h)\mathbf{V}_h\right|(\mathbf{d}_h\otimes\mathbf{d}_h)\mathbf{V}_h)_{n+\frac{1}{2}}\right]\mathrm{d}s\,,\end{aligned}$$

where $\mathbf{a}_h = \mathbf{a}_\infty - \ddot{\boldsymbol{\varphi}}_h$ is the discrete relative acceleration of the surrounding flow, and $\mathbf{V}_h = \mathbf{V}_\infty - \dot{\boldsymbol{\varphi}}_h$ the discrete relative velocity.

The added mass force, denoted as $\mathbf{F}^{am}$, is a function of the free-stream, rod acceleration, and rod configuration. Employing the midpoint rule and a standard Taylor expansion up to first order, we obtain the following approximation for $\mathbf{F}^{am}$ at the time instance $t_{n+\frac{1}{2}}$:

$$\begin{aligned}\mathbf{F}^{am}_{n+\frac{1}{2}}(\mathbf{q}_{n+1}+\Delta\mathbf{q},\dot{\mathbf{q}}_{n+1}+\Delta\dot{\mathbf{q}}) \approx \mathbf{F}^{am}_{n+\frac{1}{2}}&(\mathbf{q}_{n+1},\dot{\mathbf{q}}_{n+1})\\ &+\partial_{\mathbf{q}_{n+1}}\mathbf{F}^{am}_{n+\frac{1}{2}}(\mathbf{q}_{n+1},\dot{\mathbf{q}}_{n+1})\cdot\Delta\mathbf{q}\\ &+\partial_{\dot{\mathbf{q}}_{n+1}}\mathbf{F}^{am}_{n+\frac{1}{2}}(\mathbf{q}_{n+1},\dot{\mathbf{q}}_{n+1})\cdot\Delta\dot{\mathbf{q}}\,,\end{aligned}\tag{7.62}$$

where:

$$\begin{aligned}\mathbf{F}^{am}_{n+\frac{1}{2}}(\mathbf{q}_{n},\mathbf{q}_{n+1},\dot{\mathbf{q}}_{n},\dot{\mathbf{q}}_{n+1}) = C_1\int_0^S &\mathbf{N}^T\left\{\frac{1}{2}\left[(\mathbf{P}_{\mathbf{d}}\mathbf{a}_\infty)_n+(\mathbf{P}_{\mathbf{d}}\mathbf{a}_\infty)_{n+1}\right]\right\}\mathrm{d}s\\ -C_1\int_0^S &\mathbf{N}^T\left\{\frac{1}{\Delta t}\left[(\mathbf{P}_{\mathbf{d}}\dot{\boldsymbol{\varphi}}_h)_{n+1}-(\mathbf{P}_{\mathbf{d}}\dot{\boldsymbol{\varphi}}_h)_n\right]\right\}\mathrm{d}s\,.\end{aligned}\tag{7.63}$$

Considering (7.62) and (7.63), the corresponding tangent stiffness matrix per unit of length is:

$$\begin{aligned}\mathbf{K}^{am}_F = C_1\mathbf{N}^T\Bigg[&\frac{1}{2}\underbrace{\partial_{q^i_{n+1}}(\mathbf{P}_{\mathbf{d}}\mathbf{a}_\infty)_{n+1}}_{\mathbf{f}_1}-\frac{1}{\Delta t}\underbrace{\partial_{q^i_{n+1}}(\mathbf{P}_{\mathbf{d}}\dot{\boldsymbol{\varphi}}_h)_{n+1}}_{\mathbf{f}_2}\\ &-\frac{1}{\Delta t}\underbrace{\partial_{\dot{q}^i_{n+1}}(\mathbf{P}_{\mathbf{d}}\dot{\boldsymbol{\varphi}}_h)_{n+1}}_{\mathbf{f}_3}\Bigg]\otimes\mathbf{G}_i\,.\end{aligned}\tag{7.64}$$

We assume that both the magnitude and direction of the force vary with the altitude (or depth for marine applications). For the sake of simplicity, we consider $\mathbf{a}_\infty$ as a function of the vertical coordinate z and time t, i.e., $\mathbf{a}_\infty(z,t)$, where z depends on the current configuration of the rod, that is $z=\boldsymbol{\varphi}_h\cdot\mathbf{E}_3$. We then obtain:

$$\begin{aligned}\mathbf{f}_1 &= \left\{\underbrace{-\frac{1}{|\boldsymbol{\varphi}'_h|}\left[(\mathbf{a}_\infty\cdot\mathbf{d}_h)\mathbf{H}_{\mathbf{d}}+\mathbf{d}_h\otimes\mathbf{a}_\infty\right]_{n+1}\mathbf{N}'}_{\mathbf{K}_1}+\underbrace{\left[\mathbf{P}_{\mathbf{d}}(\partial_z\mathbf{a}_\infty\otimes\mathbf{E}_3)\right]_{n+1}}_{\mathbf{K}_2}\mathbf{N}\right\}\mathbf{G}_i\,,\\ \mathbf{f}_2 &= \underbrace{-\frac{1}{|\boldsymbol{\varphi}'_h|}\left[(\dot{\boldsymbol{\varphi}}_h\cdot\mathbf{d}_h)\mathbf{H}_{\mathbf{d}}+\mathbf{d}_h\otimes\dot{\boldsymbol{\varphi}}_h\right]_{n+1}\mathbf{N}'}_{\mathbf{K}_3}\mathbf{G}_i\,,\\ \mathbf{f}_3 &= \underbrace{\left[\mathbf{P}_{\mathbf{d}}\mathbf{N}\right]_{n+1}}_{\mathbf{K}_4}\mathbf{G}_i\,.\end{aligned}\tag{7.65}$$

Introducing (7.65) into (7.64), and recalling that $\mathbf{G}_i\otimes\mathbf{G}_i=\mathbf{I}_{3m}$ and $\Delta\dot{\mathbf{q}}=\frac{2}{h}\Delta\mathbf{q}$, we obtain:

$$\mathbf{K}_F^{am} = C_1 \mathbf{N}^T \left[\frac{1}{2}\mathbf{K}_1 \mathbf{N}' + \frac{1}{2}\mathbf{K}_2 \mathbf{N} - \frac{1}{\Delta t}\mathbf{K}_3 \mathbf{N}' - \frac{2}{\Delta t^2}\mathbf{K}_4 \mathbf{N} \right] . \tag{7.66}$$

The normal drag force, denoted as $\mathbf{F}^{cn}$, is a function of the free-stream, rod velocity, and rod configuration. The normal drag force of the surrounding flow, evaluated at $t_{n+\frac{1}{2}}$, is:

$$\mathbf{F}^{cn}_{n+\frac{1}{2}}(\mathbf{q}_n, \mathbf{q}_{n+1}, \dot{\mathbf{q}}_n, \dot{\mathbf{q}}_{n+1}) = C_2 \int_0^S \mathbf{N}^T \left\{ \frac{1}{2} \left[(|\mathbf{P}_\mathbf{d} \mathbf{V}_h| \mathbf{P}_\mathbf{d} \mathbf{V}_h)_n + (|\mathbf{P}_\mathbf{d} \mathbf{V}_h| \mathbf{P}_\mathbf{d} \mathbf{V}_h)_{n+1} \right] \right\} \mathrm{d}s \, .$$

Analogously to the tangent stiffness matrix corresponding to the added mass force derived above, the tangent stiffness matrix per unit of length associated with the normal drag force is:

$$\mathbf{K}_F^{cn} = C_2 \mathbf{N}^T \left[\frac{1}{2}\mathbf{K}_1 \mathbf{N} - \frac{1}{2}\mathbf{K}_2 \mathbf{N}' - \frac{1}{\Delta t}\mathbf{K}_3 \mathbf{N} \right] , \tag{7.67}$$

where:

$$\begin{aligned}
\mathbf{K}_1 &= |\mathbf{P}_\mathbf{d} \mathbf{V}_h| \, (2\mathbf{I} - \mathbf{P}_\mathrm{u}) \mathbf{P}_\mathbf{d} (\partial_z \mathbf{V}_\infty \otimes \mathbf{E}_3) \, , \\
\mathbf{K}_2 &= \frac{|\mathbf{P}_\mathbf{d} \mathbf{V}_h|}{|\boldsymbol{\varphi}'_h|} (2\mathbf{I} - \mathbf{P}_\mathrm{u}) \left[(\mathbf{V}_h \cdot \mathbf{d}_h) \mathbf{H}_\mathbf{d} + \mathbf{d}_h \otimes \mathbf{V}_h \right] \, , \\
\mathbf{K}_3 &= |\mathbf{P}_\mathbf{d} \mathbf{V}_h| \, (2\mathbf{I} - \mathbf{P}_\mathrm{u}) \mathbf{P}_\mathbf{d} , \\
\mathbf{P}_\mathrm{u} &= \mathbf{I} - \frac{1}{|\mathbf{P}_\mathbf{d} \mathbf{V}_h|^2} (\mathbf{P}_\mathbf{d} \mathbf{V}_h) \otimes (\mathbf{P}_\mathbf{d} \mathbf{V}_h) \, .
\end{aligned}$$

The tangential drag force, denoted as $\mathbf{F}^{ct}$, is also a function of the free-stream, rod velocity, and rod configuration. The tangential drag force of the surrounding flow, evaluated at $t_{n+\frac{1}{2}}$, is:

$$\begin{aligned}
&\mathbf{F}^{ct}_{n+\frac{1}{2}}(\mathbf{q}_n, \mathbf{q}_{n+1}, \dot{\mathbf{q}}_n, \dot{\mathbf{q}}_{n+1}) \\
&= C_3 \int_0^S \mathbf{N}^T \left\{ \frac{1}{2} \left[(|(\mathbf{d}_h \otimes \mathbf{d}_h) \mathbf{V}_h| \, (\mathbf{d}_h \otimes \mathbf{d}_h) \mathbf{V}_h)_n + (|(\mathbf{d}_h \otimes \mathbf{d}_h) \mathbf{V}_h| \, (\mathbf{d}_h \otimes \mathbf{d}_h) \mathbf{V}_h)_{n+1} \right] \right\} \mathrm{d}s \, .
\end{aligned}$$

Analogously, the tangent stiffness matrix per unit of length associated with the tangential drag force is:

$$\mathbf{K}_F^{ct} = C_3 \mathbf{N}^T \left[\frac{1}{2}\mathbf{K}_1 \mathbf{N} + \frac{1}{2}\mathbf{K}_2 \mathbf{N}' - \frac{1}{\Delta t}\mathbf{K}_3 \mathbf{N} \right] ,$$

where:

$$
\begin{aligned}
\mathbf{K}_1 &= |(\mathbf{d}_h \otimes \mathbf{d}_h)\mathbf{V}_h| \, [2\mathbf{I} - \mathbf{P}_{\mathrm{v}}] \, (\mathbf{d}_h \otimes \mathbf{d}_h)(\partial_z \mathbf{V}_\infty \otimes \mathbf{E}_3)\,, \\
\mathbf{K}_2 &= \frac{|(\mathbf{d}_h \otimes \mathbf{d}_h)\mathbf{V}_h|}{|\boldsymbol{\varphi}_h'|} \, (2\mathbf{I} - \mathbf{P}_{\mathrm{v}}) \, [(\mathbf{V}_h \cdot \mathbf{d}_h)\mathbf{H}_{\mathbf{d}} + \mathbf{d}_h \otimes \mathbf{V}_h] \ , \\
\mathbf{K}_3 &= |(\mathbf{d}_h \otimes \mathbf{d}_h)\mathbf{V}_h| \, (2\mathbf{I} - \mathbf{P}_{\mathrm{v}}) \, [\mathbf{d}_h \otimes \mathbf{d}_h] \ , \\
\mathbf{P}_{\mathrm{v}} &= \mathbf{I} - \frac{1}{|(\mathbf{d}_h \otimes \mathbf{d}_h)\mathbf{V}_h|^2} \, [(\mathbf{d}_h \otimes \mathbf{d}_h)\mathbf{V}_h] \otimes [(\mathbf{d}_h \otimes \mathbf{d}_h)\mathbf{V}_h] \ .
\end{aligned}
$$

Mass tangent stiffness matrix

Lastly, we derive the mass tangent stiffness matrix, $\mathbf{K}_M$, corresponding to the inertial contribution $\mathbf{M}(\mathbf{q})\nabla_{\dot{\mathbf{q}}}\dot{\mathbf{q}}$ of the mass operator. Similarly to the tangent stiffness matrix corresponding to the force induced by a surrounding flow in the previous subsection, we consider the resulting expression of the semi-discrete formulation after employing the implicit time integration scheme described in Section 7.3.3. Considering (7.24) together with the midpoint rule formulas, we obtain the following approximation for the inertia term of the mass operator, evaluated at $t = n + \frac{1}{2}$, which is:

$$
\begin{aligned}
\mathbf{f}^I_{n+\frac{1}{2}}(\mathbf{q}_n, \mathbf{q}_{n+1}, \dot{\mathbf{q}}_n, \dot{\mathbf{q}}_{n+1}) = \int_0^S \Bigg\{ & \frac{1}{\Delta t} \left[(\mathbf{M}\dot{\mathbf{q}})_{n+1} - (\mathbf{M}\dot{\mathbf{q}})_n \right] \\
& + \frac{1}{2} \mathbf{N}'^T \left[2\, I_\rho \left(\frac{1}{|\boldsymbol{\varphi}_h'|^3} [\mathbf{P}_{\mathbf{d}} \odot (\dot{\boldsymbol{\varphi}}_h' \otimes \mathbf{d}_h)] \dot{\boldsymbol{\varphi}}_h' \right)_n \right. \\
& \left. + 2\, I_\rho \left(\frac{1}{|\boldsymbol{\varphi}_h'|^3} [\mathbf{P}_{\mathbf{d}} \odot (\dot{\boldsymbol{\varphi}}_h' \otimes \mathbf{d}_h)] \dot{\boldsymbol{\varphi}}_h' \right)_{n+1} \right] \Bigg\} \, \mathrm{d}s \,.
\end{aligned}
\tag{7.68}
$$

Employing the standard Taylor expansion up to first order for this term leads to:

$$
\begin{aligned}
\mathbf{f}^I_{n+\frac{1}{2}}(\mathbf{q}_{n+1} + \Delta\mathbf{q}, \dot{\mathbf{q}}_{n+1} + \Delta\dot{\mathbf{q}}) \approx \ & \mathbf{f}^I_{n+\frac{1}{2}}(\mathbf{q}_{n+1}, \dot{\mathbf{q}}_{n+1}) + \partial_{\mathbf{q}_{n+1}} \mathbf{F}^I_{n+\frac{1}{2}}(\mathbf{q}_{n+1}, \dot{\mathbf{q}}_{n+1}) \cdot \Delta\mathbf{q} \\
& + \partial_{\dot{\mathbf{q}}_{n+1}} \mathbf{F}^I_{n+\frac{1}{2}}(\mathbf{q}_{n+1}, \dot{\mathbf{q}}_{n+1}) \cdot \Delta\dot{\mathbf{q}} \,.
\end{aligned}
\tag{7.69}
$$

Introducing (7.68) into (7.69), we obtain the following counterparts associated with the inertia contribution of the mass operator:

$$
\begin{aligned}
\mathbf{K}_1 &= \partial_{q^i_{n+1}} (\mathbf{M}(\mathbf{q})\dot{\mathbf{q}})_{n+1} \otimes \mathbf{G}_i = -\frac{I_\rho}{|\boldsymbol{\varphi}_h'|^3} \mathbf{N}'^T \left\{ (\mathbf{d}_h \cdot \dot{\boldsymbol{\varphi}}_h')(2\mathbf{H}_{\mathbf{d}} - \mathbf{I}) + \mathbf{d}_h \otimes \dot{\boldsymbol{\varphi}}_h' + 2\,\dot{\boldsymbol{\varphi}}_h' \otimes \mathbf{d}_h \right\} \mathbf{N}'\,, \\
\mathbf{K}_2 &= \partial_{\dot{q}^i_{n+1}} (\mathbf{M}(\mathbf{q})\dot{\mathbf{q}})_{n+1} \otimes \mathbf{G}_i = \mathbf{N}^T \mathbf{M}(\mathbf{q}_{n+1}) \mathbf{N}\,,
\end{aligned}
$$

$$
\begin{aligned}
\mathbf{K}_3 &= 2\, I_\rho \mathbf{N}'^T \partial_{q^i_{n+1}} \left(\frac{[\mathbf{P}_\mathbf{d} \odot (\dot{\boldsymbol{\varphi}}'_h \otimes \mathbf{d}_h)]\dot{\boldsymbol{\varphi}}'_h}{\left|\boldsymbol{\varphi}'_h\right|^3} \right)_{n+1} \otimes \mathbf{G}_i \\
&= \frac{-I_\rho\, \mathbf{N}'^T}{\left|\boldsymbol{\varphi}'_h\right|^4} \left\{ 2(\dot{\boldsymbol{\varphi}}'_h \cdot \mathbf{d}_h) \left[4\dot{\boldsymbol{\varphi}}'_h \odot \mathbf{d}_h + (\dot{\boldsymbol{\varphi}}'_h \cdot \mathbf{d}_h)[3\mathbf{H}_\mathbf{d} - 2\mathbf{I}] \right] - \dot{\boldsymbol{\varphi}}'_h \otimes \dot{\boldsymbol{\varphi}}'_h + (\dot{\boldsymbol{\varphi}}'_h \cdot \dot{\boldsymbol{\varphi}}'_h)[\mathbf{I} - 2\mathbf{H}_\mathbf{d}] \right\} \mathbf{N}' , \\
\mathbf{K}_4 &= 2\, I_\rho \mathbf{N}'^T \partial_{\dot{q}^i_{n+1}} \left(\frac{[\mathbf{P}_\mathbf{d} \odot (\dot{\boldsymbol{\varphi}}'_h \otimes \mathbf{d}_h)]\dot{\boldsymbol{\varphi}}'_h}{\left|\boldsymbol{\varphi}'_h\right|^3} \right)_{n+1} \otimes \mathbf{G}_i \\
&= 2 \frac{I_\rho}{\left|\boldsymbol{\varphi}'_h\right|^3} \mathbf{N}'^T \left\{ (\dot{\boldsymbol{\varphi}}'_h \cdot \mathbf{d}_h)\mathbf{H}_\mathbf{d} + \mathbf{d}_h \otimes \dot{\boldsymbol{\varphi}}'_h + 2\mathbf{P}_\mathbf{d} \odot (\dot{\boldsymbol{\varphi}}'_h \otimes \mathbf{d}_h) \right\} \mathbf{N}' .
\end{aligned}
$$

Recalling that $\Delta\dot{\mathbf{q}} = \frac{2}{h}\Delta\mathbf{q}$, we then obtain the tangent stiffness matrix per unit of length associated with the inertia term of the mass operator as follows:

$$
\mathbf{K}_M = \left[\frac{1}{\Delta t}\mathbf{K}_1 + \frac{2}{\Delta t^2}\mathbf{K}_2 + \frac{1}{2}\mathbf{K}_3 + \frac{1}{\Delta t}\mathbf{K}_4 \right] .
$$

8 Conclusions and outlook

We have presented the contributions of this thesis in terms of four publications with the main objective of developing a higher-order accurate and locking-free explicit dynamics scheme in isogeometric structural analysis. In this chapter, we summarize and highlight the main conclusions of each publication and outline the potential impact of this work and directions for future work.

8.1 Conclusions

In the first publication, we extended spectral analysis as a tool for assessing locking phenomena and comparing the effectivity of different formulations with respect to locking. This is particularly desired when studying the ability of finite element formulations to guarantee higher-order accurate explicit dynamics computations. To this end, we assessed and compared the effectivity of the standard displacement-based formulation with full and selective reduced integration, as well as three representative locking-free formulations: the B-bar method, the discrete shear/strain gap (DSG) method, and the Hellinger-Reissner formulation, for an Euler-Bernoulli circular ring subjected to membrane locking. Our results illustrate that membrane locking severely affects the standard formulation with full integration, despite mesh refinement. Using selective reduced integration removes membrane locking for finer meshes using quadratic discretizations, however, does not remove locking on coarse meshes and for polynomial degrees higher than quadratics. The B-bar, DSG, and Hellinger-Reissner methods all remove membrane locking on coarse meshes using quadratic and higher-order discretizations. They result in optimal convergence behavior in all cases. Our results from a classical p-refinement show that p-refinement itself is not an effective way to alleviate the effect of locking. Furthermore, we observed that the higher transverse modes, obtained with the standard formulation using full integration, diverge with increasing p, while they converged when using the B-bar formulation and did not diverge when using the Hellinger-Reissner formulation.

In the second publication, we introduced a variational approach based on perturbed eigenvalue analysis that reduces overestimated outlier frequencies due to reduced continuity at patch interfaces in isogeometric multipatch discretizations. This approach is especially interesting when controlling the critical time step size of explicit schemes with multipatch discretizations. We also proposed an iterative procedure to estimate effective scaling parameters of the perturbation terms, that requires (i) two input parameters: a scaling factor $f > 1$ and a reduction factor $c \in (0, 1)$; and (ii) computation of the maximum eigenfrequency and corresponding mode, which can be effectively computed via power iteration. We demonstrated that our approach is robust with respect to $f > 1$, i.e.

it reduces the outlier frequencies to approximately the same values for all $f > 1$. Moreover, a reduction factor $c = 0.9$ showed good results in all test cases. We demonstrated the effectiveness of our approach numerically via examples of bar, beam, membrane, and plate models. We numerically confirm the maintained spatial accuracy when using this approach in an explicit dynamics setting. Our results illustrated that the obtained critical time step size is larger and does not depend on the polynomial degree p of the spline basis functions.

In the third publication, we presented an isogeometric Petrov-Galerkin formulation that enables higher-order accurate mass lumping in explicit dynamics. This could help close the gap between higher-order IGA and computations based on a lumped mass matrix. Our row-sum lumped mass matrix yields the identity matrix, which eliminates the need for matrix inversion, without compromising higher-order spatial accuracy. To be able to strongly enforce the Dirichlet boundary conditions in a standard way, we replaced the dual functions that associate to these constraints by their corresponding B-splines, before dividing by the Jacobian. We confirmed the achieved higher-order accuracy of our approach in explicit dynamics via spectral analysis and convergence studies of beam and plate models.

In the fourth publication, we then extended this approach to a mixed formulation based on the Hellinger-Reissner principle with an attempt to achieve locking-free discretizations. By applying the boundary treatment [132], the outlier removal approach [122], and the reduced quadrature rule [133], our approach allows row-sum lumping of the entire mass matrix, larger critical time step size, and requires minimal number of quadrature points, respectively, without compromising the accuracy. Performing spectral analysis of a circular ring, as discussed in the first publication, showed that our approach eliminates membrane locking in the corresponding discretizations. Our convergence study of curved beam and shell models illustrated that it achieves higher-order accurate solutions in explicit dynamics, for instance in linear cases, also when the mass matrix is lumped. For geometrically nonlinear shells, our results indicated that it performs and achieves more accurate results than the Galerkin method based on a row-sum lumped mass matrix, particularly for higher-order discretizations.

In the fifth publication, we applied isogeometric discretizations to a nonlinear formulation of shear- and torsion-free rods [134], combined with a robust implicit time integration scheme. This extends the horizon of this work to such nonlinear structures in the context of implicit dynamics, which find their application in the simulation of mooring lines in offshore wind engineering. Our results indicated different convergence rates for odd and even polynomial degrees, which might result from the manifold structure of the solution space. Via two- and three-dimensional benchmarks, we illustrated that isogeometric discretizations, whose robustness is improved by the strong outlier removal approach [122], are robust and reliable for analysis of transient rods subjected to gravity, forces induced by a surrounding flow such as wind and water, and a pulsating force of different frequencies.

8.2 Potential impact

The presented results in this thesis indicate its potential application to higher-order accurate and locking-free computations for practical simulations such as impact, crash-test, and metal forming when using explicit methods with standard mass lumping, particularly with isogeometric shell elements. The introduced Petrov-Galerkin approaches enable row-sum mass lumping without compromising the accuracy. This necessarily means that a proportionate increase in accuracy with increasing polynomial degree of the employed basis functions is possible, which was not the case, as reported in state-of-the-art studies on explicit dynamics with isogeometric shells and standard mass lumping, see e.g. [116]. Another outcome is that one can exploit the potential of isogeometric analysis in this context, for instance its percise geometry representation and well-behaved spectral properties. This work is one of the first applications of the approximate dual spline functions in explicit dynamics, and thus further establishes the employment of Petrov-Galerkin methods in this field. This could open up various directions for further research of such approach, for instance its computational efficiency and error estimate. In addition, our Petrov-Galerkin mixed formulation is one of the first isogeometric mixed approaches employed in explicit dynamics to remove locking phenomena. It enables locking-free isogeometric discretizations that achieve optimal accuracy and convergence on practically coarse meshes, which makes its applications more attractive, particularly in realistic scenarios. Moreover, due to the flexibility in choosing discretization spaces for mixed formulations, such approaches are able to eliminate different locking phenomena and their combination, see e.g. [67], [81], [82], which is a potential research direction for our approach in the future. With the two competitive characteristics of higher-order accurate mass lumping and locking-free discretizations, our Petrov-Galerkin approach could be developed and adapted in commercial codes for practical applications.

Another field where this work potentially has an impact is implicit structure dynamics for nonlinear shear- and torsion-free rods [134]. In our fifth publication, it is the first time that isogeometric discretizations are applied to such a nonlinear rod formulation. It extends the application and establishes the potential of IGA and particularly of the outlier removal approach [122] for nonlinear dynamics of such rods, which are relevant for practical applications such as the simulation of mooring lines in offshore wind engineering. We emphasize that this outlier removal approach reduces the high-frequency content in the response without compromising the accuracy and without introducing any artificial damping, which plays an essential role for instance in studying the physical damping characteristic of the structure that is then not affected or mixed with any artificial one. In addition, the outlier removal approach potentially provides better insights into the effect of spurious outlier modes on the response. It helps us not only to better understand the behavior of the studied structures, particularly in nonlinear cases, but also to study and develop robust and accurate discretization schemes for nonlinear structural dynamics in the context of IGA.

8.3 Avenues for future work

The presented results in this thesis disclose various directions for future work. One aspect is to apply the proposed approaches to practical applications, particularly the Petrov-Galerkin scheme presented in the fourth publication. These could involve nonlinear material behavior, combinations of different locking phenomena, complex structural models, and geometries, such as Reissner-Mindlin shells or trimmed shells. This includes the performance study of spectral analysis as a locking indicator, discussed in the first publication, in identifying, separating, and assessing locking phenomena from their combinations, as well as its application to analysis with shell elements. Moreover, applying our Petrov-Galerkin approaches presented in the third and fourth publications to trimmed geometry consists of applying approximate dual spline functions as test functions in this context. This opens up a research direction including further challenges, where no initial idea exists. A second aspect is to combine the variational approach based on perturbed eigenvalue analysis introduced in the second publication with the Petrov-Galerkin approach in the fourth one. This is particularly interesting for realistic applications employing multipatch discretizations. It requires further studies of both approaches beforehand, such as the application of the former in the context of mass lumping, and a detailed analysis of the computational efficiency of the latter for explicit dynamics calculations. Combining these two approaches also means extending the concept of approximate dual basis as a test function space for multipatch discretizations, which is especially interesting for patch coupling in the context of mortar methods, or for preventing locking for shell elements, as studied for standard dual basis in [82], [107], [109], [110]. Coupling of multiple discretization patches is also a challenge in analysis of trimmed objects [40]–[42], which may involve the employment of finite cell methods [31]–[33], where the performance of approximate dual functions as test functions is not yet explored. Another aspect is to apply the developed Petrov-Galerkin approaches in the third and fourth publications to nonlinear dynamics of shear- and torsion-free rods in the fifth publication. It is desirable to study the performance of these approaches in such a nonlinear analysis, in particular, the application of the concept using approximate dual functions as test functions in this context and its effect on the irregular behavior of the mass matrix resulting from the rod formulation. Furthermore, one can extend this combination to multipatch discretizations and combine the variational approach presented in the second publication, which may be relevant in the case of multiple coupled rods. It is particularly interesting to study the effect of the perturbation terms on the mass matrix of the rod and whether adding these terms improves the robustness of the discretizations as the strong outlier removal approach does.

Bibliography

[1] L. Piegl and W. Tiller, *The NURBS Book*, en. Springer Science & Business Media, 1996, ISBN: 978-3-540-61545-3.

[2] L. Schumaker, *Spline Functions: Basic Theory*, en. Cambridge University Press, 2007, ISBN: 978-1-139-46343-0.

[3] I. Stroud, *Boundary Representation Modelling Techniques.* London: Springer London, 2006, ISBN: 978-1-84628-312-3.

[4] S. Bernstein, "Démonstration du théorème de Weierstrass fondée sûr le calcul dès probabilités," *Communications of the Kharkov Mathematical Society*, vol. 12, no. 2, pp. 1–2, 1912.

[5] G. G. Lorentz, *Bernstein Polynomials.* New York: Chelsea Publishing Co., 1986, ISBN: 0828403236.

[6] P. E. Bézier, *Numerical Control: Mathematics and Applications.* New York: John Wiley & Sons Ltd, 1972, ISBN: 0471071951.

[7] B. Marussig and T. J. R. Hughes, "A Review of Trimming in Isogeometric Analysis: Challenges, Data Exchange and Simulation Aspects," *Archives of Computational Methods in Engineering*, vol. 25, no. 4, pp. 1059–1127, 2018.

[8] J. Hoschek and D. Lasser, *Fundamentals of Computer Aided Geometric Design.* Vieweg+Teubner, 1992.

[9] R. Farouki and J. Hinds, "A Hierarchy of Geometric Forms," *IEEE Computer Graphics and Applications*, vol. 5, no. 5, pp. 51–78, 1985.

[10] A. Limaiem and F. Trochu, "Geometric algorithms for the intersection of curves and surfaces," *Computers & Graphics*, vol. 19, no. 3, pp. 391–403, 1995.

[11] J. R. Rossignac and A. A. G. Requicha, "Piecewise-circular curves for geometric modeling," *IBM Journal of Research and Development*, vol. 31, no. 3, pp. 296–313, 1987.

[12] N. Patrikalakis, "Surface-to-surface intersections," *IEEE Computer Graphics and Applications*, vol. 13, no. 1, pp. 89–95, 1993.

[13] D. Lasser, "Intersection of parametric surfaces in the Bernstein-Bézier representation," *Computer-Aided Design*, vol. 18, no. 4, pp. 186–192, 1986.

[14] R. Farouki, "The characterization of parametric surface sections," *Computer Vision, Graphics, and Image Processing*, vol. 33, no. 2, pp. 209–236, 1986.

[15] R. Barnhill and S. Kersey, "A marching method for parametric surface/surface intersection," *Computer Aided Geometric Design*, vol. 7, no. 1-4, pp. 257–280, 1990.

[16] C. Bajaj, C. Hoffmann, R. Lynch, and J. Hopcroft, "Tracing surface intersections," *Computer Aided Geometric Design*, vol. 5, no. 4, pp. 285–307, 1988.

[17] M. Mortenson, *Geometric modeling*, 2nd. New York: Wiley, 1997.

[18] G. Renner and V. Weiß, "Exact and approximate computation of B-spline curves on surfaces," *Computer-Aided Design*, vol. 36, no. 4, pp. 351–362, 2004.

[19] *C3D kernel documentation*, `https://c3d.ascon.net/doc/math/class_mb_surface_intersection_curve.html`, Accessed: 2023-09-10.

[20] J. Corney and T. Lim, *3D Modeling with ACIS*, 2nd. Saxe-Coburg Publications, 2002.

[21] R. F. Sarraga and W. C. Waters, "Free-form surfaces in gmsolid: Goals and issues," in *Solid Modeling by Computers: From Theory to Applications*, M. S. Pickett and J. W. Boyse, Eds. Boston, MA: Springer US, 1984, pp. 187–209.

[22] J Kosinka and T. J. Cashman, "Watertight conversion of trimmed CAD surfaces to Clough–Tocher splines," *Computer Aided Geometric Design*, vol. 37, pp. 25–41, 2015.

[23] J. Hoschek and F.-J. Schneider, "Spline conversion for trimmed rational Bézier- and B-spline surfaces," *Computer-Aided Design*, vol. 22, no. 9, pp. 580–590, 1990.

[24] G. M. Chaikin, "An algorithm for high-speed curve generation," *Computer Graphics and Image Processing*, vol. 3, no. 4, pp. 346–349, 1974.

[25] J. Warren and H. Weimer, *Subdivision methods for geometric design: a constructive approach*, 1st. San Francisco: Morgan Kaufmann Publishers, Inc., 2001.

[26] J. Shen, J. Kosinka, M. Sabin, and N. Dodgson, "Converting a CAD model into a non-uniform subdivision surface," *Computer Aided Geometric Design*, vol. 48, pp. 17–35, 2016.

[27] T. J. Cashman, U. H. Augsdörfer, N. A. Dodgson, and M. A. Sabin, "NURBS with extraordinary points: high-degree, non-uniform, rational subdivision schemes," *ACM Transactions on Graphics*, vol. 28, no. 3, pp. 1–9, 2009.

[28] T. W. Sederberg, J. Zheng, A. Bakenov, and A. Nasri, "T-splines and T-NURCCs," *ACM Transactions on Graphics*, vol. 22, no. 3, pp. 477–484, 2003.

[29] T. W. Sederberg, G. T. Finnigan, X. Li, H. Lin, and H. Ipson, "Watertight trimmed NURBS," in *ACM SIGGRAPH 2008 papers*, New York, NY, USA: ACM, 2008, pp. 1–8.

[30] T. J. R. Hughes, J. A. Cottrell, and Y. Bazilevs, "Isogeometric analysis: CAD, finite elements, NURBS, exact geometry and mesh refinement," en, *Computer Methods in Applied Mechanics and Engineering*, vol. 194, no. 39, pp. 4135–4195, 2005, ISSN: 0045-7825.

[31] M. Ruess, D. Schillinger, Y. Bazilevs, V. Varduhn, and E. Rank, "Weakly enforced essential boundary conditions for NURBS-embedded and trimmed NURBS geometries on the basis of the finite cell method," *International Journal for Numerical Methods in Engineering*, vol. 95, no. 10, pp. 811–846, 2013.

[32] E. Rank, M. Ruess, S. Kollmannsberger, D. Schillinger, and A. Düster, "Geometric modeling, isogeometric analysis and the finite cell method," *Computer Methods in Applied Mechanics and Engineering*, vol. 249-252, pp. 104–115, 2012.

[33] D. Schillinger and M. Ruess, "The Finite Cell Method: A Review in the Context of Higher-Order Structural Analysis of CAD and Image-Based Geometric Models," *Archives of Computational Methods in Engineering*, vol. 22, no. 3, pp. 391–455, 2015.

[34] A. Riffnaller-Schiefer, U. Augsdörfer, and D. Fellner, "Isogeometric shell analysis with nurbs compatible subdivision surfaces," *Applied Mathematics and Computation*, vol. 272, pp. 139–147, 2016.

[35] F. Cirak and Q. Long, "Subdivision shells with exact boundary control and non-manifold geometry," *International Journal for Numerical Methods in Engineering*, vol. 88, no. 9, pp. 897–923, 2011.

[36] X. Wei, Y. Zhang, T. J. Hughes, and M. A. Scott, "Truncated hierarchical Catmull–Clark subdivision with local refinement," *Computer Methods in Applied Mechanics and Engineering*, vol. 291, pp. 1–20, 2015.

[37] Y. Bazilevs, V. Calo, J. Cottrell, J. Evans, T. Hughes, S. Lipton, M. Scott, and T. Sederberg, "Isogeometric analysis using T-splines," *Computer Methods in Applied Mechanics and Engineering*, vol. 199, no. 5-8, pp. 229–263, 2010.

[38] M. Scott, R. Simpson, J. Evans, S. Lipton, S. Bordas, T. Hughes, and T. Sederberg, "Isogeometric boundary element analysis using unstructured T-splines," *Computer Methods in Applied Mechanics and Engineering*, vol. 254, pp. 197–221, 2013.

[39] Y. J. Zhang, *Geometric modeling and mesh generation from scanned images*, 1st. CRC Press, 2016.

[40] M. Breitenberger, A. Apostolatos, B. Philipp, R. Wüchner, and K.-U. Bletzinger, "Analysis in computer aided design: Nonlinear isogeometric b-rep analysis of shell structures," *Computer Methods in Applied Mechanics and Engineering*, vol. 284, pp. 401–457, 2015.

[41] M. Ruess, D. Schillinger, A. I. Özcan, and E. Rank, "Weak coupling for isogeometric analysis of non-matching and trimmed multi-patch geometries," *Computer Methods in Applied Mechanics and Engineering*, vol. 269, pp. 46–71, 2014.

[42] Y. Guo, M. Ruess, and D. Schillinger, "A parameter-free variational coupling approach for trimmed isogeometric thin shells," *Computational Mechanics*, vol. 59, no. 4, pp. 693–715, 2017.

[43] J. A. Cottrell, A. Reali, Y. Bazilevs, and T. J. Hughes, "Isogeometric analysis of structural vibrations," *Computer Methods in Applied Mechanics and Engineering*, vol. 195, no. 41-43, pp. 5257–5296, 2006.

[44] O. Zienkiewicz, R. Taylor, and J. Zhu, *The Finite Element Method: its Basis and Fundamentals*, seventh. Butterworth-Heinemann, Elsevier, 2013, ISBN: 9781856176330.

[45] D. Benson, S. Hartmann, Y. Bazilevs, M.-C. Hsu, and T. Hughes, "Blended isogeometric shells," *Computer Methods in Applied Mechanics and Engineering*, vol. 255, pp. 133–146, 2013.

[46] D. Benson, Y. Bazilevs, M. Hsu, and T. Hughes, "Isogeometric shell analysis: The Reissner–Mindlin shell," *Computer Methods in Applied Mechanics and Engineering*, vol. 199, no. 5-8, pp. 276–289, 2010.

[47] R. Echter, B. Oesterle, and M. Bischoff, "A hierarchic family of isogeometric shell finite elements," *Computer Methods in Applied Mechanics and Engineering*, vol. 254, pp. 170–180, 2013.

[48] J Kiendl, K. U. Bletzinger, J Linhard, and R Wüchner, "Isogeometric shell analysis with Kirchhoff-Love elements," *Computer Methods in Applied Mechanics and Engineering*, vol. 198, no. 49-52, pp. 3902–3914, 2009.

[49] B. Oesterle, R. Sachse, E. Ramm, and M. Bischoff, "Hierarchic isogeometric large rotation shell elements including linearized transverse shear parametrization," *Computer Methods in Applied Mechanics and Engineering*, vol. 321, pp. 383–405, 2017.

[50] H. Al Akhras, T. Elguedj, A. Gravouil, and M. Rochette, "Towards an automatic isogeometric analysis suitable trivariate models generation—Application to geometric parametric analysis," *Computer Methods in Applied Mechanics and Engineering*, vol. 316, pp. 623–645, 2017.

[51] J. A. Cottrell, T. J. R. Hughes, and Y. Bazilevs, *Isogeometric analysis: CAD, finite elements, NURBS, exact geometry and mesh refinement*, 1st. Wiley Publishing, 2009, ISBN: 0470748737.

[52] I. Akkerman, Y. Bazilevs, C. Kees, and M. Farthing, "Isogeometric analysis of free-surface flow," *Journal of Computational Physics*, vol. 230, no. 11, pp. 4137–4152, 2011.

[53] Y. Bazilevs, V. Calo, J. Cottrell, T. Hughes, A. Reali, and G. Scovazzi, "Variational multiscale residual-based turbulence modeling for large eddy simulation of incompressible flows," *Computer Methods in Applied Mechanics and Engineering*, vol. 197, no. 1-4, pp. 173–201, 2007.

[54] M. J. Borden, T. J. Hughes, C. M. Landis, and C. V. Verhoosel, "A higher-order phase-field model for brittle fracture: Formulation and analysis within the isogeometric analysis framework," *Computer Methods in Applied Mechanics and Engineering*, vol. 273, pp. 100–118, 2014.

[55] J. Kiendl, M. Ambati, L. De Lorenzis, H. Gomez, and A. Reali, “Phase-field description of brittle fracture in plates and shells,” *Computer Methods in Applied Mechanics and Engineering*, vol. 312, pp. 374–394, 2016, ISSN: 00457825.

[56] J. Kiendl, R. Schmidt, R. Wüchner, and K.-U. Bletzinger, “Isogeometric shape optimization of shells using semi-analytical sensitivity analysis and sensitivity weighting,” *Computer Methods in Applied Mechanics and Engineering*, vol. 274, pp. 148–167, 2014.

[57] W. A. Wall, M. A. Frenzel, and C. Cyron, “Isogeometric structural shape optimization,” *Computer Methods in Applied Mechanics and Engineering*, vol. 197, no. 33-40, pp. 2976–2988, 2008.

[58] Y. Wang and D. J. Benson, “Geometrically constrained isogeometric parameterized level-set based topology optimization via trimmed elements,” *Frontiers of Mechanical Engineering*, vol. 11, no. 4, pp. 328–343, 2016.

[59] J. A. Cottrell, T. J. R. Hughes, and A. Reali, “Studies of refinement and continuity in isogeometric structural analysis,” en, *Computer Methods in Applied Mechanics and Engineering*, vol. 196, no. 41, pp. 4160–4183, 2007, ISSN: 0045-7825.

[60] T. J. Hughes, A. Reali, and G. Sangalli, “Duality and unified analysis of discrete approximations in structural dynamics and wave propagation: Comparison of p-method finite elements with k-method NURBS,” *Computer Methods in Applied Mechanics and Engineering*, vol. 197, no. 49-50, pp. 4104–4124, 2008.

[61] T. J. Hughes, J. A. Evans, and A. Reali, “Finite element and NURBS approximations of eigenvalue, boundary-value, and initial-value problems,” *Computer Methods in Applied Mechanics and Engineering*, vol. 272, pp. 290–320, 2014.

[62] V. Puzyrev, Q. Deng, and V. Calo, “Spectral approximation properties of isogeometric analysis with variable continuity,” en, *Computer Methods in Applied Mechanics and Engineering*, vol. 334, pp. 22–39, 2018, ISSN: 0045-7825.

[63] I. Babuška and M. Suri, “On Locking and Robustness in the Finite Element Method,” *SIAM Journal on Numerical Analysis*, vol. 29, no. 5, pp. 1261–1293, 1992.

[64] M. Bischoff, W. A. Wall, K.-U. Bletzinger, and E. Ramm, “Models and Finite Elements for Thin-walled Structures,” in *Encyclopedia of Computational Mechanics*, E. Stein, R. de Borst, and T. J. R. Hughes, Eds., vol. 2, John Wiley & Sons, 2004, ch. 3, pp. 59–137.

[65] H. Stolarski and T. Belytschko, “Membrane locking and reduced integration for curved elements,” *Journal of Applied Mechanics, Transactions ASME*, vol. 49, no. 1, pp. 172–176, 1982.

[66] T. J. R. Hughes, *The Finite Element Method: Linear Static and Dynamic Finite Element Analysis*. Dover Publications, 2003, ISBN: 978-0-486-41181-1.

[67] L. Beirão da Veiga, C. Lovadina, and A. Reali, “Avoiding shear locking for the Timoshenko beam problem via isogeometric collocation methods,” *Computer Methods in Applied Mechanics and Engineering*, vol. 241-244, pp. 38–51, 2012.

[68] R. Bouclier, T. Elguedj, and A. Combescure, “Locking free isogeometric formulations of curved thick beams,” *Computer Methods in Applied Mechanics and Engineering*, vol. 245-246, pp. 144–162, 2012.

[69] W. Kanok-Nukulchai, W. Barry, K. Saran-Yasoontorn, and P. H. Bouillard, “On elimination of shear locking in the element-free Galerkin method,” *International Journal for Numerical Methods in Engineering*, vol. 52, no. 7, pp. 705–725, 2001.

[70] T. Elguedj, Y. Bazilevs, V. M. Calo, and T. J. Hughes, “B-bar and F-bar projection methods for nearly incompressible linear and non-linear elasticity and plasticity using higher-order NURBS elements,” *Computer Methods in Applied Mechanics and Engineering*, vol. 197, no. 33-40, pp. 2732–2762, 2008.

[71] C. Adam, T. J. Hughes, S. Bouabdallah, M. Zarroug, and H. Maitournam, “Selective and reduced numerical integrations for NURBS-based isogeometric analysis,” *Computer Methods in Applied Mechanics and Engineering*, vol. 284, no. August, pp. 732–761, 2015.

[72] L. Leonetti, F. Liguori, D. Magisano, and G. Garcea, “An efficient isogeometric solid-shell formulation for geometrically nonlinear analysis of elastic shells,” *Computer Methods in Applied Mechanics and Engineering*, vol. 331, pp. 159–183, 2018.

[73] Z. Zou, T. J. Hughes, M. A. Scott, R. A. Sauer, and E. J. Savitha, “Galerkin formulations of isogeometric shell analysis: Alleviating locking with Greville quadratures and higher-order elements,” *Computer Methods in Applied Mechanics and Engineering*, vol. 380, p. 113 757, 2021.

[74] C. Adam, S. Bouabdallah, M. Zarroug, and H. Maitournam, “Improved numerical integration for locking treatment in isogeometric structural elements. Part II: Plates and shells,” *Computer Methods in Applied Mechanics and Engineering*, vol. 284, pp. 106–137, 2015.

[75] P. Antolin, J. Kiendl, M. Pingaro, and A. Reali, “A simple and effective method based on strain projections to alleviate locking in isogeometric solid shells,” *Computational Mechanics*, vol. 65, no. 6, pp. 1621–1631, 2019.

[76] R. Bouclier, T. Elguedj, and A. Combescure, “Efficient isogeometric NURBS-based solid-shell elements: Mixed formulation and B-method,” *Computer Methods in Applied Mechanics and Engineering*, vol. 267, pp. 86–110, 2013.

[77] J. F. Caseiro, R. A. Valente, A. Reali, J. Kiendl, F. Auricchio, and R. J. Alves de Sousa, “Assumed natural strain NURBS-based solid-shell element for the analysis of large deformation elasto-plastic thin-shell structures,” *Computer Methods in Applied Mechanics and Engineering*, vol. 284, pp. 861–880, 2015.

[78] L. Greco, M. Cuomo, and L. Contrafatto, “A reconstructed local over(B, -) formulation for isogeometric Kirchhoff–Love shells,” *Computer Methods in Applied Mechanics and Engineering*, vol. 332, pp. 462–487, 2018.

[79] R. P. R. Cardoso and J. M. A. Cesar de Sa, “The enhanced assumed strain method for the isogeometric analysis of nearly incompressible deformation of solids,” *International Journal for Numerical Methods in Engineering*, vol. 92, no. 1, pp. 56–78, 2012.

[80] R. Echter and M. Bischoff, “Numerical efficiency, locking and unlocking of NURBS finite elements,” *Computer Methods in Applied Mechanics and Engineering*, vol. 199, no. 5-8, pp. 374–382, 2010.

[81] R. L. Taylor, “Isogeometric analysis of nearly incompressible solids,” *International Journal for Numerical Methods in Engineering*, vol. 87, no. 1-5, pp. 273–288, 2011.

[82] Z. Zou, M. Scott, D. Miao, M. Bischoff, B. Oesterle, and W. Dornisch, “An isogeometric Reissner–Mindlin shell element based on Bézier dual basis functions: Overcoming locking and improved coarse mesh accuracy,” *Computer Methods in Applied Mechanics and Engineering*, vol. 370, p. 113 283, 2020.

[83] J. Hokkanen and D. M. Pedroso, “Isogeometric thickness stretchable shell: Efficient formulation for nonlinear dynamic problems,” *International Journal for Numerical Methods in Engineering*, vol. 119, no. 2, pp. 105–127, 2019.

[84] J. Hokkanen, D. M. Pedroso, M. C. Elford, A. J. E. Stephan, and Y. Zhang, “Efficient isogeometric shell element with through-thickness stretch: application to incremental sheet forming,” *Journal of Physics: Conference Series*, vol. 1063, p. 012 189, 2018.

[85] Y. Chen, L. S.-P., O. Faruque, J. Alanoly, M. El-Essawi, and B. R., “Current Status of LS-DYNA Iso-geometric Analysis in Crash Simulation,” 14th International LS-DYNA Users Conference, Dearborn, Michigan, 2016.

[86] F. Auricchio, L. B. da Veiga, T. Hughes, A. Reali, and G. Sangalli, “Isogeometric collocation for elastostatics and explicit dynamics,” *Computer Methods in Applied Mechanics and Engineering*, vol. 249-252, pp. 2–14, 2012.

[87] J. Evans, R. Hiemstra, T. Hughes, and A. Reali, “Explicit higher-order accurate isogeometric collocation methods for structural dynamics,” *Computer Methods in Applied Mechanics and Engineering*, vol. 338, pp. 208–240, 2018.

[88] E. Marino, J. Kiendl, and L. De Lorenzis, “Explicit isogeometric collocation for the dynamics of three-dimensional beams undergoing finite motions,” *Computer Methods in Applied Mechanics and Engineering*, vol. 343, pp. 530–549, 2019.

[89] E. Hinton, T. Rock, and O. C. Zienkiewicz, “A note on mass lumping and related processes in the finite element method,” *Earthquake Engineering & Structural Dynamics*, vol. 4, no. 3, 1976.

[90] Y. Yang, H. Zheng, and M. V. Sivaselvan, "A rigorous and unified mass lumping scheme for higher-order elements," *Computer Methods in Applied Mechanics and Engineering*, vol. 319, 2017.

[91] S. Geevers, W. A. Mulder, and J. J. W. van der Vegt, "New higher-order mass-lumped tetrahedral elements for wave propagation modelling," *SIAM Journal on Scientific Computing*, vol. 40, no. 5, A2830–A2857, 2018.

[92] A. T. Patera, "A spectral element method for fluid dynamics: Laminar flow in a channel expansion," *Journal of Computational Physics*, vol. 54, no. 3, 1984.

[93] D. Schillinger, J. A. Evans, F. Frischmann, R. R. Hiemstra, M. C. Hsu, and T. J. R. Hughes, "A collocated C^0 finite element method: Reduced quadrature perspective, cost comparison with standard finite elements, and explicit structural dynamics," *International Journal for Numerical Methods in Engineering*, vol. 102, no. 3-4, 2014.

[94] S. Duczek and H. Gravenkamp, "Critical assessment of different mass lumping schemes for higher order serendipity finite elements," *Computer Methods in Applied Mechanics and Engineering*, vol. 350, pp. 836–897, 2019.

[95] S. Duczek and H. Gravenkamp, "Mass lumping techniques in the spectral element method: On the equivalence of the row-sum, nodal quadrature, and diagonal scaling methods," *Computer Methods in Applied Mechanics and Engineering*, vol. 353, pp. 516–569, 2019.

[96] I. Fried and D. S. Malkus, "Finite element mass matrix lumping by numerical integration with no convergence rate loss," *International Journal of Solids and Structures*, vol. 11, no. 4, 1975.

[97] G. Karniadakis and S. Sherwin, *Spectral/hp Element Methods for Computational Fluid Dynamics*. Oxford University Press, 2005.

[98] X. Li and D. Wang, "On the significance of basis interpolation for accurate lumped mass isogeometric formulation," *Computer Methods in Applied Mechanics and Engineering*, vol. 400, p. 115 533, 2022.

[99] Y. Voet, E. Sande, and A. Buffa, "A mathematical theory for mass lumping and its generalization with applications to isogeometric analysis," *Computer Methods in Applied Mechanics and Engineering*, vol. 410, p. 116 033, 2023.

[100] C. Anitescu, C. Nguyen, T. Rabczuk, and X. Zhuang, "Isogeometric analysis for explicit elastodynamics using a dual-basis diagonal mass formulation," *Computer Methods in Applied Mechanics and Engineering*, vol. 346, pp. 574–591, 2019.

[101] C de Boor, *On local linear functionals which vanish at all b-splines but one, theory of approximation with applications (ed. ag law and bn sahney)*, 1976.

[102] L. Coox, F. Greco, O. Atak, D. Vandepitte, and W. Desmet, "A robust patch coupling method for NURBS-based isogeometric analysis of non-conforming multipatch surfaces," *Computer Methods in Applied Mechanics and Engineering*, vol. 316, pp. 235–260, 2017.

[103] W. Dornisch, J. Stöckler, and R. Müller, “Dual and approximate dual basis functions for B-splines and NURBS – Comparison and application for an efficient coupling of patches with the isogeometric mortar method,” *Computer Methods in Applied Mechanics and Engineering*, vol. 316, pp. 449–496, 2017.

[104] D. Miao, Z. Zou, M. A. Scott, M. J. Borden, and D. C. Thomas, “Isogeometric Bézier dual mortaring: The enriched Bézier dual basis with application to second- and fourth-order problems,” *Computer Methods in Applied Mechanics and Engineering*, vol. 363, p. 112 900, 2020.

[105] A. Seitz, P. Farah, J. Kremheller, B. I. Wohlmuth, W. A. Wall, and A. Popp, “Isogeometric dual mortar methods for computational contact mechanics,” *Computer Methods in Applied Mechanics and Engineering*, vol. 301, pp. 259–280, 2016.

[106] L. Wunderlich, A. Seitz, M. D. Alaydın, B. Wohlmuth, and A. Popp, “Biorthogonal splines for optimal weak patch-coupling in isogeometric analysis with applications to finite deformation elasticity,” *Computer Methods in Applied Mechanics and Engineering*, vol. 346, pp. 197–215, 2019.

[107] Z. Zou, M. Scott, M. Borden, D. Thomas, W. Dornisch, and E. Brivadis, “Isogeometric Bézier dual mortaring: Refineable higher-order spline dual bases and weakly continuous geometry,” *Computer Methods in Applied Mechanics and Engineering*, vol. 333, pp. 497–534, 2018.

[108] E. Brivadis, A. Buffa, B. Wohlmuth, and L. Wunderlich, “Isogeometric mortar methods,” *Computer Methods in Applied Mechanics and Engineering*, vol. 284, pp. 292–319, 2015.

[109] D. Miao, Z. Zou, M. A. Scott, M. J. Borden, and D. C. Thomas, “Isogeometric Bézier dual mortaring: The Kirchhoff–Love shell problem,” *Computer Methods in Applied Mechanics and Engineering*, vol. 382, p. 113 873, 2021.

[110] B. I. Wohlmuth, “A Mortar Finite Element Method Using Dual Spaces for the Lagrange Multiplier,” *SIAM Journal on Numerical Analysis*, vol. 38, no. 3, pp. 989–1012, 2000.

[111] T. Belytschko, W. Liu, and B. Moran, *Nonlinear Finite Elements for Continua and Structures.* Wiley, 2014.

[112] G. Cocchetti, M. Pagani, and U. Perego, “Selective mass scaling and critical time-step estimate for explicit dynamics analyses with solid-shell elements,” *Computers & Structures*, vol. 127, pp. 39–52, 2013.

[113] J. A. González and K. C. Park, “Large-step explicit time integration via mass matrix tailoring,” *International Journal for Numerical Methods in Engineering*, vol. 121, no. 8, pp. 1647–1664, 2020.

[114] A.-K. Schaeuble, A. Tkachuk, and M. Bischoff, “Variationally consistent inertia templates for B-spline- and NURBS-based FEM: Inertia scaling and customization,” *Computer Methods in Applied Mechanics and Engineering*, vol. 326, pp. 596–621, 2017.

[115] A. Tkachuk and M. Bischoff, “Local and global strategies for optimal selective mass scaling,” *Computational Mechanics*, vol. 53, no. 6, pp. 1197–1207, 2014.

[116] S. Hartmann and D. J. Benson, “Mass scaling and stable time step estimates for isogeometric analysis,” *International Journal for Numerical Methods in Engineering*, vol. 102, no. 3-4, pp. 671–687, 2015.

[117] H. Askes, D. C. Nguyen, and A. Tyas, “Increasing the critical time step: Micro-inertia, inertia penalties and mass scaling,” *Computational Mechanics*, vol. 47, no. 6, 2011.

[118] R. W. Macek and B. H. Aubert, “A mass penalty technique to control the critical time increment in explicit dynamic finite element analyses,” *Earthquake Engineering & Structural Dynamics*, vol. 24, no. 10, 1995.

[119] L. Olovsson and K. Simonsson, “Iterative solution technique in selective mass scaling,” *Communications in Numerical Methods in Engineering*, vol. 22, no. 1, 2006.

[120] L. Olovsson, K. Simonsson, and M. Unosson, “Selective mass scaling for explicit finite element analyses,” *International Journal for Numerical Methods in Engineering*, vol. 63, no. 10, pp. 1436–1445, 2005.

[121] Q. Deng and V. Calo, “A boundary penalization technique to remove outliers from isogeometric analysis on tensor-product meshes,” *Computer Methods in Applied Mechanics and Engineering*, vol. 383, p. 113 907, 2021.

[122] R. R. Hiemstra, T. J. R. Hughes, A. Reali, and D. Schillinger, “Removal of spurious outlier frequencies and modes from isogeometric discretizations of second- and fourth-order problems in one, two, and three dimensions,” *Computer Methods in Applied Mechanics and Engineering*, vol. 387, p. 114 115, 2021.

[123] C. Manni, E. Sande, and H. Speleers, “Application of optimal spline subspaces for the removal of spurious outliers in isogeometric discretizations,” *Computer Methods in Applied Mechanics and Engineering*, vol. 389, p. 114 260, 2022.

[124] T. Horger, A. Reali, B. Wohlmuth, and L. Wunderlich, “A hybrid isogeometric approach on multi-patches with applications to Kirchhoff plates and eigenvalue problems,” *Computer Methods in Applied Mechanics and Engineering*, vol. 348, pp. 396–408, 2019.

[125] M. Dittmann, S. Schuß, B. Wohlmuth, and C. Hesch, “Weak C n coupling for multipatch isogeometric analysis in solid mechanics,” *International Journal for Numerical Methods in Engineering*, vol. 118, no. 11, pp. 678–699, 2019.

[126] S. Schuß, M. Dittmann, B. Wohlmuth, S. Klinkel, and C. Hesch, “Multi-patch isogeometric analysis for Kirchhoff–Love shell elements,” *Computer Methods in Applied Mechanics and Engineering*, vol. 349, pp. 91–116, 2019.

[127] M. Ainsworth and H. A. Wajid, "Optimally Blended Spectral-Finite Element Scheme for Wave Propagation and NonStandard Reduced Integration," *SIAM Journal on Numerical Analysis*, vol. 48, no. 1, pp. 346–371, 2010, ISSN: 0036-1429.

[128] V. Calo, Q. Deng, and V. Puzyrev, "Dispersion optimized quadratures for isogeometric analysis," *Journal of Computational and Applied Mathematics*, vol. 355, pp. 283–300, 2019, ISSN: 03770427.

[129] Q. Deng and V. Calo, "Outlier Removal for Isogeometric Spectral Approximation with the Optimally-Blended Quadratures," in *Computational Science – ICCS 2021*, Springer International Publishing, 2021, pp. 315–328, ISBN: 978-3-030-77964-1.

[130] V. Puzyrev, Q. Deng, and V. Calo, "Dispersion-optimized quadrature rules for isogeometric analysis: Modified inner products, their dispersion properties, and optimally blended schemes," *Computer Methods in Applied Mechanics and Engineering*, vol. 320, pp. 421–443, 2017, ISSN: 00457825.

[131] C. K. Chui, W. He, and J. Stöckler, "Nonstationary tight wavelet frames, I: Bounded intervals," *Applied and Computational Harmonic Analysis*, vol. 17, no. 2, pp. 141–197, 2004.

[132] R. R. Hiemstra, T.-H. Nguyen, S. Eisenträger, W. Dornisch, and D. Schillinger, "Higher order accurate mass lumping in explicit isogeometric methods based on approximate dual basis functions," *In preparation*, 2023.

[133] R. R. Hiemstra, F. Calabrò, D. Schillinger, and T. J. Hughes, "Optimal and reduced quadrature rules for tensor product and hierarchically refined splines in isogeometric analysis," *Computer Methods in Applied Mechanics and Engineering*, vol. 316, pp. 966–1004, 2017.

[134] C. G. Gebhardt and I. Romero, "On a nonlinear rod exhibiting only axial and bending deformations: mathematical modeling and numerical implementation," *Acta Mechanica*, vol. 232, no. 10, pp. 3825–3847, 2021.

[135] T.-H. Nguyen, R. R. Hiemstra, and D. Schillinger, "Leveraging spectral analysis to elucidate membrane locking and unlocking in isogeometric finite element formulations of the curved Euler–Bernoulli beam," *Computer Methods in Applied Mechanics and Engineering*, vol. 388, p. 114 240, 2022. DOI: `10.1016/j.cma.2021.114240`. [Online]. Available: `https://linkinghub.elsevier.com/retrieve/pii/S0045782521005636`.

[136] A. Cazzani, M. Malagù, and E. Turco, "Isogeometric analysis of plane-curved beams," *Mathematics and Mechanics of Solids*, vol. 21, no. 5, pp. 562–577, 2016.

[137] G. Engel, K. Garikipati, T. Hughes, M. Larson, L. Mazzei, and R. Taylor, "Continuous/discontinuous finite element approximations of fourth-order elliptic problems in structural and continuum mechanics with applications to thin beams and plates, and strain gradient elasticity," *Computer Methods in Applied Mechanics and Engineering*, vol. 191, no. 34, pp. 3669–3750, 2002.

[138] A. Tagliabue, L. Dedè, and A. Quarteroni, “Isogeometric analysis and error estimates for high order partial differential equations in fluid dynamics,” *Computers and Fluids*, vol. 102, pp. 277–303, 2014.

[139] D. G. Ashwell and R. Gallagher, *Finite elements for thin shells and curved members*. London: John Wiley & Sons, Ltd, 1976.

[140] E. Rank, R. Krause, and K. Preusch, “On the accuracy of p-version elements for the Reissner-Mindlin plate problem,” *International Journal for Numerical Methods in Engineering*, vol. 43, no. 1, pp. 51–67, 1998.

[141] C. R. Babu and G. Prathap, “A linear thick curved beam element,” *International Journal for Numerical Methods in Engineering*, vol. 23, no. 7, pp. 1313–1328, 1986.

[142] M. Ishaquddin, P. Raveendranath, and J. N. Reddy, “Flexure and torsion locking phenomena in out-of-plane deformation of Timoshenko curved beam element,” *Finite Elements in Analysis and Design*, vol. 51, pp. 22–30, 2012.

[143] G. Prathap, *The Finite Element Method in Structural Mechanics : Principles and Practice of Design of Field-consistent Elements for Structural and Solid Mechanics*, 1st. Dordrecht: Springer, 1993, ISBN: 9048143268.

[144] T. J. Hughes, “Equivalence of finite elements for nearly incompressible elasticity,” *Journal of Applied Mechanics*, vol. 44, pp. 181–183, 1977.

[145] D. S. Malkus and T. J. Hughes, “Mixed finite element methods - Reduced and selective integration techniques: A unification of concepts,” *Computer Methods in Applied Mechanics and Engineering*, vol. 15, no. 1, pp. 63–81, 1978.

[146] A. K. Noor and J. M. Peters, “Mixed Models and Reduced/Selective Integration Displacement Models for Nonlinear Shell Analysis.,” *American Society of Mechanical Engineers, Applied Mechanics Division, AMD*, vol. 48, no. April 1980, pp. 119–146, 1981.

[147] M. Schwarze and S. Reese, “A reduced integration solid-shell finite element based on the EAS and the ANS concept-Geometrically linear problems,” *International Journal for Numerical Methods in Engineering*, vol. 80, no. 10, pp. 1322–1355, 2009.

[148] O. C. Zienkiewicz, R. L. Taylor, and J. M. Too, “Reduced integration technique in general analysis of plates and shells,” *International Journal for Numerical Methods in Engineering*, vol. 3, no. 2, pp. 275–290, 1971.

[149] T. Belytschko and J. S.-J. Ong, “Hourglass control in linear and nonlinear problems,” *Computer Methods in Applied Mechanics and Engineering*, vol. 43, pp. 251–276, 1984.

[150] D. P. Flanagan and T. Belytschko, “A uniform strain hexahedron and quadrilateral with orthogonal hourglass control,” *International Journal for Numerical Methods in Engineering*, vol. 17, no. 5, pp. 679–706, 1981.

[151] Q. Li, Y. Liu, Z. Zhang, and W. Zhong, "A new reduced integration solid-shell element based on EAS and ANS with hourglass stabilization," *International Journal for Numerical Methods in Engineering*, vol. 104, pp. 805–826, 2015.

[152] S. Reese, "A large deformation solid-shell concept based on reduced integration with hourglass stabilization," *International Journal for Numerical Methods in Engineering*, vol. 69, no. 8, pp. 1671–1716, 2007.

[153] T. J. Hughes, "Generalization of selective integration procedures to anisotropic and nonlinear media," *International Journal for Numerical Methods in Engineering*, vol. 15, no. 9, pp. 1413–1418, 1980.

[154] D. P. Recio, R. M. N. Jorge, and L. M. S. Dinis, "Locking and hourglass phenomena in an element-free Galerkin context: the B-bar method with stabilization and an enhanced strain method," *International Journal for Numerical Methods in Engineering*, vol. 68, no. 13, pp. 1329–1357, 2006.

[155] K.-J. Bathe and E. N. Dvorkin, "Short Communication a Four-Node Plate Bending Element Based on Mindlin / Reissner Plate Theory and," *International Journal for Numerical Methods in Engineering*, vol. 21, no. March 1984, pp. 367–383, 1985.

[156] M. L. Bucalem and K. J. Bathe, "Higher-order MITC general shell elements," *International Journal for Numerical Methods in Engineering*, vol. 36, no. 21, pp. 3729–3754, 1993.

[157] J. C. Simo and T. J. Hughes, "On the variational foundations of assumed strain methods," *Journal of Applied Mechanics, Transactions ASME*, vol. 53, no. 1, pp. 51–54, 1986.

[158] J. F. Caseiro, R. A. Valente, A. Reali, J. Kiendl, F. Auricchio, and R. J. Alves De Sousa, "On the Assumed Natural Strain method to alleviate locking in solid-shell NURBS-based finite elements," *Computational Mechanics*, vol. 53, no. 6, pp. 1341–1353, 2014.

[159] R. J. Alves de Sousa, R. P. Cardoso, R. A. Fontes Valente, J. W. Yoon, J. J. Grácio, and R. M. Natal Jorge, "A new one-point quadrature enhanced assumed strain (EAS) solid-shell element with multiple integration points along thickness: Part I - Geometrically linear applications," *International Journal for Numerical Methods in Engineering*, vol. 62, no. 7, pp. 952–977, 2005.

[160] U. Andelfinger and E. Ramm, "EAS-elements for two-dimensional, three-dimensional, plate and shell structures and their equivalence to HR-elements," *International Journal for Numerical Methods in Engineering*, vol. 36, no. 8, pp. 1311–1337, 1993.

[161] M. Bischoff, E. Ramm, and D. Braess, "A class of equivalent enhanced assumed strain and hybrid stress finite elements," *Computational Mechanics*, vol. 22, no. 6, pp. 443–449, 1999.

[162] J. M. De César Sá, R. M. Natal Jorge, R. A. Fontes Valente, and P. M. Almeida Areias, "Development of shear locking-free shell elements using an enhanced assumed strain formulation," *International Journal for Numerical Methods in Engineering*, vol. 53, no. 7, pp. 1721–1750, 2002.

[163] K.-U. Bischoff, M.; Bletzinger, "Stabilized DSG plate and shell elements," *Trends in Computational Structural Mechanics*, pp. 253–263, 2001.

[164] K.-U. Bletzinger, M. Bischoff, and E. Ramm, "Unified approach for shear-locking-free triangular and rectangular shell finite elements," *Computers and Structures*, vol. 75, no. 3, pp. 321–334, 2000.

[165] F. Koschnick, M. Bischoff, N. Camprubí, and K.-U. Bletzinger, "The discrete strain gap method and membrane locking," *Computer Methods in Applied Mechanics and Engineering*, vol. 194, no. 21-24 SPEC. ISS. Pp. 2444–2463, 2005.

[166] J. G. Kim and Y. Y. Kim, "A new higher-order hybrid-mixed curved beam element," *International Journal for Numerical Methods in Engineering*, vol. 43, no. 5, pp. 925–940, 1998.

[167] S. Klinkel, F. Gruttmann, and W. Wagner, "A mixed shell formulation accounting for thickness strains and finite strain 3d material models," *International Journal for Numerical Methods in Engineering*, vol. 74, no. 6, pp. 945–970, 2008.

[168] Y. Lee, K. Yoon, and P.-S. Lee, "Improving the MITC3 shell finite element by using the Hellinger–Reissner principle," *Computers & Structures*, vol. 110-111, pp. 93–106, 2012.

[169] H. Stolarski and T. Belytschko, "On the equivalence of mode decomposition and mixed finite elements based on the hellinger-reissner principle. part I: Theory," *Computer Methods in Applied Mechanics and Engineering*, vol. 58, no. 3, pp. 249–263, 1986.

[170] Y. Lee, H.-M. Jeon, P.-S. Lee, and K.-J. Bathe, "The modal behavior of the MITC3+ triangular shell element," *Computers & Structures*, vol. 153, pp. 148–164, 2015.

[171] D. Schillinger, S. Hossain, and T. Hughes, "Reduced Bézier element quadrature rules for quadratic and cubic splines in isogeometric analysis," *Computer Methods in Applied Mechanics and Engineering*, vol. 277, pp. 1–45, 2014.

[172] G Strang and G Fix, *An Analysis of the Finite Element Method*, 2nd edition. Wellesley, Mass: Wellesley-Cambridge Press, 2008, ISBN: 978-0-9802327-0-7.

[173] R. Clough and J. Penzien, *Dynamics of Structures*. McGraw-Hill, 1993, ISBN: 9780071132411.

[174] W. Soedel, *Vibrations of Shells and Plates*. New York: Marcel Dekker, Inc., 2004, ISBN: 0-8247-5629-0.

[175] M. Haberleitner, B. Jüttler, M. A. Scott, and D. C. Thomas, "Isogeometric analysis: Representation of geometry," in *Encyclopedia of Computational Mechanics 2^{nd} Ed.* E. Stein, R. de Borst, and T. J. R. Hughes, Eds., Wiley, 2017.

[176] T. J. R. Hughes and G. Sangalli, "Mathematics of isogeometric analysis: A conspectus," in *Encyclopedia of Computational Mechanics 2^{nd} Ed.* E. Stein, R. de Borst, and T. J. R. Hughes, Eds., Wiley, 2017.

[177] D. Schillinger, "Isogeometric finite element analysis," in *Encyclopedia of Continuum Mechanics*, H. Altenbach and A. Öchsner, Eds., Springer, 2018.

[178] W. K. Liu and T. Belytschko, "Efficient linear and nonlinear heat conduction with a quadrilateral element," *International Journal for Numerical Methods in Engineering*, vol. 20, no. 5, pp. 931–948, 1984.

[179] Y. Leino and J. Pitkäranta, "On the membrane locking of h–p finite elements in a cylindrical shell problem," *International Journal for Numerical Methods in Engineering*, vol. 37, no. 6, pp. 1053–1070, 1994.

[180] E Rank, A Düster, V Nübel, K Preusch, and O. Bruhns, "High order finite elements for shells," *Computer Methods in Applied Mechanics and Engineering*, vol. 194, no. 21-24, pp. 2494–2512, 2005.

[181] M. Suri, "Analytical and computational assessment of locking in the hp finite element method," *Computer Methods in Applied Mechanics and Engineering*, vol. 133, no. 3-4, pp. 347–371, 1996.

[182] O. Weeger, U. Wever, and B. Simeon, "Isogeometric analysis of nonlinear euler–bernoulli beam vibrations," *Nonlinear Dynamics*, vol. 72, no. 4, pp. 813–835, 2013.

[183] T.-H. Nguyen, R. R. Hiemstra, S. K. Stoter, and D. Schillinger, "A variational approach based on perturbed eigenvalue analysis for improving spectral properties of isogeometric multipatch discretizations," *Computer Methods in Applied Mechanics and Engineering*, vol. 392, p. 114 671, 2022. DOI: `10.1016/j.cma.2022.114671`. [Online]. Available: `https://linkinghub.elsevier.com/retrieve/pii/S0045782522000615`.

[184] R. Szilard, *Theories and Applications of Plate Analysis: Classical, Numerical and Engineering Methods*, English. Hoboken, NJ: Wiley, 2004, ISBN: 978-0-471-42989-0.

[185] A. Ern and J.-L. Guermond, *Theory and Practice of Finite Elements.* New York, USA: Springer-Verlag New York Inc., 2004.

[186] Y. Bazilevs, L. Beirão Da Veiga, J. A. Cottrell, T. J. R. Hughes, and G. Sangalli, "Isogeometric analysis: approximation, stability and error estimates for h-refined meshes," *Mathematical Models and Methods in Applied Sciences*, vol. 16, no. 07, pp. 1031–1090, 2006.

[187] R.-C. Li, "Matrix Perturbation Theory," in *Handbook of linear algebra*, L. Hogben, Ed., First, Chapman & Hall/CRC Press, LLC, 2007, ch. 15, ISBN: 1-58488-510-6.

[188] T.-H. Nguyen, R. R. Hiemstra, S. Eisenträger, and D. Schillinger, “Towards higher-order accurate mass lumping in explicit isogeometric analysis for structural dynamics,” *Computer Methods in Applied Mechanics and Engineering*, p. 116 233, 2023. DOI: `10.1016/j.cma.2023.116233`. [Online]. Available: `https://linkinghub.elsevier.com/retrieve/pii/S0045782523003572`.

[189] T. Belytschko, J. I. Lin, and C.-S. Tsay, “Explicit algorithms for the nonlinear dynamics of shells,” *Computer Methods in Applied Mechanics and Engineering*, vol. 42, no. 2, pp. 225–251, 1984.

[190] D. J. Benson, “Computational methods in Lagrangian and Eulerian hydrocodes,” *Computer Methods in Applied Mechanics and Engineering*, vol. 99, no. 2-3, pp. 235–394, 1992.

[191] C. Canuto, M. Hussaini, A. Quarteroni, and T. Zang, *Spectral Methods: Evolution to Complex Geometries and Applications to Fluid Dynamics*. Springer, 2007.

[192] C. Willberg, S. Duczek, J. Vivar Perez, D. Schmicker, and U. Gabbert, “Comparison of different higher order finite element schemes for the simulation of Lamb waves,” *Computer Methods in Applied Mechanics and Engineering*, vol. 241–244, pp. 246–261, 2012.

[193] K. T. Danielson, “Curved node–to–face contact schemes for higher-order finite elements in lumped–mass explicit methods,” *Computer Methods in Applied Mechanics and Engineering*, vol. 395, p. 115 056, 2022.

[194] K. T. Danielson and J. L. O’Daniel, “Reliable second–order hexahedral elements for explicit methods in nonlinear solid dynamics,” *International Journal for Numerical Methods in Engineering*, vol. 85, no. 9, pp. 1073–1102, 2011.

[195] S Duczek, M Joulaian, A Düster, and U Gabbert, “Numerical analysis of lamb waves using the finite and spectral cell methods,” *International Journal for Numerical Methods in Engineering*, vol. 99, no. 1, pp. 26–53, 2014.

[196] M. A. Sprague and T. L. Geers, “Legendre spectral finite elements for structural dynamics analysis,” *Communications in Numerical Methods in Engineering*, vol. 24, no. 12, pp. 1953–1965, 2008.

[197] J. Zhang, A. Ankit, H. Gravenkamp, S. Eisenträger, and C. Song, “A massively parallel explicit solver for elasto-dynamic problems exploiting octree meshes,” *Computer Methods in Applied Mechanics and Engineering*, vol. 380, p. 113 811, 2021.

[198] IMPETUS, Afea AS, *Impetus afea solver user documentation*, 2012.

[199] H. Teng, “Recent advances on higher order 27 node hexahedral element in LS-DYNA,” in *Proceedings of the 14th International LS–DYNA Users Conference, Detroit, MI*, 2016.

[200] F. Casadei and J.-P. Halleux, “Binary spatial partitioning of the central-difference time integration scheme for explicit fast transient dynamics,” *International Journal for Numerical Methods in Engineering*, vol. 78, no. 12, pp. 1436–1473, 2009.

[201] D. Schillinger, J. A. Evans, A. Reali, M. A. Scott, and T. J. R. Hughes, “Isogeometric collocation: Cost comparison with Galerkin methods and extension to adaptive hierarchical NURBS discretizations,” *Computer Methods in Applied Mechanics and Engineering*, vol. 267, pp. 170–232, 2013.

[202] D. J. Benson, Y. Bazilevs, M.-C. Hsu, and T. J. R. Hughes, “A large deformation, rotation-free, isogeometric shell,” *Computer Methods in Applied Mechanics and Engineering*, vol. 200, no. 13, pp. 1367–1378, 2011.

[203] W. Dornisch, S. Klinkel, and B. Simeon, “Isogeometric Reissner–Mindlin shell analysis with exactly calculated director vectors,” *Computer Methods in Applied Mechanics and Engineering*, vol. 253, pp. 491–504, 2013.

[204] M.-C. Hsu and Y. Bazilevs, “Fluid-structure interaction modeling of wind turbines: Simulating the full machine,” *Computational Mechanics*, vol. 50, pp. 821–833, 2012.

[205] R. Bouclier, T. Elguedj, and A. Combescure, “An isogeometric locking-free NURBS-based solid-shell element for geometrically nonlinear analysis,” *International Journal for Numerical Methods in Engineering*, vol. 101, no. 10, pp. 774–808, 2015.

[206] S. Hosseini, J. J. C. Remmers, C. V. Verhoosel, and R. de Borst, “An isogeometric solid-like shell element for nonlinear analysis,” *International Journal for Numerical Methods in Engineering*, vol. 95, no. 3, pp. 238–256, 2013.

[207] L. Chen, N. Nguyen-Thanh, H. Nguyen-Xuan, T. Rabczuk, S. P. A. Bordas, and G. Limbert, “Explicit finite deformation analysis of isogeometric membranes,” *Computer Methods in Applied Mechanics and Engineering*, vol. 277, pp. 104–130, 2014.

[208] L. Leidinger, M. Breitenberger, A. Bauer, S. Hartmann, R. Wüchner, K.-U. Bletzinger, F. Duddeck, and L. Song, “Explicit dynamic isogeometric B-Rep analysis of penalty-coupled trimmed NURBS shells,” *Computer Methods in Applied Mechanics and Engineering*, vol. 351, pp. 891–927, 2019.

[209] C. Adam, S. Bouabdallah, M. Zarroug, and H. Maitournam, “Stable time step estimates for nurbs-based explicit dynamics,” *Computer Methods in Applied Mechanics and Engineering*, vol. 295, pp. 581–605, 2015.

[210] S. Held, S. Eisenträger, and W. Dornisch, “An efficient mass lumping scheme for isogeometric analysis based on approximate dual basis functions,” 2023. arXiv: `2306.12257`.

[211] W. Dornisch, G. Vitucci, and S. Klinkel, “The weak substitution method - an application of the mortar method for patch coupling in NURBS-based isogeometric analysis,” *International Journal for Numerical Methods in Engineering*, vol. 103, no. 3, pp. 205–234, 2015.

[212] R. R. Hiemstra, G. Sangalli, M. Tani, F. Calabrò, and T. J. R. Hughes, “Fast formation and assembly of finite element matrices with application to isogeometric linear elasticity,” *Computer Methods in Applied Mechanics and Engineering*, vol. 355, pp. 234–260, 2019.

[213] M. J. Borden, M. A. Scott, J. A. Evans, and T. J. R. Hughes, "Isogeometric finite element data structures based on Bézier extraction of NURBS," *International Journal for Numerical Methods in Engineering*, vol. 87, no. 1-5, pp. 15–47, 2011.

[214] D. Schillinger, P. K. Ruthala, and L. H. Nguyen, "Lagrange extraction and projection for NURBS basis functions: A direct link between isogeometric and standard nodal finite element formulations," *International Journal for Numerical Methods in Engineering*, vol. 108, no. 6, pp. 515–534, 2016.

[215] A. Embar, J. Dolbow, and I. Harari, "Imposing Dirichlet boundary conditions with Nitsche's method and spline-based finite elements," *International Journal for Numerical Methods in Engineering*, vol. 83, no. 7, pp. 877–898, 2010.

[216] Y. Guo, J. Heller, T. J. R. Hughes, M. Ruess, and D. Schillinger, "Variationally consistent isogeometric analysis of trimmed thin shells at finite deformations, based on the step exchange format," *Computer Methods in Applied Mechanics and Engineering*, vol. 336, pp. 39–79, 2018.

[217] D. Schillinger, I. Harari, M. C. Hsu, D. Kamensky, S. K. Stoter, Y. Yu, and Y. Zhao, "The non-symmetric Nitsche method for the parameter-free imposition of weak boundary and coupling conditions in immersed finite elements," *Computer Methods in Applied Mechanics and Engineering*, vol. 309, pp. 625–652, 2016.

[218] K. Sze, X. Liu, and S. Lo, "Popular benchmark problems for geometric nonlinear analysis of shells," *Finite Elements in Analysis and Design*, vol. 40, no. 11, pp. 1551–1569, 2004.

[219] M. L. Mika, T. J. R. Hughes, D. Schillinger, P. Wriggers, and R. R. Hiemstra, "A matrix-free isogeometric Galerkin method for Karhunen–Loève approximation of random fields using tensor product splines, tensor contraction and interpolation based quadrature," *Computer Methods in Applied Mechanics and Engineering*, vol. 379, p. 113 730, 2021.

[220] T. J. R. Hughes and W. K. Liu, "Implicit-Explicit Finite Elements in Transient Analysis: Stability Theory," *Journal of Applied Mechanics*, vol. 45, no. 2, pp. 371–374, 1978.

[221] S. Mattern, C. Schmied, and K. Schweizerhof, "Highly efficient solid and solid-shell finite elements with mixed strain–displacement assumptions specifically set up for explicit dynamic simulations using symbolic programming," *Computers & Structures*, vol. 154, pp. 210–225, 2015.

[222] N. M. Lafontaine, R. Rossi, M. Cervera, and M. Chiumenti, "Explicit mixed strain-displacement finite element for dynamic geometrically non-linear solid mechanics," *Computational Mechanics*, vol. 55, no. 3, pp. 543–559, 2015.

[223] D. J. Benson, "Stable time step estimation for multi-material Eulerian hydrocodes," *Computer Methods in Applied Mechanics and Engineering*, vol. 167, no. 1-2, pp. 191–205, 1998.

[224] M. Bischoff, E. Ramm, and B. Schneider, *Lecture notes in Advanced Computational Mechanics of Structures*, 2007.

[225] O. C. Zienkiewicz, “Displacement and equilibrium models in the finite element method by B. Fraeijs de Veubeke, Chapter 9, Pages 145–197 of Stress Analysis, Edited by O. C. Zienkiewicz and G. S. Holister, Published by John Wiley & Sons, 1965,” *International Journal for Numerical Methods in Engineering*, vol. 52, no. 3, pp. 287–342, 2001.

[226] S. Bieber, B. Oesterle, E. Ramm, and M. Bischoff, “A variational method to avoid locking-independent of the discretization scheme,” *International Journal for Numerical Methods in Engineering*, vol. 114, no. 8, pp. 801–827, 2018.

[227] J. N. Reddy, *Theory and Analysis of Elastic Plates and Shells*, 2nd. CRC Press, 2006.

[228] R. D. Blevins, *Formulas for Dynamics, Acoustics and Vibration.* John Wiley & Sons, 2015, ISBN: 9781119038115.

[229] T. Belytschko, H. Stolarski, W. K. Liu, N. Carpenter, and J. S. Ong, “Stress projection for membrane and shear locking in shell finite elements,” *Computer Methods in Applied Mechanics and Engineering*, vol. 51, no. 1-3, pp. 221–258, 1985.

[230] C. J. Benham, “An elastic model of the large-scale structure of duplex DNA,” *Biopolymers*, vol. 18, no. 3, pp. 609–623, 1979.

[231] T. Schlick, “Modeling superhelical DNA: recent analytical and dynamic approaches,” *Current Opinion in Structural Biology*, vol. 5, no. 2, pp. 245–262, 1995.

[232] Y. Shi and J. E. Hearst, “The Kirchhoff elastic rod, the nonlinear Schrödinger equation, and DNA supercoiling,” *The Journal of Chemical Physics*, vol. 101, no. 6, pp. 5186–5200, 1994.

[233] F. Boyer, G. De Nayer, A. Leroyer, and M. Visonneau, “Geometrically Exact Kirchhoff Beam Theory: Application to Cable Dynamics,” *Journal of Computational and Nonlinear Dynamics*, vol. 6, no. 4, 2011.

[234] J. Coyne, “Analysis of the formation and elimination of loops in twisted cable,” *IEEE Journal of Oceanic Engineering*, vol. 15, no. 2, pp. 72–83, 1990.

[235] A. Moore and T. Healey, “Computation of elastic equilibria of complete Möbius bands and their stability,” *Mathematics and Mechanics of Solids*, vol. 24, no. 4, pp. 939–967, 2019.

[236] B. Audoly, N. Clauvelin, and S. Neukirch, “Elastic knots,” *Phys. Rev. Lett.*, vol. 99, p. 164 301, 16 2007.

[237] T. A. Ivey and D. A. Singer, “Knot Types, Homotopies and Stability of Closed Elastic Rods,” *Proceedings of the London Mathematical Society*, vol. 79, no. 2, pp. 429–450, 1999.

[238] G. G. Giusteri and E. Fried, “Importance and Effectiveness of Representing the Shapes of Cosserat Rods and Framed Curves as Paths in the Special Euclidean Algebra,” *Journal of Elasticity*, vol. 132, no. 1, pp. 43–65, 2018.

[239] O. M. O'Reilly, *Modeling Nonlinear Problems in the Mechanics of Strings and Rods* (Interaction of Mechanics and Mathematics). Cham: Springer International Publishing, 2017.

[240] S. Antman, "The theory of rods," in *Handbuch der Physik*, Springer Berlin, 1972, pp. 641–703.

[241] S. M. Han, H. Benaroya, and T. Wei, "Dynamics of transversely vibrating beams using four engineering theories," *Journal of Sound and Vibration*, vol. 225, no. 5, pp. 935–988, 1999.

[242] S. S. Antman, "Kirchhoff's problem for nonlinearly elastic rods," *Quarterly of Applied Mathematics*, vol. 32, no. 3, pp. 221–240, 1974.

[243] S. S. Antman, *Nonlinear Problems of Elasticity* (Applied Mathematical Sciences). New York: Springer-Verlag, 2005, vol. 107.

[244] J. Langer and D. A. Singer, "Lagrangian Aspects of the Kirchhoff Elastic Rod," *SIAM Review*, vol. 38, no. 4, pp. 605–618, 1996.

[245] I. Romero and C. G. Gebhardt, "Variational principles for nonlinear Kirchhoff rods," *Acta Mechanica*, vol. 231, no. 2, pp. 625–647, 2020.

[246] I. Romero, M. Urrecha, and C. Cyron, "A torsion-free non-linear beam model," *International Journal of Non-Linear Mechanics*, vol. 58, pp. 1–10, 2014.

[247] F. Boyer and D. Primault, "Finite element of slender beams in finite transformations: a geometrically exact approach," *International Journal for Numerical Methods in Engineering*, vol. 59, no. 5, pp. 669–702, 2004.

[248] L. Greco and M. Cuomo, "An implicit multi patch B-spline interpolation for Kirchhoff–Love space rod," *Computer Methods in Applied Mechanics and Engineering*, vol. 269, pp. 173–197, 2014.

[249] F. Maurin, F. Greco, S. Dedoncker, and W. Desmet, "Isogeometric analysis for nonlinear planar Kirchhoff rods: Weighted residual formulation and collocation of the strong form," *Computer Methods in Applied Mechanics and Engineering*, vol. 340, pp. 1023–1043, 2018.

[250] C. Meier, A. Popp, and W. A. Wall, "An objective 3D large deformation finite element formulation for geometrically exact curved Kirchhoff rods," *Computer Methods in Applied Mechanics and Engineering*, vol. 278, pp. 445–478, 2014.

[251] Z. Zhao and G. Ren, "A quaternion-based formulation of Euler–Bernoulli beam without singularity," *Nonlinear Dynamics*, vol. 67, no. 3, pp. 1825–1835, 2012.

[252] M. Alaydin, D. Benson, and Y. Bazilevs, "An updated Lagrangian framework for Isogeometric Kirchhoff–Love thin-shell analysis," *Computer Methods in Applied Mechanics and Engineering*, vol. 384, p. 113 977, 2021.

[253] A. Borković, B. Marussig, and G. Radenković, "Geometrically exact static isogeometric analysis of arbitrarily curved plane Bernoulli–Euler beam," *Thin-Walled Structures*, vol. 170, p. 108 539, 2022.

[254] B. Oesterle, F. Geiger, D. Forster, M. Fröhlich, and M. Bischoff, “A study on the approximation power of NURBS and the significance of exact geometry in isogeometric pre-buckling analyses of shells,” *Computer Methods in Applied Mechanics and Engineering*, vol. 397, p. 115 144, 2022.

[255] J. Guo, Y. Zhang, C. Wei, and Y. Zhao, “Energy–momentum integration and analysis for sliding contact coupling dynamics in large flexible multibody system,” *Nonlinear Dynamics*, 2022.

[256] W. Wen, H. Li, T. Liu, S. Deng, and S. Duan, “A novel hybrid sub-step explicit time integration method with cubic B-spline interpolation and momentum corrector technique for linear and nonlinear dynamics,” *Nonlinear Dynamics*, 2022.

[257] M. Eisenberg and R. D. Guy, “A proof of the hairy ball theorem,” *American Mathematical Monthly*, vol. 86, pp. 571–574, 1979.

[258] I. Romero and M. Arnold, “Computing with Rotations: Algorithms and Applications,” in *Encyclopedia of Computational Mechanics Second Edition*, Chichester, UK: John Wiley & Sons, Ltd, 2017, pp. 1–27.

[259] R. Huston and J. Kamman, “A representation of fluid forces in finite segment cable models,” *Computers & Structures*, vol. 14, no. 3-4, pp. 281–287, 1981.

[260] F. Auricchio, L. B. Da Veiga, T. J. R. Hughes, A. Reali, and G. Sangalli, “Isogeometric Collocation Methods,” *Mathematical Models and Methods in Applied Sciences*, vol. 20, no. 11, pp. 2075–2107, 2010.

[261] J. Kiendl, F. Auricchio, L. Beirão da Veiga, C. Lovadina, and A. Reali, “Isogeometric collocation methods for the Reissner–Mindlin plate problem,” *Computer Methods in Applied Mechanics and Engineering*, vol. 284, pp. 489–507, 2015.

[262] C. G. Gebhardt, I. Romero, and R. Rolfes, “A new conservative/dissipative time integration scheme for nonlinear mechanical systems,” *Computational Mechanics*, vol. 65, no. 2, pp. 405–427, 2020.

[263] R. L. Burden and J. D. Faires, *Numerical Analysis*, 9th. Boston, MA: Brooks/-Cole, 2011.

[264] C. G. Gebhardt, B. Hofmeister, C. Hente, and R. Rolfes, “Nonlinear dynamics of slender structures: a new object-oriented framework,” *Computational Mechanics*, vol. 63, no. 2, pp. 219–252, 2019.

[265] A. Masud, C. L. Tham, and W. K. Liu, “A stabilized 3-D co-rotational formulation for geometrically nonlinear analysis of multi-layered composite shells,” *Computational Mechanics*, vol. 26, no. 1, pp. 1–12, 2000.

[266] F. Auricchio, L. Beirão da Veiga, J. Kiendl, C. Lovadina, and A. Reali, “Locking-free isogeometric collocation methods for spatial Timoshenko rods,” *Computer Methods in Applied Mechanics and Engineering*, vol. 263, pp. 113–126, 2013.

[267] H.-O. Kreiss and O. E. Ortuz, *Introduction to Numerical Methods for Time Dependent Differential Equations*. London: Wiley, 2014.